

POLYTECHNIQUE MONTRÉAL

affiliée à l'Université de Montréal

**Modélisation des écoulements de gaz raréfiés au travers de filtres fibreux par
la méthode de Boltzmann sur réseau**

JEAN-MICHEL TUCNY

Département de génie chimique

Thèse présentée en vue de l'obtention du diplôme de *Philosophiæ Doctor*

Génie chimique

Décembre 2020

POLYTECHNIQUE MONTRÉAL

affiliée à l'Université de Montréal

Cette thèse intitulée :

**Modélisation des écoulements de gaz raréfiés au travers de filtres fibreux par
la méthode de Boltzmann sur réseau**

présentée par **Jean-Michel TUCNY**

en vue de l'obtention du diplôme de *Philosophiae Doctor*

a été dûment acceptée par le jury d'examen constitué de :

Nick VIRGILIO, président

François BERTRAND, membre et directeur de recherche

David VIDAL, membre et codirecteur de recherche

Sébastien LECLAIRE, membre et codirecteur de recherche

Marc LAFOREST, membre

Junfeng ZHANG, membre externe

DÉDICACE

Aux gens qui ont perdu quelqu'un en raison de la pandémie de COVID-19,

REMERCIEMENTS

Je veux commencer par remercier mon directeur de recherche, François Bertrand, pour la confiance qu'il m'a octroyée pendant le déroulement de cette thèse. J'ai été chanceux de trouver un professeur qui reconnaît autant la valeur de la recherche fondamentale en ingénierie. Il s'est parfois passé des mois complets où dans nos réunions, je ne pouvais expliquer que des tentatives infructueuses de résolution de problème. Mais grâce à la liberté qu'il m'a donnée, j'ai éliminé les obstacles pièce par pièce, et j'ai pu produire une thèse vraiment originale. Malgré les commentaires initialement négatifs des réviseurs, j'ai pu bénéficier de sa confiance inébranlable.

Je veux aussi remercier mon codirecteur David Vidal pour sa patience au cours de ces longues années. J'ai pu profiter de ses conseils sur le débogage de la MBR, que j'ai pu suivre lors du développement de la MBR proposée dans cette thèse. Ses efforts pour m'enseigner comment mieux communiquer à l'oral et à l'écrit ont porté fruit. Avec son support au quotidien, j'ai été capable de me concentrer sur les tâches importantes de ma thèse. Je pouvais toujours compter sur sa disponibilité tôt le matin et tard le soir. Par ma faute j'en ai presque seulement profité le soir. Mais grâce à ses encouragements, maintenant je me lève presque tôt.

Je veux également remercier mon codirecteur Sébastien Leclaire pour son empathie et son écoute. Il a vraiment eu le tour de me valoriser pendant ses réunions seul à seul. Sa curiosité et sa bonne humeur sont très contagieuses. J'ai aussi eu la chance de bénéficier de ses compétences en programmation GPU avec la librairie ArrayFire, et il m'a enfin convaincu d'utiliser le logiciel de gestion de versions Git. Je regrette seulement de ne pas avoir collaboré plus tôt avec lui.

Le travail de recherche aurait été bien ennuyant sans la présence de mes collègues de l'URPÉI que j'ai eu la chance de côtoyer: Alexandre (Ahmad) Al-haiek, Rahi Avazpour, Christine Beaulieu, Tiffany Bellanger, Igor Belot, Olivier Bertrand, Charlotte van Engeland, Bastien Delacroix (Damien Delamontagne), Rémi Demol, Hicham Khelladi, Manon Lassaigne, Guillaume Matte-Deschênes, Ghazaleh Mirakhori, Laura Orabi, Faezeh Sabri, Shuli Shu, Bing Wang, Fan Zhang, j'en oublie peut-être... Je veux particulièrement remercier le professeur Bruno Blais, mon mentor bien avant le début de mon doctorat qui m'a incité à perfectionner mes connaissances en mathématiques et en physique et à continuer dans le domaine de la mécanique des fluides computationnelle. Je veux aussi remercier toutes les personnes d'origine iranienne du département de génie chimique avec qui j'ai eu la chance d'apprendre les rudiments du farsi.

Je veux remercier mes colocataires et mes anciens colocataires : Charles Brassard, Tomasz Drake, Marc-Olivier Tremblay et Jérôme Escudier, pour tous les moments qu'on a passés ensemble, pour toutes les dégustations de whisky qu'on a eues et pour l'écoute de Liebestraum par Arthur Rubinstein sans égratignures.

Je ne saurais être assez reconnaissant envers la communauté de balboa à Montréal. Découvrir la personnalité des gens à travers la danse sociale est une expérience indescriptible. On flotte toujours sur un nuage après avoir dansé le balboa. C'est une danse exigeante en termes de concentration, mais elle donne énormément en retour. Je veux remercier toutes mes partenaires qui m'ont toutes appris comment mieux lâcher prise. Je veux donner une mention spéciale à Julie Roy pour m'avoir référé au livre Feeling Good sur le traitement de la dépression et de l'anxiété. Je n'aurais pas été capable de terminer cette thèse dans les temps sans son écoute.

J'ai eu tant de conversations avec mes amis proches, la plupart étant aux études pendant mon doctorat. On s'est tant posé de questions sur la pertinence de nos études, sur notre succès, et si tout ça en valait la peine. Vous êtes trop nombreux pour que je puisse vous mentionner chacun et chacune, mais vous savez qui vous êtes.

Je veux finalement remercier mon père Michal, ma mère Nicole et mon frère Alexandre pour leur patience et leur écoute pendant ces longues années. J'ai été privilégié d'avoir une famille qui comprend bien la pertinence des longues études. C'est extrêmement rare, et j'espère glorifier leur travail par cette thèse. Je veux aussi remercier ma grand-mère Juliette de m'avoir transmis sa passion de l'enseignement, qui a motivé mon choix de poursuivre des études doctorales. Malheureusement, elle est morte de la COVID-19 quelques mois avant la remise de cette thèse, mais je suis certain qu'elle aurait été fière de moi.

RÉSUMÉ

Les particules fines suspendues dans l'air (aussi nommées aérosols) sont nocives pour la santé humaine et pour l'environnement. La filtration des aérosols (ou la séparation de ces particules de l'air) est donc un procédé d'une importance cruciale. Les filtres fibreux sont généralement choisis pour leur haute performance et leur compacité. L'ajout de nanofibres ($<1 \mu\text{m}$) déposées sur une couche de microfibres ou mélangées à des microfibres a été proposé pour améliorer ces filtres. La théorie de la fibre unique est souvent utilisée pour prédire la performance des filtres à aérosols. Cependant, cette théorie prend pour acquis que les fibres d'un filtre sont toutes du même diamètre et ignore donc les impacts potentiels de la structure multicoche. La simulation numérique directe des écoulements gazeux au travers de milieux fibreux doit être utilisée pour tenir compte des interactions entre les fibres. Or, les effets de raréfaction qui apparaissent autour des nanofibres doivent être considérés pour prédire quantitativement la performance des milieux filtrants.

Dans cette thèse, une méthode de Boltzmann sur réseau (MBR) est développée afin de calculer les écoulements de gaz raréfiés au sein des filtres fibreux. La MBR est une discrétisation de l'équation de Boltzmann, une description statistique des écoulements de gaz. Cependant, la MBR était à l'origine un solveur pour les équations de Navier-Stokes en régime du continuum. La MBR a donc été modifiée pour incorporer les phénomènes physiques suivants: a) le glissement, c'est-à-dire une vitesse d'écoulement non-nulle à la surface des fibres, et b), l'apparition de la couche de Knudsen, soit une zone de l'ordre du libre parcours moyen des molécules de gaz où la relation newtonienne entre la contrainte et le cisaillement est invalide. Pour ce faire, une condition frontière (CF) cinétique de *diffusive bounce-back* (DBB) a été étendue pour prendre en compte l'impact de la variation de la viscosité effective sur le glissement au sein de la MBR. De plus, cette CF cinétique est totalement locale, évite les références à une longueur caractéristique et définit sans ambiguïtés les populations autour des coins. Pour résoudre le problème de crénage causé par les déviations hors de l'équilibre thermodynamique, caractéristiques des écoulements raréfiés, une procédure de régularisation a été incorporée dans la MBR. De nouvelles valeurs pour les paramètres cinétiques de la DBB au sein de la MBR ont également été calculées. Finalement, un algorithme de traçage des rayons a été développé pour évaluer le champ de libre parcours moyen effectif au sein d'un milieu poreux complexe au moyen d'une intégrale numérique. Sous hypothèse de proportionnalité entre le libre parcours moyen effectif et la viscosité effective, cette dernière peut être introduite dans la MBR pour représenter la relation entre la contrainte et le cisaillement

au sein de la couche de Knudsen de milieux poreux complexes. Le potentiel de parallélisation massive de la MBR et de l'algorithme de traçage des rayons rend ce modèle particulièrement approprié pour le calcul haute performance.

Il a été prévu d'utiliser cette nouvelle MBR pour évaluer la performance des filtres fibreux au moyen d'une méthodologie en trois étapes. D'abord, un milieu filtrant est généré numériquement par un algorithme de déposition séquentielle. La MBR est ensuite utilisée pour calculer le champ d'écoulement au sein du milieu filtrant et pour évaluer sa perméabilité. Finalement, les trajectoires de particules fines générées en amont du filtre sont calculées, permettant d'évaluer l'efficacité de capture du milieu. Cette méthodologie peut être utilisée comme outil de conception afin d'optimiser la performance des filtres fibreux. Dans la première partie de ce travail, cette méthodologie en trois étapes a été vérifiée, validée, et appliquée à l'étude des impacts de la structure multicouche sur la performance de milieux filtrants microfibreux. Lors de la deuxième partie de ce travail, la nouvelle MBR a été vérifiée et validée pour des écoulements au travers d'une fente, alors qu'elle a été vérifiée pour des écoulements au travers d'arrangements de cylindres et de sphères lors de la troisième partie de ce travail. L'algorithme de traçage des rayons a été vérifié lors de la quatrième et dernière partie de ce travail. De nouvelles pistes d'investigations fondamentales sont apparues lors des tentatives de validation du modèle combiné de la MBR et de l'algorithme de traçage des rayons. La thèse conclut sur une évaluation du modèle proposé et sur une suite de tâches à effectuer pour prédire quantitativement la performance des milieux filtrants en régime raréfié.

ABSTRACT

Suspensions of fine particles (also called aerosols) are harmful to human health and the environment. The filtration of airborne particles (or the separation of these particles from the air) is therefore a process of crucial importance. Fibrous filters are generally chosen for their high performance and compactness. The addition of nanofibers ($<1 \mu\text{m}$) deposited on a layer of microfibers or mixed with microfibers has been proposed to improve these filters. The single fiber theory is often used to predict the performance of aerosol filters. However, this theory assumes that the fibers of a filter are all the same diameter and therefore ignores the potential impacts of the multilayer structure. Direct numerical simulation of gas flows through fibrous media must be used to account for the interactions between the fibers. However, the rarefaction effects that occur around nanofibers must be considered to quantitatively predict the performance of the filter media.

In this thesis, a Lattice Boltzmann method (LBM) is developed to compute rarefied gas flows within fibrous filters. The LBM is a discretization of the Boltzmann equation, a statistical description of gas flows. However, the LBM was originally a solver for the Navier-Stokes equations in the continuum regime. The LBM was thus modified to incorporate the following physical phenomena: a) slip, i.e. a non-zero flow velocity at the surface of the fibers, and b) the appearance of the Knudsen layer, a zone of the order of the mean free path of gas molecules where the Newtonian relationship between stress and shear is invalid. To do so, a kinetic diffusive bounce-back (DBB) boundary condition (BC) was extended to take into account the impact of the variation of the effective viscosity on the slip within the LBM. Moreover, this kinetic BC is totally local, avoids references to a characteristic length and unambiguously defines the populations around corners. To avoid the phenomenon of aliasing caused by deviations out of thermodynamic equilibrium, characteristic of rarefied flows, a regularization procedure has been incorporated in the LBM. New values for the kinetic parameters of the DBB within the LBM were also calculated. Finally, a ray-tracing algorithm was developed to evaluate the effective mean free path field in a complex porous medium by means of a numerical integral. Under the assumption of proportionality between the effective mean free path and the effective viscosity, the latter is introduced within the LBM to represent the relationship between stress and shear in the Knudsen layer of complex porous media. The massive parallelization potential of the LBM and of the ray-tracing algorithm makes this model particularly suitable for high-performance computing.

It was planned to use this new LBM to evaluate the performance of fibrous filters using a three-step methodology. First, a filter medium is numerically generated by a sequential deposition algorithm. The LBM is then used to calculate the flow field within the filter medium and to evaluate its permeability. Finally, the trajectories of fine particles generated upstream of the filter are computed, allowing the capture efficiency of the medium to be evaluated. This methodology can be used as a design tool to optimize the performance of fibrous filters. In the first part of this work, this three-step methodology has been verified, validated, and applied to the study of the impact of multilayering on the performance of microfibrous filter media. In the second part of this work, the new LBM was verified and validated for flows through a slit, while it was verified for flows through cylinder and sphere arrays in the third part of this work. The ray-tracing algorithm was verified in the fourth and last part of this work. New venues of fundamental investigation have emerged during the validation attempts of the combined model of the LBM and the ray-tracing algorithm. The thesis concludes with an evaluation of the proposed model and a series of tasks to be performed to quantitatively predict the performance of filter media in the rarefied regime.

TABLE DES MATIÈRES

DÉDICACE.....	III
REMERCIEMENTS	IV
RÉSUMÉ.....	VI
ABSTRACT	VIII
TABLE DES MATIÈRES	X
LISTE DES TABLEAUX.....	XV
LISTE DES FIGURES.....	XVI
LISTE DES SIGLES ET ABRÉVIATIONS	XXII
LISTE DES ANNEXES.....	XXIV
CHAPITRE 1 INTRODUCTION.....	1
1.1 Importance de la filtration	1
1.2 Historique	1
1.3 Types de particules.....	2
1.4 Caractérisation des filtres	3
1.5 Mécanismes de capture	6
1.6 Loi de Darcy	7
1.7 La théorie de la fibre unique et ses limites.....	8
1.8 Objectif général	11
CHAPITRE 2 REVUE DE LITTÉRATURE	12
2.1 Filtres fibreux multicouches.....	12
2.2 Mécanique des fluides en régime raréfié.....	15
2.2.1 Théorie cinétique des gaz.....	15
2.2.2 Le glissement aux parois	18

2.2.3	La couche de Knudsen	19
2.2.4	Mouvement des particules fines dans l'air.....	22
2.3	Méthode de Boltzmann sur réseau (MBR).....	24
2.3.1	Introduction à la MBR.....	24
2.3.2	Modélisation des écoulements raréfiés avec la MBR	28
2.3.3	Régularisation.....	30
2.4	Résumé et objectifs spécifiques	31
CHAPITRE 3 ARTICLE 1: IMPACT OF MULTILAYERING ON THE FILTRATION PERFORMANCE OF CLEAN AIR FILTER MEDIA		34
3.1	Introduction	34
3.2	Methodology	39
3.2.1	Multilayered filter medium generation	40
3.2.2	Air flow computation	41
3.2.3	Particle trajectory computation	41
3.3	Model Accuracy Assessment and Validation.....	43
3.3.1	Air flow computation assessment	43
3.3.2	Capture efficiency assessment	44
3.3.3	Capture efficiency validation	47
3.4	Numerical Investigation Plan.....	49
3.4.1	Impact of multilayering at moderate coarse-to-fine diameter ratios	50
3.4.2	Impact of interfacial flow phenomena between layers at moderate coarse-to-fine diameter ratios	51
3.4.3	Impact of interfacial flow phenomena between layers at a high coarse-to-fine ratio	53
3.5	Results and Discussion.....	54
3.5.1	Impact of multilayering at moderate coarse-to-fine diameter ratios	55

3.5.2 Impact of interfacial flow phenomena between layers at a high coarse-to-fine diameter ratio	61
3.5.3 Impact of interfacial flow phenomena between layers at a high coarse-to-fine diameter ratio	63
3.6 Conclusion and Perspectives.....	66
CHAPITRE 4 ARTICLE 2: COMPARISON OF EXISTING AND EXTENDED BOUNDARY CONDITIONS FOR THE SIMULATION OF RAREFIED GAS FLOWS USING THE LATTICE BOLTZMANN METHOD	69
4.1 Introduction	69
4.2 The Lattice Boltzmann method for Rarefied Flows.....	73
4.2.1 Propagation-collision scheme with multiple relaxation times	73
4.2.2 Relationship between relaxation times and the mean free path	76
4.2.3 Viscosity functions	77
4.2.4 Kinetic boundary conditions	79
4.2.5 Extended diffusive bounce-back boundary condition.....	83
4.3 Accuracy Assessment of the Extended Diffusive Bounce-Back Boundary Condition..	86
4.3.1 Convergence analysis	86
4.3.2 Verification of the proposed DBB BC scheme	90
4.4 Conclusions	92
CHAPITRE 5 ARTICLE 3: DEVELOPMENT OF A KINETIC SLIP BOUNDARY CONDITION FOR RAREFIED GAS FLOWS THROUGH NON-PLANAR GEOMETRIES BASED ON THE REGULARIZED LATTICE-BOLTZMANN METHOD	95
5.1 Introduction	96
5.2 Rarefied flow modeling.....	102
5.2.1 The generalized Navier-Stokes constitutive model.....	102
5.2.2 Slip flow boundary conditions	103

5.3	The regularized Lattice Boltzmann method	105
5.3.1	MRT-LBM	105
5.3.2	Regularization technique	110
5.3.3	Diffusive bounce-back boundary condition	112
5.3.4	A new diffusive bounce-back boundary condition	114
5.4	Numerical results.....	116
5.4.1	Dealiasing verification	117
5.4.2	Error analysis of a slit flow in the slip regime	119
5.4.3	Slip flow through a cylinder array.....	121
5.4.4	Slip flow around a sphere array.....	125
5.5	Further remarks on the new boundary condition	128
5.6	Conclusions	130
CHAPITRE 6 ARTICLE 4: SIMULATION OF RAREFIED GAS FLOWS THROUGH NON-PLANAR GEOMETRIES USING AN EFFECTIVE VISCOSITY FUNCTION CALCULATED FROM A RAY-TRACING ALGORITHM		153
6.1	Introduction	153
6.2	Effective viscosity functions	158
6.2.1	General formula of the effective viscosity function.....	158
6.2.2	Free path distribution functions.....	160
6.2.3	Angular distribution functions	162
6.2.4	Analytical solutions.....	163
6.3	Theoretical comparison between planar wall functions and results from Eq. (6.7).....	167
6.4	Ray-tracing algorithm	169
6.5	Ray-tracing algorithm verification	171
6.5.1	Planar flows.....	171

6.5.2 Array of cylinders.....	174
6.6 Rarefied flow verification and validation.....	178
6.6.1 Flow through a slit in the rarefied regime	179
6.6.2 Flow through a cylinder array in the rarefied regime.....	182
6.7 Conclusion.....	186
CHAPITRE 7 DISCUSSION GÉNÉRALE	193
CHAPITRE 8 CONCLUSION ET RECOMMANDATIONS	200
8.1 Synthèse des travaux	200
8.2 Recommandations	201
RÉFÉRENCES	203
ANNEXES	248

LISTE DES TABLEAUX

Tableau 1.1 Classifications des aérosols présents dans l'environnement - reproduit avec permission de [25].....	3
Tableau 1.2 Spécifications des filtres.....	5
Tableau 1.3 Standards du CEN – reproduit avec permission de [30]	5
Tableau 1.4 Classification du régime de raréfaction des écoulements gazeux	10
Table 3.1 Flow simulation parameters	43
Table 3.2 Experimental conditions used by Steffens and Coury [326] for particle diameters greater than 30 nm. The reported intervals represent the SDs around the mean values	48
Table 4.1 Velocity BCs and viscosity functions tested to verify of the extended DBB scheme.	91
Table 6.1 Effective mean free paths obtained from Eq. (6.7) for four different geometrical configurations.....	168
Table 6.2 Viscosity functions and slip coefficients for the velocity BC tested in a rarefied regime.	181

LISTE DES FIGURES

<p>Figure 1.1 Mécanisme de captures des particules fines dans l'air – reproduit avec permission de [1].....</p> <p>Figure 2.1 Représentation du glissement aux parois dans une fente.....</p> <p>Figure 2.2 Illustration du profil d'écoulement au sein de la couche de Knudsen, où \mathbf{u}_s est la véritable vitesse de glissement et $\mathbf{u}_s(ns)$ est la vitesse de glissement extrapolée à partir du champ de vitesse à l'extérieur de la couche de Knudsen</p> <p>Figure 2.3 Débit massique adimensionnalisé M_p en fonction de $k = Kn2/\pi$ – reproduit avec permission de [171].....</p> <p>Figure 2.4 Conditions frontières cinétiques pour la MBR de: a) rebond à mi-chemin, b) réflexion spéculaire, c) diffusion</p> <p>Figure 2.5 CF cinétique de réflexion spéculaire dans un coin.</p> <p>Figure 3.1 Illustration of the three-step numerical procedure used: A, a representative elementary volume of a bimodal filter medium; B, the computed flow field through the corresponding filter media; and C, the calculated particle trajectories through the same filter medium (the green and red trajectories correspond to the trajectories of the particles being intercepted by the filter medium or flowing through it, respectively)</p> <p>Figure 3.2 Comparison between dimensionless Darcy permeabilities computed with the lattice Boltzmann method and Davies' correlation. The error bars represent standard deviations obtained for triplicate numerical computations.....</p> <p>Figure 3.3 Comparison between the capture efficiencies computed with the lattice Boltzmann method-based model and literature correlation-based predictions for filter media made of: a) 3 μm; b), 5μm; and c); 7 μm fibres. The error bars represent standard deviations obtained from triplicate numerical computations</p> <p>Figure 3.4 Comparison between the capture efficiencies at the most penetrating particle size for filter media made of monodisperse fibres (with diameters ranging between 3 μm-7 μm) predicted with the lattice Boltzmann method-based model and the median of the correlation-based predictions. The x-axis error bars represent standard deviations obtained from triplicate</p>	<p>6</p> <p>18</p> <p>19</p> <p>20</p> <p>28</p> <p>30</p> <p>39</p> <p>44</p> <p>46</p>
---	--

numerical computations, whereas the y-axis error bars reflect the 50 th percentile interval around the median from all these correlation-based predictions.....	47
Figure 3.5 Comparison between single-fibre efficiencies obtained from our code to from experimental data from Steffens and Coury. [326] The x-axis error bars represent standard deviations on the single-fibre efficiency calculated from the reported data. The y-axis error bars represent standard deviations obtained from triplicate numerical computations	49
Figure 3.6 Summary of the structures and the range of the various parameters investigated in the first study.....	51
Figure 3.7 Summary of the structures and the range of the various parameters investigated in the air gap study	52
Figure 3.8 Summary of the five configurations and parameters used to test the impact of interfaces between layers on three-layered filter media made of fibres with a high coarse-to-fine diameter ratio.....	54
Figure 3.9 Examples of representative elementary volumes of filter media created by the fibre deposition algorithm to study the impact of multilayering for the: a), two-layered; b), eight-layered; and c), well-mixed cases, with $dC = 12 \mu\text{m}$ and $xF = 30\%$	56
Figure 3.10 Porosity profiles of the filter medium structures shown in Figure 3.9. Data are averaged values over 5-μm-thick slices of the filter media	57
Figure 3.11 Mean porosities of the various multilayered and well-mixed filter media for six fibre formulations. The error bars represent standard deviations obtained from triplicate computations	57
Figure 3.12 A two-dimensional cross section of a typical flow field through a well-mixed filter medium computed with the lattice Boltzmann method. Black arrows represent the three-dimensional velocity vectors passing through the cross-sectional plane in the x direction...	58
Figure 3.13 Effects of the multilayered filter medium structure and fibre formulation on: A, permeability; B, capture efficiency; and C, the quality factor at the most penetrating particle size ($\sim 300 \text{ nm}$). The error bars represent standard deviations obtained from triplicate computations. Note that the impact of RCF on the various properties cannot be readily assessed because of the variations in porosity and thickness.....	60

Figure 3.14 Impact of the insertion of seven air gaps in an eight-layered filter media on the: A, pressure drop; B, capture efficiency; and C, quality factor at the most penetrating particle size (~ 300 nm). The pressure drop was normalized to the pressure drop in the case with no air gaps. The error bars represent a 95% binomial confidence interval, assuming the capture process follows a Bernoulli process [326]	63
Figure 3.15 Examples of representative elementary volumes of filter media created by the fibre deposition algorithm to study the impact of multilayering at $RCF = 10$, namely the: A, gap; and B, sandwiched configurations	64
Figure 3.16 Pressure drop through the different three-layered configurations for three randomly generated sets of filter media. Note the truncated scale	65
Figure 3.17 Comparison of the contribution of a single coarse fibre to the pressure drop when it is between two layers of fine fibres (sandwiched minus gap configurations), next to one layer of fine fibres (upstream minus no gap configurations), or isolated (alone configuration).....	66
Figure 4.1 D2Q9 velocity set used for LBM where \mathbf{c}_i is the velocity vector in direction i	75
Figure 4.2 Kinetic BC schemes for LBM: (a) the bounce-back BC, (b) the specular reflection BC, and (c) the diffusive scattering BC. The parameter Δ sets the position of the wall at the frontier node. As half-way BCs are used here, $\Delta = 12$	80
Figure 4.3 Schematic of specular reflection at a corner. The destination of the population at location \mathbf{x}_f is not well defined: both destinations \mathbf{x}_f^* and \mathbf{x}_f^{**} should be considered.....	85
Figure 4.4 Schematic representation of the slit flow test case.	87
Figure 4.5 L_2 relative error for the BGK-LBM scheme without slip for the slit flow test case..	88
Figure 4.6 L_2 relative error of the MRT-LBM scheme with slip for a fixed Knudsen number $Kn = 1$ and a τ_s defined by Eq. (4.15) for the slit flow test case.	89
Figure 4.7 L_2 relative error of the MRT-LBM scheme with slip for a fixed $\tau_s = 1$ and a corresponding Knudsen number defined by Eq. (4.15) for the slit flow test case.	90
Figure 4.8 Predictions of the normalized mass flow for a rarefied slit flow for LBM with the extended DBB BC compared with experimental data and other methods. Acronyms refer to the cases presented in Table 4.1.	92

Figure 5.1 Illustration of the velocity in the Knudsen layer. The true slip velocity us is smaller than the Navier-Stokes fictitious velocity $us(ns)$ that would be recovered if the Navier-Stokes equations were used inside the Knudsen layer.....	105
Figure 5.2 D2Q9 velocity set used for the LBM where \mathbf{c}_i is the velocity in direction i . The wall is located half-way from the node.....	109
Figure 5.3 D3Q15 velocity set used for the LBM where \mathbf{c}_i is the velocity in direction i . The wall was omitted here for the sake of clarity. It is located half-way from the node to the destination of populations 6, 11, 12, 13, and 14.....	109
Figure 5.4 Schematic representation of (a) the square-cylinder flow case, (b) the slit flow case, (c) the cylinder array case, and (d) the sphere array case. Except for the slit flow case for which there are walls at the x-boundaries, periodic BCs were imposed along every outer boundary, which repeats the structure infinitely in every direction.....	117
Figure 5.5 Norm of the y-component of the velocity for the flow around a square-section cylinder obtained with (a) the non-regularized MRT-LBM and (b) the regularized MRT-LBM.....	118
Figure 5.6 L_2 relative error ($E(v)$) of the velocity computed using the regularized MRT-LBM scheme and the D2Q9 lattice with slip and $\Psi\mathbf{x} = 1$ at $Kn = 1$ as a function of lattice spacing δx for the slit flow test case.....	120
Figure 5.7 L_2 relative error ($E(v)$) of the velocity computed using the regularized MRT-LBM scheme and the D3Q15 lattice with slip and $\Psi\mathbf{x} = 1$ at $Kn = 1$ as a function of lattice spacing δx for the slit flow test case.....	121
Figure 5.8 Schematic representation of Pich's original analytical hypothesis	122
Figure 5.9 Predictions of the normalized face velocity for a slip flow through a cylinder array for the new D2Q9 regularized MRT-LBM scheme at different 2D lattice resolutions compared to the modified Pich analytical solution (Eq. (5.47)).	124
Figure 5.10 Predictions of the normalized face velocity for a flow around a cylinder for the new D3Q15 regularized MRT-LBM scheme at different 3D lattice resolutions compared to the modified Pich analytical solution (Eq. (5.47)) for a slip flow around a cylinder.....	125

Figure 5.11 Predictions of the normalized face velocity for a flow through a sphere array for the new D3Q15 regularized MRT-LBM scheme compared with the modified Datta and Deo's analytical solution (Eq. (5.53)) for a slip flow around a sphere.....	127
Figure 6.1 Directional mean free path expressions derived in Subsection 6.2.2 and from the literature	162
Figure 6.2 Comparison of four effective mean free paths calculated with a wall-function in the case of (a) a point, (b) the interior of a cylinder, (c) the interior of a sphere, and (d) a slit. The chosen point is always located one bulk mean free path λ away from the solid object.....	168
Figure 6.3 Illustration of the ray-tracing procedure on a regular Cartesian grid containing solid objects (in black).	171
Figure 6.4 Illustration of the ray-tracing procedure with: (a) a non-rotated ray direction base and (b) a rotated ray direction base.....	172
Figure 6.5 L_2 relative error $E\Psi$ of the effective viscosity function Ψ using the ray-tracing algorithm for a slit geometry with (full symbols) and without (empty symbols) ray direction base rotation and for two different ray steps (Δr).	173
Figure 6.6 Effective mean free path ($\lambda e(\mathbf{x})$) fields around an element of a periodic array of cylinders, as a function of the number of angles used: (a) $N\theta = 4$, (b) $N\theta = 32$, (c) $N\theta = 64$	176
Figure 6.7 L_2 relative error $E\Psi$ of the effective viscosity function Ψ for a cylinder array geometry using the ray-tracing algorithm, as a function of the angular step.....	177
Figure 6.8 L_2 relative error $E\Psi$ of the effective viscosity function Ψ for a cylinder array geometry using the ray-tracing algorithm, as a function of grid size.....	178
Figure 6.9 Schematic representations of the flow simulated through: (a) a slit and (b) an array of cylinders.	179
Figure 6.10 Relative error of the volumetric flow rate for a slit geometry using the LBM code as an extended Navier-Stokes solver with the viscosity function computed using the ray-tracing algorithm.	180

Figure 6.11 Prediction of the normalized mass flow for a rarefied slit flow using the LBM w/RT code as an extended Navier-Stokes solver compared with numerical solution of the linearized Boltzmann equation [171] and experimental results [352] reported by Guo et al. [236]. Acronyms refer to the methods presented in Table 6.2.....	182
Figure 6.12 Relative error of the volumetric flow rate for a periodic array of cylinders using the LBM w/RT code as an extended Navier-Stokes solver with the viscosity function computed using the ray-tracing algorithm.	183
Figure 6.13 Predictions of the normalized mass flow for a cylinder array using the LBM w/RT code as an extended Navier-Stokes solver with the viscosity function computed with the ray-tracing algorithm.	184

LISTE DES SIGLES ET ABRÉVIATIONS

BC	<i>Boundary condition</i>
BE	<i>Boltzmann equation</i>
BGK	Bhatnagar-Gross-Krook
CEN	Comité européen de normalisation
CBBSR	<i>Combined bounce-back and specular reflection</i>
CF	Condition frontière
COVID-19	Maladie à coronavirus 2019
D2Q9	Réseau bidimensionnel à 9 populations
D2Q25	Réseau bidimensionnel à 25 populations
D2Q4624	Réseau bidimensionnel à 4624 populations
D2Q4761	Réseau bidimensionnel à 4761 populations
D3Q15	Réseau tridimensionnel à 15 populations
DBB	<i>Diffusive bounce-back</i>
DOM	<i>Discrete ordinate method</i>
DSMC	<i>Direct simulation Monte-Carlo</i>
DSR	<i>Diffusive specular reflection</i>
DUGKS	<i>Discrete unified gas kinetic scheme</i>
DVM	<i>Discrete velocity method</i>
LBM	<i>Lattice Boltzmann method</i>
MBR	Méthode de Boltzmann sur réseau
MBR-TRM	Méthode de Boltzmann sur réseau à temps de relaxations multiples
MD	<i>Molecular dynamics</i>
MEMS	<i>Microelectromechanical systems</i>

MRT-LBM *Multiple relaxation times Lattice Boltzmann method*

NEMS *Nanoelectromechanical systems*

NS *Navier-Stokes*

NSEs *Navier-Stokes equations*

RT *Ray-tracing*

TRM *Temps de relaxations multiples*

LISTE DES ANNEXES

ANNEXE A EXPRESSIONS POUR LE DIAMÈTRE ÉQUIVALENT	248
ANNEXE B MODÈLES POUR LE FACTEUR DE CUNNINGHAM	251
ANNEXE C RÉSEAUX D2Q9 ET D3Q15.....	253
ANNEXE D TEMPS DE RELAXATIONS MULTIPLES AVEC LA MBR POUR LES RÉSEAUX D2Q9 ET D3Q15	255

CHAPITRE 1 INTRODUCTION

1.1 Importance de la filtration

La filtration est un procédé utilisé dans un vaste nombre d'applications dans la vie quotidienne et en milieu industriel. Parmi les exemples de la vie quotidienne figurent : a) les filtres à café, qui servent à filtrer les graines du café, b) les masques faciaux, qui servent à filtrer les particules fines de l'air, et c) les filtres à osmose inverse, qui servent à capturer des ions de l'eau [2]. Comme procédé industriel, l'opération de filtration peut remplir deux objectifs : retirer un contaminant d'un fluide afin de rendre ce dernier plus pur, ou retirer un produit d'intérêt d'un fluide dans le but d'en extraire le plus possible [3]. D'après une définition librement traduite de l'anglais du *Handbook of Filter Media*, l'équipement employé pour ce procédé, un milieu filtrant est :

« [...] tout matériau qui, sous les conditions d'opérations du filtre, est perméable à un ou plusieurs composants d'un mélange, d'une solution ou d'une suspension, et est imperméable au reste des composants. » [3]

Pour ce travail de recherche en particulier, nous nous intéresserons à la filtration des particules fines suspendues dans l'air, aussi nommées aérosols. Ces particules sont nocives pour la santé humaine et pour l'environnement. Le smog, partiellement composé de particules fines, engendre des problèmes de santé majeurs dans la population [4, 5]. Des bactéries et des virus peuvent être absorbées par la voie respiratoire et causer des irritations et des maladies [6]. Plus de patients avec des maladies cardiovasculaires fréquentent les hôpitaux lorsque la concentration en particules fines présentes dans l'air est élevée [7]. Des poussières peuvent également être inhalées en milieu de travail. Les gouvernements, les industries et la population en général sont davantage conscients des impacts sur la santé et investissent pour s'attaquer à ce fléau de notre société contemporaine [6, 8].

1.2 Historique

Le problème de la poussière industrielle a été mentionné il y a presque 2000 ans par Pline l'Ancien dans sa célèbre encyclopédie *Histoire naturelle* [9]. Historiquement, la protection des travailleurs qui œuvrent dans les milieux où il y a des poussières dangereuses et la protection contre les armes chimiques ont motivé le développement de la technologie de filtration des aérosols [9].

L'utilisation de chiffons humides contre la fumée aurait également été décrite par Léonard de Vinci. Agricola (1494-1555) discute des problèmes respiratoires causés par la poussière dans les mines et a proposé des respirateurs pour les mineurs [10]. Paracelsus (1493-1541), fondateur de la toxicologie [11], aurait également décrit des maladies causées par les poussières [12, 13]. Le premier respirateur comme tel aurait été fabriqué par Brisé Faden en 1814, qui consistait en une boîte remplie de coton avec un tube pour y respirer au travers [13].

Au XXème siècle, maintes innovations portant sur la filtration des aérosols ont vu le jour. Diverses conceptions comportant des polymères, des fibres cellulosiques et des résines solidifiantes ont permis de mélanger des fibres de tailles différentes et de concevoir des filtres multicouches [6, 14]. Certains matériaux comme les céramiques et les métaux ont été utilisés pour opérer à des températures plus élevées au sein de procédés chimiques [6, 14]. L'utilisation de fibres avec des diamètres de l'ordre du micromètre [9], puis à l'échelle nanométrique (de 300 nm [15] jusqu'à 10 nm [16]) a été proposée pour améliorer les filtres à haute efficacité.

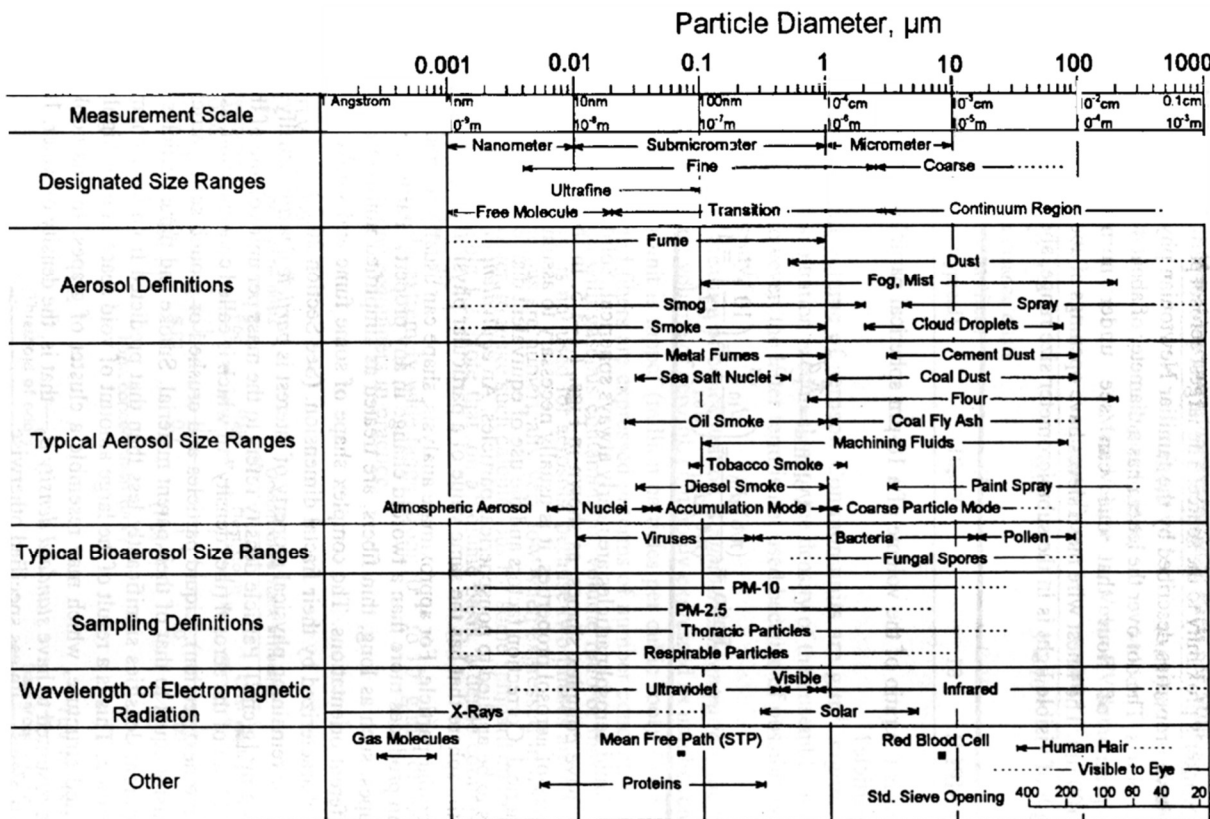
Le port des masques chirurgicaux s'est normalisé au sein des blocs opératoires vers les années 1920 [17]. Les masques jetables à usage unique ont été introduits au milieu des années 1960 afin de réduire les coûts et d'assurer la stérilité des environnements [18]. La lutte contre la pandémie de COVID-19 a provoqué une hausse vertigineuse de l'utilisation des masques jetables [19]. L'approvisionnement en masques faciaux est devenu un moyen de pression diplomatique peu après le début de la pandémie [20-22]. Pour sécuriser ses chaînes logistiques, le gouvernement du Québec a versé des fonds pour une production nationale de masques faciaux [23]. À plus long terme, la viabilité de ces nouvelles industries dépendra des innovations visant à améliorer la performance des masques et à réduire leur coût. Des initiatives de masques biodégradables ont aussi été avancées afin de limiter la production de déchets [24].

1.3 Types de particules

Les particules fines sont catégorisées selon leur forme et leur taille, qui peut aller de 2 nm à 100 µm [9, 25]. Par exemple, les fumées, générées par les condensations de produits de combustions, sont distinguées des poussières, produites par la désintégration d'un matériau originel (ex. : une machine, un textile ou une roche), qui sont elles-mêmes distinguées d'un brouillard, l'eau condensée sous forme de particules liquides [25]. Le smog, dont le terme est dérivé de *smoke*

(fumée) et *fog* (brouillard), peut désigner les particules fines créées par les oxydes d'azote, de soufre ou d'ammoniac relâché dans l'atmosphère, mais inclut également les particules provenant de pots d'échappement ou de cheminées [25, 26]. Cependant, le smog comprend aussi l'ozone troposphérique, qui reste sous forme gazeuse et n'est donc pas composé de particules. Le tableau 1.1 résume bien les différentes catégorisations des aérosols.

Tableau 1.1 Classifications des aérosols présents dans l'environnement - reproduit avec permission de [25]



1.4 Caractérisation des filtres

Les écoulements au sein des filtres à aérosols sont généralement mués par une différence de pression entre l'entrée et la sortie du filtre [3, 6]. La conception du filtre employé dépend principalement de quatre paramètres : le débit d'air à filtrer, les dimensions maximales du filtre, l'efficacité de capture acceptable et la perte de charge acceptable [3, 6, 9, 14, 25]. Par exemple, un masque facial doit rester compact, occasionner une perte de charge inférieure à 50 Pa [27] et avoir

une efficacité de capture conséquente avec les types de particules auxquelles la personne sera exposée.

Maintes catégories de filtres à aérosols peuvent être distinguées selon le type de médium poreux ou la forme du filtre. Les filtres en céramiques et en métal, quant à eux, sont plus rigides et résistent à des températures plus élevées [16]. Les matières fibreuses sont les plus économiques pour des concentrations faibles de particules fines [3, 6, 28].

La forme extérieure des filtres dépend principalement des contraintes de dimension posées par le système. On distingue les coussinets, qui sont très plats, des sacs, des poches et des panneaux [3, 6]. Ces derniers sont plus volumineux, mais plus appropriés pour de grands débits d'air [29]. Les capsules, quant à elles, sont des filtres de petite dimension utilisés principalement dans l'industrie pharmaceutique. Mentionnons également les dévésiculeurs, qui ont pour objectif d'enlever les gouttelettes d'eau d'un courant d'air [30]. Ces derniers sont utilisés autant en contexte industriel que dans des contextes domestiques (ex. un système d'air climatisé) [3, 31].

En ce qui a trait à la forme intérieure, les filtres présentant le plus de variabilité sont les filtres constitués de matière fibreuse. Ces derniers peuvent être plats, ou plissés (*pleated filters*) pour agrandir la surface de capture [31, 32]. Ils peuvent être monocouches comme multicouches afin d'améliorer les propriétés mécaniques des filtres, telle que la résistance à des contraintes [29, 33]. En pratique, les systèmes de filtration pour les bâtiments sont souvent composés de plusieurs sous-systèmes. Les filtres peuvent s'encrasser rapidement avec de grosses particules : or, celles-ci sont généralement capturées en amont par des filtres grossiers peu dispendieux. En aval, un sous-système composé de microfibres ou même de nanofibres peut être employé. L'ajout d'une couche de nanofibres améliore la performance des filtres, mais beaucoup de travaux de recherche doivent encore être effectués pour mieux comprendre l'impact de la structure multicouche. Ce projet de doctorat s'inscrit dans cette démarche plus large d'optimisation des filtres fibreux.

Pour mieux comprendre le fonctionnement des filtres fibreux, les termes permettant leur caractérisation quantitative seront énoncés. Le tableau 1.2 résume les définitions de la porosité, l'efficacité de capture, la perte de charge et du facteur de qualité.

Tableau 1.2 Spécifications des filtres

Caractéristique	Définition	Unité SI
Porosité	$\epsilon = \frac{\text{Volume d'air}}{\text{Volume total}}$	Adimensionnel
Efficacité de capture	$E = \frac{\# \text{ Particules capturées}}{\# \text{ Particules en amont}}$	Adimensionnel
Perte de charge	$\Delta P = P_{\text{entrée}} - P_{\text{sortie}}$	Pa
Facteur de qualité	$q_F = \frac{-\ln(1 - E)}{\Delta P}$	Pa ⁻¹

En pratique, le choix des filtres pour une application donnée se base surtout sur leur certification. Le tableau 1.3 résume par exemple les standards du Comité européen de normalisation (CEN) pour les équipements de filtration d'air, qui classifie les filtres selon l'utilisation prévue et l'efficacité de capture [31].

Tableau 1.3 Standards du CEN – reproduit avec permission de [30]

Type	Eurovent class	CEN EN779 class	Efficiency (%)	Measured by	Standards
Coarse dust filter	EU1	G1	<65	Synthetic dust weight	ASHRAE 52-76
	EU2	G2	65<80	arrestance	Eurovent 4/5
	EU3	G3	80<90		
	EU4	G4	>90		
Fine dust filter	EU5	F5	40<60	Atmospheric dust spot efficiency	BS 6540
	EU6	F6	60<80		
	EU7	F7	80<90		DIN 24 185
	EU8	F8	90<95		
	EU9	F9	>95		EN 779
High efficiency particulate air filter (HEPA)	EU10	H10	85	Sodium chloride	BS 3928
	EU11	H11	95	or liquid	Eurovent 4/5
	EU12	H12	99.5	aerosol	DIN 24 184
	EU13	H13	99.95		(DIN 24 183)
	EU14	H14	99.995		
Ultra low penetration air filter (ULPA)	EU15	U15	99.9995	Liquid aerosol	DIN 24 184
	EU16	U16	99.99995		(DIN 24 183)
	EU17	U17	99.999995		

1.5 Mécanismes de capture

Les particules suspendues dans l'air peuvent être capturées de quatre manières différentes [3, 6]. Quand le diamètre d'une particule est plus grand que le pore d'un filtre, la particule est capturée par une barrière de surface. Quand la particule parvient initialement à pénétrer le filtre, mais rencontre un pore trop petit, la particule est capturée par une barrière de profondeur. Quand des particules accumulées en amont empêchent les particules subséquentes de passer, on parle de filtration avec un gâteau. Quand une particule adhère au filtre dépendamment de sa trajectoire au sein du filtre, on parle de filtration en profondeur.

Pour les aérosols, les deux derniers mécanismes sont prépondérants en raison de la faible taille des particules à capturer [3, 28]. En pratique, les gâteaux se forment surtout lorsque la concentration en particules fines est élevée. Pour beaucoup d'applications, la concentration en particules fines est faible et c'est la filtration en profondeur qui domine [3]. La filtration en profondeur peut s'expliquer par cinq mécanismes de capture [1, 32] : l'impaction inertia, l'interception, la diffusion brownienne, les forces électrostatiques et la force gravitationnelle. Ces cinq mécanismes sont représentées à la Figure 1.1 [1].

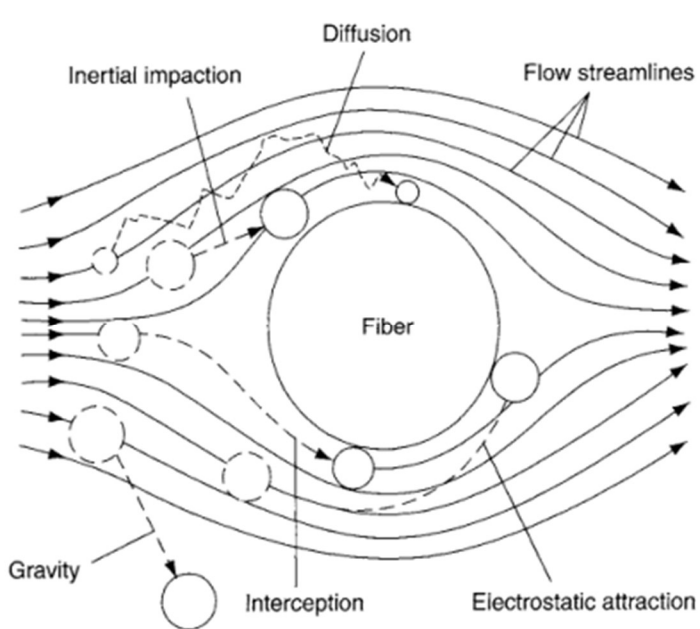


Figure 1.1 Mécanisme de captures des particules fines dans l'air – reproduit avec permission de [1].

L'impaction inertia se produit lorsqu'une particule, en raison de son inertie, percute une fibre et est capturée [1]. Ce mécanisme est prépondérant lorsque la vitesse de l'air est grande et que les particules sont relativement grosses [6, 32, 34]. Les particules capturées grâce à ce mécanisme s'accumulent généralement en amont de la fibre [35]. L'interception résulte du patron d'écoulement autour des fibres. Si une particule est située dans une ligne de courant passant à moins d'un rayon de particule de la fibre, elle peut être

capturée [1]. Ce mécanisme est prépondérant pour des particules relativement grosses lorsque la vitesse de l'écoulement est faible [32, 34]. La diffusion brownienne est causée par le mouvement aléatoire des molécules d'air autour d'une particule, qui peut approcher une particule d'une fibre [1]. Ce mécanisme est prépondérant pour de petites particules [3, 6, 32, 34]. Les forces électrostatiques sont causées par l'attraction entre des charges de signes opposés situées sur la particule et sur le filtre. Ces forces peuvent améliorer grandement l'efficacité d'un filtre : cependant, elles impliquent que le filtre soit chargé électriquement, du moins localement [6]. Pour certaines applications, comme les masques faciaux et les machines à air climatisé, l'humidité relative élevée tend à neutraliser les charges présentes au sein du filtre [32]. Pour terminer, le mécanisme de gravité se produit lorsque les particules finissent par tomber sur les fibres d'un filtre. Ce mécanisme est seulement notable pour de très grosses particules ($>10 \mu\text{m}$) et est souvent faible comparé au mécanisme inertiel [32]. Les forces électrostatiques et gravitationnelles seront négligées au cours de ce travail.

1.6 Loi de Darcy

Un des facteurs les plus déterminants dans la conception d'un filtre est sa perte de charge, c.-à-d. la chute de pression causée par la résistance à l'écoulement. En négligeant la gravité, la loi de Darcy prédit une relation linéaire entre la vitesse d'un fluide \mathbf{u}_0 et le gradient de pression dans le milieu ∇P [36] :

$$\mathbf{u}_0 = \frac{\mathbf{q}}{A} = -\frac{\kappa}{\mu} \cdot \nabla P \quad (1.1)$$

où \mathbf{q} est le débit moyen du fluide, κ est le tenseur de perméabilité du milieu poreux, A est la surface normale à l'écoulement et μ est la viscosité du fluide considéré. Lorsque le milieu est isotrope, la perméabilité est un scalaire multiplié par un tenseur identité. En supposant une perte de charge est unidirectionnelle au sein d'un milieu isotrope, la relation suivante est retrouvée :

$$u_0 = \frac{\kappa \Delta P}{\mu h} \quad (1.2)$$

où ΔP est la perte de charge dans la direction du milieu et h est l'épaisseur du milieu poreux. En supposant que les fibres ont un diamètre uniforme d_f , l'analyse dimensionnelle des filtres fibreux donne une expression pour la perte de charge [37]:

$$\kappa = \frac{d_f^2}{f(\alpha)} \quad (1.3)$$

où $f(\alpha)$ est une fonction qui dépend de la géométrie et de la fraction de solide $\alpha = 1 - \epsilon$. En mécanique des milieux continus, la perméabilité est donc une caractéristique intrinsèque d'un milieu poreux, qui dépend purement de sa structure et non de l'écoulement du fluide au travers [36]. La valeur de la perméabilité peut varier fortement entre filtres de différentes constitutions, d'au moins un ordre de grandeur [38]. Cependant, pour des milieux nanoporeux, où la mécanique des milieux continus ne tient plus, la valeur de la perméabilité peut augmenter de plusieurs ordres de grandeur [39, 40]. La loi de Darcy n'est également valide qu'en régime laminaire. L'équation de Forcheimer est préférée en régime turbulent, où une composante quadratique à la relation de la perte de charge avec le débit est rajoutée [41].

1.7 La théorie de la fibre unique et ses limites

La théorie de la fibre unique tente de prédire l'efficacité d'un filtre fibreux à l'aide d'un modèle simplifié : les fibres forment un arrangement parallèle, régulier, et ont toutes de même diamètre. Ces hypothèses sont défendables dans la mesure où les fibres ont typiquement peu de contact entre elles en raison de leur grande porosité [1, 28]. Le mouvement macroscopique des particules doit aussi suivre celui de l'air. Finalement, une particule est considérée comme capturée lorsqu'elle se situe à moins d'un rayon de particule de la surface d'une fibre. L'efficacité de capture d'une seule fibre est développée en reliant l'efficacité de capture aux autres caractéristiques mesurables du filtre : diamètre des fibres, porosité, vitesse de l'écoulement, etc. À l'aide d'un bilan de matière sur les particules d'un filtre, l'efficacité du filtre complet prend la forme suivante [1, 28, 34, 42, 43] :

$$E = 1 - \exp\left(-\frac{4\alpha h}{\pi d_f(1-\alpha)} \eta_\Sigma\right) \quad (1.4)$$

où η_Σ est l'efficacité de capture de fibre unique causée par l'ensemble des mécanismes.

L’efficacité d’un filtre croît donc avec son épaisseur. Or, selon la loi de Darcy, la perte de charge augmente linéairement avec l’épaisseur du filtre. Pour comparer des filtres d’épaisseurs différentes, on utilise le facteur de qualité q_F :

$$q_F = \frac{-\ln(1 - E)}{\Delta P} \quad (1.5)$$

En insérant la loi de Darcy (équation (1.2)) et la théorie de la fibre unique (équation (1.4) dans la définition du facteur de qualité (équation (1.5)), l’expression résultante est indépendante de l’épaisseur du filtre.

Typiquement, pour calculer l’efficacité de capture de fibre unique, chaque mécanisme est considéré séparément [28, 32, 42]. En première approximation, il est supposé que les mécanismes s’additionnent :

$$\eta_{\Sigma} = \eta_I + \eta_R + \eta_D \quad (1.6)$$

où η_I , η_R et η_D sont respectivement les efficacités de fibre unique causées par l’impaction inertuelle, l’interception et la diffusion. *A priori*, il n’y a aucune raison de penser que c’est le cas [12, 28, 44]. Certains modèles incluent donc des termes mixtes, qui sont des efficacités de capture causées par l’interaction entre certaines.

Avec la théorie de la fibre unique, la prédiction du facteur de qualité se réduit donc à des expressions empiriques, semi-empiriques ou analytiques. Une compilation extensive de ces expressions peut se trouver dans cette revue [42], où le facteur de qualité dépend de la géométrie choisie, du régime d’écoulement et des interactions entre fibres. Par conséquent, les hypothèses sous-jacentes à la théorie de la fibre unique ne permettent pas une modélisation universelle du facteur de qualité. Pire encore, certains phénomènes se produisant dans les filtres réels ne peuvent pas être pris en compte.

D’abord, la théorie de la fibre unique ne permet pas de comprendre l’impact de distributions polydispersées de diamètres de fibres. Les fibres organiques comportent un relativement haut degré de polydispersité, mais même les fibres synthétiques sont polydispersées [37]. De plus, pour le mécanisme brownien, l’efficacité de capture peut diminuer au travers du filtre [45, 46]. La théorie

de la fibre unique ne permet donc pas de savoir *a priori* l'impact d'une géométrie multicouche réelle.

La théorie de la fibre unique est d'une validité encore plus douteuse lorsque l'incorporation de nanofibres dans les filtres est considérée. Les nanofibres ont une taille caractéristique L_c qui est de l'ordre du libre parcours moyen de l'air $\lambda = 66 \text{ nm}$ à température et pression normale. Dans un milieu fibreux, le nombre de Knudsen (défini comme $Kn = \lambda/L_c = 2\lambda/d_f$) n'est donc plus négligeable. L'hypothèse du continuum ne s'applique plus et les écoulements d'air autour de nanofibres sont dits raréfiés. Le tableau 1.4 montre la classification des régimes raréfiés la plus utilisée pour les filtres fibreux [42, 47-54] :

Tableau 1.4 Classification du régime de raréfaction des écoulements gazeux

Régime de raréfaction	Plage de nombres de Knudsen
Continuum (sans glissement)	$Kn < 0,001$
Continuum (avec glissement)	$0,001 < Kn < 0,25$
Knudsen (ou transition)	$0,25 < Kn < 10$
Moléculaire libre	$Kn > 10$

Le régime du continuum sans glissement est l'hypothèse classique en mécanique des fluides. L'équation de Navier-Stokes, ou une de ses approximations peut être résolue en posant une condition frontière (CF) de vitesse nulle aux parois. En régime du continuum avec glissement, l'équation de Navier-Stokes est valide si une condition de glissement aux parois est imposée. Les écoulements moléculaires libres représentent la limite à $Kn \rightarrow \infty$ où les molécules de gaz ont plus de contacts avec les fibres qu'entre elles-mêmes. Le régime de Knudsen est situé entre celui du continuum avec glissement et le régime moléculaire libre. En régime de Knudsen, les interactions entre les molécules de gaz ne peuvent être négligées, mais les hypothèses du continu sont également invalides. En fait, c'est la loi de Newton de la viscosité, ou la relation linéaire entre la contrainte et le cisaillement, qui est brisée [55].

Pour modéliser le facteur de qualité au sein d'un filtre, le régime d'écoulement pour chaque partie du filtre doit être connu. Or, à l'interface entre un substrat de fibres grossières et une couche

de nanofibres dans un filtre multicouche, la transition entre le régime raréfié et continu n'est pas toujours nette. Pire encore, lorsqu'un mélange fibreux est considéré, l'interface entre les nanofibres et les fibres grossières est potentiellement partout au sein du milieu filtrant. Pour mieux prédire le facteur de qualité des filtres à aérosols, l'aspect tridimensionnel et la position des fibres au sein du milieu filtrant doivent être considérés. Il faut donc sortir du cadre de la théorie de la fibre unique.

La simulation numérique directe des écoulements au sein de milieux filtrants est la voie privilégiée pour s'affranchir des limitations de la théorie de la fibre unique. Quel que soit le phénomène à modéliser, les méthodes numériques ont plusieurs avantages sur les méthodes expérimentales. Quand le modèle numérique est vérifié et validé, les simulations numériques sont moins coûteuses en temps et en argent que les méthodes expérimentales. De plus, il est généralement plus facile de faire des études paramétriques. Même quand ces modèles ne reproduisent pas tous les phénomènes, il est possible d'identifier les éléments manquants à notre compréhension. Un modèle plus raffiné peut ensuite être proposé pour mieux prédire le comportement des phénomènes d'intérêt.

1.8 Objectif général

L'objectif général de cette thèse doctorale est de développer un modèle numérique pour calculer les champs d'écoulements de gaz raréfiés au travers des filtres fibreux, du régime continu au régime de Knudsen. Il sera alors possible de prédire le facteur de qualité de milieux filtrants constitués de microfibres et de nanofibres.

CHAPITRE 2 REVUE DE LITTÉRATURE

Pour mieux cerner les défis posés par la modélisation numérique des écoulements raréfiés au sein des milieux fibreux, il faudra s'y pencher plus en détail. Cette problématique se divise en trois parties, qu'il convient de placer en ordre logique. D'abord, dans la section 2.1, certains enjeux non résolus dans la littérature quant à la structure multicouche des milieux filtrants microfibreux et nanofibreux seront résumés. Les limites des approches décrites dans cette section motiveront de prendre en compte la physique des écoulements de gaz raréfiés : ce sujet sera abordé dans la section 2.2. Dans la section 2.3, il sera établi que la méthode de Boltzmann sur réseau (MBR) est la meilleure approche pour la simulation directe des écoulements raréfiés, et les limites des MBR actuelles seront explicitées. Finalement, la revue de la littérature sera résumée et les objectifs spécifiques de ce projet seront présentés à la section 2.4.

2.1 Filtres fibreux multicouches

L'incorporation de nanofibres, avec une gamme de diamètres de 40 à 1000 nm a reçu intérêt marqué en raison de leur performance au sein de filtres fibreux, qui a été attribuée en partie à leur plus grand ratio surface-volume [54, 56, 57]. Les nanofibres sont déposées en couche sur des microfibres principalement pour quatre raisons : a) des propriétés mécaniques accrues, b) l'évitement des effets tunnel, c) de plus grandes durées de vie, et d) certains procédés qui nécessitent la fabrication en couche tels que la fonte soufflée (*melt-blown fibers*) et l'électrofilage (*electrospinning*) [51, 58-66]. La fonte soufflée consiste en la fusion d'un polymère (typiquement le polypropylène) à travers des orifices et en leur refroidissement à l'air sur un collecteur [28]. Lors du processus d'électrofilage une solution de polymères (typiquement le polyacrylonitrile) passe au travers d'une très grande différence de potentiel pour déposer des fibres sur un collecteur [66-69]. L'électrofilage a été identifié comme très prometteur en raison du contrôle plus serré des paramètres de conception des filtres [58, 70-74]. Cependant, certains procédés produisent naturellement des mélanges de fibre avec des tailles différentes, notamment : le procédé des «îles dans la mer» (*islands-in-the-sea*) [75], l'assemblage supramoléculaire [76-83] et l'électrofilage avec emploi de deux solutions polymériques [81-84].

La question de savoir s'il est préférable d'incorporer les nanofibres au travers d'un support microfibreux ou de créer une structure multicouche est d'un grand intérêt pratique. Dans un filtre

multicouche, la morphologie, la fraction solide et le diamètre des fibres changent au travers des filtres. Les hypothèses sous-tendant la loi de Darcy et la théorie de la fibre unique ne sont donc pas remplies au sein de filtres multicouches [85]. Les mélanges de fibres avec des diamètres différents, quant à eux, ne respectent évidemment pas la théorie de la fibre unique.

Des tentatives d'extension de la théorie de la fibre unique ont été proposées dans la littérature pour prédire la performance de distributions fibreuses polydispersées. L'incorporation d'un indice de polydispersité dans l'équation de Darcy et l'équation de la simple fibre, par exemple, prédit un effet de la structure multicouche [86-88] :

$$E = 1 - \exp\left(-\frac{\eta_\Sigma \alpha h}{\pi(1-\alpha)\bar{d}(1+\delta)}\right) \quad (2.1)$$

$$\Delta P = \frac{\mu U_0 \alpha h f(\alpha)}{\bar{d}^2(1+\delta)} \quad (2.2)$$

$$\delta = \frac{\bar{d}^2 - \bar{d}^2}{\bar{d}^2} \quad (2.3)$$

où δ est l'indice de polydispersité, qui est vraiment un coefficient de variation. La forme de cette modification ne serait cependant valide que pour des polydispersités «modérées», donc invalide pour des mélanges de microfibres et de nanofibres.

Cependant, il a été également proposé de prendre en compte l'effet d'un mélange de fibres en supposant que la structure multicouche n'a aucun impact sur la performance des filtres. Par exemple, dans le modèle sériel, les fibres de chaque diamètre sont considérées comme des couches superposées, où les pertes de charge sont additionnées, et les perméances sont multipliées [89-91] :

$$\Delta P = \sum_i \Delta P_i \quad (2.4)$$

$$E = 1 - \prod_i (1 - E_i) \quad (2.5)$$

où i représente chaque diamètre de fibre. Cette approche néglige les interactions non linéaires potentiellement causées par le positionnement des fibres, et prend donc pour acquis qu'il n'y a pas

de différence entre un filtre bien mélangé ou multicouche [92]. L'utilisation d'un diamètre caractéristique a été proposée pour pondérer les effets de la polydispersité. Plusieurs exemples de diamètres caractéristiques ont été proposés dans la littérature et sont énoncés dans l'annexe A [92-98]. Pour toutes ces pondérations, des distributions polydispersées avec des coefficients de variation différents peuvent toutes avoir le même diamètre équivalent. Il est donc clair que cette méthode entre en conflit avec la méthode de l'indice de polydispersité. Tous ces modèles ayant été « validés » expérimentalement, la littérature sur la prédiction de l'impact d'une distribution polydispersée semble donc contradictoire et insatisfaisante, et ce, même pour les mélanges microfibreux.

D'après la classification des régimes de raréfaction présentée au tableau 1.4, les écoulements au sein de milieux faits de nanofibres sont en régime de glissement ou en régime de Knudsen. Le diamètre de fibre n'est cependant pas le seul paramètre ayant un impact sur les écoulements de gaz. La fraction solide [99-102], sa fluctuation [89, 103-112], ainsi que les dimensions [70, 113] et la géométrie [114, 115] des pores sont aussi déterminantes, en régime du continuum comme dans les régimes raréfiés. Ces paramètres peuvent difficilement être isolés expérimentalement, ce qui en complique l'étude théorique. La simulation directe d'écoulements au sein de milieux fibreux tridimensionnels est donc la méthodologie requise pour étudier l'impact de la structure multicouche sur la performance des filtres fibreux.

Les simulations numériques directes des écoulements dans les filtres fibreux se basent généralement sur une méthodologie séquentielle en trois étapes [94, 96, 97, 116-120] :

1. Une structure fibreuse est générée;
2. Les équations de Navier-Stokes ou une version simplifiée sont résolues directement au sein de la structure fibreuse au moyen d'un solveur numérique de mécanique des fluides. La perméabilité est déduite du champ de vitesse.
3. Les trajectoires des particules sont calculées à l'aide du champ de vitesse obtenu. L'efficacité de capture est déduite des trajectoires des particules.

Avec cette méthodologie séquentielle en trois étapes, l'écoulement d'air est donc découplé du mouvement des particules. La validité de cette hypothèse sera discutée plus en détail au chapitre 2.2.4. À la connaissance de l'auteur, aucun solveur numérique n'a été employé pour étudier des milieux fibreux complexes en régime de Knudsen. À l'heure actuelle, la simulation des

écoulements se limite soit à imposer une condition de glissement [63, 102, 121-127] ou à négliger l'impact de la couche de nanofibres sur l'écoulement [115, 128-134]. Ces deux hypothèses sont logiquement contradictoires : pour une géométrie donnée, soit les nanofibres doivent être considérées, soit elles peuvent ne pas l'être. Malgré le fort intérêt de la simulation numérique directe des écoulements de Knudsen dans les filtres fibreux, aucun modèle suffisant n'a été présenté dans la littérature pour arriver à cet objectif.

2.2 Mécanique des fluides en régime raréfié

Pour produire un modèle qui compte des écoulements de Knudsen, certains principes fondamentaux de la mécanique des fluides en régime raréfié devront être bien compris. D'abord, les éléments de la théorie cinétique des gaz à l'introduction de l'équation de Boltzmann seront présentés à la section 2.2.1. Deux phénomènes apparaissant en régime raréfié, le glissement aux parois et la couche de Knudsen, seront présentés respectivement à la section 2.2.2 et 2.2.3. Les enjeux concernant le mouvement des particules fines seront examinés à la section 2.2.4.

2.2.1 Théorie cinétique des gaz

La théorie cinétique des gaz s'appuie sur une description statistique de la matière, où un gaz est considéré comme un grand nombre de molécules régies par la mécanique classique. En utilisant le théorème de Liouville [135, 136], il est possible de définir de manière rigoureuse l'existence d'une population $f(\mathbf{x}, \mathbf{c})$, soit le nombre de molécules à la position \mathbf{x} avec une vitesse située entre ξ et $\xi + d\xi$. En supposant que les molécules de gaz n'interagissent que lors de collisions binaires et élastiques, l'équation de Boltzmann décrit l'évolution de ces populations au sein d'un écoulement gazeux [135-138]:

$$\frac{\partial f}{\partial t} + \xi \frac{\partial f}{\partial \mathbf{x}} = \underbrace{\int (f'_1 f'_2 - f_1 f_2) \mathbf{g} b db d\epsilon d\xi_1}_{\Omega} + \mathcal{F} \quad (2.6)$$

où l'indice ' réfère à des populations post-collision, l'indice 1 et 2 sur les populations réfère, sans perte de généralité, à des collisions entre deux populations, ξ_1 est la vitesse des populations précollision, $\mathbf{g} = \xi_2 - \xi_1$ est la vitesse relative entre les deux populations, $b \in [0, \infty[$ est un paramètre d'impact, ϵ est l'angle azimutal d'impact et \mathcal{F} est un terme de force sur les populations

(par exemple, la gravité). Le côté gauche et droit de l'équation de Boltzmann sont respectivement nommés termes de propagation et de collision.

Sous cette forme, l'équation de Boltzmann est une équation intégro-différentielle assez difficile à manipuler, d'autant plus qu'il est difficile de définir b et ϵ . En pratique, un modèle de collision est généralement employé pour simplifier le terme de droite. Le modèle Bhatnagar-Gross-Krook (BGK), où la déviation par rapport à l'équilibre évolue à l'aide d'un seul temps de relaxation τ , est le plus simple [137, 139] :

$$\boldsymbol{\Omega} = -\frac{1}{\tau}(f - f^{(eq)}) \quad (2.7)$$

où $f^{(eq)}$ est la distribution maxwellienne d'une population à l'équilibre dans un espace tridimensionnel [140] :

$$f^{eq}(\boldsymbol{\xi})d\boldsymbol{\xi} = \left(\frac{m}{2\pi kT}\right)^{3/2} \exp\left(-\frac{m\boldsymbol{\xi}^2}{2kT}\right) d\boldsymbol{\xi} \quad (2.8)$$

où m est la masse d'une molécule de gaz, k est la constante de Boltzmann et T est la température. L'équation de Boltzmann-BGK résulte de l'incorporation de l'opérateur BGK au sein de l'équation de Boltzmann.

Ultimement, les descriptions microscopiques de la matière ont pour but de comprendre des phénomènes macroscopiques. Dans ce travail de doctorat, les deux propriétés macroscopiques d'intérêt sont la densité ρ et la quantité de mouvement $\rho\mathbf{v}$, qui sont récupérées de la manière suivante :

$$\rho(\mathbf{x}, t) = \int m f(\mathbf{x}, \boldsymbol{\xi}, t) d\boldsymbol{\xi} \quad (2.9)$$

$$\rho\mathbf{v}(\mathbf{x}, t) = \int m \boldsymbol{\xi} f(\mathbf{x}, \boldsymbol{\xi}, t) d\boldsymbol{\xi} \quad (2.10)$$

Les quantités récupérées grâce à des intégrales sur les populations sont aussi appelées «moments».

Sous les hypothèses mentionnées plus haut, l'équation de Boltzmann est valide, quel que soit le nombre de Knudsen. Avec l'hypothèse additionnelle de faibles nombres de Knudsen et de Mach, l'équation de Navier-Stokes peut être récupérée au moyen d'une expansion de Chapman-Enskog [137, 138] ou de la méthode des moments de Grad [141] :

$$\rho \left(\frac{\partial \mathbf{u}}{\partial t} + \mathbf{u} \times \nabla \mathbf{u} \right) = -\nabla P - \mu \Delta^2 \mathbf{u} + \rho \mathbf{g} \quad (2.11)$$

où ∇P est le gradient de la pression P , et \mathbf{g} est une accélération volumique imposée de l'extérieur. Bien qu'il soit possible de s'affranchir de l'hypothèse de faible nombre de Knudsen avec des équations constitutives d'ordre plus élevé (citons notamment Burnett, Super-Burnett, les 13 ou 26 moments de Grad, etc.), ces équations requièrent la définition de CFs d'ordre plus élevé [142-151]. Elles sont généralement aussi incapables de récupérer les bons champs de vitesse à $Kn > 1$ [138, 149-152]. Si l'existence d'une solution unique et régulière à l'équation de Navier-Stokes est toujours un problème irrésolu (c'est d'ailleurs un des sept problèmes du millénaire), il est bien connu que la solution à l'équation de Boltzmann-BGK donne parfois lieu à des singularités, même pour des écoulements simples comme un plan semi-infini [138]. De toute façon, il serait impossible de résoudre directement l'équation de Boltzmann pour un milieu fibreux complexe, puisque cette équation est à six dimensions, dont trois dimensions dans l'espace des vitesses qui peut être non borné (aller de l'infini négatif à l'infini positif) et qui peut avoir des solutions discontinues [153].

Il serait donc préférable, dans le cadre de ce projet, de se limiter à une description phénoménologique des profils d'écoulements gazeux en régime raréfié. Certains résultats élémentaires sur les gaz à l'état d'équilibre seront mentionnés en guise de conclusion de cette sous-section. D'abord, pour un gaz à l'équilibre thermodynamique qui respecte les hypothèses nécessaires à la dérivation de l'équation de Boltzmann, la loi des gaz parfaits peut être dérivée [154] :

$$P = \frac{\rho \mathcal{R} T}{M} \quad (2.12)$$

M est la masse moléculaire du gaz, $\mathcal{R} = k/N_A$, est la constante des gaz parfaits, et où N_A est le nombre d'Avogadro. Avec l'hypothèse additionnelle de faible taille des molécules en comparaison avec le libre parcours moyen, l'expression suivante peut être développée pour le libre parcours moyen en fonction de la pression et de la viscosité [155] :

$$\lambda = \frac{\mu}{P} \sqrt{\frac{\pi \mathcal{R} T}{2}} \quad (2.13)$$

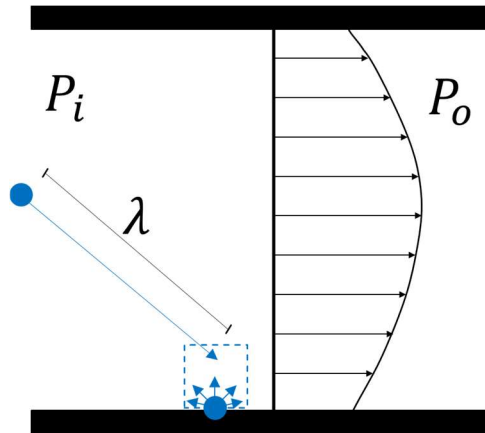


Figure 2.1 Représentation du glissement aux parois dans une fente

2.2.2 Le glissement aux parois

Macroscopiquement, le glissement apparaît comme une discontinuité dans le champ de vitesse d'un écoulement. Plutôt que d'adhérer à la surface solide, le gaz situé à la surface solide s'écoule à une vitesse finie donnée (voir Figure 2.1). L'origine de ce phénomène est explicable d'un point de vue microscopique lorsque le nombre de Knudsen augmente : des molécules en provenance d'une région où la vitesse macroscopique est non nulle contribuent à la vitesse macroscopique du gaz à une paroi solide [156]. Maxwell est le premier à avoir relié le glissement à la force de cisaillement appliquée par le gaz pour une surface plane [137, 138, 157] :

$$\mathbf{u}_s = A_1 \lambda \frac{\partial \mathbf{u}}{\partial \mathbf{x}} \quad (2.14)$$

où $A_1 = (2 - \sigma)/\sigma$ est un coefficient qui dépend d'un modèle phénoménologique proposé par Maxwell, où les populations en interaction avec la surface d'un gaz sont divisées en deux composantes : une fraction σ diffusée qui prend la valeur de la fonction d'équilibre f^{eq} , et une fraction $(1 - \sigma)$ qui est réfléchie spéculairement, c.-à-d. où la seule composante modifiée de la vitesse est celle normale à la surface solide. La fraction $0 \leq \sigma \leq 1$ est aussi nommée « coefficient d'accommodation ». Une extension du modèle pour des nombres de Knudsen plus élevée a également été proposée [158] :

$$\mathbf{u}_s = A_1 \lambda \frac{\partial \mathbf{u}}{\partial \mathbf{x}} - A_2 \lambda^2 \frac{\partial^2 \mathbf{u}}{\partial \mathbf{x}^2} \quad (2.15)$$

où A_1 et A_2 sont des coefficients phénoménologiques déterminés expérimentalement ou à l'aide de modèles théoriques. Des modèles d'ordre plus élevé ont été proposés, mais l'interprétation théorique de dérivées d'ordre supérieur à 1 reste incomplète [158].

Des conséquences contre-intuitives peuvent surgir en raison des conditions de glissement lorsque des surfaces curvilignes sont considérées. Par exemple, dans un écoulement de Couette cylindrique où le cylindre intérieur est en rotation et le cylindre extérieur est statique, la vitesse

maximale peut être située à une certaine distance du cylindre intérieur si le coefficient d'accommodation est suffisamment bas [159-166]. Des résultats analytiques pour un écoulement autour d'une sphère ont également montré que la force centrifuge jouait un rôle important dans l'apparition du glissement sur une surface courbe. Si la force centrifuge était omise, la force de traînée visqueuse serait négative, ce qui est clairement non-physique [160, 167]. Pour cette raison, la condition de glissement suivante a été proposée [159, 160, 163] :

$$\mathbf{u}_s = A_1 \lambda \frac{\partial \mathbf{u}}{\partial \mathbf{n}} - A_2 \lambda^2 \frac{\partial^2 \mathbf{u}}{\partial \mathbf{n}^2} \quad (2.16)$$

où \mathbf{n} est la normale par rapport à la surface solide. Notons finalement que les écoulements raréfiés ont une plus grande propension à glisser sur une surface convexe que sur une surface concave [159, 168, 169].

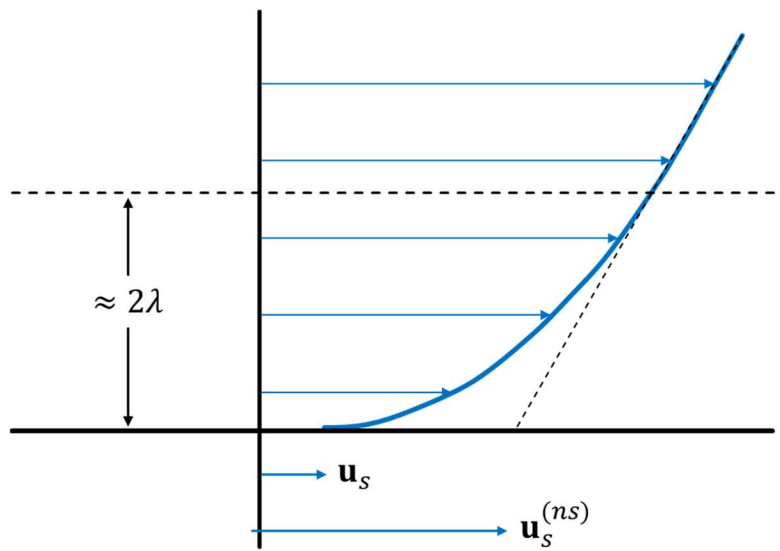


Figure 2.2 Illustration du profil d'écoulement au sein de la couche de Knudsen, où \mathbf{u}_s est la véritable vitesse de glissement et $\mathbf{u}_s^{(ns)}$ est la vitesse de glissement extrapolée à partir du champ de vitesse à l'extérieur de la couche de Knudsen

glissement doit également être modifiée pour éviter une surprédiction de la vitesse de glissement (aussi illustrée à la Figure 2.2).

2.2.3 La couche de Knudsen

La couche de Knudsen est définie comme la région de l'écoulement d'une grandeur de l'ordre de $\approx 2\lambda$ où la relation entre la contrainte et le cisaillement dévie de manière notable avec la loi de Newton [158, 159, 168]. Une illustration de la couche de Knudsen est fournie à la Figure 2.2. Lorsque cette région devient prépondérante au sein d'une géométrie, l'équation de Navier-Stokes ne peut être utilisée pour récupérer un champ de vitesse adéquat [170]. La condition de

La couche de Knudsen peut avoir des conséquences dramatiques sur la prédiction du débit massique dans une fente. Le paradoxe de Knudsen (illustré à la Figure 2.3) montre que le débit massique atteint un minimum en fonction du nombre de Knudsen [171]. Alors que les équations

de Navier-Stokes sans glissement et avec glissement prédisent un débit massique décroissant monotone, la couche de Knudsen tend à faire augmenter le débit passé une zone appelée le minimum de Knudsen [172].

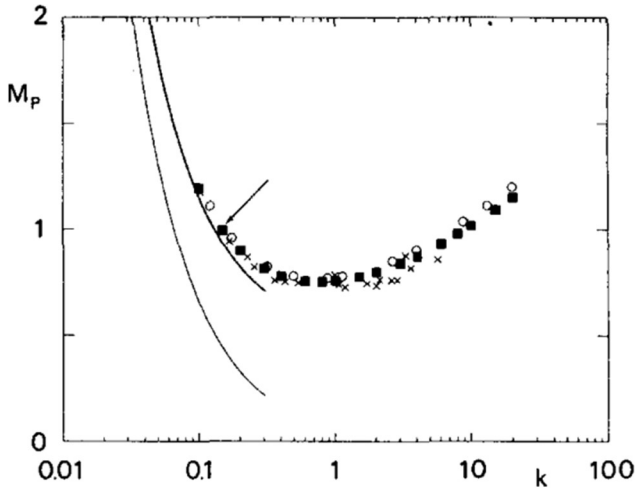


Figure 2.3 Débit massique adimensionnalisé M_p en fonction de $k = Kn\sqrt{2/\pi}$ – reproduit avec permission de [171]

relation entre la contrainte τ et le cisaillement $\dot{\gamma}$ s'exprimerait donc ainsi :

$$\tau = -\mu_e(\mathbf{x})\dot{\gamma} \quad (2.17)$$

L'insertion de cette viscosité effective dans l'équation de Navier-Stokes porte le nom d'« équation de Navier-Stokes étendue » (ou généralisée).

Les premiers modèles de viscosité effective ne dépendaient à l'origine que du nombre de Knudsen, et étaient basés sur des régressions de résultats sur des écoulements de Couette planaire [173-179] et des écoulements mués par une différence de pression [179-182]. Cependant, telle que mentionnée dans l'introduction, la définition d'un nombre de Knudsen est ambiguë dans un milieu poreux complexe. Ces modèles avaient aussi pour défaut d'être indépendants de la position \mathbf{x} au sein du domaine: or, le but d'une fonction de viscosité est justement de prédire la diminution de la viscosité effective au sein de la couche de Knudsen. Néanmoins, un grand nombre d'articles ont utilisé ce modèle de viscosité effective pour modéliser des écoulements poreux, à la fois sur des géométries planaires [183-193] comme sur des géométries non-planaires [194-216].

En étudiant des solutions à l'équation de Boltzmann pour une géométrie planaire semi-infinie, certaines équipes de recherche ont proposé des fonctions de mur [217-224]. La viscosité effective est donc calculée à l'aide de la distance du gaz au mur solide. L'avantage de cette approche est sa prise en compte de variation spatiale de la viscosité effective, du moins dans le cas d'un mur semi-infini. Cependant, il est difficile *a priori* de savoir si cette approche permet de modéliser des milieux poreux complexes.

La dernière approche proposée dans la littérature est le calcul de la viscosité effective au moyen du libre parcours moyen effectif [225]. L'équation (2.12) montre un libre parcours moyen pour un système où les molécules se propagent librement et n'entrent en collision qu'avec une autre molécule de gaz. Cependant, dans la couche de Knudsen, les molécules de gaz sont entravées par la présence de murs solides. En supposant que la relation de proportionnalité entre le libre parcours moyen et la viscosité tient dans la couche de Knudsen, une fonction de viscosité notée $\Psi(\lambda, \mathbf{x})$ pourrait être dérivée:

$$\Psi(\mathbf{x}, \lambda) = \frac{\lambda_e(\mathbf{x})}{\lambda} = \frac{\mu_e(\mathbf{x})}{\mu} \quad (2.18)$$

où $\lambda_e(\mathbf{x})$ est le libre parcours moyen effectif, qui varie dans l'espace. Puisque le libre parcours moyen effectif est toujours inférieur au libre parcours moyen, $0 < \Psi(\mathbf{x}, \lambda) < 1$. L'hypothèse de proportionnalité entre le libre parcours moyen effectif et la viscosité effective aurait été validée avec la méthode de simulations directes Monte-Carlo [226, 227] et de dynamique moléculaire [228-230]. Des formules analytiques ont été proposées pour des géométries planaires [170, 225, 226, 231-234] et des géométries cylindriques concentriques [161, 162, 235]. À la connaissance de l'auteur, il n'existe cependant toujours pas de méthode permettant de calculer un libre parcours moyen effectif au sein d'une géométrie poreuse complexe.

Pour inclure l'effet de la couche de Knudsen sur la valeur de la vitesse de glissement, la condition de glissement suivante a été proposée par Guo et al. [225]:

$$\mathbf{u}_s = A_1 \lambda_e \frac{\partial \mathbf{u}}{\partial \mathbf{n}} - A_2 \lambda_e \left(\frac{\partial}{\partial \mathbf{n}} \left(\lambda_e \frac{\partial \mathbf{u}}{\partial \mathbf{n}} \right) \right) \quad (2.19)$$

À l'aide de ce modèle, les profils de vitesses auraient été correctement récupérés dans plusieurs études sur des écoulements planaires et cylindriques concentriques, du régime du continuum à la limite supérieure du régime de Knudsen [161, 170, 236, 237].

2.2.4 Mouvement des particules fines dans l'air

Pour calculer la trajectoire de particules fines, un bilan des forces peut être établi sur chacune des particules fines qui voyage au sein d'un filtre fibreux. Considérons une particule fine sphérique de diamètre d_p se déplaçant dans l'air avec une vitesse \mathbf{V} constante. Dans la mécanique des milieux continus, en supposant un régime laminaire, établi et en régime permanent, l'équation de Stokes est valide et donne le résultat suivant pour la force de traînée \mathbf{F}_D [154]:

$$\mathbf{F}_D = 3\pi\mu\mathbf{V}d_p \quad (2.20)$$

Cette équation devient invalide lorsque le diamètre des particules est trop faible pour deux raisons. D'abord, le diamètre de la particule peut être de l'ordre du libre parcours moyen, et les effets de raréfaction doivent être considérés. Ensuite, le mouvement brownien donne une composante stochastique au déplacement d'une particule en raison des collisions aléatoires des molécules de gaz avec la particule.

Typiquement, les effets de raréfaction sont pris en compte grâce au facteur de Cunningham C_C [238]:

$$\mathbf{F}_D = \frac{3\pi\mu\mathbf{V}d_p}{C_C} \quad (2.21)$$

Des corrélations en fonction du nombre de Knudsen $Kn_p = 2\lambda/d_p$, sont présentées à l'annexe B. La plupart de ces corrélations ont été obtenues à l'aide de régressions sur des données expérimentales.

Le mouvement brownien est décrit mathématiquement par des accumulations de déplacements infinitésimaux. Dans le cas d'une particule fine dans l'air, ces déplacements sont occasionnés par le transfert de quantité de mouvement lors des collisions avec des molécules d'air. Pour un mouvement brownien, les accumulations de déplacements sont indépendantes, stationnaires, et peuvent être décrites par une loi normale [239, 240]. Bien que la dérivée de la

position d'une particule en mouvement brownien n'existe pas au sens classique, il est possible de définir la force brownienne avec la fonction d'autocorrélation $\Gamma(t)$ suivante [241] :

$$\langle \Gamma_i(t)\Gamma_j(t') \rangle = \frac{2kT}{m_p} \delta_{ij} \delta(t - t') \quad (2.22)$$

où i et j représentent des directions spatiales, δ_{ij} est le delta de Kronecker et $\delta(t - t')$ est la distribution de Dirac. L'équation de Langevin permet finalement de donner la position $\mathbf{r}(t)$ d'une particule brownienne :

$$\frac{d}{dt} \mathbf{r}(t) = \mathbf{V}(t) \quad (2.23)$$

$$\frac{d}{dt} \mathbf{V}(t) = \frac{3\pi d_p \mu}{m_p C_C} (\mathbf{u}(\mathbf{r}, t) - \mathbf{V}(t)) + \boldsymbol{\Gamma}(t) \quad (2.24)$$

où m_p est la masse d'une particule. Lors de la formulation de l'équation de Langevin, il est pris pour acquis qu'il n'y a aucun couplage entre les particules et le fluide et que les interactions entre les particules fines sont négligeables. Pour des fractions volumiques suffisamment faibles ($< 10^{-6}$), cette hypothèse est valide [242]. Si les aérosols ont une densité de 1000 kg/m^3 , ce qui est standard [25], une fraction volumique de 10^{-6} est supérieure de plusieurs ordres de grandeur aux pires concentrations en particules fines observées jusqu'à présent dans le monde ($\sim 1000 \mu\text{g/m}^3$) [243].

Lorsqu'une particule fine est en contact avec une fibre, les forces de Van der Waals ainsi que les forces de tension pour des liquides sont responsables de son adhésion [244]. Deux phénomènes peuvent retirer une particule fine d'une fibre : le rebond et le réentraînement.

Un rebond pourrait se produire si une particule possède une énergie cinétique suffisante au contact avec une fibre. Cela pourrait arriver pour des particules relativement denses avec une vitesse conséquente. Cependant, la probabilité de rebondissement serait très faible pour des particules possédant moins de 10^{-1} J , ce qui est généralement le cas pour des particules plus petites que $10 \mu\text{m}$ et d'une vitesse inférieure à 1 m/s [245]. Un rebond thermique pourrait également être observé en raison du mouvement brownien, mais cet effet n'a été rapporté que pour des particules avec un diamètre inférieur à $4,5 \text{ nm}$ [57, 246].

Un ré entraînement pourrait également se produire si le courant d'air est suffisamment fort pour détacher la particule d'une fibre. Les écoulements avec une vitesse inférieure à 1 m/s n'occasionnent pas de ré entraînement [12], tandis que les particules individuelles d'un diamètre inférieur à 10 μm sont peu susceptibles d'être ré entraînées [244]. Ces conclusions ne sont pas forcément valides pour un filtre encrassé : cependant, dans cette thèse de doctorat, seuls les filtres propres seront considérés.

Jusqu'à présent, seules des particules individuelles ont été considérées. Il peut arriver, en raison de l'humidité, que des particules fines s'agglomèrent [244, 247]. Généralement, cela facilite la capture [247-249]. L'absence d'agglomérations est donc une hypothèse conservatrice lors de la formulation d'un modèle prédictif de la capture des particules fines.

2.3 Méthode de Boltzmann sur réseau (MBR)

Dans cette section, une revue de la méthode de Boltzmann sur réseau (MBR) sera effectuée dans le but de connaître l'état de l'art sur la simulation des écoulements de Knudsen avec cette méthode. La section 2.3.1 servira à expliquer les principes de la méthode, à élucider ses forces et à argumenter pourquoi la MBR est la méthode la plus appropriée pour réussir l'objectif général de cette thèse. Ensuite, l'état de l'art quant à la modélisation du glissement avec la MBR sera exposé à la section 2.3.2. Finalement, la procédure de régularisation, parfois employée pour la modélisation de gaz raréfiés avec la MBR, sera expliquée à la section 2.3.3.

2.3.1 Introduction à la MBR

La MBR est une discréétisation en espace, en temps et en vitesses de l'équation de Boltzmann sur une grille cartésienne. Contrairement à l'équation de Boltzmann, un nombre fini de populations est employé pour représenter l'écoulement, et l'ensemble de vitesses discrètes coïncide avec un réseau cartésien structuré lors du déplacement des populations. L'évolution des populations dans la MBR s'effectue donc, comme l'équation de Boltzmann, à l'aide d'un schéma de collision-propagation. L'opérateur de propagation est discréétisé au moyen d'un schéma de type différences finies [250-253]:

$$f_i(\mathbf{x} + \mathbf{c}_i \Delta t, t + \Delta t) - f_i(\mathbf{x}, t) = \Omega_i + F_i \Delta t \quad (2.25)$$

où f_i est une population avec un indice i associé à une vitesse \mathbf{c}_i , Δt est le pas de temps, Ω_i est un opérateur de collision et F_i est un terme de force appliqué à chaque population. Comme pour l'équation de Boltzmann, l'opérateur de collision le plus simple est également le modèle BGK :

$$\Omega_i = - \left(\frac{f_i - f_i^{(eq)}(\rho, \mathbf{u})}{\tau} \right) \quad (2.26)$$

où τ est le temps de relaxation unique et $f_i^{(eq)}(\rho, \mathbf{u})$ est une distribution à l'équilibre calculé à partir de la densité ρ et de la vitesse \mathbf{u} . Pour les réseaux D2Q9 et D3Q15 (le nom de réseau est défini comme DaQ b , où a est le nombre de dimensions et b est le nombre de populations) qui seront employés dans cette thèse (présentés à l'annexe C), $f_i^{(eq)}$ prend la forme suivante :

$$f^{(eq)} = w_i \rho \left(1 + \frac{\mathbf{c}_i \cdot \mathbf{u}}{c_s^2} + \frac{(\mathbf{c}_i \cdot \mathbf{u})^2}{2c_s^4} - \frac{\mathbf{u} \cdot \mathbf{u}}{2c_s^2} \right) \quad (2.27)$$

où w_i sont les poids des différentes populations du réseau définis à l'annexe C et $c_s = \sqrt{3RT}$ est la «vitesse du son» du réseau. Cette vitesse ne correspond pas forcément à la vitesse du son physique : elle est plutôt liée à la vitesse maximale de transmission de l'information imposée par le schéma de propagation du réseau. Comme pour l'équation de Boltzmann continue, les paramètres macroscopiques sont récupérés à l'aide d'une somme sur les populations [250] :

$$\rho = \sum_{i=0}^{Q-1} f_i \quad (2.28)$$

$$\rho \mathbf{u} = \sum_{i=0}^{Q-1} f_i \mathbf{c}_i \quad (2.29)$$

où Q est le nombre de populations. La viscosité est reliée au temps de relaxation en MBR de la manière suivante [250]:

$$\mu = \rho c_s^2 \left(\tau - \frac{1}{2} \right) \Delta t \quad (2.30)$$

Avec la MBR, la couche de Knudsen peut être prise en compte en remplaçant la viscosité par une viscosité effective. L'équation de Navier-Stokes étendue est ainsi naturellement récupérée. Le temps de relaxation avec la MBR prend ainsi la forme suivante :

$$\tau = \frac{1}{2} + \sqrt{\frac{6}{\pi}} \frac{\lambda}{\Delta x} \Psi(\lambda, \mathbf{x}) \quad (2.31)$$

où Δx est le pas d'espace et où $\Psi(\lambda, \mathbf{x})$ est la fonction de viscosité définie à l'équation (2.18).

À l'aide d'une expansion de Chapman-Enskog ou des moments de Grad, l'équation de Navier-Stokes est aussi récupérée à partir des réseaux D2Q9 et D3Q15 sous l'hypothèse de faibles nombres de Mach et de Knudsen [250-252]. La propagation à l'aide du schéma de différences finies facilite grandement la discrétisation du domaine du gaz au sein du milieu fibreux [254]. De plus, puisque les calculs de l'opérateur de collision s'effectuent totalement localement pour chaque maille du réseau, la parallélisation en mémoire distribuée de la MBR est particulièrement efficace même pour un milieu poreux complexe [255, 256].

En régime raréfié, plusieurs méthodes numériques ont été proposées pour résoudre l'équation de Boltzmann. La simulation directe Monte-Carlo procède à cette fin également à l'aide d'un schéma de collision-propagation : cependant, le gaz est représenté sous forme d'un grand nombre de particules lagrangiennes [257, 258]. Le caractère lagrangien et probabiliste de cette méthode rend difficile l'emploi de cette méthode pour des écoulements à faible vitesse en comparaison avec la vitesse du son (c.-à-d. quand $Ma \ll 1$). De plus, le nombre de particules requis augmente en régime continu [257, 258]. Des schémas hybrides avec décomposition du domaine avec une partie du domaine résolue avec une méthode de milieu continu hors de la couche de Knudsen ont également été proposés [259-266]. La performance computationnelle reste limitée par la fraction où la simulation directe Monte-Carlo doit être utilisée. Cette décomposition ne serait également pas triviale pour un milieu fibreux.

La méthode *Discrete Unified gas kinetic scheme* (DUGKS) a été proposée relativement récemment pour résoudre l'équation de Boltzmann pour tous les régimes de raréfaction à l'aide d'un schéma de type volumes finis [267]. La discrétisation en volumes finis permet d'utiliser des maillages non structurés, ce qui aurait pu être un avantage en milieu fibreux complexe. DUGKS peut également être utilisé pour résoudre des écoulements turbulents [268, 269], thermiques et

compressibles [270, 271]. Cependant, pour de hauts nombres de Knudsen, un nombre élevé de populations est requis pour capturer correctement la physique des écoulements raréfiés, et ce nombre n'est pas connu pour une géométrie donnée *a priori*.

Dans le même ordre d'idée, il a été proposé d'utiliser des réseaux d'ordre plus élevé que les schémas D2Q9 ou D3Q15 avec la MBR pour récupérer des équations différentielles d'ordre plus élevé que les équations de Navier-Stokes. Mentionnons, par exemple, pour des écoulements bidimensionnels, les schémas D2Q16, D2Q25, D2Q4624 et D2Q4761 [272-276]. Le défaut fondamental de ces méthodes, tout comme la méthode DUGKS, est leur utilisation accrue en mémoire et en ressources computationnelles [273, 275-281]. Le réseau cartésien deviendrait même un défaut pour un grand ensemble de populations, puisque la décomposition du domaine requiert la communication de populations provenant de mailles plus éloignées [277]. L'efficacité parallèle de la MBR serait ainsi grandement diminuée, ce qui enlèverait le principal attrait de la MBR [255, 256]. Pour le restant de cette thèse, la résolution d'écoulements raréfiés sera donc effectuée à l'aide d'un réseau d'ordre peu élevé comme le D2Q9 et le D3Q15.

2.3.2 Modélisation des écoulements raréfiés avec la MBR

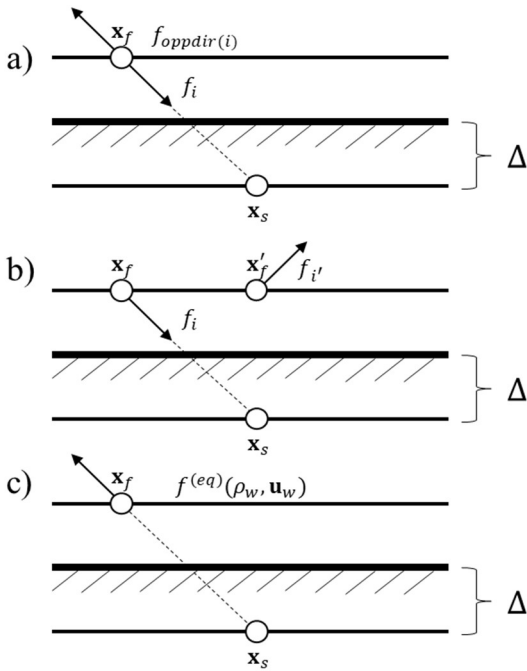


Figure 2.4 Conditions frontières cinétiques pour la MBR de: a) rebond à mi-chemin, b) réflexion spéculaire, c) diffusion

de Langmuir aurait également été proposée, mais cette CF fait explicitement référence à une longueur caractéristique de l'écoulement, qui est difficile à définir pour un milieu poreux [284].

Des dérivations analytiques pour la CF cinétique de Maxwell sous sa forme discrétisée ont montré que les valeurs des coefficients phénoménologiques de glissement obtenus à partir de la forme continue de l'équation de Boltzmann ne sont pas récupérées correctement avec la version discrétisée de la CF de Maxwell pour la MBR [285]. Toutes les combinaisons possibles des CFs cinétiques définies à la Figure 2.4 ont été proposées pour mieux récupérer le glissement [250]. Par exemple, la combinaison de rebond à mi-chemin et de réflexion spéculaire (notée CBBSR) est représentée ainsi [286]:

$$f_i = (1 - \alpha)f_i^{(SR)} + \alpha f_i^{(BB)} \quad (2.32)$$

L'imposition de CFs adéquates est d'une importance primordiale en simulation de la mécanique des fluides. Plutôt que d'imposer des conditions frontières (CFs) sur des variables macroscopiques comme la densité ou la vitesse, la MBR impose des relations sur les populations au moyen de CFs cinétiques. Pour des écoulements en régime du continuum sans glissement, la condition cinétique de rebond à mi-chemin (telle que présentée à la Figure 2.4 a) est typiquement employée [282]. Cette CF permet une convergence d'ordre 2 en temps et en espace [283]. Pour modéliser le glissement, les CFs cinétiques de réflexion spéculaire et de diffusion proposées par Maxwell ont également été discrétisées, telles que présentées à la Figure 2.4 b) et c). Notons que la condition de réflexion spéculaire est non locale. Une CF cinétique

où $0 \leq \alpha \leq 1$ est le coefficient d'accomodation pour la CF cinétique de CBBSR, qui représente l'importance relative du rebond à mi-chemin dans la CF cinétique.

D'autres analyses théoriques ont montré que le modèle de collision BGK était incapable de reproduire la CF de deuxième ordre définie à l'équation (2.15) [287]. Il a donc été proposé d'utiliser un opérateur à temps de relaxation multiples (TRM) pour effectuer les calculs sur des moments définis par les populations plutôt que directement sur les populations [288] :

$$\Omega_i = - \sum_{j=0}^{Q-1} (\mathbf{M}^{-1} \mathbf{S} \mathbf{M})_{ij} \left(f_j(\mathbf{x}, t) - f_j^{(eq)}(\rho, \mathbf{u}) \right) \quad (2.33)$$

\mathbf{M} est une matrice de transformation vers les moments $\mathbf{m} = \mathbf{M}\mathbf{f}$ (tels que la densité, la quantité de mouvement, l'énergie et la contrainte), et \mathbf{S} est une matrice diagonale qui contient les temps de relaxations $\tau_i = 1/s_i$ reliés à ces moments. Les matrices \mathbf{M} et \mathbf{S} ainsi que le vecteur $\mathbf{m} = \mathbf{M}\mathbf{f}$ sont présentées à l'annexe D pour les réseaux D2Q9 et D3Q15. Le temps de relaxation relié à la contrainte τ_s prend la valeur suivante [250] :

$$\tau_s = \frac{1}{2} + \sqrt{\frac{6}{\pi}} \frac{\lambda}{\Delta x} \Psi(\lambda, \mathbf{x}) \quad (2.34)$$

Pour représenter la CF de Guo et al. [225] présentée à l'équation (2.18), qui tient compte de la couche de Knudsen, une relation pour le coefficient d'accomodation de la CBBSR a été développé à l'aide d'un bilan sur les populations et les moments :

$$\alpha = \frac{1}{1 + \chi A_1 + \frac{\tau'_{sw} \Delta x}{8 \left(\tau_{sw} - \frac{1}{2} \right)^2}} \quad (2.35)$$

où τ'_{sw} est la dérivée dans la direction normale au mur du temps de relaxation lié à la contrainte au mur τ_{sw} . Cette dérivée est nécessaire pour prendre en compte la variation spatiale de la fonction de viscosité effective sur la condition de glissement (voir l'équation (2.34)). Le temps de relaxation relié au flux de chaleur, τ_q , a également été modifié par Guo et al. [236]:

$$\tau_q = \frac{1}{2} + \frac{\pi A_2 (2\tau_{sw} - 1)^2 + 3 \tau'_{sw} \Delta x (12 + 30 (\tau_{sw} - \frac{1}{2}) \chi A_1)}{8(2\tau_{sw} - 1) \cdot 16 (\tau_{sw} - \frac{1}{2})^2} \quad (2.36)$$

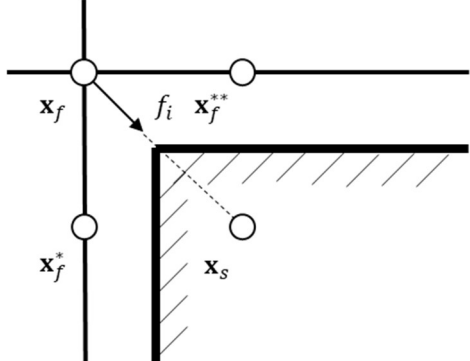


Figure 2.5 CF cinétique de réflexion spéculaire dans un coin.

La CF cinétique de CBBSR a cependant deux défauts cruciaux. D'abord, tel que mentionné précédemment, la réflexion spéculaire est une CF cinétique non-locale. Ensuite, dans les coins tels que représentés à la Figure 2.5, la direction dans laquelle la population doit être réfléchie est ambiguë. Une combinaison de CFs de rebond à mi-chemin et de diffusion, notée DBB, n'aurait pas ce problème [289]. Cependant, la DBB proposée actuellement ne prend pas en compte la variation spatiale de la fonction de viscosité au sein de la couche de Knudsen. La DBB mériterait d'être étendue pour pouvoir récupérer la CF de l'équation (2.19).

2.3.3 Régularisation

L'équation de Navier-Stokes étendue est récupérée avec la MBR en se bornant à résoudre des moments d'ordres égaux ou inférieurs à 2 avec les réseaux D2Q9 et D3Q15 [290]. Or, d'après les vecteurs des moments **m** présentés à l'annexe D, il est évident que certains moments des réseaux D2Q9 et D3Q15 sont d'ordres supérieurs à 2 : en particulier, le moment relié au flux d'énergie est d'ordre 3. Certaines études ont rapporté l'apparition de jets non physiques alignés sur le réseau pour des écoulements non-planaires [195, 291-297]. Ce phénomène nommé crénelage (ou *aliasing*) en anglais serait causé par les moments d'ordres égaux ou supérieurs à 3.

La procédure de régularisation a été proposée afin de retirer les composantes hors de l'équilibre des moments d'ordres supérieurs à 2 [290, 298, 299]. D'abord, les populations sont divisées en leurs composantes à l'équilibre $f_i^{(eq)}$ et hors de l'équilibre $f_i^{(neq)}$:

$$f_i^{(neq)} = f_i - f_i^{(eq)} \quad (2.37)$$

Les composantes hors de l'équilibre sont alors reprojectées sur la base polynômiale d'Hermite associée au réseau pour obtenir des populations hors de l'équilibre régularisées $f_i^{(neqr)}$:

$$f_i^{(neqr)} = \frac{w_i}{2c_s^2} H_{i\alpha\beta}^{(2)} \left(\frac{\mathbf{c}_i}{c_s} \right) : \sum_{i=0}^{Q-1} f_i^{(neq)} \mathbf{c}_{i\alpha} \mathbf{c}_{i\beta} \quad (2.38)$$

où $H_{i\alpha\beta}^{(2)} \left(\frac{\mathbf{c}_i}{c_s} \right) = \mathbf{c}_{i\alpha} \mathbf{c}_{i\beta} / c_s^2$ est le polynôme d'Hermite de deuxième ordre, $\mathbf{c}_{i\alpha} \mathbf{c}_{i\beta}$ est le produit dyadique (ou extérieur), et : représente le double-produit de deux tenseurs. La population post-régularisation $f_i^{(r)}$ s'écrit donc :

$$f_i^{(r)} = f_i^{(eq)} + f_i^{(neqr)} \quad (2.39)$$

Les populations post-régularisations sont ensuite réinsérées dans l'équation de la MBR-TRM, et la nouvelle équation dite de MBR-TRM régularisée s'écrit maintenant ainsi :

$$f_i(\mathbf{x} + \mathbf{c}_i \delta_t, t + \delta_t) = f_i^{(eq)} + \mathbf{M}^{-1} (\mathbf{I} - \mathbf{S}) \mathbf{M} f_i^{(neqr)} + F_i \delta_t \quad (2.40)$$

La procédure de régularisation ne pose pas de problème supplémentaire en matière de parallélisation : toutes les opérations sont locales au sein d'une maille du réseau. Cependant, malgré le grand nombre d'articles ([195, 198, 203, 207, 208, 210, 211, 215, 291-297, 300-304]) ayant utilisé la procédure de régularisation couplée avec les CFs de glissement proposées à la sous-section 2.3.2, il n'a jamais été prouvé que les valeurs développées pour les coefficients d'accommodation, qui prenaient en compte le moment relié au flux d'énergie d'ordre 3, étaient en mesure de récupérer convenablement la CF de glissement.

2.4 Résumé et objectifs spécifiques

Au cours de cette revue de littérature, il a été constaté qu'un problème pratique tel que l'impact de la structure multicouche au sein des filtres nanofibreux et microfibres requérait une méthode de simulation directe des écoulements gazeux en régime raréfié. Une méthodologie en trois étapes avait déjà été proposée pour s'attaquer à ce problème. La génération numérique de milieux filtrants (première étape) et le calcul des trajectoires de particules au sein d'un écoulement d'air à l'aide de l'équation de Langevin (troisième étape) ne posent pas de problèmes particuliers pour un milieu filtrant constitué de nanofibres. Cependant, il n'existe pas auparavant de méthode numérique permettant de récupérer le profil de vitesse d'un écoulement en régime de Knudsen.

Bien que l'équation de Boltzmann soit valide *a priori* pour tous les régimes de raréfaction, la résolution de cette équation (ou même des approximations directes des équations différentielles d'ordre plus élevé que Navier-Stokes) est loin d'être aisée pour un écoulement au sein d'un milieu poreux complexe. Il serait beaucoup plus pratique de s'en tenir à une description phénoménologique des effets de raréfaction, soient le glissement aux parois des fibres et la modification de la relation entre la contrainte et le cisaillement au sein de la couche de Knudsen. Le modèle de Guo et al. ne réfère pas à des longueurs caractéristiques et prend en compte l'influence de la couche de Knudsen sur la condition de glissement. Ce sont des qualités essentielles pour modéliser le glissement dans un milieu poreux complexe en régime de Knudsen. Il est également possible de prendre en compte la relation modifiée entre la contrainte et le cisaillement au sein de la couche de Knudsen avec la définition d'une viscosité effective dans une équation de Navier-Stokes étendue. Des fonctions de viscosité ont été définies dans la littérature sous la forme de fonctions de mur, mais celles-ci sont inapplicables pour un milieu poreux complexe. Certaines de ces fonctions de mur ont été dérivées en supposant que le libre parcours moyen effectif et la viscosité effective soient proportionnelles. Cette hypothèse aurait été validée pour des écoulements planaires et des écoulements au sein de cylindres concentriques. Cependant, il n'existe pas dans la littérature de procédure permettant de calculer un libre parcours moyen effectif dans un milieu poreux complexe.

La MBR est vue comme la méthode de choix pour simuler des écoulements au sein de milieux poreux en raison de son caractère local et explicite, qui facilite sa distribution sur des nœuds de calcul parallèle. Un cadre était déjà établi dans la littérature pour la simulation des écoulements raréfiés avec la MBR, notamment avec une combinaison de discrétisation des conditions de glissements de Maxwell et de la CF classique de rebond à mi-chemin. Cependant, les conditions de glissement actuelles ne permettent pas de prendre en compte à la fois la présence de coins et la variation spatiale de la viscosité effective. De plus, l'impact de la procédure de régularisation sur l'imposition de la condition frontière n'a pas du tout été étudié dans la littérature. Ces problèmes devront être résolus un à un.

Ainsi, pour développer un modèle fiable de prédiction de la performance des milieux filtrants en régime raréfié, les meilleures descriptions phénoménologiques du glissement et de la couche de Knudsen devront être implémentées dans la MBR. Les objectifs spécifiques de ce travail seront de :

1. Vérifier et valider un modèle prédictif de la performance des milieux filtrants en régime du continuum basé sur la méthodologie en trois étapes en régime du continuum. Une fois le modèle vérifié et validé, il sera possible, en toute confiance, d'appliquer la méthodologie en trois étapes à l'étude de l'impact de la structure multicouche d'un milieu filtrant sur sa performance.
2. Développer une CF cinétique de DBB à la résolution de l'équation de Navier-Stokes étendue, avec une prise en compte de la procédure de régularisation sur la formulation de cette CF cinétique. Cette CF cinétique devra être vérifiée et validée sur des écoulements planaires, et vérifié sur des écoulements non-planaires simplifiés pour lesquels il existe des solutions analytiques.
3. Développer un algorithme de traçage des rayons pour calculer le libre parcours moyen effectif au sein d'un milieu poreux complexe, et le vérifier à l'aide des fonctions de mur existants dans la littérature pour un écoulement planaire. Ces fonctions de viscosité résultant de l'algorithme de traçage des rayons seront par la suite introduites dans la MBR. Le modèle de simulation des gaz raréfiés sera par la suite vérifié et validé pour des écoulements non-planaires simplifiés pour lesquels il existe des solutions numériques à l'équation de Boltzmann.

Les travaux reliés au premier objectif spécifique ont déjà été publiés sous la forme d'un article scientifique, qui sera présenté au Chapitre 3. Les travaux reliés au deuxième objectif spécifique ont été divisés en deux parties : un article scientifique publié portant sur les écoulements planaires au Chapitre 4, puis un article scientifique soumis sur les écoulements non-planaires au Chapitre 5. Finalement, pour ce qui est du troisième objectif, les travaux d'un autre article scientifique soumis sont présentés au chapitre 6.

CHAPITRE 3 ARTICLE 1: IMPACT OF MULTILAYERING ON THE FILTRATION PERFORMANCE OF CLEAN AIR FILTER MEDIA

Jean-Michel Tucny, David Vidal, François Drolet, François Bertrand – publié le 25 mai 2020 dans *The Canadian Journal of Chemical Engineering* – p. 1-16

Abstract. Fibrous filter media are commonly used to remove airborne particles that are harmful to human health and the environment. Although filter media are often multilayered for various reasons, no systematic study of the impact of multilayering on filter media performance has been reported. In this paper, direct numerical simulations with the lattice Boltzmann method are used in order to shed light on the impact of multilayering on the performance of clean bimodal fibrous filter media in a Stokes flow regime. Virtual model clean filter media with up to eight layers and various fibre formulations are compared in terms of permeability or pressure drop, capture efficiency, and quality factor. A careful analysis of the results revealed that multilayering had no statistically significant impact on the performance of the clean filter media. At best, the impact of multilayering was similar to that of the inherent variability of such random structures. Fibre formulation was found to be a more efficient way of improving the performance of the filter media. Placing interlayered air gaps between fibrous layers also slightly improved the quality factor by facilitating the flow at the interfaces of the fibrous layers. These findings will guide future studies on the performance of multilayered filters with more complex flow conditions, such as those encountered with inertial or nanofibre-made filter media and with the fouling of filter media.

KEYWORDS: air filtration, lattice Boltzmann method, multilayering, fibrous media, aerosol filtration

3.1 Introduction

Airborne particles are hazardous to human health and the environment. As human activities become increasingly concentrated indoors, the filtration of airborne particles in buildings has become a greater concern as the particles tend to accumulate in confined spaces. [5] This has reinforced the need for proper ventilation and filtration systems. The air filter market has grown at

a 6.7% annual rate from 2011 to 2018, and totaled US\$12.3 billion in 2018. [305] Fibrous filters are the preferred means for capturing airborne particles because they are economical and the most efficient filters for moderate temperature air flows and relatively low aerosol concentrations. These advantages derive from the high porosity inherently associated with fibrous filters. [3, 6, 16, 28]

Two important characteristics of air filter media are the aerosol capture efficiency and pressure drop required to achieve the desired flow rate. Aerosol capture efficiency refers to the ratio of particles captured by filter media to the particles in the incoming stream, while pressure drop is related to the resistance of the filter media to air flow. Although life duration is also an important characteristic of air filter media, only clean filter media without electrostatic effects will be considered. The performance of clean filters is a topic of its own for understanding how to improve filters as they represent the worst-case scenario in terms of aerosol capture. In the rest of the text, filter media will refer to clean filter media. The single-fibre theory is commonly used to predict the capture efficiency of a clean filter media. [28, 154] It assumes that an air filter medium can be approximated by a regular and parallel array of fibres in which the fibres have no influence on each other. The capture efficiency of a whole clean filter, E is given by:

$$E = 1 - \exp\left(-\frac{4\alpha h}{\pi(1-\alpha)d_f}\eta\right) \quad (3.1)$$

where α is the fibre volume fraction; h is the filter media thickness; η is the single fibre efficiency; and d_f is the fibre diameter. Several capture mechanisms (mainly inertial impaction, interception, and Brownian diffusion) contribute to single-fibre efficiency, and numerous analytical, semiempirical, or empirical models exist in the literature to account for them and are reported elsewhere. [28, 154, 306]

Knowing the permeability, the pressure drop through a filter media can be found in the laminar flow regime using Darcy's law, and is given by:

$$v_0 = \frac{K\Delta P}{\mu h} \quad (3.2)$$

where v_0 is the superficial flow velocity in the direction of the pressure drop ΔP ; and μ is the viscosity of the fluid. To compare filter media on a basis independent of their thickness, the quality factor Q_f , also sometimes called the figure of merit, has been defined as [28]:

$$Q_f = -\frac{\ln(1 - E)}{\Delta P} \quad (3.3)$$

Three promising design strategies have been identified and involve the use of inertial filter media, filter media incorporating nanofibres, and multilayered filter media, respectively.[57]

Inertial filter media are specifically designed structures meant to promote inertial impaction as the main capture mechanism by forcing particles to depart from the streamlines and collide with the fibres and/or by forcing the flow to become inertial and thus nonlaminar.

Filter media incorporating nanofibres take advantage of the slip flow caused by an apparent gas rarefaction resulting from a smaller structural characteristic length induced by the presence of nano-scale fibres. The importance of slip on the flow around a fibre is characterized by the Knudsen number $Kn = \lambda/d_f$, where λ is the mean free path of air that, at standard pressure and temperature, is ~ 66 nm. A direct consequence of slip flow is a decrease in the pressure drop across the filter media. [48] The flow pattern around fibres also changes, which may increase the capture efficiency of filter media. [49]

Lastly, filter media may have a multilayered structure in some applications for various reasons. Nanofibres are often deposited onto layers of coarser fibres to overcome poor mechanical properties such as the low stiffness of filter media made of such nanofibres. [33] Also, multilayered filter media for which a specific layer has been functionalized [307] or coated [308] to take advantage of the electrostatic properties of airborne particles are commonly used. The limiting factor for the service life of filters made of nanofibres is often their lower clogging capacity. [59, 62] The costs associated with the regular replacement of fouled or damaged ultrafine filters can be offset by adding a layer of coarser fibres in order to capture the biggest particles first. [60, 61] In the same vein, electret filters, in which a layer of fibres is electrically charged to enhance capture, lose efficiency as the filter clogs or the effect of the charges diminishes, for instance when the filter moisture increases. [309] Coarser fibres delay the clogging of the filter by capturing some of the particles before they reach the functionalized layer. In other filters such as medical masks, the fibres are purposely distributed throughout the thickness of the filter media so that layers with fibres of different diameters are formed. [310]

The formation of a wake can have a major impact on flow interactions between the fibre layers, as evidenced using the numerical flow simulations reported by Liu and Wang. [311] They found that, even at low Reynolds numbers close to 0.02, interactions between fibres can dramatically change the streamlines in the void space between two fibres. Such effects can only be accounted for by solving the full Navier-Stokes equations. It can thus be postulated that interfacial effects between layers may have an impact on the quality factor of multilayered filter media.

When multiple fibre sizes or polydisperse fibre distributions are used to fabricate filters, a theoretical question that has been puzzling filter manufacturers for a long time is whether it is preferable, in terms of the quality factor, to distribute fibres uniformly throughout the thickness of the filter media or to segregate fibres of different sizes into a multilayered structure. To predict the impact of a polydisperse fibre distribution, serial models have been proposed both for pressure drop and capture efficiency in which the whole filter medium is regarded as a superposition of thinner filter media of a single size i :

$$\Delta P = \sum_i \Delta P_i \quad (3.4)$$

$$E = 1 - \prod_i (1 - E_i) \quad (3.5)$$

Furthermore, based on Darcy's law (Equation (3.2)) and the pressure drop serial model (Equation (3.4)), a resistance model for the permeability of a filter media can be written such that:

$$K = t / \sum_i \frac{t_i}{K_i} \quad (3.6)$$

By definition, these serial and resistance models in fact consider well-mixed filter media as segregated multilayered structures and are thus unable to make a distinction between these two types of filter media. These models have been reported to be accurate in experimental investigations [312, 313] but inaccurate in others [89, 111] that suggested that they can be improved by considering interactions between fibres in a well-mixed filter medium. Further experimental reports on bilayered (Bałazy and Podgórski [112] according to Hasolli et al [314]) and tri-layered media[314] suggested that such additive models are inaccurate. To study the impact of

multilayering in isolation, a limited number of filters made of layers of various monodisperse fibres were prepared, and their permeability and capture efficiency were studied experimentally. [91] The authors reported that the differences between the various formulations tested were within the limits of experimental error and that a clear impact of multilayering could not be deduced from the laboratory results. Furthermore, these authors assumed that the order of the various layers within the filter had no impact on performance and thus did not study this aspect despite earlier contradictory results. [308] However, the goal of this later reference relates to the fluid imbibition process. The predominance of capillary forces may thus explain these results. The contradictory findings reported in the literature highlight the need for further work on the impact of multilayering on filter media performance.

To the best of our knowledge, there have been no comprehensive and systematic investigations of the impact of the formulation and the order of layers in a multilayered filter medium in a continuous laminar flow regime. Such studies are needed and should aim at unveiling the impact of layer compositions and possible interfacial effects between layers, which is a difficult experimental task. Assessing the impact of multilayering in such a regime is a prerequisite for understanding the impact of multilayers in more challenging and interesting situations such as in nanofilter media involving slip flows. Direct numerical simulation is the most appropriate method for answering these questions. For instance, it was used to study polydisperse fibre diameter distributions, [94, 116, 118, 315] and dust loading. [316, 317] It was also used to study the performance of layers of nanofibres. However, it was assumed in those simulations that nanofibres had no impact on the flow field. [129-132] Such a hypothesis should be verified. In this paper, flow through microfibrous layers will be considered to serve as a basis of comparison for an upcoming study in slip flow regime. Section 3.2 presents the numerical methodology used to determine the impact of multilayering on filter media performance in the laminar flow regime. Then, in Section 3.3, the accuracy of flows computed using the lattice Boltzmann method through several single layers of monodisperse fibres is assessed. Section 3.4 details the three numerical studies carried out to determine the impact of multilayering and interfacial flow phenomena on filter media performance. Section 3.5 analyzes the impact of the number of layers and voids of increasing thicknesses between layers to quantify the impact of multilayering and interfacial effects. Lastly, Section 3.6 presents a discussion of the practical industrial implications that can be deduced from the present study and proposes avenues of investigation for improving filter medium performance.

3.2 Methodology

This section describes the numerical procedure used to verify the impact of multilayering on the performance of air filter media. This methodology was based on the numerical procedure detailed in Rebai et al. [120]. Three successive steps were carried out: (1) the numerical generation of a representative filter medium structure using a fibre deposition algorithm, (2) the simulation of the flow through the filter medium using the lattice Boltzmann method (LBM), and (3) the calculation of airborne particle trajectories by solving a Langevin equation. Steps 2 and 3 allowed us to determine the permeability and capture efficiency of the filter media, respectively. Based on these two properties, the quality factor (defined in Equation (3.3)) could then be obtained at a given flow rate using Darcy's law (Equation (3.2)). As the air particle concentrations considered were lower than 0.001 mL/L, the airborne particle trajectories could be calculated using one-way coupling, meaning that the air flow affects particle trajectories but that the presence of the airborne particles is neglected when computing the flow field. [242] This three-step methodology is illustrated in Figure 3.1, and the different steps are detailed in the following subsections.

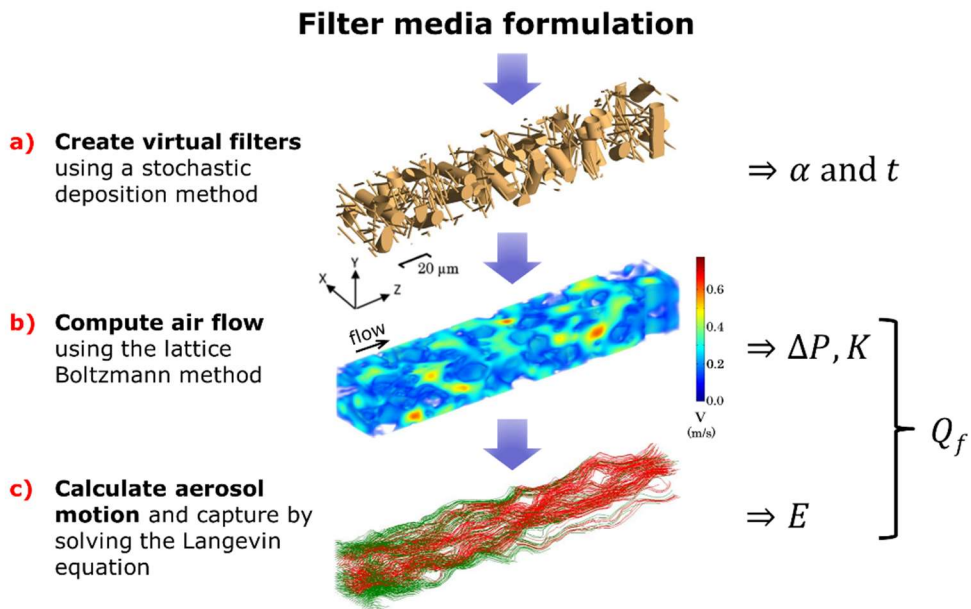


Figure 3.1 Illustration of the three-step numerical procedure used: A, a representative elementary volume of a bimodal filter medium; B, the computed flow field through the corresponding filter media; and C, the calculated particle trajectories through the same filter medium (the green and red trajectories correspond to the trajectories of the particles being intercepted by the filter medium or flowing through it, respectively)

3.2.1 Multilayered filter medium generation

In the first step of our methodology, representative sections of fibre mats were virtually constructed using a stochastic algorithm that sequentially deposits fibres. This algorithm was previously developed to study the structure of paper and its response to compressive forces. [318] It was also generalized to describe wood-fibre composites such as oriented strand-boards. [319] In our study, fibres, approximated as straight cylinders, were deposited sequentially over the X-Y plane. Fibre position and orientation were chosen based on a random uniform distribution, while the sequence of fibre diameters to be deposited was chosen either to create a multilayered or a uniformly distributed filter media (the latter hereinafter referred to as a well-mixed filter medium). The domain was periodic in the X-Y plane so that when only part of a fibre fell inside the domain, the remainder of the fibre was added to the opposite side of the domain. The fibre length used (L_f) and the total number of fibres depended on the fibre diameter chosen and thus varied with the case investigated (see Section 3.4).

To make sure that the domain was large enough in the normal direction to the flow such that this domain consisted of a representative elementary volume of a given fibre formulation, the Brinkman's screening length criterion defined by Clague and Phillips[94] was used. This required that the lateral size of the domain L (ie, the dimension in the direction normal to the flow) should satisfy $L > \sim 14\sqrt{K}$, where K is Darcy's permeability.

Each solid structure resulting from the deposition of the fibres within the computational domain was then mapped onto a Cartesian structured grid, often referred to as a lattice, which was used as a spatial discretization of the domain for computing the flow field with LBM. The lattice spacing used for all structures analyzed was $\Delta x = 0.1 \mu m$, which was small enough to limit the discretization error to less than 0.2% for permeability and 2% for capture efficiency, with convergence orders of 2.8 and 1.3, respectively, as evaluated by a grid independence study and using Richardson extrapolation. [320] In this lattice, solid and pore phase cells were encoded in a Boolean manner. In addition to the filter medium structure itself, a 20-cell-thick buffer zone was added both upstream and downstream from the filter medium structures in the flow direction (ie, the Z direction). The size of the buffer was chosen to limit computational costs as much as possible. Comparisons with a 300-voxel-thick buffer zone showed only 0.06% and 1% relative differences in pressure drop and capture efficiency, respectively. The resulting structures were then

characterized and compared in terms of porosity profiles, which were straightforwardly obtained from the determination of phase fractions across 5- μm slices of the Boolean cell map throughout the thickness of the filter medium (ie, the Z direction).

3.2.2 Air flow computation

In the second step, LBM was used to compute the flow field in the pore space using the structured grid previously generated. LBM is a discretization of the Boltzmann equation in the velocity, space, and time domains on a Cartesian structured grid. Rather than directly solving the Navier-Stokes equations, LBM evolves probability distribution functions (also called populations) according to a collision-propagation scheme that mimics the statistical microdynamic interactions of molecules.

Within the limits of low Mach and Knudsen numbers, it has been proven through a multiscale Chapman-Enskog expansion procedure that LBM recovers the Navier-Stokes equations at the second order in space. [250] The parallelization of LBM is straightforward and efficient due to its local explicit scheme. [255, 256] Furthermore, the use of a Cartesian structured grid renders the meshing process trivial, which is particularly useful for the simulation of complex porous media. The reader is referred to Krüger et al. [251] for additional information about LBM. Once the flow field is obtained, the permeability in the thickness direction can be calculated from Darcy's law (Equation (3.2)). For more details on the implementation of the LBM code used for the computations, the reader is referred to previous studies on air filtration. [120, 321] All the computations reported here were performed on parallel computer clusters from Calcul Québec. The computational times for the 126 structures investigated varied from 24 hours (for a lattice size of $1802 \times 380 \times 380$ voxels) to 120 hours (for a lattice size of $3782 \times 2140 \times 260$ voxels) on three nodes of an 8-core Dual Intel Sandy Bridge EP E5-2670.

3.2.3 Particle trajectory computation

In the third and last step, the capture efficiency of the filter media was predicted by calculating the trajectories of particles of various sizes regularly distributed on the domain entry plane upstream from the filter media (ie,, in the buffer zone) using the previously calculated velocity field. As already mentioned, it was assumed that the concentration of particles is sufficiently low that interactions between the particles and between the particles and the fluid can

be neglected, resulting in a one-way coupling between the fluid and the particles. Because of this simplification and the range of Reynolds numbers involved, the flow could be considered as being at steady state. Newton's second law of motion was thus solved independently for each particle considering both the drag force and Brownian motion. Electrostatic and gravitational forces were neglected, as uncharged particles of size smaller than 1 μm were considered. [154] The problem thus takes the form of a stochastic differential Langevin equation [322]:

$$\frac{d}{dt}\mathbf{v} = \frac{d^2\mathbf{r}}{dt^2} = \gamma(\mathbf{u}(\mathbf{r}) - \mathbf{v}) + \boldsymbol{\Gamma}(t) \quad (3.7)$$

where \mathbf{r} is the position of the particle; \mathbf{v} is the velocity of the particle; \mathbf{u} is the fluid velocity; $\gamma = \frac{3\pi d_p \mu}{m C_C}$ is the drag coefficient; d_p is the particle diameter; m is the particle mass; and C_C is the Cunningham slip correction factor.

Particle trajectories for each of the 20 diameter classes considered in this work (see Section 3.3) and regularly distributed within the 30 nm-900 nm range were computed. The capture efficiency reported in Section 3.5 corresponds to the efficiency of the most penetrating particle size (MPPS) (ie, the lowest capture efficiency obtained for all the diameter classes considered). The spacing of the particle launching sites in the domain entry plan was taken as 200 nm. This number of trajectories was sufficient to render statistically significant values.

A particle was assumed captured when its centre of mass was located at a distance of one particle radius or less from a fibre surface. Re-entrainment, thermal and inertial rebounds, as well as clogging of the filter were neglected. According to Davies, [12] it is unlikely that a particle may be re-entrained if the air velocity is lower than 1 m/s, which was the case in our simulations as the superficial air velocity was much lower than this limit (0.05 m/s). Also, according to Ellenbecker et al, [245] there is a low probability that particles with diameters smaller than 10 μm and velocities smaller than 1 m/s rebound because of their low inertia. Additional parameters used for the simulations are presented in Table 3.1.

Table 3.1 Flow simulation parameters

Particle density	1000 kg/m^3
Air temperature	300 K
Air density	1.225 kg/m^3
Air viscosity	$1.8 \times 10^{-5} \text{ Pa} \cdot \text{s}$
Superficial velocity	0.05 m/s
Reynolds number	< 1

3.3 Model Accuracy Assessment and Validation

To assess the proposed model, the accuracy of the LBM flow computation and the resulting capture efficiency calculation is examined for single layers of monodisperse fibres for which existing literature correlations exist. The model is also validated by comparing experimental data for capture efficiency and results obtained from our numerical model.

3.3.1 Air flow computation assessment

The air flow model is assessed by comparing Darcy's permeabilities, obtained by computing the flow field using the LBM, with Davies' correlation (Equation (3.2)). Unconsolidated filters of various thicknesses (from 30 μm -602 μm) made of a single layer of a given number of monodisperse fibres (varying from 20 fibres-980 fibres) with diameters ranging from 3 μm -21 μm were created. Their porosity was varied from 76%-96% by changing the aspect ratio of the fibres. Three different structures for each filter medium were created to account for the inherent variability of such structures. The dimensionless permeability predictions as a function of porosity are compared in Figure 3.2. A good agreement between permeabilities computed by the LBM and the ones predicted by Davies' correlation is found, particularly above $\sim 85\%$ porosity. Below $\sim 85\%$, more variability within the triplicate structures is observed as the number of fibres involved in these calculations is smaller (20 fibres) than for the other cases (80 fibres-980 fibres), but the numerical data follow Davies' correlation well on average.

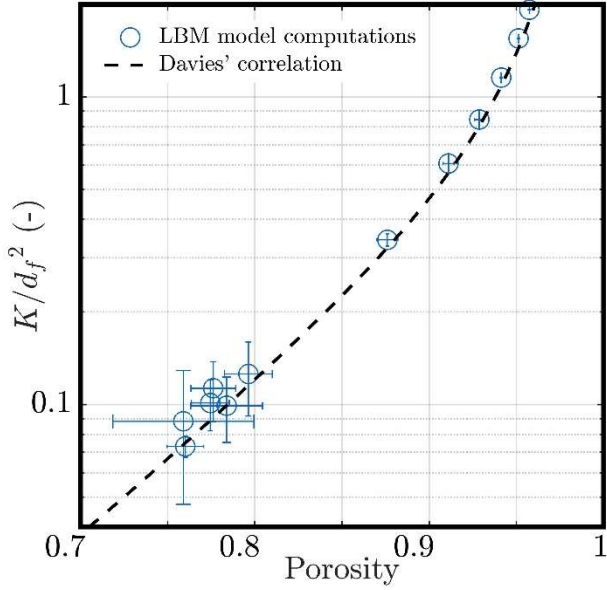
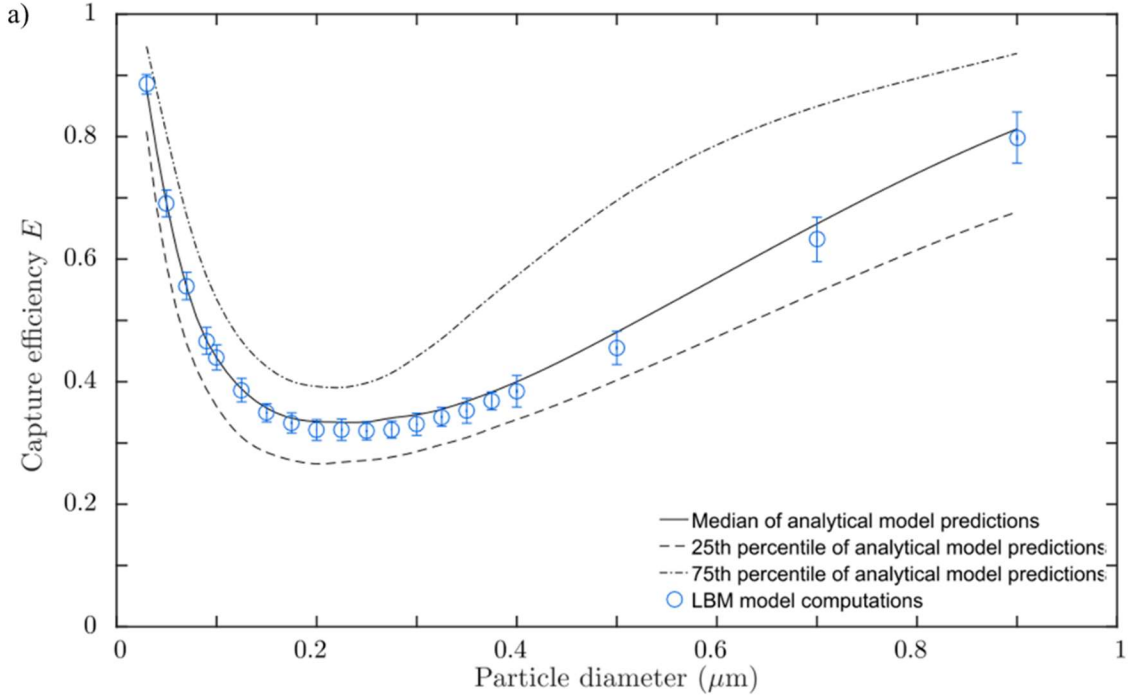


Figure 3.2 Comparison between dimensionless Darcy permeabilities computed with the lattice Boltzmann method and Davies' correlation. The error bars represent standard deviations obtained for triplicate numerical computations

3.3.2 Capture efficiency assessment

To assess the capture efficiency predictions, the LBM-based model calculations are compared with analytical and empirical correlations from the literature. Unconsolidated structures of filters of various thicknesses (from 46 μm -106 μm) and porosities (from 75.9%-78.4%) made of a single layer of monodisperse fibres (from 3 μm -7 μm in diameter) were generated for this purpose. In addition, a program to generate predictions from 40 analytical and empirical correlations for the single fibre efficiency due to interception, diffusion, and inertial mechanisms reported in the literature was built. [28, 306] Considering the range of validity of each correlation, a total of ~ 7000 predictions from the various combinations of these correlations were accounted for. Figure 3.3a)-c) presents the range of predictions from these literature correlations (continuous and dashed lines) for the three fibre diameters in terms of capture efficiency as a function of particle diameter. Our LBM-based model predictions fall within the spread of the correlation-based predictions and most of time are relatively close to the median of these predictions, particularly if one considers that the uncertainty associated with the LBM results are the three structures used for each data point. Finally, for all the filter media considered here, the capture efficiencies at the MPPS (ie, the most

penetrating airborne particle size usually around $0.2 \mu\text{m}$ - $0.4 \mu\text{m}$) are plotted against the correlation-based predictions in Figure 3.4. As can be seen, all data points fall close to the bisector line, which confirms the soundness of the proposed approach and justifies its use to assess the impact of multilayering.



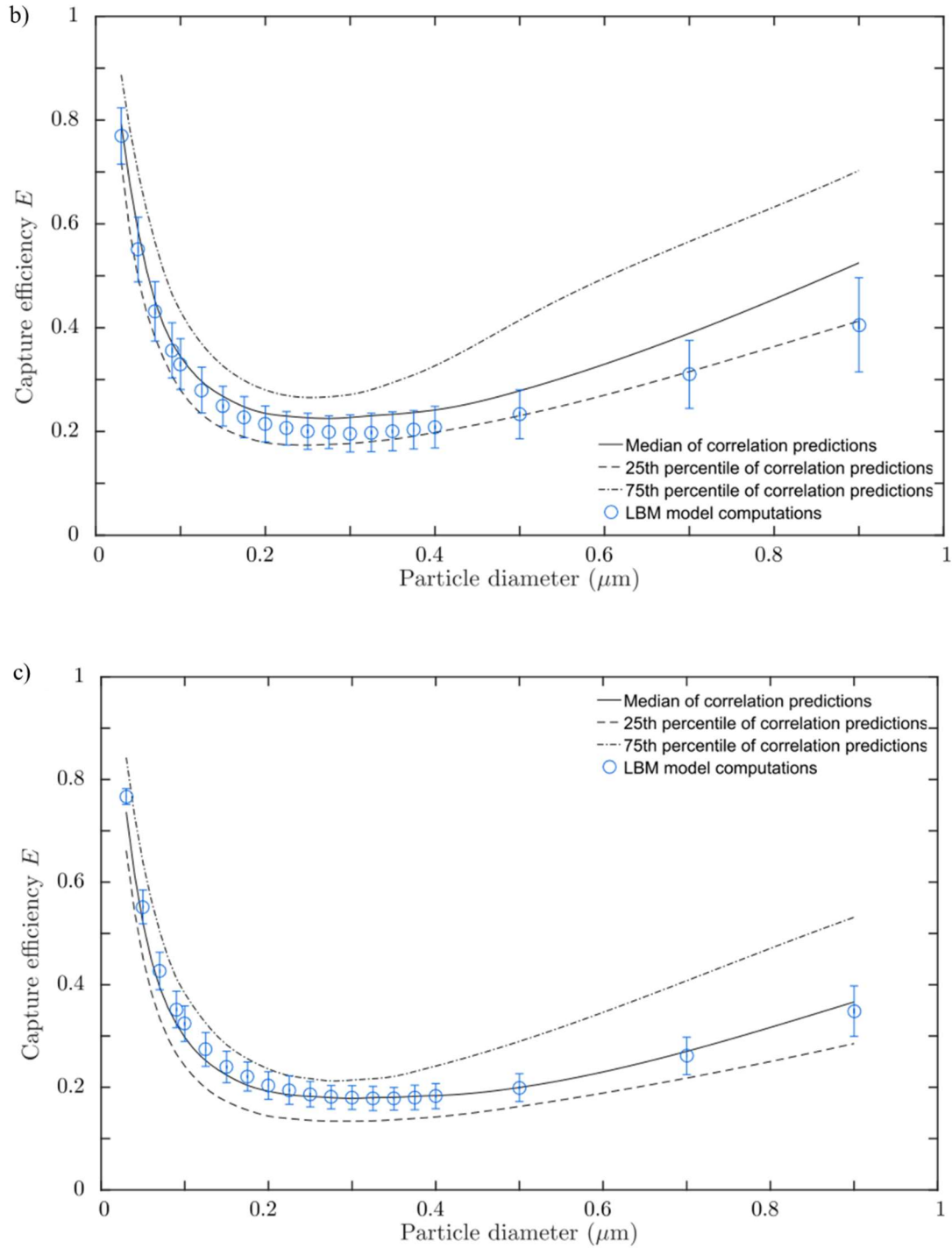


Figure 3.3 Comparison between the capture efficiencies computed with the lattice Boltzmann method-based model and literature correlation-based predictions for filter media made of: a) 3 μm ; b) 5 μm ; and c); 7 μm fibres. The error bars represent standard deviations obtained from triplicate numerical computations

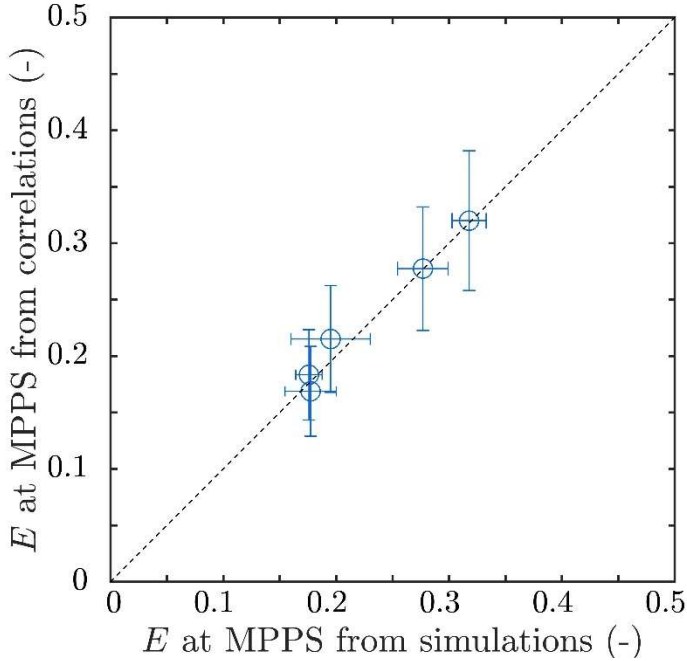


Figure 3.4 Comparison between the capture efficiencies at the most penetrating particle size for filter media made of monodisperse fibres (with diameters ranging between 3 μm -7 μm) predicted with the lattice Boltzmann method-based model and the median of the correlation-based predictions. The x-axis error bars represent standard deviations obtained from triplicate numerical computations, whereas the y-axis error bars reflect the 50th percentile interval around the median from all these correlation-based predictions

3.3.3 Capture efficiency validation

To validate the capture efficiency predictions, the LBM-based model is compared to experimental results from Steffens and Coury, [323] which measured the single-fibre efficiency obtained from polyester fibre mats made of nearly monodisperse fibres for various NaCl particle sizes. Table 3.2 summarizes the experimental conditions used.

Table 3.2 Experimental conditions used by Steffens and Coury [326] for particle diameters greater than 30 nm. The reported intervals represent the SDs around the mean values

Fibre diameter (μm)	Mat porosity (%)	Face velocities (m/s)	Particle diameter (nm)
16.0 ± 1.0	88.2 ± 0.3	0.030	37.2 ± 3.1
		0.064	46.8 ± 2.2
		0.128	85.2 ± 3.2
		0.250	94.8 ± 4.5

As the capture efficiency algorithm used is known to provide an imprecise prediction of Brownian diffusion for particle sizes below 30 nm, [322] only the larger particle diameters from Steffens and Coury were retained. Three virtual mats of $221 \pm 10 \mu\text{m}$ in thickness containing 20 straight fibres each were created and their capture efficiency evaluated using the procedure explained in Section 3.2. The long-range curvature of the polyester fibres used for fabricating the filter were neglected. Indeed, fibre kinks only slightly affect the long-range variability of permeability and capture efficiency, which are both determined at a smaller scale (the so-called Brinkman's screening length) closely related to the fibre diameter, as evidenced by Davies correlation and the single-fibre theory expressions. [94] As a matter of fact, the effect of fibre curvature was investigated and found to be negligible. [324] Figure 3.5 reports a parity plot comparing the capture efficiency values obtained numerically to the experimental data in terms of single-fibre efficiency. The model does not take into account the electrostatic capture mechanism, which may have played a role although no discussion was made by Steffens and Coury. [323] As can be seen, the agreement is good in general, thus suggesting a negligible impact of electrostatic charges. Only results from the smallest particle size with the slowest face velocities (ie, blue circles in the upper right corner of the graph) slightly depart from the bisecting line. This can be explained by the inaccurate predictions of Brownian diffusion for small particles as the 37.2 nm size is close to the 30 nm threshold mentioned above. From these results and the accuracy assessment presented in Section 3.3.2, one can conclude the adequacy of the proposed particle capture model.

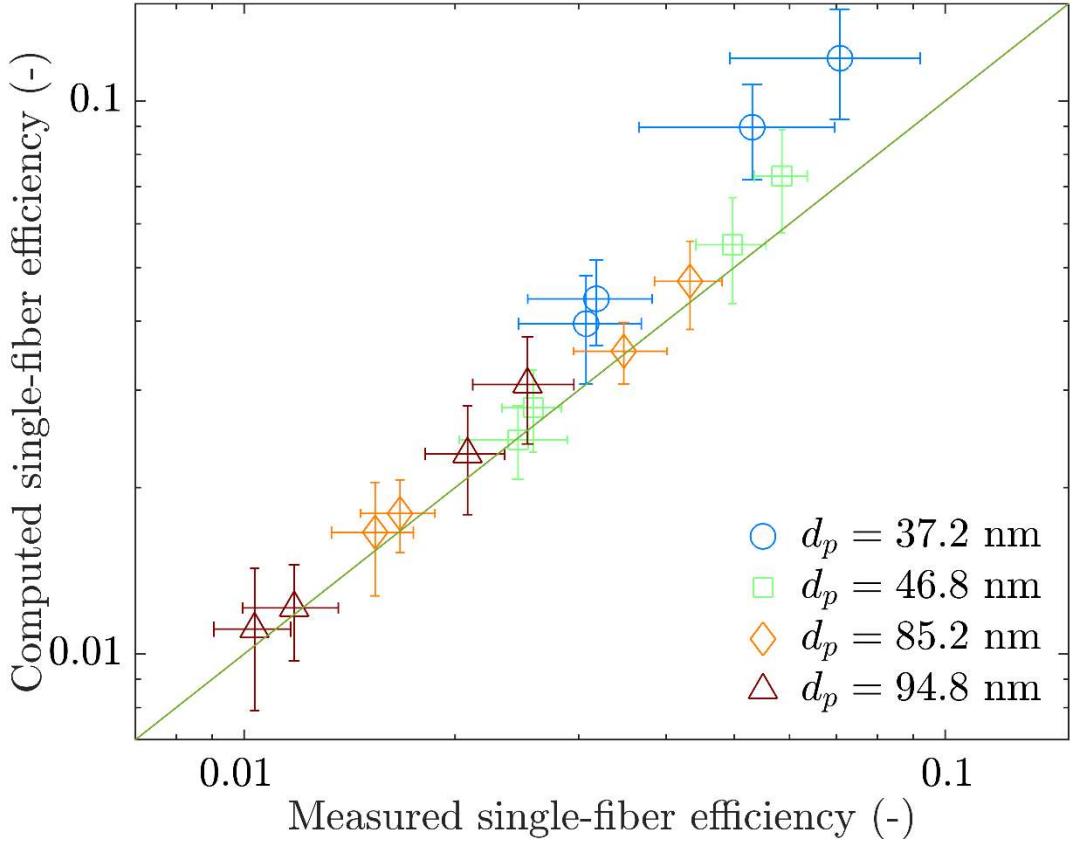


Figure 3.5 Comparison between single-fibre efficiencies obtained from our code to from experimental data from Steffens and Coury. [326] The x-axis error bars represent standard deviations on the single-fibre efficiency calculated from the reported data. The y-axis error bars represent standard deviations obtained from triplicate numerical computations

3.4 Numerical Investigation Plan

To determine the impact of multilayering on filter medium performance (in terms of pressure drop/permeability, capture efficiency, and the overall filter medium quality factor), three sets of numerical computations were carried out, all performed on multilayered structures made of fine and coarse fibre blends (ie, bimodal fibre distributions). The first set of computations consisted of evaluating the impact of multilayering on filter media with moderate coarse-to-fine fibre diameter ratios (hereinafter referred to as $R_{CF} = \frac{d_C}{d_F}$, where d_C and d_F are, respectively, the diameters of the

coarse and fine fibres). Given that the impact of multilayering might be triggered by flow phenomena occurring at the interface between successive layers, a second set of computations was carried out to investigate the impact of changing the interface behaviour by adding empty transition zones between the layers (hereinafter referred to as air gaps) of increasing thickness. To verify whether the conclusions obtained at moderate R_{CF} were still valid at much higher R_{CF} , several multilayered configurations at a large R_{CF} were also investigated in a third set of computations. The exact motivations for the second and third sets of computations will become clear in Section 3.5, which addresses questions raised after the analysis of the results of the first set of computations experiments. These three studies will altogether be described more in detail in the next subsections. Note that, to evaluate the inherent variability of the performance of the various filter medium structures due to the random nature of the fibre layers involved, all random structures in the first and third studies were done in triplicate.

3.4.1 Impact of multilayering at moderate coarse-to-fine diameter ratios

To study the effects of the layering order in a filter medium, several two-, four-, six-, and eight-layered structures of bimodal fibre formulations were compared to structures made of the same fibre formulations but for which the fibres were randomly deposited (ie, a well-mixed structure). Each of the multilayered structures was thus made of either fine or coarse fibres, and the fibre size was varied in alternating fashion from one layer to the next. Six different bimodal fibre formulations were considered and differed in terms of the fine fibre volume fraction ($x_F = 10\%, 20\%, \text{ or } 30\%$) and coarse fibre diameter ($d_C = 9 \mu\text{m}$ or $d_C = 12 \mu\text{m}$). In all cases, the fine fibre size was kept constant at $d_F = 3 \mu\text{m}$. Furthermore, to ensure that all layers with coarse fibres contained at least three of them, a fixed amount of 24 coarse fibres was chosen for all the structures generated. Note, however, that fixing the total number of coarse fibres had the detrimental effect of limiting the range of R_{CF} that could be investigated due to the prohibitive computational power requirements associated with large fibres when the lattice spacing is kept constant. For the same reason, the volume fraction of fine fibres was restricted to $x_F \leq 30\%$ to limit the domain dimensions determined by the number of fine fibres and the resulting filter medium thicknesses to manageable sizes that could fit on the computational resources available. Figure 3.6 summarizes the filter medium structures investigated in this first study.

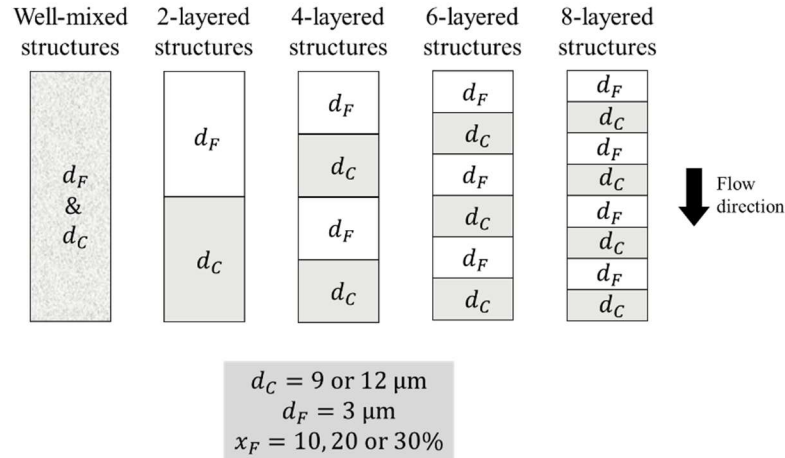


Figure 3.6 Summary of the structures and the range of the various parameters investigated in the first study

Lastly, the length for both the fine (L_F) and coarse (L_C) fibres was taken such that $L_F = L_C = 4 \times d_C$. In addition, the lateral sizes of the domain (ie, L_X and L_Y) were chosen as $L_X = L_Y = L_C + 2 \mu\text{m}$ to avoid self-penetration of fibres due to the periodic boundary conditions used.

Particles were sequentially released at the inlet of the domain from a regular array with a $0.2\text{-}\mu\text{m}$ spacing. As the domains for the filter media with $9\text{-}\mu\text{m}$ and $12\text{-}\mu\text{m}$ coarse fibre diameters were, respectively, $38 \mu\text{m}$ and $50 \mu\text{m}$ in size, 36 100 and 62 500 particles were launched for each particle diameter. This was sufficient to ensure statistical significance.

3.4.2 Impact of interfacial flow phenomena between layers at moderate coarse-to-fine diameter ratios

To evaluate the impact of flow phenomena on filter medium performance at the interfaces between layers, individual layers were constructed and were then merged, with identical air gaps of varying thicknesses inserted between the layers. The intent was to decrease the magnitude of the interfacial flow phenomena as the air gaps increased in thickness and, consequently, isolate their impact from the inherent performance variability resulting from the random positioning and

orientation of the fibres within the layers. While it must be noted that this filter configuration may sound unrealistic, the purpose of this set of computations is not to reproduce filter media as they are usually produced in practice, but rather to reveal the possible existence of interfacial effects between layers. To maximize the potential impact of the air gaps on pressure drop and capture efficiency, filter media with eight layers, and thus seven identical gaps, were created. Nine different air gaps ranging in size from 0 μm -30 μm were tested. The volume fraction of fine fibres was kept constant at 10%, meaning that the first, third, fifth, and seventh layers were each composed of ten 3- μm fibres, while the other layers were each composed of six 12- μm fibres. Figure 3.7 summarizes the structures considered in this second study. The same fibre aspect ratios, lateral domain dimensions, and buffer sizes as in the first study were also considered here. A constant number of 62 500 particle trajectories were computed to determine the capture efficiency of the various filter media structures.

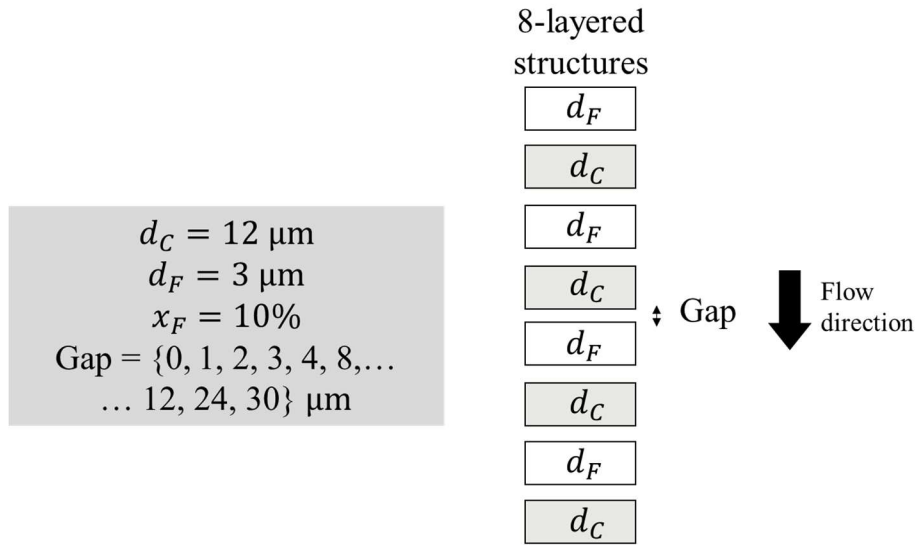


Figure 3.7 Summary of the structures and the range of the various parameters investigated in the air gap study

3.4.3 Impact of interfacial flow phenomena between layers at a high coarse-to-fine ratio

The first two studies were carried out using moderate coarse-to-fine diameter ratios, mainly because of limitations in computational power and the constraints set by the number of coarse fibres and layers in the filter media. To verify whether the conclusions drawn still held at higher R_{CF} , some of these constraints were relaxed in this third study to reach $R_{CF} = 10$. Here, a three-layered filter medium base configuration was used, with a single coarse fibre layer composed of a single 30- μm diameter large fibre layer sandwiched between two layers of 3- μm diameter fine fibres. While the R_{CF} is higher than what is commonly encountered in multilayered filters ($R_{CF} \sim 2\text{-}4$), the goal of this study is to use an extreme R_{CF} to possibly unveil interfacial effects between layers that would not be apparent at lower values. In addition, note that fibre diameters of 30 μm are not so uncommon in the literature (eg, they have been blended with 7 μm fibres by Balazy et al [309]).

Two additional choices were made to better determine the impact, if any, of multilayering on the filter media. First, the porosity of each layer was chosen to be equal to $\epsilon = 89\%$ in order to reduce the impact of porosity fluctuations on the permeability of the filter media. Second, the volume fraction of fine fibres was set to 91% in order to maximize the coefficient of variation (COV) of the fibre size distribution. As a result of these two additional choices, the degrees of freedom of the fibre system were reduced as the fibre length, domain dimensions, porosity, and volume fraction of fine fibres of the whole filter medium were interdependent. In addition, to limit the required computational resources, the domain dimension in the direction of the axis of the large fibre (X direction) was set to $L_X = L_C = L_F + 2 \mu\text{m}$, where the length of the fine and coarse fibres were taken, respectively, as $L_F = 8 \times D_F = 24 \mu\text{m}$ and $L_C = 26 \mu\text{m}$ (note that because $L_X = L_C$ and the boundary condition is periodic, this choice made the coarse fibre infinite). To satisfy all these choices, the domain dimensions in the Y and Z directions were taken, respectively, as $L_Y = 214 \mu\text{m}$ and $L_Z = 350 \mu\text{m}$ (the latter dimension included two 12- μm -thick buffers).

As the number of layers was here limited to three, this sandwiched base filter medium (hereinafter referred to as the sandwiched configuration) was compared to four alternate layered configurations in which the presence or the order of some layers was modified. These configurations are illustrated in Figure 3.8. The main intent was to verify the impact of interfaces

between layers on the performance of multilayered filter media. First, the coarse fibre was simply removed from the base sandwiched configuration to isolate its impact on filter medium performance (hereinafter referred to as the gap configuration). Second, the gap left from the removal of the coarse fibre was also removed with all the fine fibres from the original layers keeping the same X-Y position (hereinafter referred to as the no gap configuration). The impact of the gap itself was scrutinized here. Third, the impact of an isolated coarse fibre alone on filter media performance was evaluated (hereinafter referred to as the alone configuration). The intent here was to quantify the importance of interface phenomena on the performance of the multilayered filter media by determining whether the addition of the respective performances of the alone and gap configurations was exactly the same as that of the sandwiched configuration, which would imply that interface phenomena had no impact. Lastly, a configuration in which the coarse fibre was positioned upstream from the two fine fibre layers was evaluated to further study the impact of interfaces (hereinafter referred to as the upstream configuration).

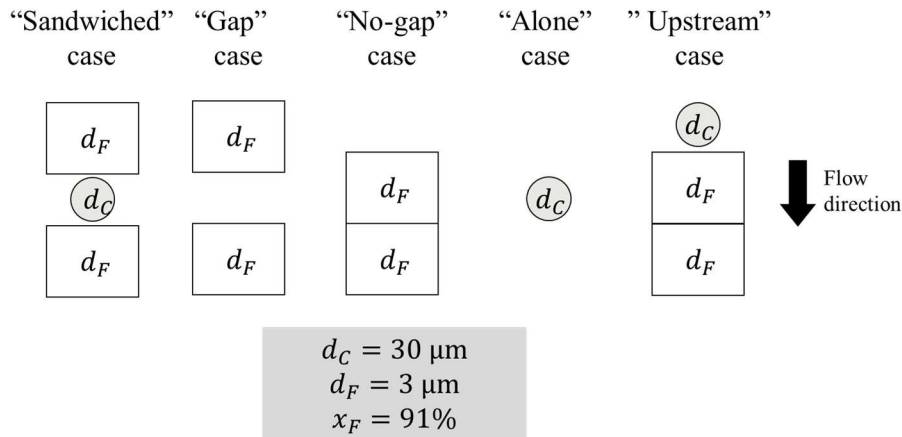


Figure 3.8 Summary of the five configurations and parameters used to test the impact of interfaces between layers on three-layered filter media made of fibres with a high coarse-to-fine diameter ratio

3.5 Results and Discussion

In this section, the performances predicted by numerical simulations of the multilayered filter medium structures made of bimodal fibre distributions involved in each of the three studies described in Section 3.4 are presented and discussed. The intent was to quantify the impact on filter medium performance of multilayering in the laminar flow regime, ie, in terms of pressure drop or

permeability (one being the inverse of the other within a constant following Darcy's law (Equation (3.2))), particle capture efficiency, and overall quality factor, the latter of which is the intrinsic performance of the filter medium combining filtration efficiency and pressure drop in a single measure independent of its thickness. First, filter media at moderate R_{CF} are examined. Second, the impact of air gaps in between layers for filter media at moderate R_{CF} is scrutinized in detail to characterize the importance of interfacial effects between layers to the overall impact of multilayering. Lastly, filter media structures at a high R_{CF} are examined to verify whether the conclusions drawn at lower R_{CF} still held.

3.5.1 Impact of multilayering at moderate coarse-to-fine diameter ratios

If multilayering does affect filter medium performance, it might be related to the variation in porosity that it induces throughout the structure, as porosity impacts both permeability and capture efficiency (through the fibre volume fraction in Equation (3.1)). Figures 3.9a)-c) and 10 present, respectively, typical random structures and the corresponding porosity profiles for the two-layered, eight-layered, and well-mixed configurations. Fibres with higher aspect ratios naturally tend to create more porous structures due to the non-compressive sequential fibre deposition used. As can be seen in Figure 3.10, and despite some natural local fluctuations, layers of finer fibres in the two- and eight-layered structures tend to be more porous, whereas porosity varies around a constant value throughout the thickness of the well-mixed structure. Nevertheless, for a given fibre formulation, the mean porosities of the various structures are similar, as can be seen in Figure 3.11. Therefore, if any impact of multilayering on the performance of filter media can be measured, two effects can be foreseen: (a) the first effect results from the difference in porosities between the various layers and a well-mixed structure and (b) the second effect results from the sudden variations in porosity at the interfaces between layers.

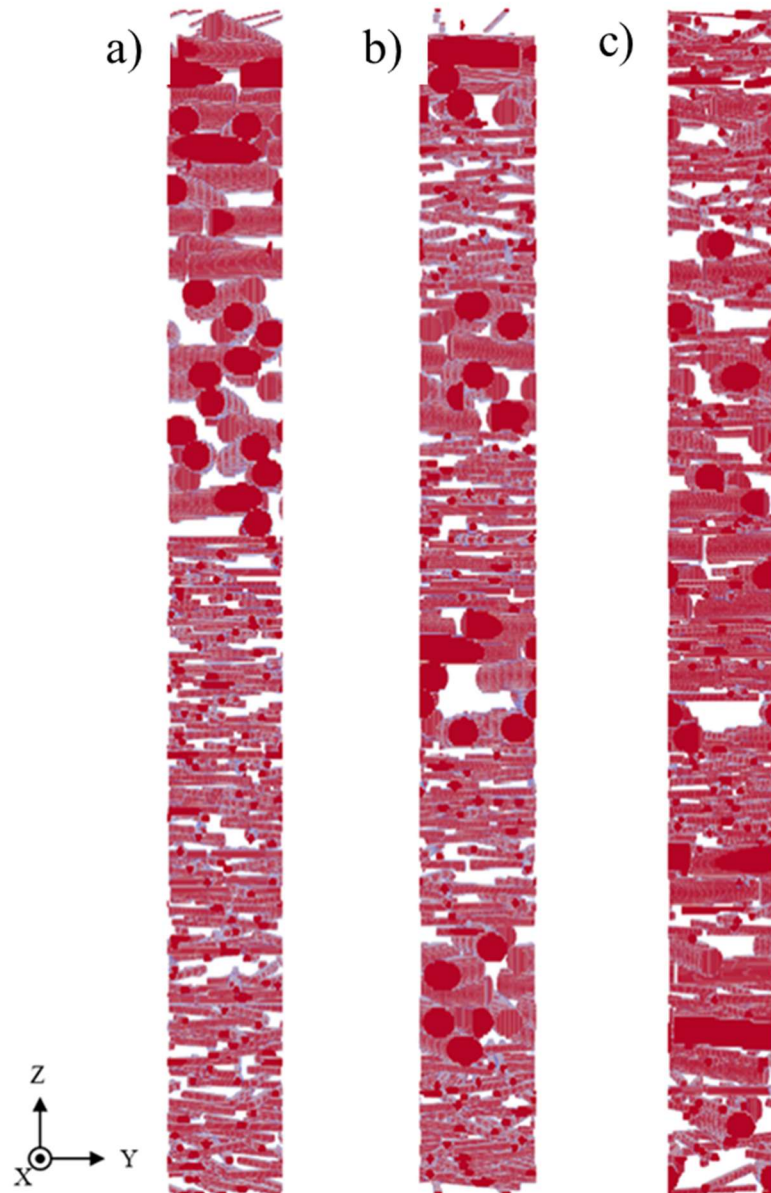


Figure 3.9 Examples of representative elementary volumes of filter media created by the fibre deposition algorithm to study the impact of multilayering for the: a), two-layered; b), eight-layered; and c), well-mixed cases, with $d_C = 12 \mu\text{m}$ and $x_F = 30\%$

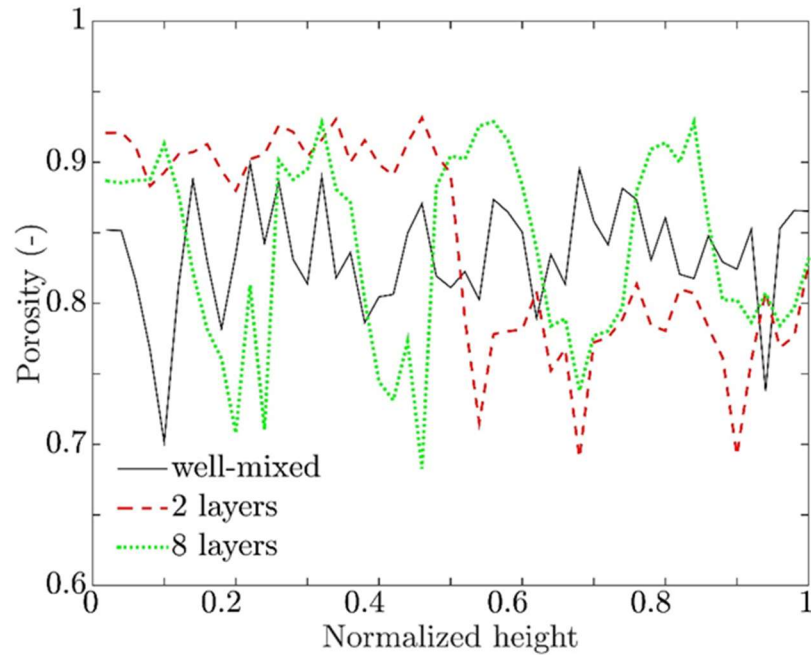


Figure 3.10 Porosity profiles of the filter medium structures shown in Figure 3.9. Data are averaged values over 5- μm -thick slices of the filter media

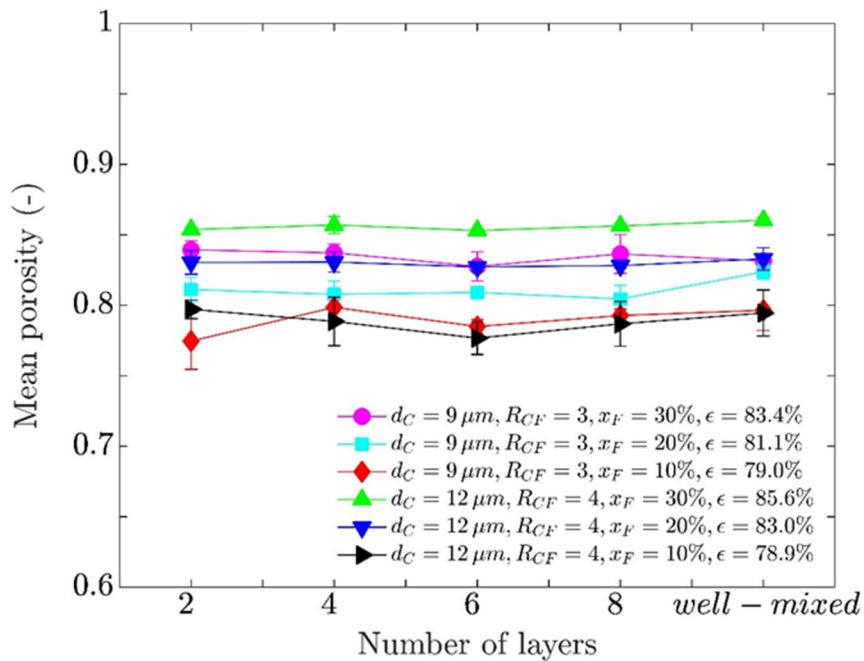


Figure 3.11 Mean porosities of the various multilayered and well-mixed filter media for six fibre formulations. The error bars represent standard deviations obtained from triplicate computations

A typical flow field resulting from the LBM is shown at Figure 12. The macroscopic properties that determine filter medium performance (i.e., permeability, capture efficiency, and quality factor) obtained from the numerical simulations are presented in Figure 13a-c for the six fiber formulations, in the case of the 2-,4-,6-, 8-layered and well-mixed structures.

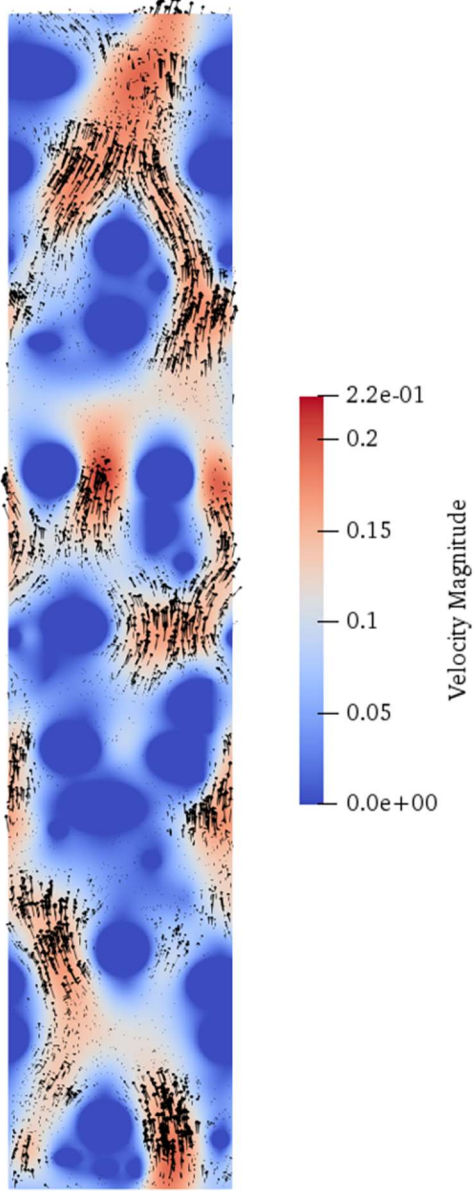
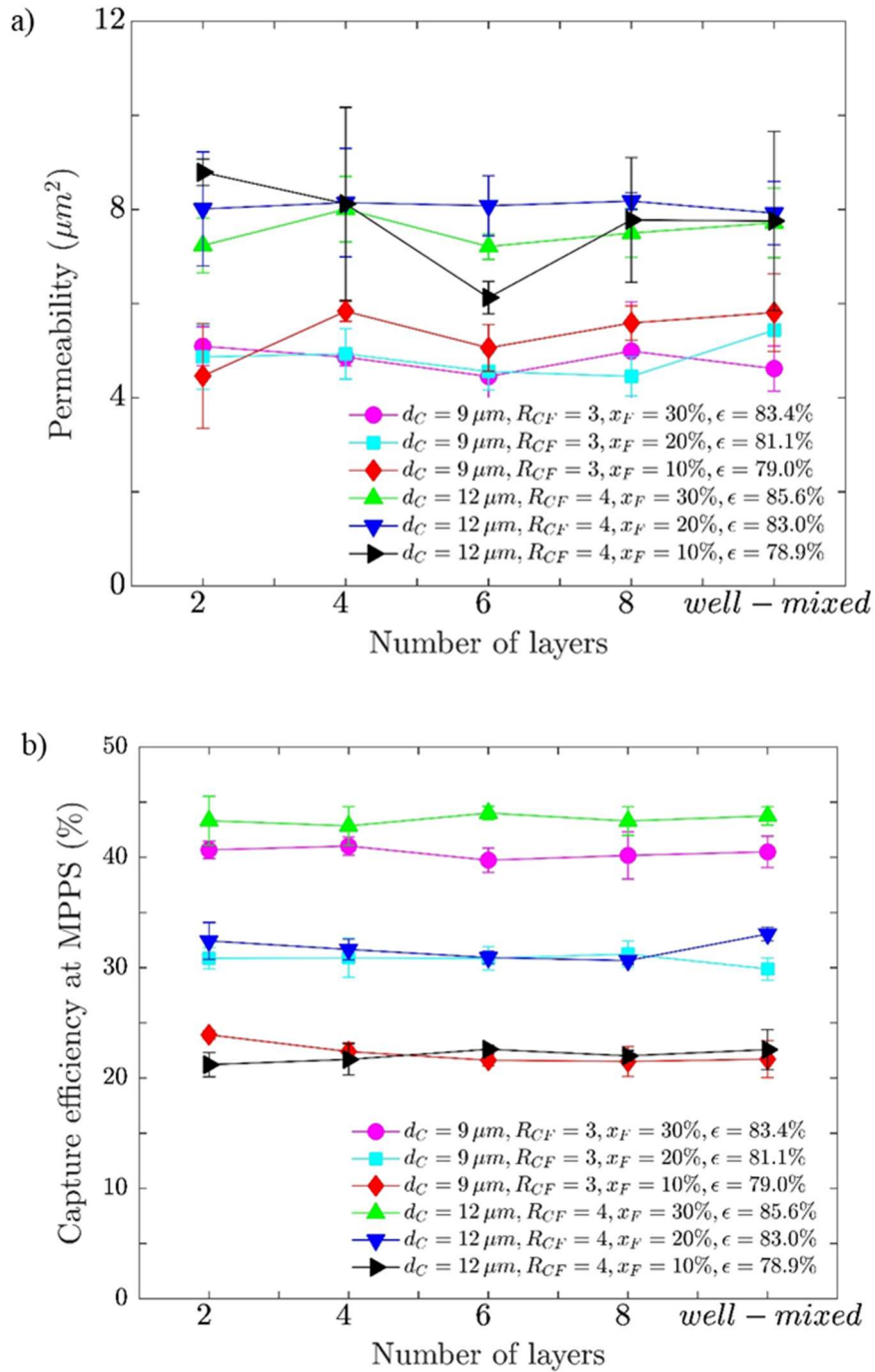


Figure 3.12 A two-dimensional cross section of a typical flow field through a well-mixed filter medium computed with the lattice Boltzmann method. Black arrows represent the three-dimensional velocity vectors passing through the cross-sectional plane in the x direction



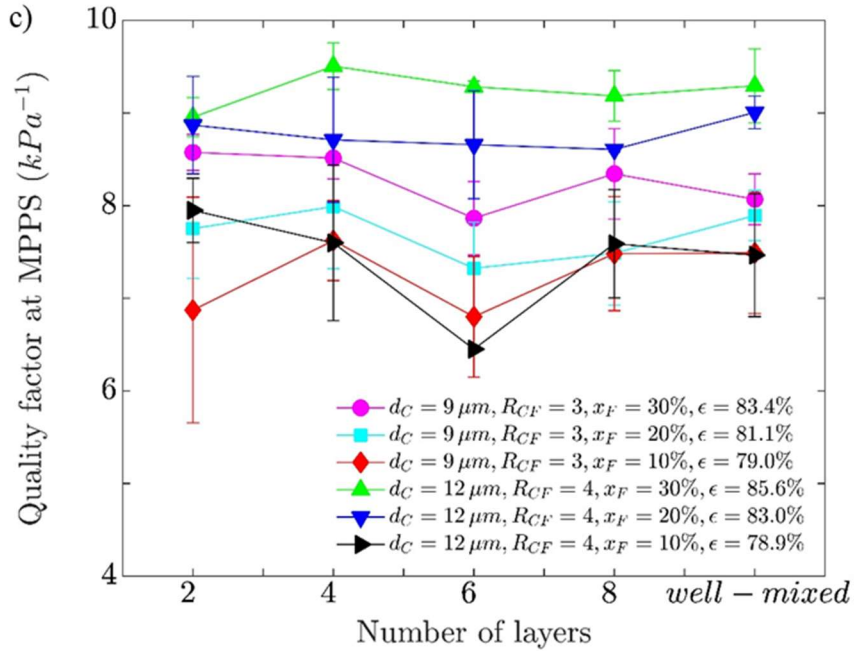


Figure 3.13 Effects of the multilayered filter medium structure and fibre formulation on: A, permeability; B, capture efficiency; and C, the quality factor at the most penetrating particle size (~ 300 nm). The error bars represent standard deviations obtained from triplicate computations. Note that the impact of R_{CF} on the various properties cannot be readily assessed because of the variations in porosity and thickness

For all the properties measured, it can readily be seen that the number of layers does not seem to have a clear impact, or, in other words, that the differences observed between the different multilayered structures for a same formulation are not statistically significant. In addition, the same can be said for the differences between the multilayered structures and the well-mixed structures. Indeed, because of the inherent variability of the random structures generated and the direct impact of this variability on the various filter media properties (ie, permeability, capture efficiency and quality factor) from triplicate computations, it is not statistically possible to attribute any variations observed when the number of layers is changed to the sole impact of multilayering. If there is an impact, it is smaller than the impact that can be attributed to the inherent variability of these random structures. In fact, a statistical test was unable to rule out the null hypothesis, ie, that there is no relationship between the various filter media properties investigated and the number of layers for the multilayered structures investigated. The p-values for permeability (0.42), capture efficiency

(0.50), and quality factor (0.85) calculated using Statistica are all higher than the threshold value of 0.05 below which statistical significance can be assigned. [325] The best that can be concluded is that, for the structures investigated at moderate R_{CF} , there is no strong evidence in a laminar flow regime of any impact of multilayering that is greater than the impact of the intrinsic variability of such random multilayered or well-mixed structures.

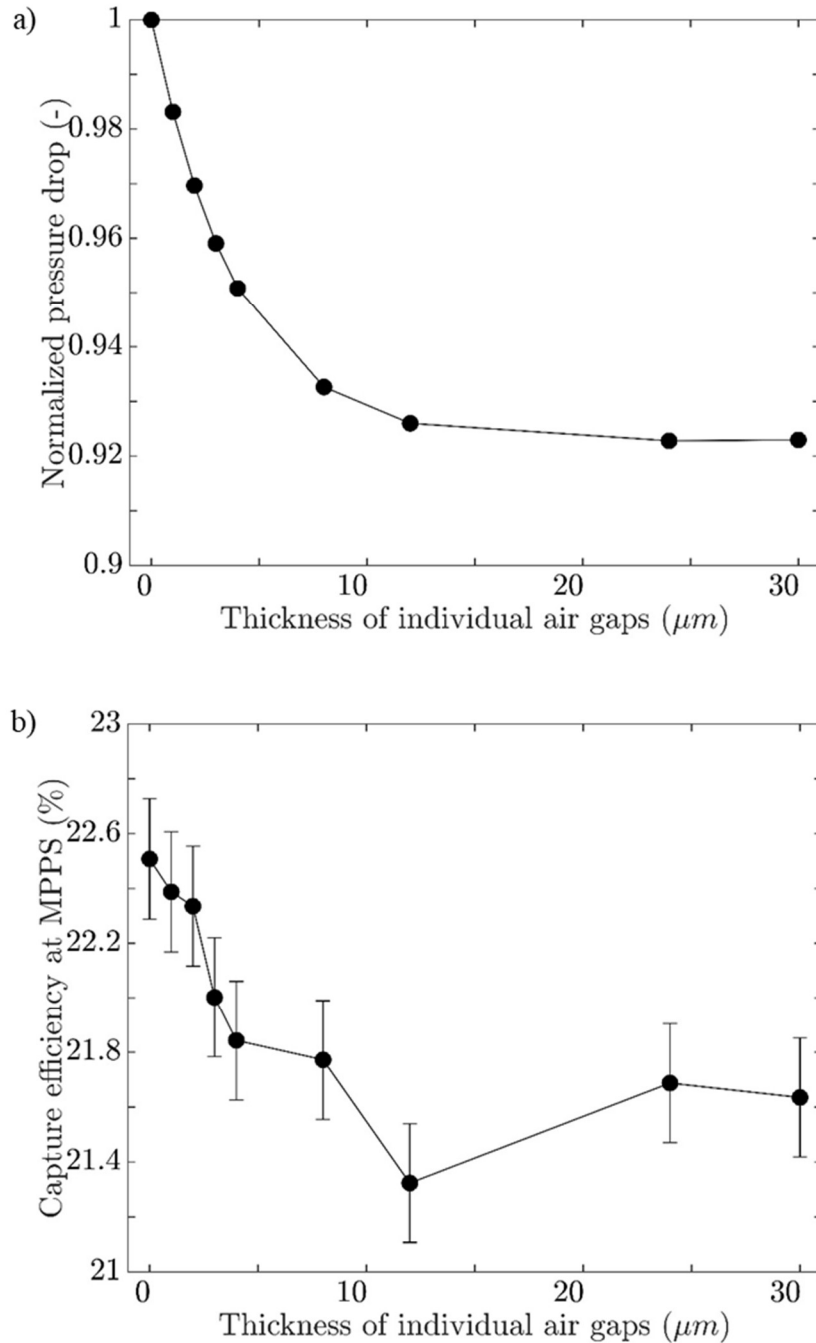
Based on the simulations performed and the results in Figure 3.13a)-c), it appears that the best way to improve filter media performance is to investigate a range of fibre formulations, which in this case, indicates that filter medium performance improves with higher R_{CF} and fibre content. More precisely, larger coarse fibres (ie, higher R_{CF}) tends to open up the structure and create preferential pathways for the flow, which results in higher permeability, while adding a larger fine fibre content improves capture efficiency. Overall, the formulation at $R_{CF} = 4$ and $x_F = 30\%$ leads to a filter medium with the highest quality factor, indicating that the effect of R_{CF} is the most influential variable among all the cases investigated.

3.5.2 Impact of interfacial flow phenomena between layers at a high coarse-to-fine diameter ratio

To test the potential impact of interfacial phenomena between layers on filter medium performance, a new set of computations involving the insertion of air gaps between fibre layers was devised as described in Section 3.4.2. Eight layers, four fine fibre layers (with a resulting average thickness of 17 μm) and four coarse fibre layers (with a resulting average thickness of 55 μm), were separately generated and were interlayered with increasingly large air gaps inserted between them (from 0 μm -30 μm). The effective thickness of the filter media remained constant. It should be recalled that larger air gaps should result in a smaller impact of the interfacial phenomena between the layers on filter media performance.

Figure 3.14a)-c) shows the impact of the insertion of the seven air gaps between the eight layers. The pressure drop (normalized here by the pressure drop obtained for a filter with no air gaps) decreases monotonously with an increase of the size of the air gaps and reaches a plateau at ~12 μm . Inserting such air gaps reduces the overall pressure drop by ~8%. This can be explained by the increase in local porosity that occurs near the fibres in the vicinity of an air gap, which helps

redistribute the pressure field. In other words, interfacial phenomena that occur when no air gaps are present are detrimental as they increase the pressure drop, ie, they reduce permeability. On the other hand, capture efficiency is increased by ~5% in the absence of air gaps. Overall, the quality factor of the filter media decreases by ~3% in the absence of air gaps. This result shows that interfacial flow phenomena are, as a whole, detrimental and that inserting air gaps between layers can be used to cancel the negative impact, although the gain is relatively small.



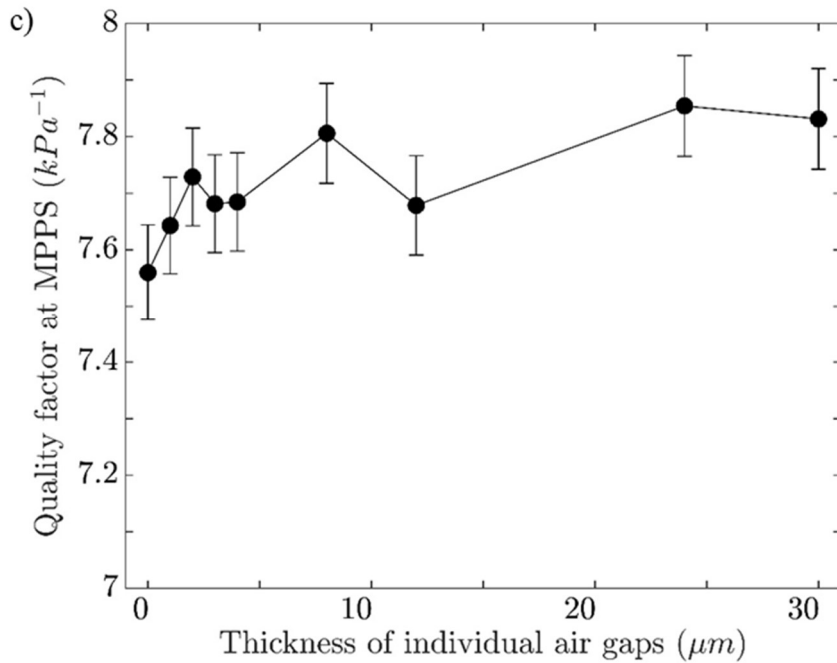


Figure 3.14 Impact of the insertion of seven air gaps in an eight-layered filter media on the: A, pressure drop; B, capture efficiency; and C, quality factor at the most penetrating particle size (~ 300 nm). The pressure drop was normalized to the pressure drop in the case with no air gaps. The error bars represent a 95% binomial confidence interval, assuming the capture process follows a Bernoulli process [326]

3.5.3 Impact of interfacial flow phenomena between layers at a high coarse-to-fine diameter ratio

At moderate R_{CF} , the impact of multilayering on filter medium performance, if any, is weak to the point that it cannot be distinguished from the effect of the inherent variability of the structures formed due to the random deposition of fibres. Furthermore, the overall impact of flow phenomena at the interfaces between the layers is detrimental to the performance of the filter media if no air gaps are inserted between the layers. It is, however, legitimate to ask whether these conclusions would hold at higher R_{CF} values. This was the rationale for performing a new set of computations at $R_{CF} = 10$, for which the methodology was adapted to three-layered structures given that larger multilayered structures would be too demanding in terms of computational power.

Figure 3.15 illustrates two of the three-layered structures studied, namely the sandwiched and gap configurations.

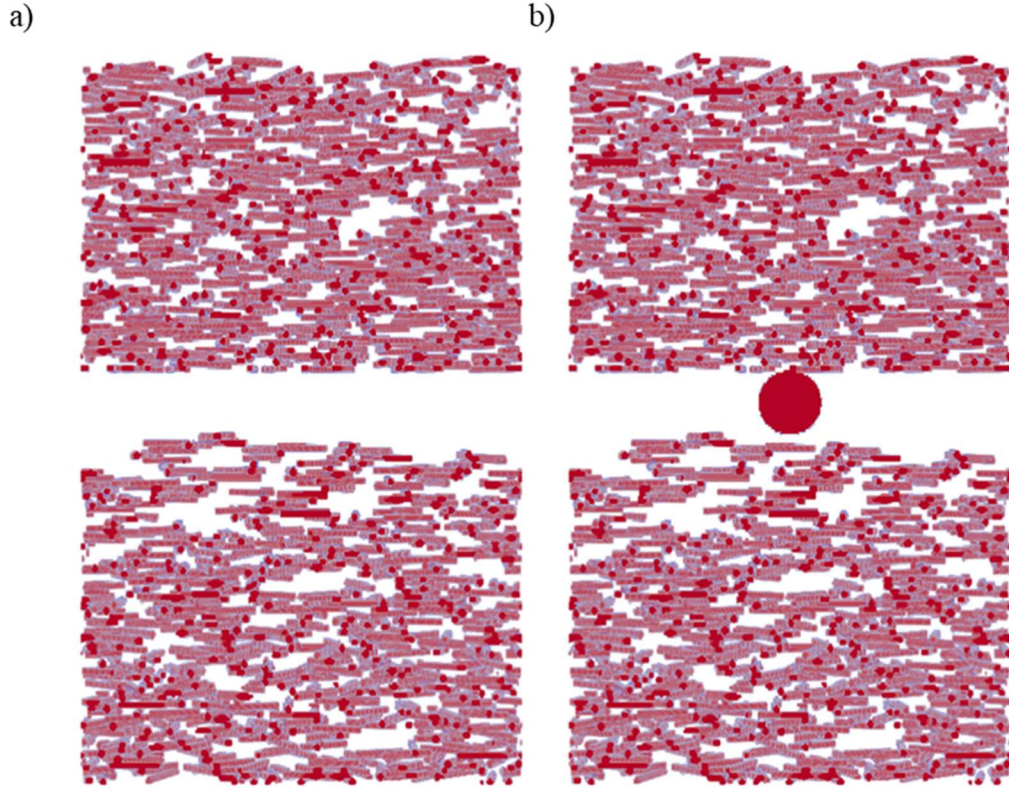


Figure 3.15 Examples of representative elementary volumes of filter media created by the fibre deposition algorithm to study the impact of multilayering at $R_{CF} = 10$, namely the: A, gap; and B, sandwiched configurations

Figure 3.16 shows the pressure drop for the four three-layered configurations described in Section 3.4.3 that contain two layers of fine fibres. The four configurations display small differences (at most in the order of 1.2%) that are systematic throughout the triplicate repeats performed for each configuration. Despite the limited number of repeats, and like the results obtained at moderate R_{CF} , the magnitude of the differences seemed to be lower than the inherent variability observed among the repeats. Furthermore, the gap filter media have smaller pressure drops than the no gap ones, which is in agreement with the results presented in Section 3.5.2. There is no noticeable difference between the sandwiched and upstream configurations, indicating that the order of the layers does not have much impact on filter media performance, as suggested by

Clague and Phillips. [31] On the other hand, as expected, both configurations have somewhat higher pressure drops than the gap filter media as the coarse fibres create additional resistance to the air flow.

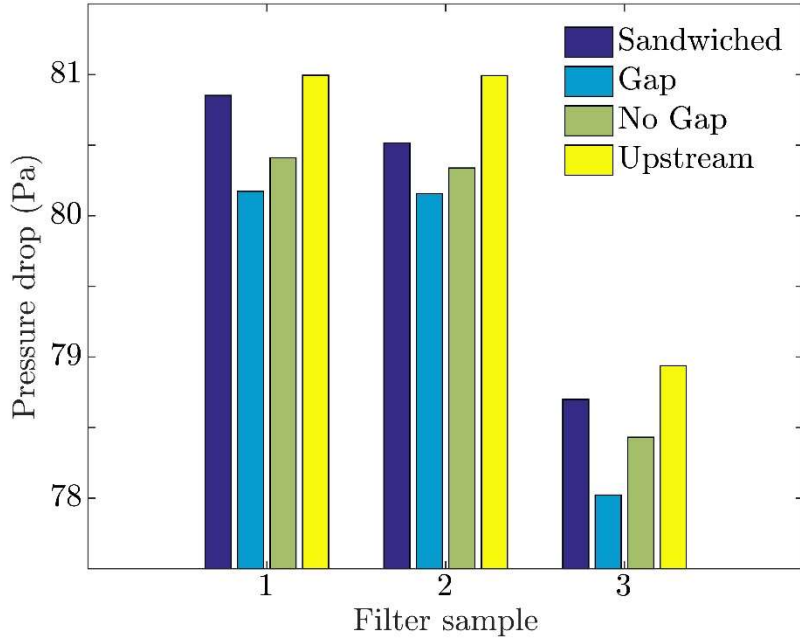


Figure 3.16 Pressure drop through the different three-layered configurations for three randomly generated sets of filter media. Note the truncated scale

If no interfacial flow phenomena were present, subtracting the pressure drop for the sandwiched configuration from the pressure drop for the gap configuration should recover the pressure drop around a single coarse fibre (the alone configuration). Similarly, subtracting the pressure drop for the upstream configuration from the pressure drop for the no gap configuration should also recover the pressure drop around a single coarse fibre. Figure 3.17 shows the results of these calculations for each repeat. The coarse fibre layer alone has a significantly smaller pressure drop than when it is interacting with the fine fibre layers. Despite this confirmation of the presence of flow phenomena at the interface between the layers, the magnitude of the impact of these phenomena remains small overall (~ 0.5 Pa) compared to the overall pressure drop through the filter media (~ 80 Pa).

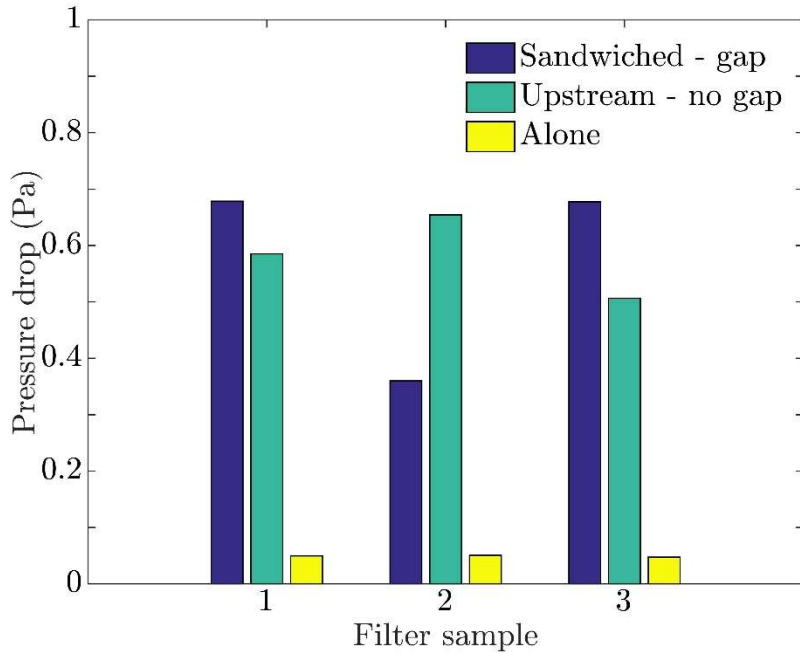


Figure 3.17 Comparison of the contribution of a single coarse fibre to the pressure drop when it is between two layers of fine fibres (sandwiched minus gap configurations), next to one layer of fine fibres (upstream minus no gap configurations), or isolated (alone configuration)

A similar analysis was attempted for capture efficiency, but as was seen in Section 3.5.2, the impact of interfacial flow phenomena on capture efficiency was lower than on pressure drop and, as such, was difficult to characterize. Furthermore, the capture efficiency of the coarse fibre alone was so low that an unpractical large number of particles would have to be launched to provide a statistically significant result. The stochastic nature of the algorithm creates a statistical variance that is too large in proportion of the capture efficiency. The analysis performed for the pressure drop could thus not be carried out for capture efficiency.

3.6 Conclusion and Perspectives

While multilayered filter media are ubiquitous in industry for various reasons, the impact of multilayering on the performance of bimodal fibrous clean filter media in a Stokes regime has never been systematically investigated. As the effect of multilayering could be attributed both to

the succession of layers with varying structural properties (porosity and specific surface area) and interfacial flow phenomena between layers, three sets of numerical computations were conducted using a three-step numerical procedure to quantify the relative importance of these mechanisms.

In the first study for the six bimodal fibre formulations chosen, the number of layers (ranging from 2-8) was shown to have no statistically significant impact on either the permeability, capture efficiency, or quality factor of the clean filter media. In addition, there were no statistically significant differences between the well-mixed clean filter media and the various multilayered clean filter media. This does not mean that multilayering has no effect on the filter medium quality factor, but rather that the impact of multilayering is at best limited for the filter medium configurations investigated, ie, of the same order of magnitude as the effect resulting from the inherent variability due to the random nature of the fibre structures. This is somewhat in agreement with experimental results from Payen et al, [111] who reported that differences between the various multilayered structures tested were within the experimental error and that a clear impact could not be inferred.

For the second study, the impact of flow phenomena at interfaces between layers was investigated by artificially inserting air gaps and by varying their sizes. The interfacial effects when no air gaps between the layers were present increased the pressure drop by ~8% and the capture efficiency by 5%, resulting in a decrease of ~3% in the quality factor of the clean filter media. This result suggested that adding air gaps between layers to help redistribute the flow and reduce local pressure surges has a positive albeit limited impact on filter medium performance and that this occurs at the expense of the overall thickness of the clean filter media.

In the third study, the impacts of multilayering and flow phenomena at interfaces between layers were evaluated at a much higher coarse-to-fine fibre diameter ratio ($R_{cf} = 10$) than the two previous studies. Similar conclusions were drawn, ie, multilayering has, at best, a limited impact.

Despite the relatively limited scope of the present study, it can still be concluded that multilayering has little or no impact on filter medium performance. The findings presented here also suggest that controlling the microstructure through fibre formulation is a more promising avenue for improving performance than multilayering per se, at least in the Stokes regime for clean filter media. However, studying fouling processes within filter media might reveal impacts not brought to light in the present study. Furthermore, in contexts where filter media are designed to

take advantage of non-linear slip and inertial flow regimes, different results can be foreseen. Studies on the performance of nanofilter media in conjunction with multilayering would thus be a logical follow-up to the present study.

Acknowledgements

The authors gratefully acknowledge the financial support of the Natural Sciences and Engineering Research Council of Canada (NSERC) through the CREATE Simulation-Based Engineering Science (SBES) program and the SENTINEL Bioactive Paper Network, as well as the computer resource allocations provided by Compute Canada and Calcul Québec. They also want to extend their thanks to Prof. Bernard Clément for his help with the statistical analysis of the data and to Prof. Sébastien Leclaire for useful discussions and comments.

CHAPITRE 4 ARTICLE 2: COMPARISON OF EXISTING AND EXTENDED BOUNDARY CONDITIONS FOR THE SIMULATION OF RAREFIED GAS FLOWS USING THE LATTICE BOLTZMANN METHOD

Jean-Michel Tucny, David Vidal, Sébastien Leclaire, François Bertrand – publié le 16 avril 2020 dans le *International Journal of Modern Physics C* – p. 2050070-1-21

Abstract. Accurate imposition of boundary conditions (BCs) is of critical importance in fluid flow computation. This is especially true for the Lattice Boltzmann method (LBM) where BC imposition is done through operations on populations rather than directly on macroscopic variables. While the regular Cartesian structure of the lattices is an advantage for flow simulation through complex geometries such as porous media, imposition of correct BCs remains a topic of investigation for rarefied flows, where slip BCs need to be imposed. In this work, current kinetic BCs from the literature are reviewed for rarefied flows and an extended version of a technique that combines bounce-back and diffusive reflection (DBB BC) is proposed to solve such flows that exhibit effective viscosity gradients. The extended DBB BC is completely local and addresses ambiguities as regards to the definition of boundary populations in complex geometries. Numerical tests of a rarefied flow through a slit were performed confirming the intrinsic second-order convergence of the proposed extended DBB BC. It settles a long-standing debate regarding the convergence of BCs in rarefied flows. Good agreement was also found with existing numerical schemes and experimental data.

Keywords: Rarefied flow; Lattice Boltzmann method; boundary condition; Knudsen regime; Extended Navier-Stokes equation

4.1 Introduction

The lattice Boltzmann method (LBM) has received considerable attention for its ability to simulate gas flows through porous media [250-252]. LBM has been used to conduct studies in various fields such as shale gas [253] and microelectromechanical systems (MEMS) [327]. Porous media for these applications often involve micro/nanoflows, for which the mean free path of the gas molecules (λ) may be comparable to the characteristic length of the flow (L_C). The ratio of

these two quantities, i.e., the Knudsen number $Kn = \lambda/L_C$, thus takes a value in the order of unity, which undermines the continuum hypothesis underlying the Navier-Stokes equations. Gas molecule interactions with the wall become more important, which leads to two consequences: (1) the no-slip boundary condition (BC) breaks down, and (2) the Knudsen layer, a region where the length varies as $O(\lambda)$ and where the stress-strain relationship is modified, becomes preponderant throughout the flow. The Navier-Stokes equations can thus not be used for high Knudsen flows. Instead of solving the Navier-Stokes equations, LBM simulates the evolution of probability distribution functions of gas molecules (hereinafter referred to as populations) according to a collision-propagation scheme. The main advantages of LBM for the simulation of porous media are: (1) its explicit and local nature, which makes it easily parallelizable, and (2) its simple Boolean representation for encoding fluid and solid phases using a simple Cartesian grid.

LBM is a particular case of the discrete velocity method (also called the discrete ordinate method) [328] and is a discretization in time, space and velocity of the Boltzmann equation. Despite its statistical mechanics origin, LBM was initially developed to solve the weakly compressible and isothermal Navier-Stokes equations [250-252]. Based on the assumption of a low Knudsen number, the Navier-Stokes equations can be recovered by applying a Chapman-Enskog expansion procedure to the LBM collision-propagation scheme. Following this procedure, perturbations around the local equilibrium of the lattice Boltzmann equation are analyzed using a multiscale analysis, with the Knudsen number as the perturbation parameter. The chosen population set should have sufficient isotropy to evaluate exactly the moments involved in the constitutive equations [231, 275]. For a two-dimensional flow for instance, a nine-velocity set (a so-called D2Q9 lattice) can only solve the flow at the Navier-Stokes equations level. In principle, by using a richer population set, constitutive equations of a higher-order (Burnett, Super-Burnett, Grad's moment method, etc.) can be modeled using LBM [231, 275, 294], and high Knudsen flows can thus be solved. While some improvements in planar flows have been obtained compared to the Navier-Stokes equations [273, 294, 329], it has also been reported [138, 150, 151, 272, 330, 331] that solving higher-order constitutive equations cannot accurately represent the dynamics inside the Knudsen layer for high Knudsen flows. Furthermore, complex geometry flows with a twenty-one-velocity set (D2Q21) have not shown improvement compared to the D2Q9 model [291, 293]. It should also be noted that higher memory and computation costs are associated with the use of a richer velocity set. Hybrids of LBM and Direct Simulation Monte-Carlo (DSMC) have also been

proposed to speed-up computations relative to pure DSMC, however the computational efficiency is still limited by the fraction of the domain in which the DSMC is solved [265, 266].

Rather than trying to model high Knudsen flows by directly expanding perturbations around local equilibrium, it has been proposed that a local viscosity by means of a wall function within a continuum mechanics framework be used to solve rarefied gas flows [217, 225, 231, 332]. It is well known from kinetic theory that the viscosity of a gas is related to its mean free path [137, 138]. Gas molecule paths are restricted close to a solid wall, which diminishes the mean free path locally, inducing a local effective viscosity. Provided the distribution of paths is known locally, it is possible to determine the effective viscosity of a gas. The resulting modified momentum equation has been called the extended or generalized Navier-Stokes equations. This approach has been favored to simulate high Knudsen flows with LBM [236, 287, 291, 293, 333, 334].

The imposition of slip BCs is key to simulating rarefied gas flows. Slip BCs are usually formulated as discontinuities in the velocity field at the surface. However, in LBM, BCs are imposed on populations, not directly on velocity. For the continuous form of the Boltzmann equation, Maxwell [157] proposed two mechanisms of gas-wall interactions: diffusive reflection, by which gas molecules are reemitted in random directions, and specular reflection, by which molecules bounce in a mirror fashion from the wall. In its discrete form for LBM, diffusive reflection was first proposed separately [335, 336] and was then combined with specular reflection [337, 338] to represent surfaces that are not completely diffusive, which leads to so-called diffusive specular reflection (DSR) BC. A combination of bounce-back (typically used for no-slip flows) and specular reflection BCs (so-called CBBSR) [286] and a combination of bounce-back and diffusive reflection (diffusive bounce-back hereinafter referred to as DBB) have also been proposed [339]. These three combinations (DSR, CBBSR, and DBB) were tested for the D2Q9 scheme and were found to be equivalent for a rectilinear slip flow [339].

Effective viscosity functions have an impact on BCs. A lengthy development for the CBBSR BC [236] found that the ratio of bounce-back associated with slip of CBBSR BC and two of the relaxation times had to be modified to take effective viscosity variations throughout the domain into consideration. To the best of our knowledge, such an extension has never been reported in the literature for the DBB BC. It remains to be proven whether the extension for DBB BC will produce the same results as the CBBSR BC. A definite advantage of the DBB BC would be to

resolve the indetermination for some populations reflecting from non-planar BCs (particularly in corners) and associated with the specular reflection part of DSR and CBB SR BCs. Indeed, there is a certain confusion in the literature regarding how to treat corners when specular reflection is involved [114, 289, 340]. The issue is even more pronounced for three-dimensional BCs as a greater number of populations are ill-defined. In fact, to the best of our knowledge, there are no reports in the literature that explicitly explain how to stream specularly reflected populations in corners.

The choice of the LBM collision operator is key to the validity of BCs. A theoretical analysis [285] of the three BCs with the Bhatnagar-Gross-Krook (BGK) operator [139] showed that slip velocity had three contributions: a first-order contribution (in terms of the Knudsen number), a second-order contribution, and an unphysical grid-dependent contribution. Furthermore, the second-order contribution is not tunable with respect to the parameters of the kinetic BC. Further theoretical analyses [236, 334, 339, 341] of discrete BCs with a multiple relaxation time (MRT) collision operator showed that slip velocity depends on higher-order moments of LBM, which must thus be relaxed with their corresponding relaxation time to properly impose the slip BC. A comprehensive study of the whole scheme is thus essential for simulating rarefied gas flows with LBM.

In a different line of thought, an alternative method was proposed [342-344] to explicitly impose Maxwell's slip BC on populations rather than by adjusting kinetic ratios. Using the known populations at the wall in the case of a D2Q9 lattice, moments of these populations were expressed explicitly in the case of planar flow to calculate the slip velocity. Unknown populations at the wall were reconstructed using the slip flow. This procedure allowed for a decoupling of the relaxation rate from the slip magnitude. While this method is independent of the collision operator, it cannot be straightforwardly generalized to complex BCs because the underlying explicit formulation of moments is geometry-dependent by nature and anisotropic. Note that a formulation proposed by Guo et al. [38] proposed a formulation for the DBB that proved efficient for slip flows.

With suitable BCs, LBM is a second-order accurate scheme for solving the incompressible Navier-Stokes equations in the continuous limit [250-252]. As shown by [345] for flows in the continuous regime, LBM has a quadratic relationship between the time step and the grid size ($\delta_t \sim O(\delta_x^2)$). However, the simulation of rarefied flows with LBM induces convective scaling

$(\delta_t \sim O(\delta_x))$ through the relationship between the relaxation rate and the Knudsen number [231, 287, 338]. As reported in [339], this necessarily implies a Mach number (Ma) equal to a finite grid-independent constant rather than Ma going asymptotically to zero as the grid is refined. In this context, for an incompressible slit flow problem, one study reported a second-order convergence [236] while another reported a first-order convergence [334]. Another study using the explicit imposition of slip velocity reported a second-order convergence on a compressible slit flow [342], while another study on a compressible slit flow reported a first-order convergence but attributed it to the compressibility of the problem [339]. There is thus a controversy in the literature regarding the convergence order of rarefied gas schemes with LBM. To solve this controversy, the compressibility of the physical problem must be decoupled from the compressibility of the scheme by choosing test cases with no compressibility effects.

The objectives of the present article are thus: (1) to resolve the controversy regarding the convergence order of the rarefied gas scheme for LBM, and (2) to develop an extended DBB BC that takes into consideration spatial variations of viscosity near the walls by using an effective viscosity function for the numerical simulation of rarefied gas flows in porous media. The remainder of the article will be organized as follows. In Section 4.2, MRT-LBM will first be revisited, the DSR, CBBSR, and DBB BCs will be reviewed in detail, and an extension of DBB BC will be developed. In Section 4.3, a convergence analysis of the numerical scheme as well as a numerical verification will be described for a slit flow. In Section 4.4, some concluding remarks will be made.

4.2 The Lattice Boltzmann method for Rarefied Flows

This section is divided into five sub-sections. First, as LBM slip BCs require the use of multiple relaxation times, the principle of MRT-LBM will be recalled. Second, the relationship between mean free path and relaxation times will be described. Third, the wall viscosity functions used in the literature will be briefly reviewed. Fourth, details about the various kinetic BCs in the context of the simulation of rarefied flows will be given. Lastly, an extension of DBB BC will be proposed.

4.2.1 Propagation-collision scheme with multiple relaxation times

The propagation-collision scheme of LBM is expressed as follows:

$$f_i(\mathbf{x} + \mathbf{c}_i \delta_t, t + \delta_t) - f_i(\mathbf{x}, t) = \Omega_i + F_i \delta_t \quad (4.1)$$

where $f_i(\mathbf{x}, t)$ is the population at position \mathbf{x} and time t in the i direction, and \mathbf{c}_i is its associated discrete velocity, F_i is the forcing term, Ω_i is the collision operator and δ_t is the time step. The left-hand side of the equation is called the propagation step while the right-hand side is called the collision step. In the MRT scheme, the collision operator transforms populations into moments (such as density, momentum, kinetic energy, etc.) [288]:

$$\Omega_i = - \sum_{j=1}^N (\mathbf{M}^{-1} \mathbf{S} \mathbf{M})_{ij} \left(f_j(\mathbf{x}, t) - f_j^{(eq)}(\rho, \mathbf{u}) \right) \quad (4.2)$$

where N is the number of populations, \mathbf{M} is the transformation matrix between populations and moments, \mathbf{S} is the relaxation rate diagonal matrix and $f_j^{(eq)}(\rho, \mathbf{u})$ is the equilibrium distribution calculated from the macroscopic fluid density ρ and velocity \mathbf{u} . For the present study, the D2Q9 discrete velocity set is used (also illustrated in Figure 4.1):

$$\mathbf{c}_i = \begin{cases} (0,0) \frac{\delta_x}{\delta_t} & \text{for } i = 0 \\ \left(\cos\left(i * \frac{\pi}{2}\right), \sin\left(i * \frac{\pi}{2}\right) \right) \frac{\delta_x}{\delta_t} & \text{for } i = 1, \dots, 4 \\ \sqrt{2} \left(\cos\left(\frac{(2i+1)\pi}{4}\right), \sin\left(\frac{(2i+1)\pi}{4}\right) \right) \frac{\delta_x}{\delta_t} & \text{for } i = 5, \dots, 8 \end{cases} \quad (4.3)$$

with its associated weights w_i :

$$w_i = \begin{cases} 4/9 & \text{for } i = 0 \\ 1/9 & \text{for } i = 1, \dots, 4 \\ 1/36 & \text{for } i = 5, \dots, 8 \end{cases} \quad (4.4)$$

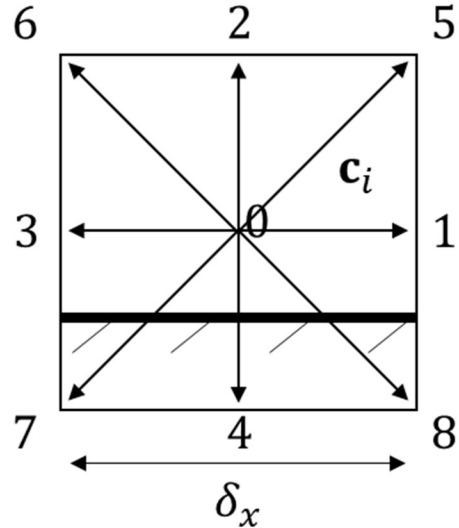


Figure 4.1 D2Q9 velocity set used for LBM where \mathbf{c}_i is the velocity vector in direction i

The equilibrium distribution functions following a linearized Maxwell-Boltzmann distribution up to second-order terms are given for the D2Q9 lattice as follows:

$$f_i^{(eq)} = w_i \rho \left(1 + \frac{\mathbf{c}_i \cdot \mathbf{u}}{c_s^2} + \frac{(\mathbf{c}_i \cdot \mathbf{u})^2}{c_s^4} - \frac{u^2}{2c_s^2} \right) \quad (4.5)$$

with the so-called lattice sound velocity c_s :

$$c_s = \sqrt{\frac{\delta_x}{3\delta_t}} \quad (4.6)$$

where δ_x is the lattice grid spacing. The associated transformation (**M**) and relaxation rate (**S**) matrices are [288]:

$$\mathbf{M} = \begin{pmatrix} 1 & 1 & 1 & 1 & 1 & 1 & 1 & 1 & 1 \\ -4 & -1 & -1 & -1 & -1 & 2 & 2 & 2 & 2 \\ 4 & -2 & -2 & -2 & -2 & 1 & 1 & 1 & 1 \\ 0 & 1 & 0 & -1 & 0 & 1 & -1 & -1 & 1 \\ 0 & -2 & 0 & 2 & 0 & 1 & -1 & -1 & 1 \\ 0 & 0 & 1 & 0 & -1 & 1 & 1 & -1 & -1 \\ 0 & 0 & -2 & 0 & 2 & 1 & 1 & -1 & -1 \\ 0 & 1 & -1 & 1 & -1 & 0 & 0 & 0 & 0 \\ 0 & 0 & 0 & 0 & 0 & 1 & -1 & 1 & -1 \end{pmatrix} \quad (4.7)$$

$$\mathbf{S} = \text{diag}(s_\rho, s_e, s_\epsilon, s_j, s_q, s_j, s_q, s_s, s_s) \quad (4.8)$$

where s_ρ , s_e , s_ϵ , s_j , s_q , and s_s are, respectively, the relaxation rates related to density, kinetic energy, kinetic energy squared, momentum, energy flux, and stress. Typically, relaxation rates s_i are expressed as relaxation times τ_i :

$$\tau_i = \frac{1}{s_i} \quad (4.9)$$

When relaxation times are all equal, the MRT model reduces to the BGK model, for which there is a single relaxation time.

The dynamic viscosity μ can be related to the stress relaxation time $\tau_s = 1/s_s$ [250]:

$$\mu = p \left(\tau_s - \frac{1}{2} \right) \delta_t \quad (4.10)$$

where $p = \rho c_s^2$ is the pressure of the fluid. The force term in Eq. (4.1) was generalized from the BGK to the MRT collision operator [287]:

$$F_i = \mathbf{M}^{-1} \left(\mathbf{I} - \frac{\mathbf{S}}{2} \right) \mathbf{M} \bar{F}_i \quad (4.11)$$

with:

$$\bar{F}_i = w_i \left(\frac{\mathbf{c}_i \cdot \mathbf{F}}{c_s^2} + \frac{\mathbf{u} \mathbf{F} \cdot (\mathbf{c}_i \mathbf{c}_i - c_s^2 \mathbf{I})}{c_s^4} \right) \quad (4.12)$$

where \mathbf{F} is a given body force.

4.2.2 Relationship between relaxation times and the mean free path

The Knudsen number is a fundamental dimensionless parameter that determines flow behavior. When continuum flows are modeled using LBM, it is considered that $Kn \rightarrow 0$. However, with rarefied flows, the Knudsen number has a non-negligible value, which removes the degree of freedom on the relaxation time τ_s linked to stress.

Based on the kinetic theory of gases, the mean free path is related to the physical and thermodynamic properties of the gas [138]:

$$\lambda = \frac{\mu}{p} \sqrt{\frac{\pi RT}{2}} \quad (4.13)$$

where R is the ideal gas constant and T is the absolute temperature of the gas. In the D2Q9 velocity set, the temperature is related to the lattice velocity c_s :

$$c_s = \sqrt{RT} \quad (4.14)$$

Combining Eq. (4.13) with the definition of the lattice sound velocity c_s (Eq. (4.14)) and the definition of bulk viscosity (Eq. (4.10)), the following relationship can be derived for MRT-LBM [231]:

$$\tau_s = \frac{1}{2} + \sqrt{\frac{6}{\pi} \frac{\lambda}{\delta_x} \Psi(\lambda, \mathbf{x})} = \frac{1}{2} + \sqrt{\frac{6}{\pi} Kn \cdot N \cdot \Psi(\lambda, \mathbf{x})} \quad (4.15)$$

where Ψ is a viscosity function purposely introduced to account for local variations of the mean free path, which will be explained in more detail in Section 4.2.3, and $N = \frac{L_c}{\delta_x}$ is the grid cell number along the characteristic length.

An immediate consequence of the latter relationship is that as the numerical grid spacing gets finer ($\delta_x \rightarrow 0$), the relaxation time grows without bounds $\tau_s \rightarrow \infty$. Inserting τ_s from Eq. (4.15) into Eq. (4.10) also shows that a convective scaling ($\delta_t \sim O(\delta_x)$) is imposed and, consequently, the conditions of the convergence analysis usually considered for the LBM scheme are changed.

4.2.3 Viscosity functions

Within the Knudsen layer, a region of length varying as $O(\lambda)$ near the solid boundaries of the system, gas molecule paths are restricted in the vicinity of the solid walls. The mean free path in this region will thus be shorter than the bulk mean free path. In the extended Navier-Stokes equations, it is assumed that Eq. (4.13) which relates the effective mean free path and the effective viscosity, holds in the Knudsen layer. In other words, the mean free path remains proportional to

the viscosity defined by the local stress-strain relationship of the fluid. A viscosity function $\Psi(\lambda, \mathbf{x})$ can thus be defined as:

$$\Psi(\lambda, \mathbf{x}) = \frac{\lambda_e}{\lambda} = \frac{\mu_e}{\mu} \quad (4.16)$$

where the subscript e in this context indicates a local effective quantity. As the mean free path is always shorter than the unrestricted bulk mean free path, $0 < \Psi(\lambda, \mathbf{x}) < 1$.

The expression of the viscosity function is geometry dependent, which can be difficult to evaluate for a complex geometry [287]. Analytical solutions have been developed for a slit flow bounded by two parallel planes located at $x = -\frac{H}{2}$ and $x = \frac{H}{2}$. Assuming free paths follow an exponential distribution, Guo et al. [225] derived the following viscosity function:

$$\Psi(\lambda, \mathbf{x}) = \frac{1}{2} \left(\psi \left(\frac{x - \frac{H}{2}}{\lambda} \right) + \psi \left(\frac{x + \frac{H}{2}}{\lambda} \right) \right) \quad (4.17)$$

where the function ψ is defined [346] as:

$$\psi(x) = 1 + (x - 1) \exp(-x) - x^2 E_i(x) \quad (4.18)$$

and where $E_i(x)$ is the exponential integral function:

$$E_i(x) = \int_1^\infty t^{-1} \exp(-xt) dt \quad (4.19)$$

According to Strops [346], an exponential distribution of molecular free paths is valid for gas systems under the assumption of thermodynamic equilibrium. However, in the Knudsen layer, assuming thermodynamic equilibrium is not valid because of insufficient collisions between gas molecules. An alternative proposed by Dongari et al. [228] is to change the exponential distribution function for a power-law function. It was argued that a fat-tailed distribution would be more appropriate to represent the non-equilibrium effects in the Knudsen layer. The following viscosity function was later proposed for a planar wall [233]:

$$\begin{aligned}
\Psi(\lambda, \mathbf{x}) = & 1 - \frac{1}{96} \left(\left(1 + \frac{x + \frac{H}{2}}{a} \right)^{1-n} + \left(1 + \frac{\frac{H}{2} - x}{a} \right)^{1-n} \right. \\
& + 4 \sum_{i=1}^8 \left(1 + \frac{x + \frac{H}{2}}{a \cdot \cos \left(\frac{(2i-1)\pi}{32} \right)} \right)^{1-n} \\
& + 4 \sum_{i=1}^8 \left(1 + \frac{H/2 - x}{a \cdot \cos \left(\frac{(2i-1)\pi}{32} \right)} \right)^{1-n} \\
& + 2 \sum_{i=1}^7 \left(1 + \frac{x + \frac{H}{2}}{a \cdot \cos \left(\frac{i\pi}{16} \right)} \right)^{1-n} \\
& \left. + 2 \sum_{i=1}^7 \left(1 + \frac{\frac{H}{2} - x}{a \cdot \cos \left(\frac{i\pi}{16} \right)} \right)^{1-n} \right) \tag{4.20}
\end{aligned}$$

where $a = \lambda(n - 2)$ and n is the exponent of the power-law distribution. When $n \rightarrow \infty$, the exponential distribution is recovered. n was chosen here to be equal to 3 as in [162, 170, 235].

4.2.4 Kinetic boundary conditions

Slip BCs in the context of rarefied flows are generally imposed with the LBM by a combination of weighted individual kinetic schemes. Three individual kinetic boundary conditions are presented here: bounce-back, specular reflection, and diffusive reflection or scattering. Solid walls are taken as static, i.e., $\mathbf{u}_w = 0$. Figure 4.2 illustrates these three BCs. The bounce-back BC is used on its own to impose no-slip BCs:

$$f_i^{(BB)} = f_{oppdir(i)} \tag{4.21}$$

where the subscript $oppdir(i)$ indicates the population coming from the opposite direction $\mathbf{c}_{oppdir(i)} = -\mathbf{c}_i$ and superscript (BB) stands for bounce-back. Specular reflection may be used to impose slip BCs:

$$f_i^{(SR)} = f_{i'} \tag{4.22}$$

where the subscript i' indicates the velocity reflected from the wall with $\mathbf{c}_{i'} = \mathbf{c}_i - 2(\mathbf{c}_i \cdot \mathbf{n})\mathbf{n}$, \mathbf{n} is the normal unit vector pointing to the exterior of the surface and superscript (SR) stands for specular reflection. By imposing an equilibrium distribution at the wall on boundary populations, the diffusive BC can also be used to impose slip BCs [335]:

$$f_i^{(D)} = K f_i^{(eq)}(\rho_w, \mathbf{0}) \quad (4.23)$$

where ρ_w is the density at the wall, superscript (D) stands for diffusive and factor K ensures that the gas does not penetrate through the solid boundary through the following definition:

$$K = \frac{\sum_{\mathbf{c}_i \cdot \mathbf{n} < 0} |\mathbf{c}_i \cdot \mathbf{n}| f_i}{\sum_{\mathbf{c}_i \cdot \mathbf{n} < 0} |\mathbf{c}_i \cdot \mathbf{n}| f_i^{(eq)}(\rho_w, \mathbf{0})} \quad (4.24)$$

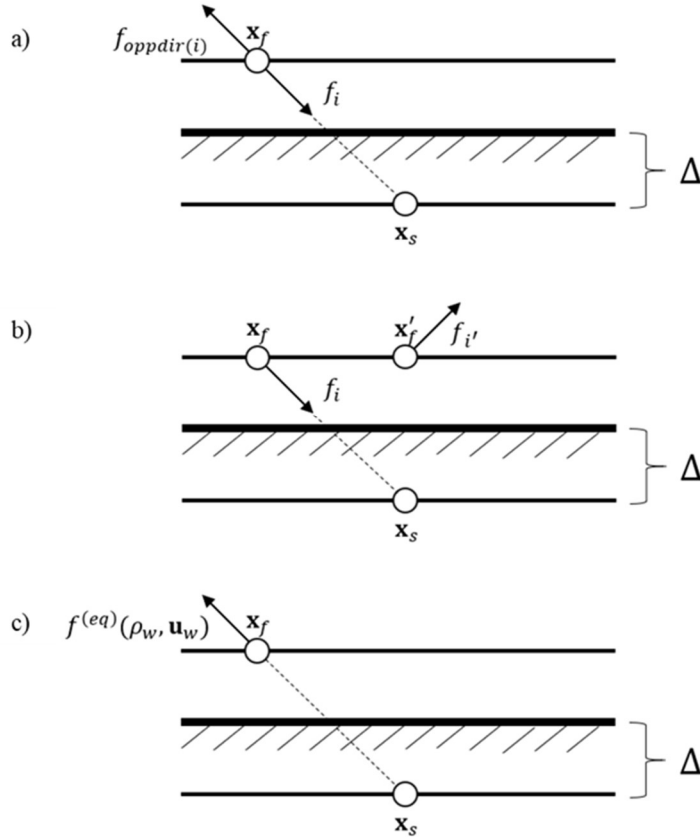


Figure 4.2 Kinetic BC schemes for LBM: (a) the bounce-back BC, (b) the specular reflection BC, and (c) the diffusive scattering BC. The parameter Δ sets the position of the wall at the frontier node. As half-way BCs are used here, $\Delta = \frac{1}{2}$.

In some versions of diffusive BC [347, 348], population 2 was actually bounce-backed, while the diffusive BC was used for populations 5 and 6. In another version of diffusive BC [289], the K factor was omitted. In those articles, only flows perpendicular to solid walls were investigated. Most articles in the literature use the diffusive reflection defined with Eqs. (4.23) and (4.24).

Several combinations of these BCs reported in the literature have been used to simulate rarefied flows. Maxwell's original diffusive specular reflection in its discretized form (DSR) is formulated as [337, 338]:

$$f_i = (1 - \sigma_v)f_i^{(SR)} + \sigma_v f_i^{(D)} \quad (4.25)$$

where $0 \leq \sigma_v \leq 1$ is the discrete accommodation coefficient for DSR BC, which represents the relative importance of diffusive scattering with respect to the overall BC response. The combined bounce-back and specular reflection (CBBSR) is formulated as [286]:

$$f_i = (1 - \alpha)f_i^{(SR)} + \alpha f_i^{(BB)} \quad (4.26)$$

where $0 \leq \alpha \leq 1$ is the accommodation coefficient for CBBSR, which represents the relative importance of the bounce-back with respect to the overall BC response. DBB BC is formulated as [339]:

$$f_i = (1 - r)f_i^{(D)} + r f_i^{(BB)} \quad (4.27)$$

where $0 \leq r \leq 1$ is the accommodation coefficient for DBB, which represents the relative importance of the bounce-back with respect to the overall BC response.

In the continuum mechanics framework, slip BCs are formulated through relationships to velocity, not populations. The Maxwell second-order BC is often used in engineering applications for its simplicity. A version including effective viscosity (μ_e) effects via the local mean free path λ_e and relation (4.16) has been proposed in Ref. [236]:

$$\mathbf{u}_s = A_1 \lambda_e \frac{\partial \mathbf{u}}{\partial \mathbf{n}} - A_2 \lambda_e \left(\frac{\partial}{\partial \mathbf{n}} \left(\lambda_e \frac{\partial \mathbf{u}}{\partial \mathbf{n}} \right) \right) \quad (4.28)$$

where u_s is the velocity of the fluid at the wall and A_1 and A_2 are coefficients that depend on gas-solid interactions obtained from theoretical models or experimental results [158].

Although it was initially thought that LBM was able to simulate slip flows by discretizing DSR BC with kinetic accommodation coefficients obtained experimentally without resorting to an explicit velocity BC, a theoretical analysis of the D2Q9 scheme [285] showed discrepancies between continuous Boltzmann equation solutions and LBM solutions. Any discrete velocity model collapses molecular velocities to finite solid angles. Equation (4.15) shows that as the Knudsen number increases, populations are less relaxed. In a Poiseuille flow, this results in discrete populations never being streamed toward a wall and thus unrealistically out of equilibrium, which almost surely never happens in the continuous Boltzmann equation. In Ref. [349], it was proposed to add a partial diffusion to all fluid lattice sites weighted by a certain probability of molecules interacting with the wall. An explicit characteristic length must be defined, which would be difficult to determine for complex geometries. Rather than relying on a characteristic length, expressions between accommodation coefficients (i.e., σ_v , α , and r in Eqs. (4.25)-(4.27)) and macroscopic velocity coefficients (A_1 and A_2) have thus been derived for the DSR, CBBSR [285], and DBB [289] schemes by studying flows on a planar geometry. For the CBBSR scheme, for instance:

$$\alpha = \frac{1}{1 + \chi A_1} \quad (4.29)$$

where $\chi = \sqrt{\pi/6}$. Further theoretical analysis of a rectilinear slip flow (without Knudsen layer effects) [339] showed that the DSR, CBBSR, and DBB schemes all produce the expected parabolic flow. The following simple relationship relates all the aforementioned BCs:

$$\alpha = \frac{\sigma_v}{2} = \frac{1 + r}{2} \quad (4.30)$$

It must be noted that the validity of Eq. (4.30) is restricted by the condition that the accommodation coefficients α , σ_v , and r must be positive and inferior or equal to unity when used. This is not an issue for the CBBSR BC, but it is for DSR and DBB BCs. For example, DSR BC cannot be used when $A_1 < 1/\chi \approx 1.382$. However, all macroscopic velocity BCs compiled in a review paper on slip models [158] lead to $A_1 < 1/\chi$. It is thus difficult to apply DSR BC in practice to a real physical system. This is why this BC will not be considered any further. Based on the same

argument, DBB BC cannot be applied if $A_1 > 1/\chi$. However, this is not the case for any of the models mentioned in the aforementioned compilation. It can thus be concluded that DBB BC is applicable to real physical systems and should thus be favored on this basis.

The development of relationships between kinetic and macroscopic velocity BCs also showed [287] that the energy flux relaxation time τ_q must be modified to recover the exact slip velocity at the boundary. For the D2Q9 population set, the expression for the relaxation time τ_q is given by:

$$\tau_q = \frac{1}{2} + \frac{\pi A_2 (2\tau_s - 1)^2 + 3}{8(2\tau_s - 1)} \quad (4.31)$$

These relationships were derived without considering effects of the Knudsen layer. Recalling Eq. (4.15), the relaxation time τ_s should be a function of position. For the CBBSR scheme, a more general expression for the relaxation time τ_q as well as a new accommodation coefficient were developed for a spatially varying relaxation time [236]:

$$\alpha = \frac{1}{1 + \chi A_1 + \frac{\tau'_{sw} \delta_x}{8 \left(\tau_{sw} - \frac{1}{2} \right)^2}} \quad (4.32)$$

$$\tau_q = \frac{1}{2} + \frac{\pi A_2 (2\tau_{sw} - 1)^2 + 3}{8(2\tau_{sw} - 1)} \frac{\tau'_{sw} \delta_x (12 + 30 \left(\tau_{sw} - \frac{1}{2} \right) \chi A_1)}{16 \left(\tau_{sw} - \frac{1}{2} \right)^2} \quad (4.33)$$

where the subscript w represents a value at the wall and τ'_{sw} is the derivative of τ_{sw} in the direction normal to the wall. When Knudsen layer effects are not considered, Ψ equals 1 everywhere, $\tau'_{sw} = 0$, and Eqs. (4.32) and (4.33) reduce to Eqs. (4.29) and (4.31).

4.2.5 Extended diffusive bounce-back boundary condition

In this section, an extension of DBB BC, including effective viscosity gradients throughout the geometry, is presented given that such an extension has never been addressed before in the literature. Relationships for α and τ_q expressed in Eqs. (4.32) and (4.33) for CBBSR BC have been demonstrated through a lengthy development [236] for a rectilinear flow for which a variable

effective viscosity is considered. Although relatively straightforward, this development has not been reported out in the literature for DBB BC. To obtain the corresponding parameters (i.e. r and τ_q) for DBB BC, one of the premises of the development related to the definition of BC needs to be changed. Equation (43) in [236] gives a relationship between incoming and outgoing populations (the latter populations being marked with a tilde) at the wall located at the bottom of a flow such that: $f_5 - f_6 = (1 - 2\alpha)(\tilde{f}_8 - \tilde{f}_7)$ (with directions corresponding to those illustrated in Figure 4.1). For DBB, the outgoing populations at the boundary are given by:

$$\begin{aligned} f_2 &= r\tilde{f}_4 + (1 - r)Kf_2^{(eq)}(\rho_w, \mathbf{0}) \\ f_5 &= r\tilde{f}_7 + (1 - r)Kf_5^{(eq)}(\rho_w, \mathbf{0}) \\ f_6 &= r\tilde{f}_8 + (1 - r)Kf_6^{(eq)}(\rho_w, \mathbf{0}) \end{aligned} \quad (4.34)$$

As $f_5^{(eq)}(\rho_w, \mathbf{0}) = f_6^{(eq)}(\rho_w, \mathbf{0})$, it follows from the DBB scheme that:

$$f_5 - f_6 = -r(\tilde{f}_8 - \tilde{f}_7) \quad (4.35)$$

Eq. (4.35) stays true for variable effective viscosities, as this equation relates populations locally in the boundary lattice and is thus independent of viscosity gradients. The following relationship is thus straightforwardly derived from Eq. (4.30) for the DBB:

$$r = \frac{1 - \chi A_1 - \frac{\tau'_{sw} \delta_x}{8 \left(\tau_{sw} - \frac{1}{2} \right)^2}}{1 + \chi A_1 + \frac{\tau'_{sw} \delta_x}{8 \left(\tau_{sw} - \frac{1}{2} \right)^2}} \quad (4.36)$$

Eq. (4.33), initially developed for the CBBSR BC scheme, continues to hold true for τ_q as this part of the derivation is not modified.

An advantage of this extended DBB BC is its locality. According to Eq. (4.34), populations from a solid wall are calculated from populations from the same lattice and macroscopic variables from the wall. For CBBSR BC, as can be seen in Figure 4.2b, in the half-way bounce back case, reflected populations should be reflected on the next lattice. Specular reflection is thus non-local.

At steady state, for flows considered to be incompressible through rectilinear geometries such as a semi-infinite plane or a rectilinear channel, the velocity only varies in the direction normal to the surface. In these cases, the issue of streaming the reflected population to the next lattice in the specular reflection scheme is hidden. Furthermore, in corners such as the one represented in Figure 4.3, the direction in which the population should be reflected is ambiguous [114, 289, 340]. Any attempt to solve this ambiguity would be difficult in a three-dimensional complex geometry as a great number of exceptions would need to be considered for corners. The extended DBB BC presented in this section would in principle get around all these issues and would thus offer an unambiguous and relatively simple scheme.

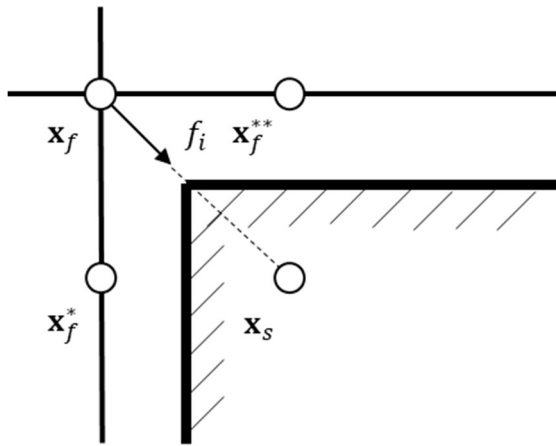


Figure 4.3 Schematic of specular reflection at a corner. The destination of the population at location \mathbf{x}_f is not well defined: both destinations \mathbf{x}_f^* and \mathbf{x}_f^{**} should be considered.

Another extension of the DBB BC was proposed previously [184], where the bounce-back ratio is explicitly related to the Knudsen number for a planar flow. While satisfactory results were obtained for a slit flow, it requires an explicit definition of the characteristic length, which would be difficult to define for a complex geometry. This problem can be avoided with the DBB BC proposed in this paper.

One potential caveat that must however be mentioned is mass conservation at the boundary for the diffusive part of the BC. As populations outgoing from a wall are calculated from macroscopic variables, mass conservation is not a priori guaranteed. However, in practice, no such problems were found in papers [114, 195, 289, 291, 292, 295, 300, 339, 340, 350, 351].

4.3 Accuracy Assessment of the Extended Diffusive Bounce-Back Boundary Condition

Most LBM schemes for rarefied gas flows impose a dependence between the grid spacing, the relaxation time, the Knudsen number and the viscosity through Eq. (4.15). This imposes a reduction in the degrees of freedom, which may impact the convergence order of the scheme, and a finite grid-independent constant Mach number. In Sec. 4.3.1, the impact of this dependence will be analyzed via different cases for a slip flow through a slit, for which it will be ensured that both the Mach number and pressure gradients have a negligible effect on the flow. The extended DBB BC will be assessed in this section. In Sec. 4.3.2, a numerical example of a rarefied flow through a slit will be conducted to assess the performance of this extended DBB BC. Figure 4.4 represents the slit flow test case. The lattice unit system [251] has been used here with $\delta_x = \delta_t = 1$. To enforce a pressure drop through the slit, a body force term of $F_y = 10^{-5}$ in lattice units was used, which guaranteed $Ma < 0.01$ for all the simulations. DBB BC was used to impose slip boundary conditions on the x -boundaries, while periodic conditions were used for the y -boundaries. The number of lattices in the y -direction was always equal to 2 as the invariability of the flow made it possible to reduce the number of lattices in that direction. Unless stated otherwise, relaxation times were chosen in the following way: τ_s with Eq. (4.15), τ_q with Eq. (4.33), $\tau_\rho = \tau_j = 1$, $\tau_e = 1.1$ and $\tau_\epsilon = 1.2$. Note that the last four relaxation times had very little impact on the results. The density of the gas at the wall used in Eq. (4.24) for the diffusive part of the BC was taken to be equal to the density at the center of the boundary fluid node. It was verified that for all simulations carried out in this article, mass was always conserved and that there were no density gradients.

4.3.1 Convergence analysis

The convergence of DBB BC was verified using simulations of a slit flow between two planes in $x = \pm B$, where B is half the distance between the two planes. The analytical solution of a two-dimensional slit flow for constant viscosity is [340]:

$$v_{y,anal} = \frac{\rho a B^2}{2\mu} \left(1 - \frac{x^2}{B^2} + 4A_1 Kn + 8A_2 Kn^2 \right) \quad (4.37)$$

where $Kn = \frac{\lambda}{2B}$ and x is the position in the x -direction as shown in Figure 4.4. The relative error is defined by the Euclidian L^2 -norm as:

$$E(v) = \frac{\|v_{y,LBM} - v_{y,anal}\|_2}{\|v_{y,anal}\|_2} \quad (4.38)$$

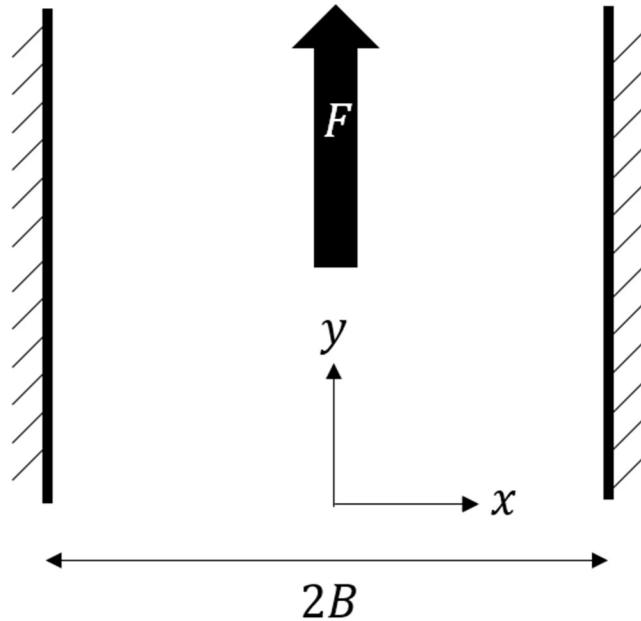


Figure 4.4 Schematic representation of the slit flow test case.

Three cases were considered for the convergence analysis. In the first case, a no-slip BC (i.e. $A_1 = A_2 = 0$) was simulated, with all relaxation times equal to one. MRT-LBM thus reduced to the BGK-LBM formulation. All considerations of slip phenomena were thus removed in this case. The results reported in Figure 4.5 show a second-order convergence, as expected [250-252]. While this case did not give any information on the convergence of the scheme for slip flows, the implementation of the code was verified for standard continuous no-slip flows.

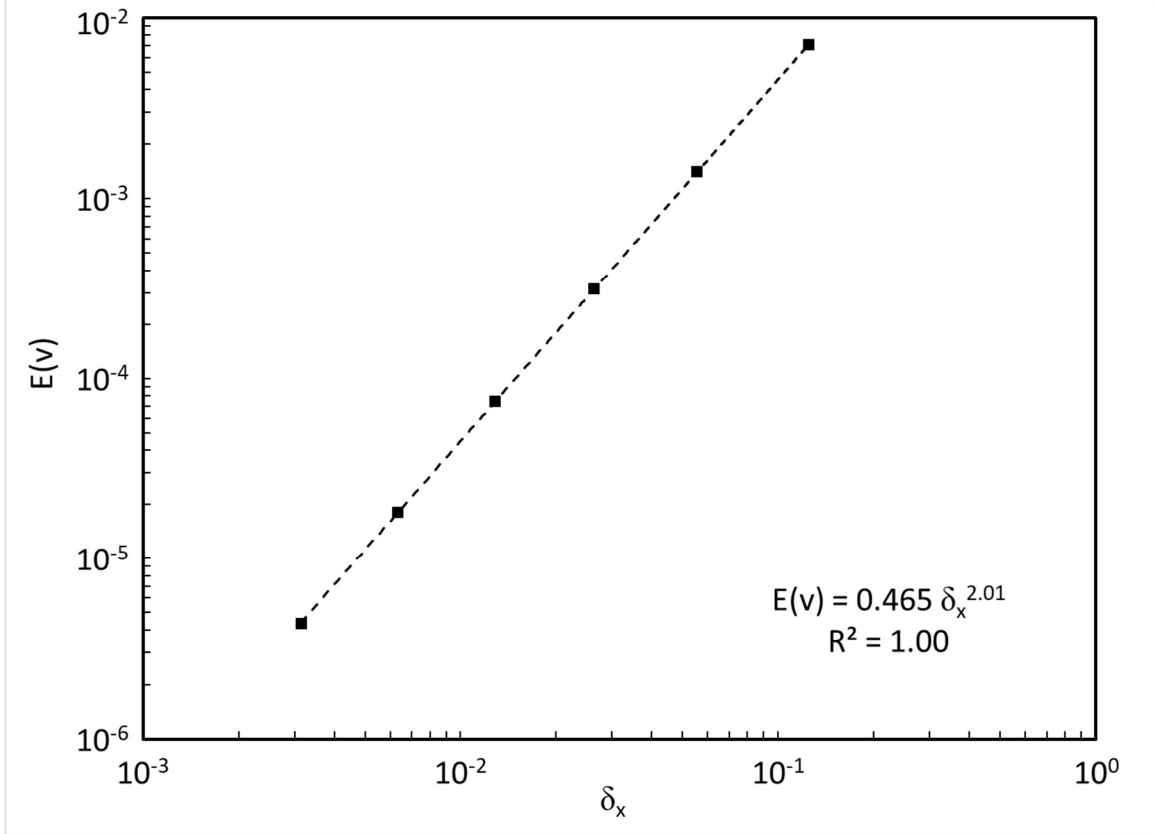


Figure 4.5 L^2 relative error for the BGK-LBM scheme without slip for the slit flow test case.

In the second case, a slit flow with slippage at the wall was simulated with $A_1 = 1$ and $A_2 = 0.5$ as in [225]. The Knudsen number was kept constant at $Kn = 1$ and the relaxation rate τ_s thus increased with the refinement of the grid. Figure 4.6 shows that a first-order convergence for this scheme was recovered in this case. Although a body force term was used as a driving force, the order of convergence obtained was similar to the one obtained for a compressible flow with pressure boundary conditions in x as in [339].

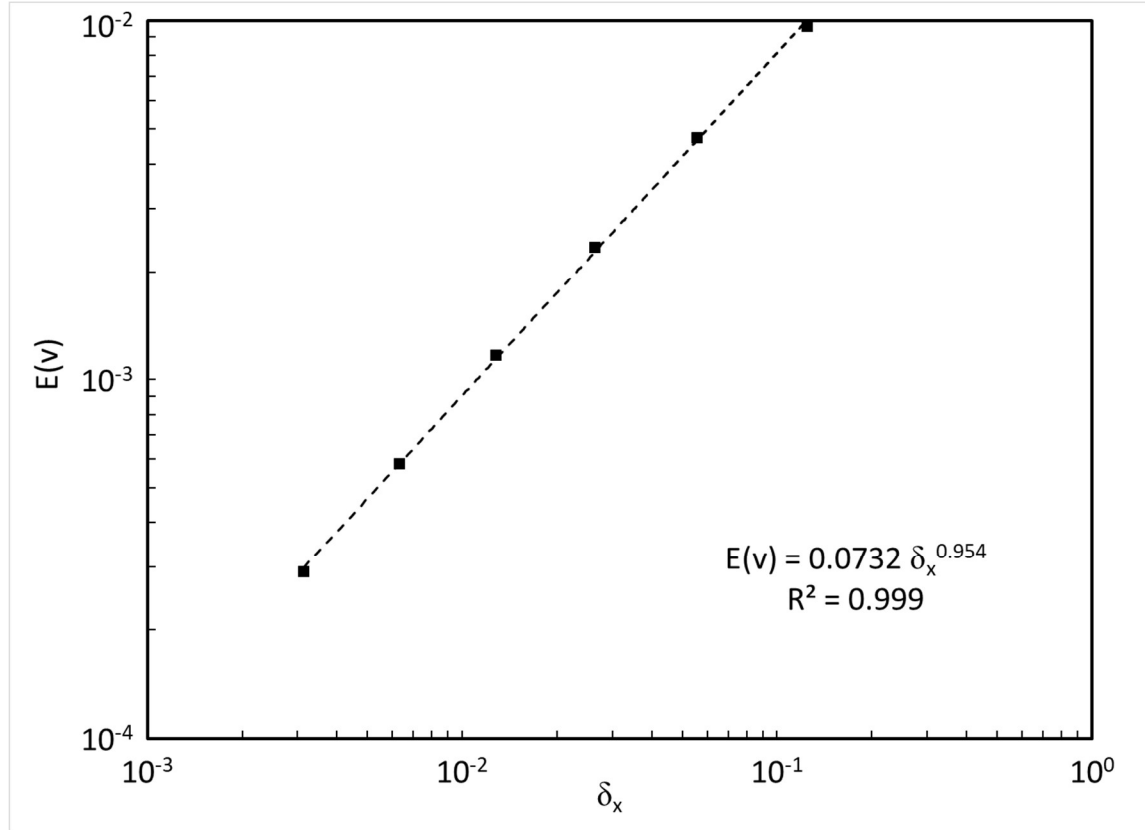


Figure 4.6 L^2 relative error of the MRT-LBM scheme with slip for a fixed Knudsen number $Kn = 1$ and a τ_s defined by Eq. (4.15) for the slit flow test case.

In the third case, the constants were kept at $A_1 = 1$ and $A_2 = 0.5$. However, the Knudsen number was modified according to Eq. (4.15) to keep $\tau_s = 1$ for each individual grid size. Various degrees of slippage were thus used to carry out the convergence test, with $0.001 < Kn < 0.05$. It can be seen from Figure 4.7 that a second-order convergence was obtained in this case.

There were no compressibility effects for all three cases as the Mach number was lower than 10^{-3} for all the tests and as the planar channel flows were driven by a constant body force for all the tests considered. Given this, the cause of the degradation of the convergence order of the MRT-LBM scheme for rarefied flows cannot be attributed to compressibility effects or pressure gradients. When a constant relaxation time was used to carry out the convergence test, a second-order convergence was recovered. It was therefore the increase in τ_s with grid refinement that was responsible for the apparent degradation of the convergence order. This would explain the apparent contradictory results reported in the literature for slip velocity BCs adjusted through combinations

of kinetic BCs [236, 334, 339], while the approach proposed in [342] explicitly setting the slip velocity through the moments cannot be used as a basis of comparison. These results showed that, when a convergence analysis is performed in this context, the choice as to whether to keep relaxation times or the Knudsen number constant has a fundamental impact on the convergence order of MRT-LBM that can be recovered due to the reduced degree of freedom resulting from the dependence between the grid spacing, the relaxation time, the Knudsen number, and the viscosity.

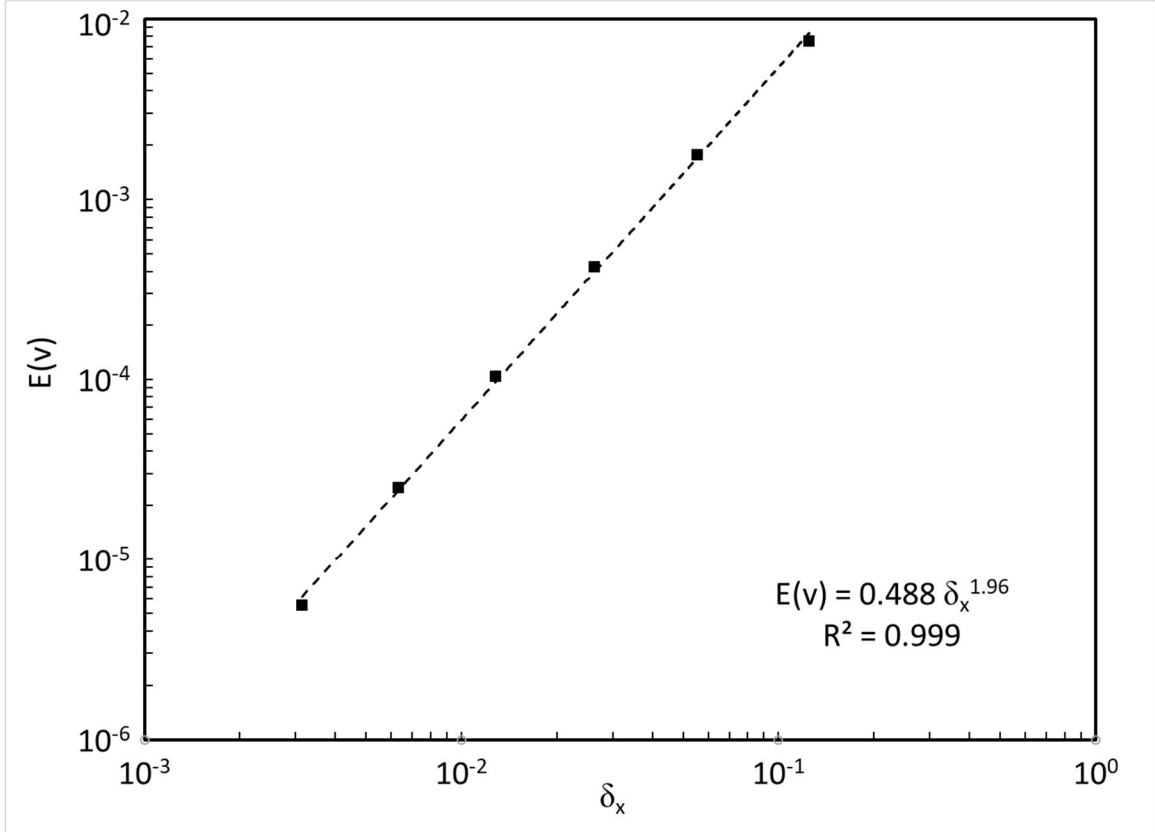


Figure 4.7 L^2 relative error of the MRT-LBM scheme with slip for a fixed $\tau_s = 1$ and a corresponding Knudsen number defined by Eq. (4.15) for the slit flow test case.

4.3.2 Verification of the proposed DBB BC scheme

The extended DBB BC was applied to a slit rarefied flow driven by a body force on a wide range of Knudsen numbers (from $0.05 < Kn < 10$). Several combinations of coefficients A_1 and A_2 from the Maxwell second-order macroscopic velocity BC and viscosity functions were tested, as shown in Table 4.1. These results were compared to those of a numerical solution of the linearized Boltzmann equation [171], those from the Virtual Wall Collision LBM (VWC-LBM)

combined with pure diffusive BC [349], and experimental results [352] reported by Guo et al. [236].

Table 4.1 Velocity BCs and viscosity functions tested to verify of the extended DBB scheme.

Solving method	Case	A_1	A_2	Ψ	Ref.
Analytical solution of the Navier-Stokes equations with no-slip BCs	NS	0	0	1	-
Virtual Wall Collision LBM	VWC-LBM	N/A	N/A	1	[349]
DBB BC with Cercignani's slip velocity coefficients	LBM-1	1.146	0.9796	1	[138]
Extended DBB BC	LBM-2	0.8183	0.6531	Eq. (4.17)	[236]
Extended DBB BC	LBM-3	1	0.31	Eq. (4.20)	[233]

Predictions of the normalized mass flow M are shown in Figure 4.8 for the LBM simulations combined with the aforementioned BCs. It can be seen that, on the one hand, the Navier-Stokes equations are unable to recover experimental measurements and solutions of the Boltzmann equation over the range of the Kn values tested, while LBM combined with DBB BC but without a viscosity function (LBM-1) is only valid for $Kn < 0.1$. In addition, it can be seen that the VWC-LBM provides, without the explicit use of a viscosity function, good agreement with the experimental data up to $Kn \sim 1$, but diverges rapidly beyond this point. On the other hand, the LBM simulations for the extended DBB BC combined with Guo et al.'s slip coefficients (i.e. A_1 and A_2) and Stops' viscosity function (LBM-2), and for the extended DBB BC combined with Dongari et al.'s slip coefficients and a viscosity function (LBM-3) both reproduce well the flow for the whole range of Knudsen numbers investigated, with the latter being more accurate than the former, especially for $0.5 < Kn < 10$.

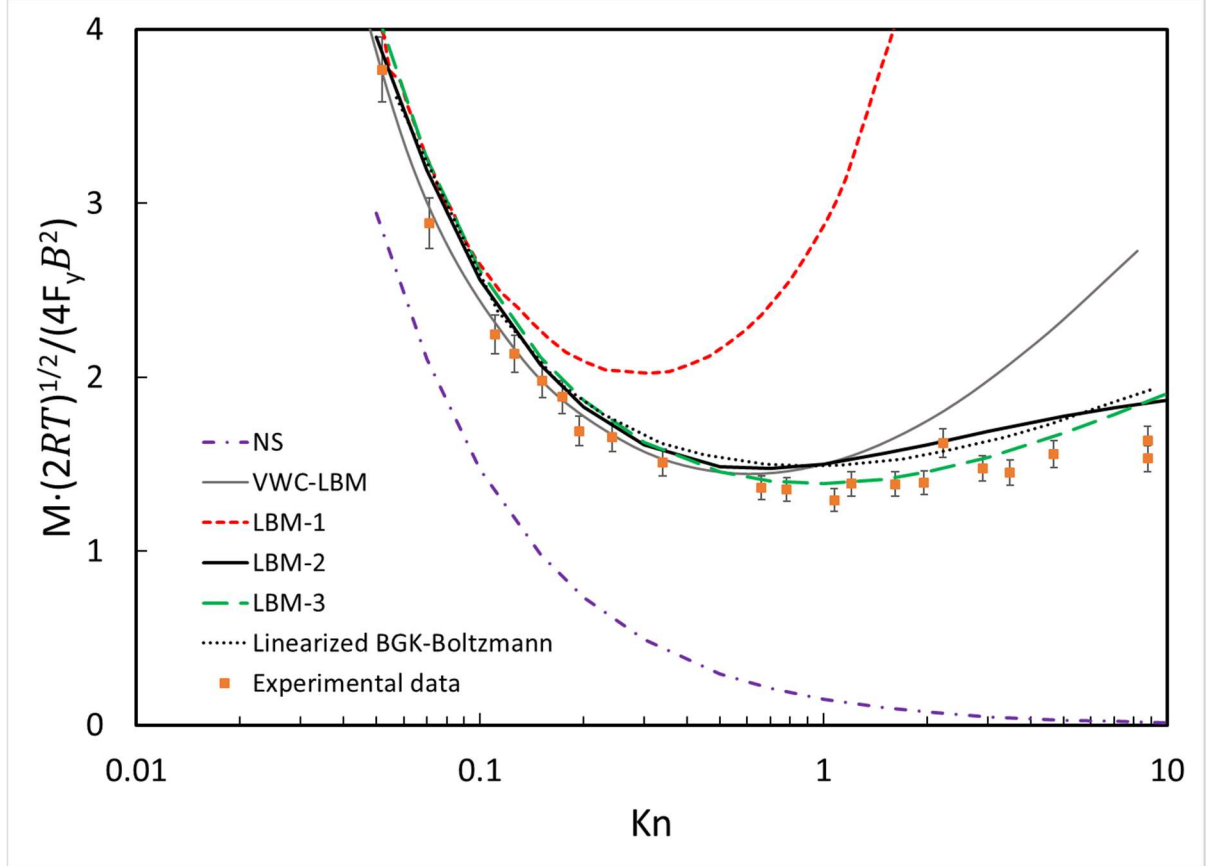


Figure 4.8 Predictions of the normalized mass flow for a rarefied slit flow for LBM with the extended DBB BC compared with experimental data and other methods. Acronyms refer to the cases presented in Table 4.1.

It must also be noted that while the LBM-2 results presented in Figure 8 were obtained with the extended DBB BC, identical results were reported with CBBSR BC in Ref. [236]. The degree of agreement between the two BCs is so good that the two curves would have been undistinguishable if plotted together. This is why only one curve is given in Figure 8. This also shows that the extended DBB BC is able to recover results obtained with previous BCs with a very high precision.

4.4 Conclusions

In this article, the three kinetic boundary conditions (DSR, CBBSR and DBB BCs) found in the literature for the simulation of rarefied gas flows with LBM have been reviewed. DBB BC was extended to include Knudsen layer effects and the associated local effective viscosity as

previously reported for CBBSR BC. A new relationship was derived for the accommodation coefficient representing the relative importance of the bounce-back with respect to the overall BC response. The generalized Navier-Stokes equations were thus recovered with the extended DBB BC. A few additional advantages of the present method are the absence of ambiguities in the treatment of corners on non-planar solid boundaries, space locality, and the relative ease of implementation in a three-dimensional lattice system, unlike methods involving specular reflection, namely DSR and CBBSR.

Contradictory findings in the literature regarding the convergence order of the rarefied scheme for the LBM have been examined. Test cases decoupling the compressibility of the scheme from the compressibility of the physical flow were carried out in this work to solve this controversy. It is shown here that fixing the relaxation time and varying the Knudsen number produces a second-order convergence, while a first-order convergence is recovered with a fixed Knudsen number. For a fixed Knudsen number, refining the grid increased the relaxation time. This proves that the scaling of the problem results in a reduction from second- to first-order convergence, regardless of the compressibility effect of the physical problems considered.

The extended DBB BC was tested using a rarefied slit flow driven by a body force term and then compared to experimental data and solutions to the Boltzmann equation. The extended DBB BC, with two combinations of macroscopic velocity BCs and viscosity functions, was able to recover the volumetric flow rate over a wide range of Knudsen numbers, as previously reported for CBBSR BC [236].

It must be mentioned that, although the extended DBB BC is intended to simplify simulations in complex geometries, all the tests reported in the present article were carried out on planar BCs. Several articles [195, 292-295, 300-302] have specifically discussed the phenomena of velocity aliasing in complex geometries caused by the presence of numerical artefacts in the higher-order moments of the flow. A regularization procedure (presented in [290]) was used to ensure the isotropy of the LBM scheme. To the best of our knowledge, the influence of this regularization procedure on kinetic slip boundary conditions for the LBM has not yet been studied in the literature. This will be the focus of our future work.

Acknowledgements

Financial support from the Simulation-based Engineering Science (Génie Par la Simulation) program funded through the CREATE program from the Natural Sciences and Engineering Research Council of Canada is gratefully acknowledged.

Declaration of Interest

The authors declare no conflicts of interest.

CHAPITRE 5 ARTICLE 3: DEVELOPMENT OF A KINETIC SLIP BOUNDARY CONDITION FOR RAREFIED GAS FLOWS THROUGH NON-PLANAR GEOMETRIES BASED ON THE REGULARIZED LATTICE-BOLTZMANN METHOD

Jean-Michel Tucny, David Vidal, Sébastien Leclaire et François Bertrand – soumis le 19 octobre 2020 à la revue *Physical Review E* – p. XXX – XXX (Note : le texte présenté ici peut ne pas correspondre à la version finale)

Abstract. The simulation of rarefied gas flows through complex porous media is challenging due to the tortuous flow pathways inherent to such structures. The Lattice Boltzmann method (LBM) has been identified as a promising avenue to solve flows through complex geometries due to the simplicity of its scheme and its high parallel computational efficiency. It has been proposed to model the stress-strain relationship with the extended Navier-Stokes equations rather than attempting to directly solve the Boltzmann equation through a high-order velocity scheme. However, a regularization technique is required to filter out non-resolved higher-order components with a low-order velocity scheme. Although accurate imposition of boundary conditions (BCs) is of critical importance in the LBM and has been used for the non-regularized multiple relaxation time LBM (MRT-LBM) for planar geometries, previous slip BCs have never been verified extensively on non-planar or complex geometries. In this work, following an extensive literature review on the imposition of slip boundary conditions for rarefied flows with the LBM, it is proven that earlier values for kinetic parameters developed to impose slip BCs with the non-regularized MRT-LBM are inaccurate for the regularized MRT-LBM and differ between the D2Q9 and D3Q15 schemes. The error was eliminated for planar flows and good agreement between analytical solutions for arrays of cylinders and spheres was found with a wide range of Knudsen numbers.

Keywords: lattice Boltzmann method (LBM), boundary condition (BC), rarefied flow, non-planar geometry

5.1 Introduction

Porous media are among the most complex geometries found in nature and industry. The macroscopic transport properties of porous media, such as permeability, are determined by their microscopic structure. Detailed knowledge of flow fields inside porous media can thus provide a better understanding of this structure, allowing the systems or processes involving porous media to be optimized. Numerical simulations have attracted interest for their potential to determine porous media transport properties. Despite the increase in computational power in recent years, traditional CFD methods are still limited with respect to the direct simulation of gas flows through realistic three-dimensional porous media for two reasons: (1) the presence of multiple scales of characteristic length in the same porous medium, and (2) the solid-fluid boundaries with convoluted topologies often found inside porous media [353].

The presence of several magnitudes of characteristic length implies that regions where the molecular mean free path λ is comparable to the characteristic length of the flow L_C can occur throughout the domain. The Knudsen number $Kn = \lambda/L_C$ gives a measure of flow rarefaction by indicating the extent to which gas molecules propagate before collisions exchange momentum and energy between gas molecules. In the Knudsen layer, a $\sim 2\lambda$ region near solid surfaces, local thermodynamic equilibrium is not reached, the continuum hypothesis no longer applies, and the Navier-Stokes equations (NSEs) no longer represent gas flow dynamics. Four regimes of rarefaction can be considered based on Devienne's original classification: (1) continuous flow ($Kn < 0.001$), (2) slip flow ($0.001 < Kn < 0.1$), (3) transition (or Knudsen) flow ($0.1 < Kn < 10$), and (4) free molecular flow ($Kn > 10$) [52]. In the continuous flow regime, the NSEs can be used with no-slip boundary conditions (BCs). In the slip flow regime, gas molecules incoming from a region with a finite flow velocity contribute to a non-zero slip velocity at the boundary. However, the NSEs are still considered to be valid in the bulk of the flow. In the transition or Knudsen flow regime, the Knudsen layer becomes large compared to the bulk of the flow, and the NSEs become invalid. In the free molecular flow regime, collisions between gas molecules are negligible. Limits between those regimes may vary depending on the authors [55, 149, 158, 354-357] and should depend on the physics involved [355-357] and the geometry [55].

Although the Boltzmann equation is generally accepted as valid for all Knudsen numbers, analytical solutions have been developed only for a few simple geometries [137, 138, 257]. Most

numerical methods currently used in the literature are not adapted for both continuum and rarefied flow regimes. The expansion of hydrodynamical equations from the Boltzmann equation, such as the Chapman-Enskog expansion [137, 138] or Grad's moment method [141], requires the specification of higher-order BCs [142-151] and is unable to recover proper flow fields at high Knudsen numbers ($Kn > 1$) [138, 149-152]. Lagrangian methods such as molecular dynamics (MD) and direct-simulation Monte-Carlo (DSMC) involve the simulation of a very large number of molecules and are thus unsuitable for continuum flows, especially in the low Mach number limit [257, 258]. Although hybrid continuum-DSMC schemes based on domain decomposition have been proposed [259-266], computational performance is still limited by the fraction of the domain in which the DSMC must be used. Furthermore, in complex porous media, this decomposition would be more difficult than for planar flows. Another discretization of the Boltzmann equation, called the unified gas kinetic scheme (UGKS), has been proposed [258, 358, 359] and has been improved in the discrete unified gas kinetic scheme (DUGKS) [267]. Accurate results have been reported for the DUGKS scheme for all rarefaction regimes [267] as well as in combination with turbulent [268, 269], thermal, and compressible flows [270, 271]. However, for high Knudsen numbers, a large number of discrete velocity populations are required, and the number of discrete populations necessary to obtain an acceptable error is generally unknown *a priori*. The drawbacks of all the aforementioned methods are exacerbated when considering a flow inside a complex porous medium.

The Lattice Boltzmann method (LBM) is an alternative and well-proven approach for solving gas flows through porous media [250-253]. It is based on a discretization of the Boltzmann equation in which populations with a finite velocity set evolve according to a propagation-collision scheme on a regular Cartesian grid with a finite-difference scheme in time. It is possible to show that the LBM recovers the Navier-Stokes equations (NSEs) under continuum and weak compressibility assumptions through a Chapman-Enskog expansion [250-252]. The local and explicit nature of the LBM enables its massive parallelization and thus the simulation of multiple scales of characteristic length in porous media. The representation of solid and fluid lattices with a simple Boolean geometry facilitates BC discretization. Given all these advantages, studies have been conducted using the LBM on gas flows through porous media in various research fields such as shale gas [185, 186, 188, 192, 193, 195-197, 201, 203, 204, 207-215, 295, 296, 360-373],

microelectromechanical systems (MEMS) [183, 187, 189, 199, 200, 206, 297, 304, 334, 337, 340, 348, 374-390], catalytic reactions [301, 302, 391], and air filtration [120, 121, 123, 317, 392-399].

Alternatively, the NSEs can be recovered with the LBM through a Hermite polynomial expansion, as has been done for the continuous version of the Boltzmann equation with Grad's moment method [275, 400]. This approach better illustrates the relationship between the number of populations used to discretize the velocity space and rarefied flow behavior recovery. The size of the velocity set is determined by the quadrature of the Gauss-Hermite polynomial [275]. For example, it is well established that, in two dimensions, the D2Q9 model with its 9-velocity set is sufficient to capture the NSEs [250-252, 275, 400, 401]. Higher-order Gauss-Hermite quadratures containing larger velocity sets have been used to attempt to capture rarefied flow behavior. Theoretical derivations showed that such higher-order quadratures are able to recover the Burnett and Super-Burnett equations and that they can potentially recover even higher-level approximations [275]. Although these equations have been described as numerically unstable, no numerical instabilities have been found when using well-posed higher-order LBMs to solve equations at the Burnett, Super-Burnett, or arbitrarily higher level, [272, 273, 276, 277, 291, 293, 294, 303, 329, 350, 402]. Tests involving higher-order Gauss-Hermite quadratures on domains without boundaries [273] and with planar boundaries [272, 274, 276-281, 403, 404] have shown an improvement relative to the D2Q9 scheme compared to solutions of the linearized Boltzmann equation. One study [294] claimed agreement between the empirical correlations of Klinkenberg [39] and Beskok and Karniadakis [180] for rarefied flows through porous media. However, studies on the influence of the number of velocities showed that lattices with an odd number of velocities (D2Q25) could perform worse than lattices with an even number of velocities (D2Q16) [272-274] despite the larger size [275]. The same conclusion was reached for very high-order quadratures (D2Q4761 and D2Q4624) [276]. Insufficient discretization at the boundary has been suggested as one source of the discrepancy between DSMC simulations and linearized Boltzmann equation solutions. Given that higher-order moments (in particular, the energy flux, a third-order moment) are not recovered accurately at the boundary [279-281, 403], a solution has been proposed to avoid velocity schemes with zero velocity [274, 276, 278, 279, 281, 403], thus also avoiding the free-streamers described in [349]. Averaging two lattices of even and odd Gauss-Hermite expansion order may improve the computation of the stress-strain relationship for a planar flow [278]. Further improvements have been made by creating anisotropic velocity sets, either through increased

refinement in specific directions [281] or half-range polynomials [403, 405-409]. Despite these advances, it remains difficult to know *a priori* the required Hermite polynomial expansion order required to simulate rarefied gas flows, especially for complex solid-fluid boundaries.

A more permanent drawback of the use of higher-order Gauss-Hermite quadratures is their larger velocity sets, which require more memory and computational resources [273, 275-281]. Large velocity sets also include velocities that are propagated further in the domain, which in parallel computing would require significantly larger ghost layers [277]. Communication times would thus increase relative to local computations, which would reduce their parallel efficiency [255, 256]. This would negate one of the main advantages of the LBM for simulating gas flows through porous media.

A proposed alternative to the direct approximation of the Boltzmann equation with the LBM is to represent the modification of the stress-strain relationship in rarefied flows with a local viscosity function. This approach has been referred to as the extended or generalized NSE. Its main advantage is its low computational cost. It has been used to simulate intermediate to high Knudsen flows with low-order LBM solvers [184, 187-189, 193, 198, 201, 204, 207, 208, 210-212, 214-216, 223, 225, 231, 236, 287, 291, 293, 295, 296, 332-334, 350, 364, 369, 380, 381, 384, 386, 391, 410-413]. Despite these potential advantages, simulating slip flows through complex porous media with a small velocity set poses intrinsic challenges that need to be understood both separately and as a whole, namely, avoiding an explicit characteristic length definition, managing BCs in corners, analyzing relationships between higher-order moments and populations, avoiding references to multiple populations, and incorporating the regularization procedure to filter out unresolved higher-order non-equilibrium components of populations.

Slip BCs with the LBM are imposed on populations as for the continuous Boltzmann equation. Unknown populations incoming from the wall at boundary nodes need to be specified. It has been proposed to explicitly impose macroscopic velocity slip BCs from the Maxwell BC [157] on populations through the moments generated on planar walls [342, 343], but such a method is intrinsically geometry dependent and difficult to generalize to complex domains. It has also been proposed to use the Langmuir slip model [284], in which molecule interactions with solid boundaries are assumed to absorb and desorb with a lag. This model requires an explicit definition of the characteristic length of the flow. However, the characteristic length of a complex geometry

is difficult to define without ambiguities for all geometries. For example, taking the pore size cannot work in open geometries such as that in the Kremer's problem, or in the case of flows around isolated objects such as cylinders and spheres. Also, the Langmuir slip model has to be modified artificially to include a second-order slip velocity [193]. Despite these shortcomings, the Langmuir slip model has been implemented in the LBM successfully for closed geometries [188, 211, 360, 370, 377, 385, 414-416].

For the reasons given above, the preferred approach in the literature has been to directly discretize slip BCs based on Maxwell's diffusive and specular reflections [157] with the LBM [286, 335-338, 417]. Maxwell slip BCs have also been combined with the bounce-back BCs previously used for non-slip flows [339]. However, theoretical developments in the slip regime have revealed divergences between the diffusive BCs expressed for the continuous Boltzmann equation and its direct discretization for the D2Q9 scheme [285]. Algebraic relationships between macroscopic velocity BCs and kinetic BCs had to be developed and imposed explicitly. It was found that combinations of these three schemes all produce the same result for a planar flow through an equivalence relationship on their kinetic ratios [237, 339]. For complex BCs, however, it has been argued that specular reflection BCs should be avoided as they are more difficult to define in complex boundaries and that a combination of bounce-back and diffusive reflection BCs, also called diffusive bounce-back (DBB BC), would be simpler to manage [194, 204, 210, 237, 289, 296, 340, 378].

A theoretical analysis with these kinetic BCs has shown that the classical Bhatnagar-Gross-Krook (BGK) collision operator [139] typically used to solve the continuous Boltzmann equation introduces unphysical grid-dependent contributions to the D2Q9 scheme [285]. An analysis conducted with a multiple relaxation time (MRT) collision operator has shown that the relaxation rate related to the energy flux has an impact on slip flow behavior as it is not solved in the D2Q9 scheme for extended NSEs [418, 419]. The energy flux relaxation rate has thus been adjusted for the D2Q9 scheme to recover the proper magnitude of the slip velocity on the wall [114, 236, 339, 341]. Values derived for the energy flux relaxation rate have been implemented as is the case for the D3Q15 and D3Q19 models [197, 212, 214, 291, 292, 364, 420]. However, to the authors' knowledge, no theoretical analysis has been carried out to determine whether the value of the energy flux relaxation rate developed for the D2Q9 lattice is accurate for any three-dimensional lattice.

To avoid the calibration of the energy flux relaxation rate, multireflection BCs have also been proposed [421] to model slip BCs. In these models, a closure relationship is developed to find the missing populations incoming from a wall by interpolating several populations interacting with it [418, 422]. The closure relationship has been calibrated for slip flows on both planar walls [421] and a cylindrical Couette geometry [423]. This approach requires extrapolation from lattices located further from the wall, which makes it less generalizable to complex geometries [420]. For example, one may consider a case where the multireflection BC requires information from a solid lattice, which is a possibility if the solid domain is not convex. This would also increase the size of the ghost layers during parallelization, which would decrease the parallel efficiency of the LBM. Furthermore, only flows in the slip regime were considered in these studies. For all these reasons only DBB BCs will be considered for the remainder of this paper.

As the Knudsen number increases, non-equilibrium components of higher-order moments become preponderant. However, the velocity set becomes too small to solve the higher-order moments, which creates a directional grid-dependent error in the flow (also called an aliasing error). For this reason, a regularization procedure (presented in [290, 298, 299]) has been proposed to filter out these non-equilibrium components of moments of order higher than second-order [195, 198, 203, 207, 208, 210, 211, 215, 291-297, 300-304]. Although comparisons between non-regularized and regularized LBMs have shown that, for planar flows, the regularization procedure might be unnecessary when the extended NSEs are solved [293, 350], rarefied flows modeled with the D2Q9 lattice show significant degradation of the flow field, with unphysical jets appearing from the solid corners [195, 291-297]. The regularization technique is thus vital for simulating rarefied gas flows through porous media with the LBM. As the energy flux is a third-order moment, this necessarily changes the value of the energy flux relaxation rate required to recover the proper slip velocity [421]. However, to the authors' knowledge, this has never been taken into account for an LBM model, including the adequate treatment of kinetic BCs, the regularization technique and local effective viscosity functions. This may explain the losses in accuracy reported in the literature [198, 202, 210] for the regularized MRT-LBM in the slip and transition flow regimes through complex geometries.

In this paper, a new DBB BC will be introduced and fully described for solving the extended NSEs with the regularized LBM for the D2Q9 and D3Q15 lattices. The remainder of this paper will be organized as follows. In Section 5.2, the generalized Navier-Stokes constitutive model and

the slip flow model used to simulate rarefied flows will be recalled. In Section 5.3, the basic principles of the MRT-LBM, the relationship between mean free path and relaxation time, the DBB BC, and the regularization technique will be exposed, and new relationships for the kinetic ratio and for energy flux relaxation discussed. In Section 5.4, the accuracy of the proposed model, will be assessed with a convergence analysis for a slit flow as well as a numerical verification for slip flows around arrays of cylinders and spheres. In Section 5.5, the development of the new DBB BC will be discussed further. Lastly, in Section 5.6, conclusions with respect to the main findings and contributions of this work will be drawn.

5.2 Rarefied flow modeling

The generalized Navier-Stokes constitutive model and the slip models used for rarefied flow modeling in this paper are presented in Sections 5.2.1 and 5.2.2, respectively.

5.2.1 The generalized Navier-Stokes constitutive model

The NSEs rely upon the hypothesis of local thermodynamic equilibrium. In the region of a thickness of the order of the mean free path λ of a solid surface (also called the Knudsen layer), gas molecules do not collide sufficiently between themselves and thus do not satisfy this hypothesis. Therefore, the NSEs break down in this region. In classical NSEs, the stress-strain relationship is linear, and there is a constant of proportionality between stress and strain called viscosity μ . Guo et al. [225] proposed a generalized NSE, which models the non-linearity of the stress-strain relationship using a spatially dependent effective viscosity $\mu_e(\mathbf{x})$:

$$\boldsymbol{\tau} = -\mu_e(\mathbf{x})\dot{\boldsymbol{\gamma}} \quad (5.1)$$

where $\boldsymbol{\tau}$ and $\dot{\boldsymbol{\gamma}}$ are, respectively, the shear stress and shear rate.

The kinetic theory of gases predicts that the viscosity of an unbounded gas μ in local thermodynamic equilibrium is proportional to the mean free path of the gas molecules [138]:

$$\lambda = \frac{\mu}{p} \sqrt{\frac{\pi R T}{2}} \quad (5.2)$$

where T is the gas temperature, R is the perfect gas constant associated with the gas, and p is the pressure of the gas, which gives:

$$p = \rho RT \quad (5.3)$$

where ρ is the density of the gas.

In a bounded gas, however, the paths of the gas molecules are obstructed, which diminishes the mean free path locally near solid boundaries. Assuming relationship (5.2) holds inside the Knudsen layer and knowing the probability distribution function for the free path of gas molecules, it is possible to find an effective mean free path λ_e at each point and a spatially dependent viscosity function $\Psi(\mathbf{x})$, which can be defined as:

$$\Psi(\mathbf{x}) = \frac{\lambda_e}{\lambda} = \frac{\mu_e}{\mu} \quad (5.4)$$

As the effective mean free path is always smaller than the mean free path for an unbounded gas, $0 \leq \Psi(\mathbf{x}) \leq 1$.

5.2.2 Slip flow boundary conditions

Macroscopically, a slip flow appears as a gas velocity discontinuity on a solid surface. Based on the condition that changes to the properties of a gas are negligible over the distance of a mean free path (in other words, small deviations from thermodynamic equilibrium and thus low Knudsen number), Maxwell [157] derived a relationship for the slip velocity in the case of a planar wall, which was later extended to curved surfaces [163] as follows:

$$\mathbf{u}_s = \left(\frac{2 - \sigma}{\sigma} \right) \lambda \cdot \frac{\delta \mathbf{u}}{\delta \mathbf{n}} \quad (5.5)$$

where \mathbf{u}_s is the velocity of the gas at the wall relative to the wall (also called slip velocity), \mathbf{u} is the velocity vector, \mathbf{n} is the normal vector to the wall, and σ is the tangential momentum accommodation coefficient (TMAC). Maxwell introduced TMAC to describe the probability that gas molecules are diffusively reflected ($\sigma = 1$) or specularly reflected ($\sigma = 0$) when interacting with solid surfaces. For a diffusively reflected gas, a finite slip velocity would be recovered, whereas for a completely specularly reflected gas, no momentum would be transferred tangentially

to the fluid and thus an infinite slip velocity would be recovered. To take into account higher Knudsen number flows, Maxwell's relationship has been extended to a second-order shear rate $\frac{\delta \mathbf{u}}{\delta \mathbf{n}}$, and even higher-orders according to several approaches compiled in review [158].

The main issue with the Maxwell slip BC comes from its hypothesis of thermodynamic equilibrium. As fluid macroscopic properties should vary little in a region of approximately one mean free path of a given location, it does not take into account the variation in effective viscosity inside the Knudsen layer. Consequently, the slip velocity is overpredicted when the velocity is extrapolated from outside the Knudsen layer, as shown in Figure 5.1. A proper slip velocity relationship should thus consider the variation in the effective viscosity near solid boundaries. A good slip velocity relationship should also be robust, stable numerically and, for complex geometries, should avoid relying on an explicit definition of the Knudsen number that requires defining a local characteristic length. One slip velocity relationship that fulfills all these criteria was proposed by Guo et al. [225]:

$$\mathbf{u}_s = A_1 \lambda_e \frac{\partial \mathbf{u}}{\partial \mathbf{n}} - A_2 \lambda_e \left(\frac{\partial}{\partial \mathbf{n}} \left(\lambda_e \frac{\partial \mathbf{u}}{\partial \mathbf{n}} \right) \right) \quad (5.6)$$

where A_1 and A_2 are phenomenological constants derived from theoretical models or experimental values. This model was successfully used in several studies [161, 170, 236, 237] for planar and curvilinear flows over a broad range of Knudsen numbers, from the continuum limit to the higher end of transition flows.

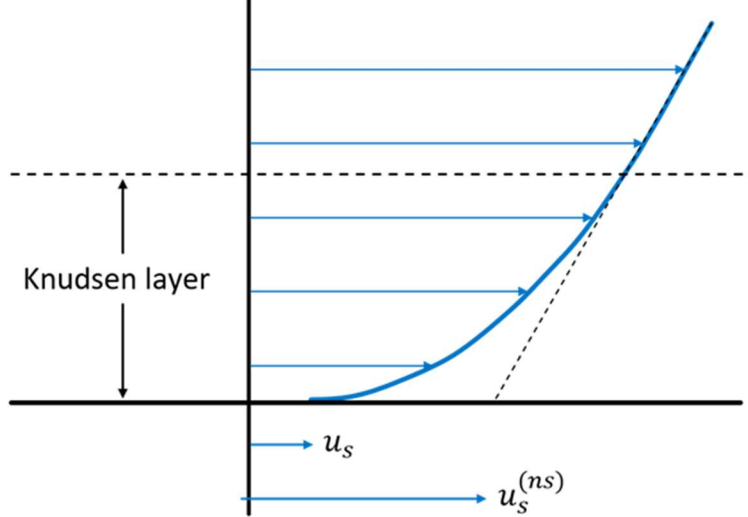


Figure 5.1 Illustration of the velocity in the Knudsen layer. The true slip velocity u_s is smaller than the Navier-Stokes fictitious velocity $u_s^{(ns)}$ that would be recovered if the Navier-Stokes equations were used inside the Knudsen layer.

5.3 The regularized Lattice Boltzmann method

In this section, the regularized LBM is presented. First, as multiple relaxation times are required to accurately impose the DBB BC in rarefied flows, the MRT-LBM is recalled. Second, the principle of regularization to manage non-planar solid-fluid boundaries is explained. Third, the DBB BC recently proposed in [237] for the classical MRT-LBM is described and the limitations of the approach highlighted. Lastly, new expressions for the DBB BC that accurately impose the slip BC introduced in Eq. (5.6) with the regularized MRT-LBM are presented.

5.3.1 MRT-LBM

The LBM is a discretized form of the Boltzmann equation, where a discretized set of gas molecule populations f_i evolve according to a propagation-collision scheme:

$$f_i(\mathbf{x} + \mathbf{c}_i \delta_t, t + \delta_t) - f_i(\mathbf{x}, t) = \Omega_i + F_i \delta_t \quad (5.7)$$

where \mathbf{c}_i is the velocity of the population set f_i , Ω_i is the collision operator, F_i is a forcing term applied to each population, and δ_t is the time step. The density and the momentum of the gas are recovered from the populations as follows:

$$\rho = \sum_{i=0}^{Q-1} f_i \quad (5.8)$$

$$\rho \mathbf{u} = \sum_{i=0}^{Q-1} f_i \mathbf{c}_i + \mathbf{F} \frac{\delta_t}{2} \quad (5.9)$$

where \mathbf{F} is the force vector and Q is the number of velocities in the lattice.

In the MRT scheme, populations are transformed into moments (such as density, momentum, energy, stress, etc.) so as to relax each moment with a different relaxation time. The post-collision moments are then transformed back into populations. The MRT collision operator is thus given by:

$$\Omega_i = - \sum_{j=0}^{Q-1} (\mathbf{M}^{-1} \mathbf{S} \mathbf{M})_{ij} (f_j - f_j^{(eq)}) \quad (5.10)$$

where \mathbf{M} is a transformation matrix from the populations to the moments and \mathbf{S} is a diagonal matrix containing the relaxation rates. The MRT-LBM equation is thus traditionally written as:

$$f_i(\mathbf{x} + \mathbf{c}_i \delta_t, t + \delta_t) - f_i(\mathbf{x}, t) = - \sum_{j=0}^{Q-1} (\mathbf{M}^{-1} \mathbf{S} \mathbf{M})_{ij} (f_j - f_j^{(eq)}) + F_i \delta_t \quad (5.11)$$

Each lattice is associated with a transformation matrix and a relaxation rate diagonal matrix. The superscript (eq) stands for the equilibrium distribution functions, which are calculated with the macroscopic variables. To recover the extended NSEs, the equilibrium distribution functions must have the following form [236]:

$$f_i^{(eq)} = w_i \rho \left(1 + \frac{\mathbf{c}_i \cdot \mathbf{u}}{c_s^2} + \frac{(\mathbf{c}_i \cdot \mathbf{u})^2}{c_s^4} - \frac{\mathbf{u}^2}{2c_s^2} \right) \quad (5.12)$$

where w_i are the weights associated with each population, which are dependent on the lattice used, and c_s is the lattice sound speed, which may depend on the lattice model. The forcing term F_i

applied to each population in the MRT-LBE (Eq. (5.7)) has been generalized from BGK to MRT [287]:

$$F_i = \mathbf{M}^{-1} \left(\mathbf{I} - \frac{\mathbf{S}}{2} \right) \mathbf{M} \bar{F}_i \quad (5.13)$$

with:

$$\bar{F}_i = w_i \left(\frac{\mathbf{c}_i \cdot \mathbf{u}}{c_s^2} + \frac{\mathbf{u} \mathbf{F} : (\mathbf{c}_i \mathbf{c}_i - c_s^2 \mathbf{I})}{c_s^4} \right) \quad (5.14)$$

In this paper, two lattices are considered: the D2Q9, which is a bidimensional scheme with a discretized set of 9 velocities (see Figure 5.2), and the D3Q15 lattice, which is a tridimensional scheme with a discretized set of 15 velocities (see Figure 5.3). The D3Q15 lattice is fully presented in Appendix 5.A. For the D2Q9 lattice, the velocity set is given as [288]:

$$\begin{aligned} c_0 &= (0,0)c \\ c_1 &= -c_3 = (1,0)c \\ c_2 &= -c_4 = (0,1)c \\ c_5 &= -c_7 = (1,1)c \\ c_6 &= -c_8 = (-1,1)c \end{aligned} \quad (5.15)$$

where the lattice velocity $c = \delta_x/\delta_t$ is the ratio of the grid size δ_x and the time step δ_t . The weights associated with each population are:

$$\begin{aligned} w_0 &= 4/9 \\ w_{1-4} &= 1/9 \\ w_{5-8} &= 1/36 \end{aligned} \quad (5.16)$$

The moment set associated with the D2Q9 lattice is:

$$m_k = \mathbf{M} f_i = (\rho, e, \epsilon, j_x, q_x, j_y, q_y, p_{xx}, p_{xy})^T \quad (5.17)$$

where $m_0 = \rho$ is the density, $m_1 = e$ is the energy, $m_2 = \epsilon$ is the energy squared, $(m_3, m_5) = (j_x, j_y)$ is the momentum, $(m_4, m_6) = (q_x, q_y)$ is the energy flux, $m_7 = p_{xx}$ is the diagonal

component of the stress tensor, and $m_8 = p_{xy}$ is the non-diagonal component of the stress tensor. Moment space equilibria for the D2Q9 scheme are:

$$m_k^{(eq)} = \mathbf{M}f_i = \rho(1, -2 + 3u^2, 1 - 3u^2, u_x, -u_x, u_y, -u_y, u_x^2 - u_y^2, u_x u_y)^T \quad (5.18)$$

The corresponding transformation matrix \mathbf{M} is:

$$\left(\begin{array}{cccccccc} 1 & 1 & 1 & 1 & 1 & 1 & 1 & 1 & 1 \\ -4 & -1 & -1 & -1 & -1 & 2 & 2 & 2 & 2 \\ 4 & -2 & -2 & -2 & -2 & 1 & 1 & 1 & 1 \\ 0 & 1 & 0 & -1 & 0 & 1 & -1 & -1 & 1 \\ 0 & -2 & 0 & 2 & 0 & 1 & -1 & -1 & 1 \\ 0 & 0 & 1 & 0 & -1 & 1 & 1 & -1 & -1 \\ 0 & 0 & -2 & 0 & 2 & 1 & 1 & -1 & -1 \\ 0 & 1 & -1 & 1 & -1 & 0 & 0 & 0 & 0 \\ 0 & 0 & 0 & 0 & 0 & 1 & -1 & 1 & -1 \end{array} \right) \quad (5.19)$$

while the relaxation rates diagonal matrix \mathbf{S} are:

$$\mathbf{S} = \text{diag}(s_\rho, s_e, s_\epsilon, s_j, s_q, s_j, s_q, s_s, s_s) \quad (5.20)$$

Each relaxation rate corresponds to the moment set described in Eq. (5.17).

In the LBM, it is sometimes mathematically simpler to discuss relaxation times τ_i rather than relaxation rates s_i , which are by definition:

$$\tau_i = \frac{1}{s_i} \quad (5.21)$$

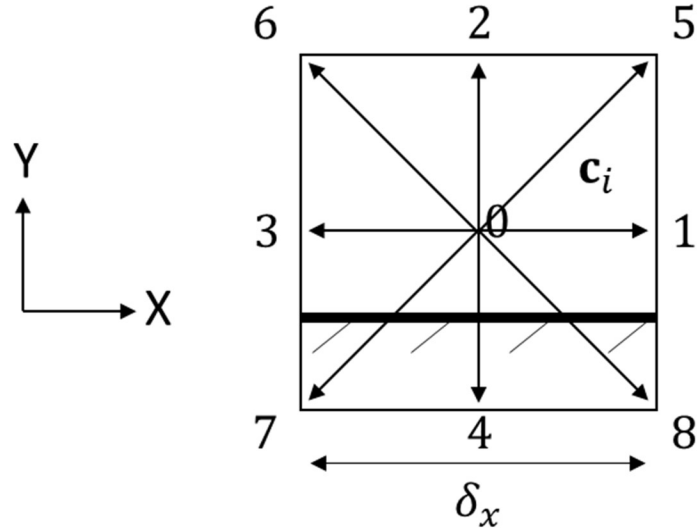


Figure 5.2 D2Q9 velocity set used for the LBM where \mathbf{c}_i is the velocity in direction i . The wall is located half-way from the node.

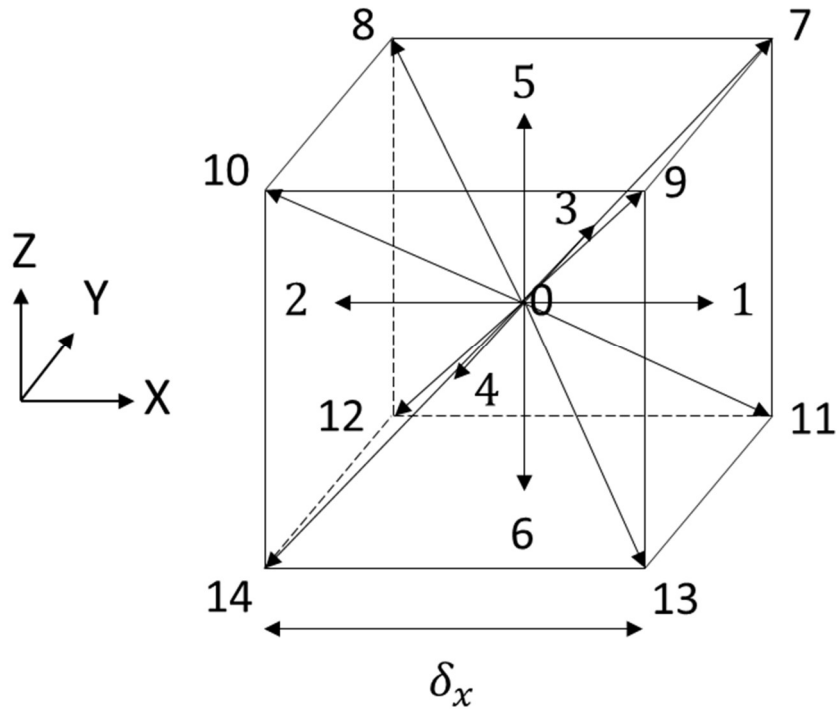


Figure 5.3 D3Q15 velocity set used for the LBM where \mathbf{c}_i is the velocity in direction i . The wall was omitted here for the sake of clarity. It is located half-way from the node to the destination of populations 6, 11, 12, 13, and 14.

A relationship between the relaxation time and the effective mean free path is derived below. First, it must be noted that, for both the D2Q9 and the D3Q15 lattices, the speed of sound is related to temperature as follows [250]:

$$c_s = \frac{c}{\sqrt{3}} = \sqrt{RT} \quad (5.22)$$

Also, in the MRT-LBM, the relaxation time associated with stress τ_s is traditionally related to the viscosity as follows [250]:

$$\mu = \rho c_s^2 \left(\tau_s - \frac{1}{2} \right) \delta_t \quad (5.23)$$

In this work, however, non-constant effective viscosities were considered. To do so, an expression was derived for an effective viscosity relaxation time, noted τ_s throughout the paper. Eqs. (5.2), (5.3), (5.4), and (5.22) were introduced into Eq. (5.23) to give:

$$\tau_s = \frac{1}{2} + \sqrt{\frac{6}{\pi} \frac{\lambda}{\delta_x} \Psi(\lambda, \mathbf{x})} = \frac{1}{2} + \sqrt{\frac{6}{\pi} Kn \cdot N \cdot \Psi(\lambda, \mathbf{x})} \quad (5.24)$$

where $N = L_C / \delta_x$ is the number of grid cells along the characteristic length L_C . The middle term of Eq. (5.24) is the preferred way of expressing the scheme in complex geometries as the characteristic length is not involved and thus does not have to be explicitly defined.

In the MRT-LBM scheme, it is common practice to use lattice-units, with $\delta_x = \delta_t = 1$. This induces both a lattice velocity $c = \frac{\delta_x}{\delta_t} = 1$ for the D2Q9 and D3Q15 schemes and thus the following lattice speed of sound:

$$c_s = \frac{1}{\sqrt{3}} \quad (5.25)$$

5.3.2 Regularization technique

While the D2Q9 and D3Q15 lattices have sufficient isotropy to recover the extended NSEs, attempts to simulate high Knudsen flows solely using the method presented in Section 5.3.1 have shown that grid-dependent spurious jets strongly degrade the solution for non-planar cases [195,

291-297]. The introduction of the regularization technique can be explained by the passage from kinetic equations to hydrodynamic equations.

First, in the LBM, regardless of the size of the lattice velocity set, there are more populations than moments that can be accurately represented through the solution of the full Boltzmann equation [290]. For example, the D2Q9 and D3Q15 lattices include third- and fourth-order energy flux and energy squared moments, respectively. These higher-order moments, despite not being accurately resolved, still exist in these lattices, as shown in Section 5.3.1 and Appendix A.

Second, regardless of whether the Chapman-Enskog or the Hermite polynomial expansion approach is used [252], the NSEs are recovered from the LBM under the assumption that deviations from equilibrium for higher-order moments are negligible. For high Knudsen flows, the non-equilibrium component of the population distribution becomes more important. It can be readily seen in Eq. (5.24) that the relaxation time related to stress τ_s becomes larger. However, in the traditional LBM, $\tau_s \sim O(1)$.

Lastly, in the LBM, the evolution of the system is split between a collision and a propagation phase. While moment equilibrium components can be accurately represented by the lattice before propagation, they are generally not well represented after propagation [298, 299, 424]. Although this error, which is introduced at the propagation step, can be neglected in the continuum regime, it cannot be neglected for high Knudsen flows. When non-planar boundary conditions are considered, unphysical patterns emerge and are propagated from the boundaries.

For all these reasons, the regularization technique [290] has been proposed in the context of high Knudsen flows to remove non-equilibrium high-order moments [303]. In this work, all contributions of order higher than 2 were filtered from the population distributions, resulting in new regularized non-equilibrium population distributions. Before the collision takes place, populations f_i are split between their non-equilibrium $f_i^{(neq)}$ and equilibrium $f_i^{(eq)}$ parts:

$$f_i^{(neq)} = f_i - f_i^{(eq)} \quad (5.26)$$

The non-equilibrium components of the populations are then reprojected on the polynomial basis of the lattice:

$$f_i^{(neqr)} = \frac{w_i}{2c_s^2} H_{i\alpha\beta}^{(2)} \left(\frac{\mathbf{c}_i}{c_s} \right) : \sum_{i=0}^{O-1} f_i^{(neq)} \mathbf{c}_{i\alpha} \mathbf{c}_{i\beta} \quad (5.27)$$

where $H_{i\alpha\beta}^{(2)} \left(\frac{\mathbf{c}_i}{c_s} \right) = \mathbf{c}_{i\alpha} \mathbf{c}_{i\beta} / c_s^2$ is the Hermite polynomial of second order, $\mathbf{c}_{i\alpha} \mathbf{c}_{i\beta}$ is a dyadic or outer product and $:$ represents the double dot product of two tensors. The post-regularization population $f_i^{(r)}$ is thus written as:

$$f_i^{(r)} = f_i^{(eq)} + f_i^{(neqr)} \quad (5.28)$$

The post-regularization populations defined in Eq. (5.28) are next inserted in Eq. (5.11), and the regularized MRT-LBM equation is thus written as:

$$f_i(\mathbf{x} + \mathbf{c}_i \delta_t, t + \delta_t) = f_i^{(eq)} + \mathbf{M}^{-1} (\mathbf{I} - \mathbf{S}) \mathbf{M} f_i^{(neqr)} + F_i \delta_t \quad (5.29)$$

5.3.3 Diffusive bounce-back boundary condition

As discussed in the Introduction, the DBB BC is the most suitable approach for modeling slip BCs on complex geometries [194, 204, 210, 237, 289, 296, 340, 378]. In this work, solid boundaries were assumed to be static. The bounce-back BC generally used to impose no-slip BCs sets the population outgoing from the wall with direction \mathbf{c}_i as equal to the population incoming from the opposite direction $\mathbf{c}_{oppdir(i)} = -\mathbf{c}_i$:

$$f_i^{(BB)} = f_{oppdir(i)} \quad (5.30)$$

where the superscript (BB) stands for bounce-back and the subscript $oppdir(i)$ indicates the index of the population opposite in direction from i . Diffusive reflection imposes an equilibrium distribution on the population outgoing from the wall [335]:

$$f_i^{(D)} = K f_i^{(eq)}(\rho_w, \mathbf{0}) \quad (5.31)$$

where the superscript (D) stands for diffusive, ρ_w is the density at the wall, and the factor K imposes a non-penetration condition on the solid boundary through the following definition:

$$K = \frac{\sum_{\mathbf{c}_i \cdot \mathbf{n} < 0} |\mathbf{c}_i \cdot \mathbf{n}| f_i}{\sum_{\mathbf{c}_i \cdot \mathbf{n} < 0} |\mathbf{c}_i \cdot \mathbf{n}| f_i^{(eq)}(\rho_w, \mathbf{0})} \quad (5.32)$$

The first such slip BC, which includes the effect of a non-constant effective viscosity function, was not proposed for the DBB BC but rather for a combination of bounce-back and specular reflection (CBBSR BC) conditions [236]. Specular reflection has the disadvantage of being non-local and is thus unsuitable for non-planar geometries [237]. A combination of bounce-back and diffusive reflection conditions, called the diffusive bounce-back boundary condition (DBB BC) has been proposed to overcome these issues [289]:

$$f_i = r f_i^{(BB)} + (1 - r) f_i^{(D)} \quad (5.33)$$

where $0 \leq r \leq 1$ is the kinetic ratio for the DBB BC, which represents the proportion of bounce-back in the outgoing population relative to the diffusive reflection part. For the D2Q9 scheme, the proper relationships for r and the relaxation time related to energy flux τ_q required to recover Eqs. (5.5) and (5.6) are [237]:

$$r = \frac{1 - \chi A_1 - \frac{\tau'_{sw} \delta_x}{8 \left(\tau_{sw} - \frac{1}{2} \right)^2}}{1 + \chi A_1 + \frac{\tau'_{sw} \delta_x}{8 \left(\tau_{sw} - \frac{1}{2} \right)^2}} \quad (5.34)$$

$$\tau_q = \frac{1}{2} + \frac{\pi A_2 (2\tau_{sw} - 1)^2 + 3 \tau'_{sw} \delta_x (12 + 30 \left(\tau_{sw} - \frac{1}{2} \right) \chi A_1)}{8(2\tau_{sw} - 1) \left(\tau_{sw} - \frac{1}{2} \right)^2} \quad (5.35)$$

where $\chi = \sqrt{\pi/6}$, τ_{sw} is the so-called viscosity relaxation rate at the wall given by Eq. (5.24) and τ'_{sw} is the derivative of τ_{sw} in the direction normal to the wall.

While the convergence of the DBB BC with Eqs. (5.34) and (5.35) for the traditional MRT-LBM (Eq. (5.11)) has been shown in [237], preliminary results carried out here have indicated that the slip velocity is not well captured when the same DBB BC is used in combination with the regularized MRT-LBM (Eq. (5.29)). To the authors' knowledge, none of the kinetic BCs presented in this section have ever been analyzed in combination with the regularized MRT-LBM. In

addition, it has never been proven that the application of kinetic BCs developed for 2D lattices works for 3D lattices.

5.3.4 A new diffusive bounce-back boundary condition

As discussed in Section 5.3.2, the goal of the regularization technique is to remove the non-equilibrium components of higher than second order moments presented in Section 5.3.1 from the model. The energy flux, a third-order moment, was involved in the recovery of Eqs. (5.34) and (5.35) in Guo et al.'s development [236]. Values for r and τ_q must therefore be redeveloped for the DBB BC with the regularized MRT-LBM to solve the extended NSEs and recover the accurate slip velocity presented in Eq. (5.6).

In Section 5.2, the extended NSEs and the slip BCs were formulated in terms of the macroscopic velocity. However, as explained in Section 5.3.1, in the LBM, the flow evolves according to a population balance. It would be difficult to find such relationships between populations and all the moments involved in the imposition of slip velocity for a complex porous medium in the general case. To simplify the problem, a force-driven, steady-state, incompressible laminar flow in the x -direction through a planar geometry was considered. The flow was thus assumed to be at steady-state, well-developed, and unidimensional. This simplification has produced successful results when applied to complex geometries [289, 340, 418, 420]. Under the same assumptions, the inertial terms of the extended NSEs are neglected and using Eqs. (5.1), (5.23) and (5.24), the following equation is solved:

$$\partial_y(v_e \partial_y u) = -a \quad (5.36)$$

where $v_e = c_s^2(\tau_s - 0.5)\delta_t$ and $a = \mathbf{F}/\rho$.

The treatment of the force term requires special care so that the method used in Guo et al.'s original paper [236] can be applied and successfully extended from the CBBSR BC to the DBB BC. In the case of CBBSR BC, both components of an outgoing population from the solid wall, the bounce-back part and the specular reflection part, originate from a population already present in the flow. However, in the DBB BC, the diffusive reflection contribution outgoing from the solid wall is simply the equilibrium distribution calculated using the density and velocity at the wall. On an outgoing population from a wall, the force term must be applied regardless of the

form of the BC on every fraction r_i of every population f_i . Equation (5.29), which relates post-collision populations to pre-collision populations, must thus be rewritten as follows:

$$\begin{aligned}\tilde{f}_i = r_i & \left(f_i^{(eq)} + \mathbf{M}^{-1}(\mathbf{I} - \mathbf{S})\mathbf{M} f_i^{(neqr)} \right) + (1 - r_i)K f_i^{(eq)}(\rho, \mathbf{0}) \\ & + F_i \delta t\end{aligned}\quad (5.37)$$

where the tilde \sim represents the post-collision variable, and:

$$r_i = \begin{cases} r & \text{if the population } i \text{ leads to a solid boundary} \\ 1 & \text{otherwise} \end{cases} \quad (5.38)$$

The redevelopment of expressions for the kinetic ratio r and the energy flux relaxation time τ_q requires a population balance on the boundary node and the neighboring fluid node, which depends on the lattice. Only the final results are presented in this section. For the sake of completeness, the detailed development for the D2Q9 and D3Q15 lattices are provided in Appendices B and C, respectively. For both D2Q9 and D3Q15 lattices, the expression for r is:

$$r = \frac{\tilde{\tau}_{sw}^2(1 - A_1\chi) + \delta_x \tilde{\tau}'_{sw} \left(-\frac{1}{8} + \tilde{\tau}_{sw}(1 - A_1\chi) \right)}{\tilde{\tau}_{sw}^2(1 + A_1\chi) + \delta_x \tilde{\tau}'_{sw} \left(\frac{1}{8} + \tilde{\tau}_{sw}(1 + A_1\chi) \right)} \quad (5.39)$$

Only the expression for τ_q depends on the lattice type, where for the D2Q9:

$$\tau_q = \frac{-(8\tilde{\tau}_{sw}^2(1 + A_1\chi) + \delta_x \tilde{\tau}'_{sw}(1 + 8\tilde{\tau}_{sw}(1 + A_1\chi)))}{6(\tilde{\tau}_{sw} - 4\tilde{\tau}_{sw}^2 + 8A_2\chi^2\tilde{\tau}_{sw}^3 + \delta_x \tilde{\tau}'_{sw}(5 - 4\tilde{\tau}_{sw} + 10A_1\chi\tilde{\tau}_{sw} + 8A_2\chi^2\tilde{\tau}_{sw}^2))} \quad (5.40)$$

while for the D3Q15 lattice:

$$\tau_q = \frac{-7(8\tilde{\tau}_{sw}^2(1 + A_1\chi) + \delta_x \tilde{\tau}'_{sw}(1 + 8\tilde{\tau}_{sw}(1 + A_1\chi)))}{30\tilde{\tau}_{sw} - 136\tilde{\tau}_{sw}^2 - 16A_1\chi\tilde{\tau}_{sw}^2 + 240A_2\chi^2\tilde{\tau}_{sw}^3 + \delta_x \tilde{\tau}'_{sw}(148 - 136\tilde{\tau}_{sw} + 284A_1\chi\tilde{\tau}_{sw} + 240A_2\chi^2\tilde{\tau}_{sw}^2)} \quad (5.41)$$

The resulting Eqs. (5.39) and (5.40) obtained with the regularized MRT-LBM are different from Eqs. (5.34) and (5.35) obtained with the traditional MRT-LBM for the D2Q9 scheme. Hence, if Eqs. (5.34) and (5.35) are used with the regularization technique, an incorrect analytical expression of the slip velocity, proving the necessity of the current development. The same can be said if the

value for τ_q obtained from Eq. (5.40) developed for the D2Q9 lattice is used for the D3Q15 lattice instead of Eq. (5.41).

All previous reports in the literature about regularized MRT-LBM schemes driven by a force term have used the momentum relaxation rate $s_j = 1$ without justification [203, 210, 291, 292, 295-297]. In Appendices 5.B and 5.C, it is proven that, to recover the correct coefficient in front of the force term in Eq. (5.9) for the regularized MRT-LBM, the value of s_j must necessarily be set to 1.

5.4 Numerical results

In this section, the accuracy of the new DBB BC for the regularized MRT-LBM is assessed using four different test cases. In Section 5.4.1, an example of dealiasing the MRT-LBM solution of the flow through complex geometries is discussed. In Section 5.4.2, the error of the schemes with the new bounce-back r and energy flux relaxation time τ_q are compared with the error of the scheme with previously used values. Next, slip flows through complex geometries are compared with analytical solutions for arrays of cylinders and spheres in Sections 5.4.3 and 5.4.4, respectively. All the test cases are presented in Figure 5.4. For all the simulations reported hereafter, the lattice-unit system was used, with $\delta_x = \delta_t = 1$. The body force term was chosen to be small enough to ensure an incompressible flow ($Ma < 0.01$) and large enough to prevent subtraction round-off errors. Equations were developed symbolically in terms of populations to remove all redundant operations. Unless otherwise stated, relaxation times were chosen as follows: τ_s with Eq. (5.24), τ_q with Eqs. (5.40) and (5.41) for the D2Q9 and D3Q15 schemes, respectively, with $\tau_j = 1$, $\tau_e = 1.1$, and $\tau_\epsilon = 1.2$. Note that τ_ρ and τ_t do not appear in any part of the collision term and the force term, and that the last two relaxation times had very little impact on the results. Although the diffusive part of the DBB BC was computed using the density at the center of the boundary node instead of at the wall, the total mass in the system was always conserved up to machine precision for planar flows and 10^{-7} for non-planar flows, with the deviation from mass conservation growing with the Mach number in both cases.

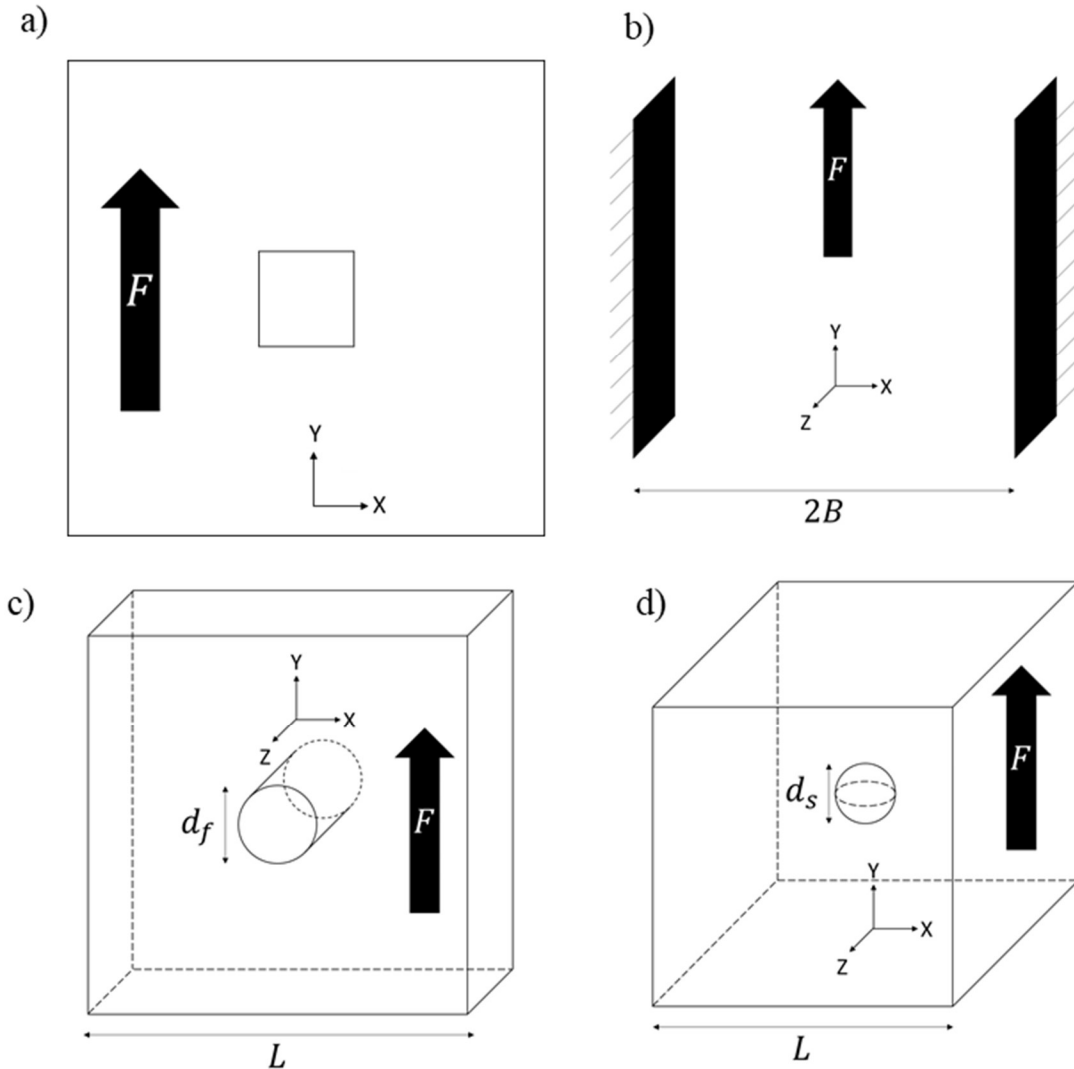


Figure 5.4 Schematic representation of (a) the square-cylinder flow case, (b) the slit flow case, (c) the cylinder array case, and (d) the sphere array case. Except for the slit flow case for which there are walls at the x -boundaries, periodic BCs were imposed along every outer boundary, which repeats the structure infinitely in every direction.

5.4.1 Dealiasing verification

To emphasize the importance of the regularization technique in complex geometries, a gas flow was simulated with the D2Q9 scheme around a square section cylinder that was one-fifth of the domain length, both without the regularization technique (solving the traditional MRT-LBM in Eq. (5.11) and using Eqs. (5.34) and (5.35)) and with the regularization technique (solving the

regularized MRT-LBM in Eq. (5.37) and using Eqs. (5.39) and (5.40)). The Knudsen number, defined as the ratio between the mean free path and the lateral size of the square-section cylinder, was set at $Kn = 1$. The resulting flow fields are presented in Figure 5.5. Significant differences in the flow fields between the two methods clearly appear, with the generation of fluid jets originating from sharp corners in the lattice structure dominating the flow field for the non-regularized MRT-LBM. These unphysical fluid jets disappear with the regularization technique, thus demonstrating its necessity for LBMs with small velocity sets.

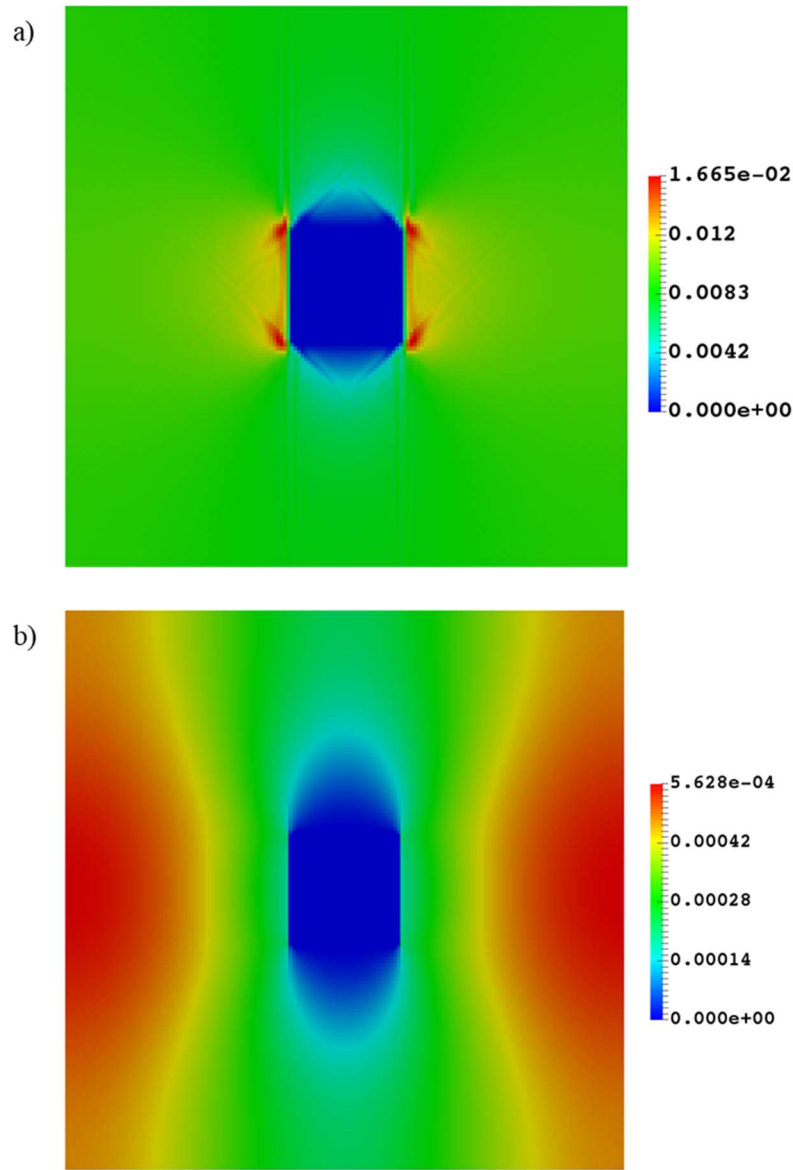


Figure 5.5 Norm of the y-component of the velocity for the flow around a square-section cylinder obtained with (a) the non-regularized MRT-LBM and (b) the regularized MRT-LBM.

5.4.2 Error analysis of a slit flow in the slip regime

The accuracy of the new DBB BC with the regularized MRT-LBM was first verified using a convergence analysis of a slit flow in the slip regime. The new DBB BC was applied on the x -boundaries, while periodic BCs were applied on the y -boundaries for the D2Q9 scheme and the y - and z -boundaries for the D3Q15 scheme. Assuming a constant viscosity, the analytical solution of a slit flow with boundaries located at $x = \pm B$ writes as [194]:

$$v_{y,anal} = \frac{\rho a B^2}{2\mu} \left(1 - \frac{x^2}{B^2} + 4A_1 Kn + 8A_2 Kn^2 \right) \quad (5.42)$$

where B is the half-distance between the two planes, $Kn = \lambda/2B$, and x is the x -direction position, as shown in Figure 5.4b). The relative error was defined by the Euclidian L^2 -norm:

$$E(v) = \frac{\|v_{y,LBM} - v_{y,anal}\|_2}{\|v_{y,anal}\|_2} \quad (5.43)$$

where $v_{y,LBM}$ and $v_{y,anal}$ are, respectively, the numerical and analytical solutions.

To show the inaccuracy of the expressions of r and τ_q developed for the non-regularized MRT-LBM when using the regularized MRT-LBM and how these expressions are lattice-dependent, the regularized MRT-LBM scheme was tested with all the values of r and τ_q shown in Sections 5.3.3 and 5.3.4. The results for the D2Q9 and D3Q15 lattices are shown in Figures 5.6 and 5.7, respectively. One may observe that using Eqs. (5.39) and (5.40), which were developed for the D2Q9 lattice, and Eqs. (5.39) and (5.41), which were developed for the D3Q15 scheme, produce a negligible error (in the order of 10^{-5} - 10^{-7}). However, using the values (Eqs. (5.34) and (5.35)) developed for the non-regularized MRT-LBM with the D2Q9 lattice and interchanging the values of r and τ_q between the D2Q9 and D3Q15 lattices both create a huge error in the slip velocity. This can be explained by the form of the new relationships obtained in Eqs. (5.39) and (5.40) for the D2Q9 scheme and Eqs. (5.39) and (5.41) for the D3Q15 scheme, where τ_q does not approach the same value as $\delta_x \rightarrow 0$ (as $\tilde{\tau}_{sw} \rightarrow \infty$). This result is far from trivial or even intuitive, as numerous researchers have used values determined for the non-regularized D2Q9 MRT-LBM scheme without considering the impact of regularization or the lattice [197, 212, 214, 291, 292,

[364, 420]. The development of the scheme with the relaxation rate s_j related to velocity as a free parameter also created huge error in the slip velocity (not shown here) for reasons explained in Appendices B and C. The condition $s_j = 1$ is thus necessary.

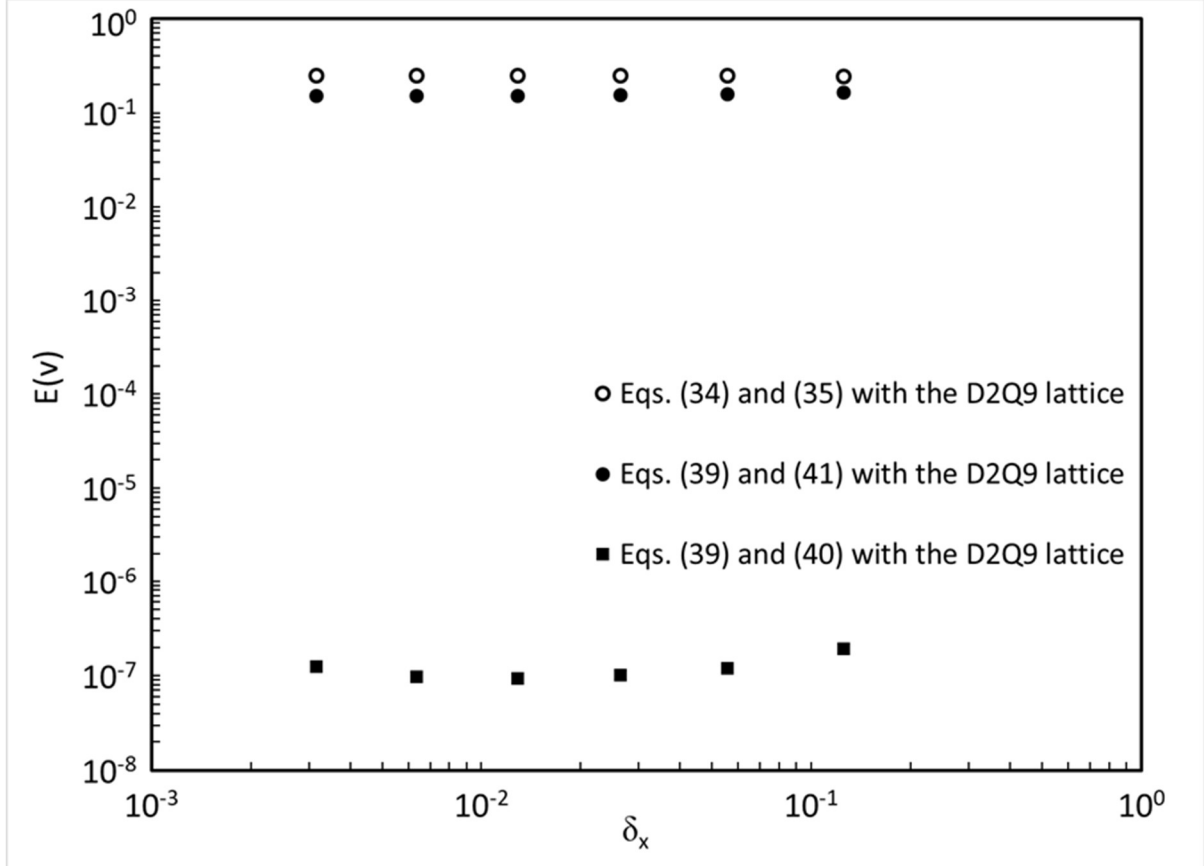


Figure 5.6 L^2 relative error ($E(v)$) of the velocity computed using the regularized MRT-LBM scheme and the D2Q9 lattice with slip and $\Psi(\mathbf{x}) = 1$ at $Kn = 1$ as a function of lattice spacing δ_x for the slit flow test case.

Figures 5.6 and 5.7 also show a very small L^2 error (in the order of 10^{-7} and 10^{-5} for the D2Q9 and D3Q15 lattices, respectively) at $Kn=1$ as a function of lattice resolution. They also show that this error does not diminish with refinement. This rather constant error is caused by the adimensionalization process, where all operations on populations are computed with $\rho = 1$. Because of the low Mach number requirement, the truncation of non-equilibrium population components occurs during the regularization process and the transformation into the moment space. Higher values in the transformation matrix \mathbf{M} along with lower weights for the D3Q15 lattice vs. the D2Q9 lattice explain why the error is higher for the D3Q15 lattice than for the D2Q9 lattice.

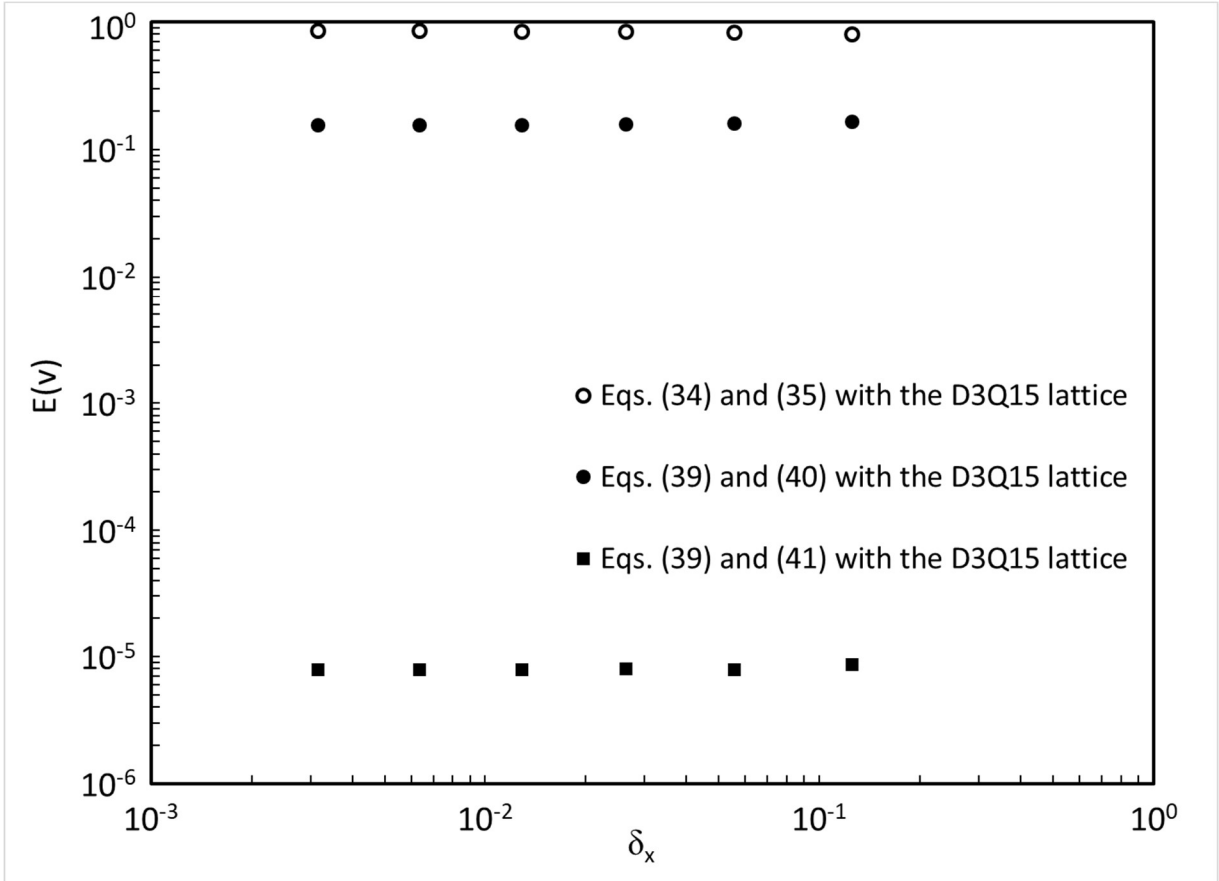


Figure 5.7 L^2 relative error ($E(v)$) of the velocity computed using the regularized MRT-LBM scheme and the D3Q15 lattice with slip and $\Psi(\mathbf{x}) = 1$ at $Kn = 1$ as a function of lattice spacing δ_x for the slit flow test case.

Results from a previous paper (Fig. 8 of Ref. [237]) for a rarefied regime slit flow with non-constant effective viscosity functions were reproduced with a difference only in the 4th digit of the volumetric flow rate. This validated the regularized MRT-LBM scheme in the rarefied regime for planar flows. The graph is not shown in this paper as the results are visually identical.

5.4.3 Slip flow through a cylinder array

The regularized MRT-LBM with the new DBB BC was applied to a slip flow through a cylinder array. The use of periodic BCs can reduce the computational domain to a square (in 2D) or parallelepipedic (in 3D) domain of side L with a cylinder of diameter d at its center (see Figure 5.8). A ratio of $d/L = 0.2$ was chosen for all the simulations and the solid-fluid boundary at the cylinder surface was treated with the new DBB BC.

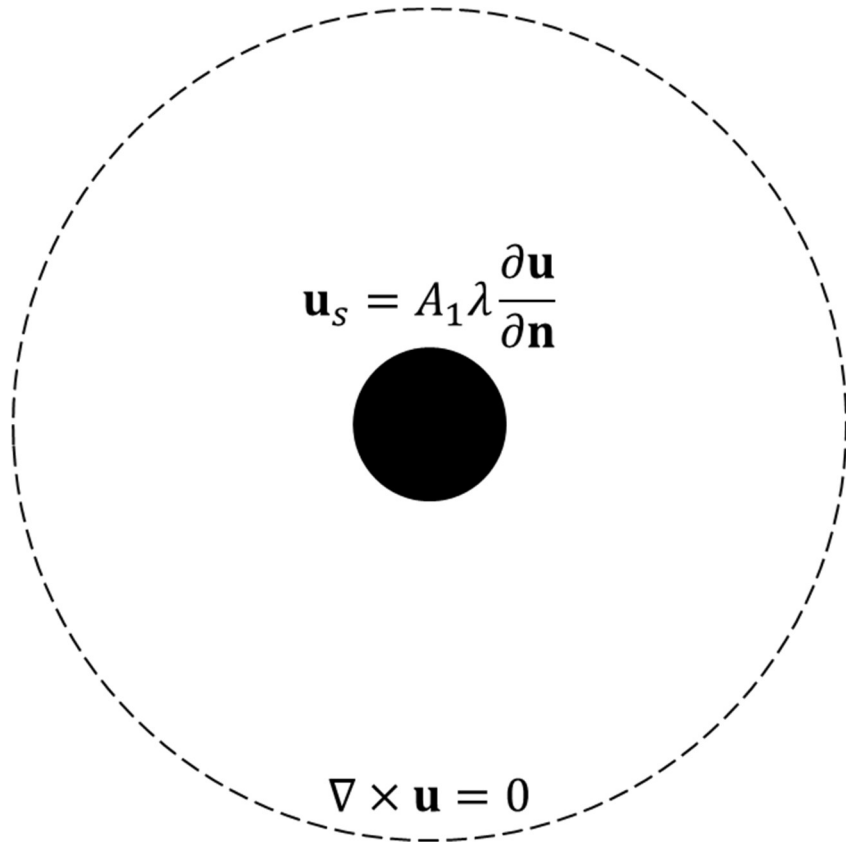


Figure 5.8 Schematic representation of Pich's original analytical hypothesis

Under the assumption of an irrotational laminar flow around a cylindrical closed surface with the same diameter as the domain size, a constant Newtonian viscosity μ , and a first-order Maxwell slip velocity BC \mathbf{u}_s at the solid boundary ($A_1 = 0.998$), Pich [425] developed an analytical solution for the drag force F_D per unit length in the X direction exerted on a cylinder given by:

$$F_D = \frac{4\pi\mu U_f (1 + 2A_1 Kn)}{-\frac{3}{4} - \frac{1}{2}\ln\beta + \beta - \frac{1}{4}\beta^2 + A_1 Kn \left(-\frac{1}{2} - \ln\beta + \frac{1}{2}\beta^2 \right)} \quad (5.44)$$

where β is the solid fraction volume, $Kn = 2\lambda/d$, and U_f is the face velocity far from the cylinder. A schematic representation of this problem with the underlying hypothesis is presented in Figure 5.8.

Pich's solution was derived using the vorticity equation, and the volumetric force term (or an equivalent pressure gradient term) was thus not explicitly stated. To compare the face velocity with the proposed force-driven LBM, a force balance must be carried out. At steady state, based on Newton's second and third laws, the force exerted on the cylinder is equal to the integral of the body force exerted on the fluid domain to displace it. As the body force is constant throughout the fluid domain, the following relationship is derived:

$$F_D = \rho a L^2 (1 - \beta) \quad (5.45)$$

where the solid fraction β is given by:

$$\beta = \frac{\pi d^2}{4L^2} \quad (5.46)$$

Here, $\beta = \pi/100$. The expression for the analytical face velocity as a function of a body force is thus, using Eq. (5.45):

$$U_f = \frac{\rho a (1 - \beta) d^2 \left(-\frac{3}{4} - \frac{1}{2} \ln \beta + \beta - \frac{1}{4} \beta^2 + A_1 Kn \left(-\frac{1}{2} - \ln \beta + \frac{1}{2} \beta^2 \right) \right)}{4 \beta \mu (1 + 2A_1 Kn)} \quad (5.47)$$

Numerical predictions of face velocities at various lattice resolutions are presented in Figures 5.9 and 5.10, for the D2Q9 and D3Q15 lattices, respectively, for a slip flow around a cylinder where $\Psi(\mathbf{x}) = 1$ (without a reduction in effective viscosity) for $0.05 \leq Kn \leq 5$. Most of the points lie clearly in the transition regime, where effective viscosity reduction was not negligible in physical reality. However, the goal of this section is not to find the physical solution to a transition regime flow, but rather to verify the precision of the slip BC imposed through the DBB BC with the new relationships for r and τ_q compared to an analytical hypothetical solution.

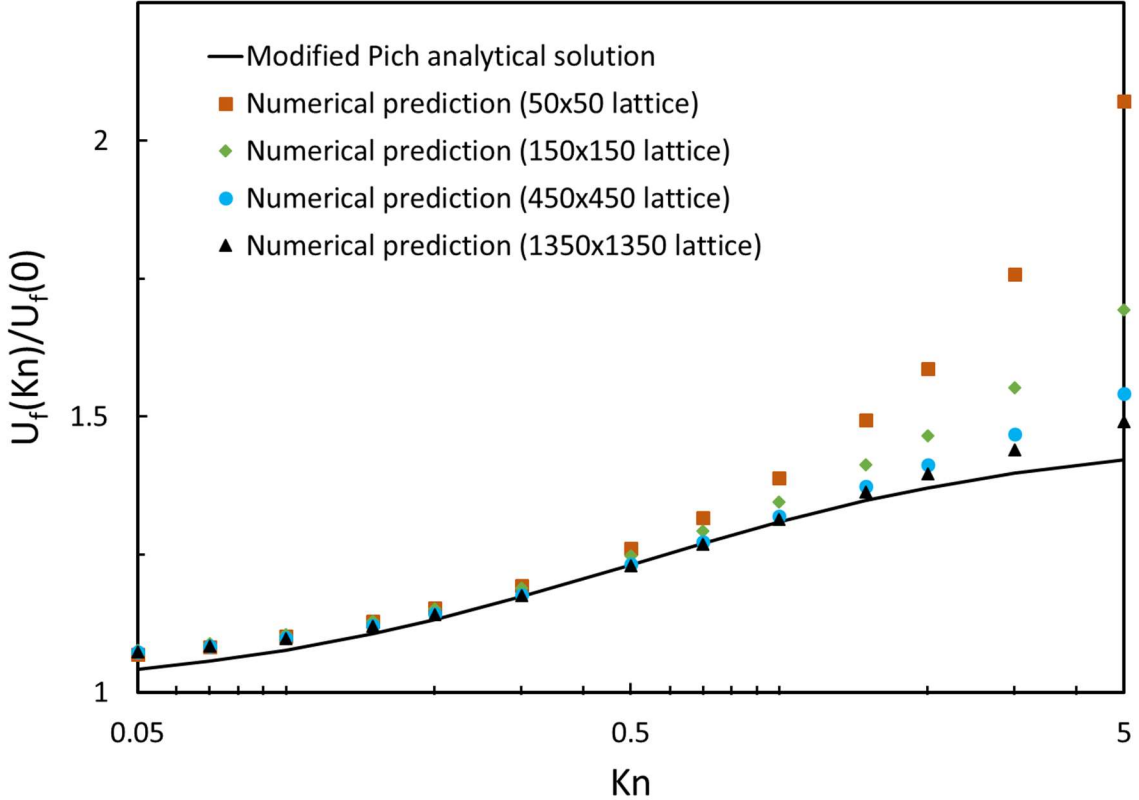


Figure 5.9 Predictions of the normalized face velocity for a slip flow through a cylinder array for the new D2Q9 regularized MRT-LBM scheme at different 2D lattice resolutions compared to the modified Pich analytical solution (Eq. (5.47)).

At $Kn = 0.05$, the results for the coarsest grid (50x50) were indistinguishable from the results for the finest grid (1350x1350) for both the D2Q9 and the D3Q15 lattices. As the Knudsen number increased, the lattice resolution had a greater impact on the result. An order of convergence of ≈ 0.99 was obtained at $Kn = 5$. This first-order convergence is explained in [237] as the result of the convective scaling implied with Eq. (5.24) when the Kn number is fixed. Even for the finest grid, however, there was a small discrepancy between the face velocity predicted by Pich's correlation and the finest grid MRT-LBM simulations. Part of the discrepancy can be explained by differences between the hypothesis of an irrotational flow over a cylindrical envelope for the analytical solution and the force-driven flow.

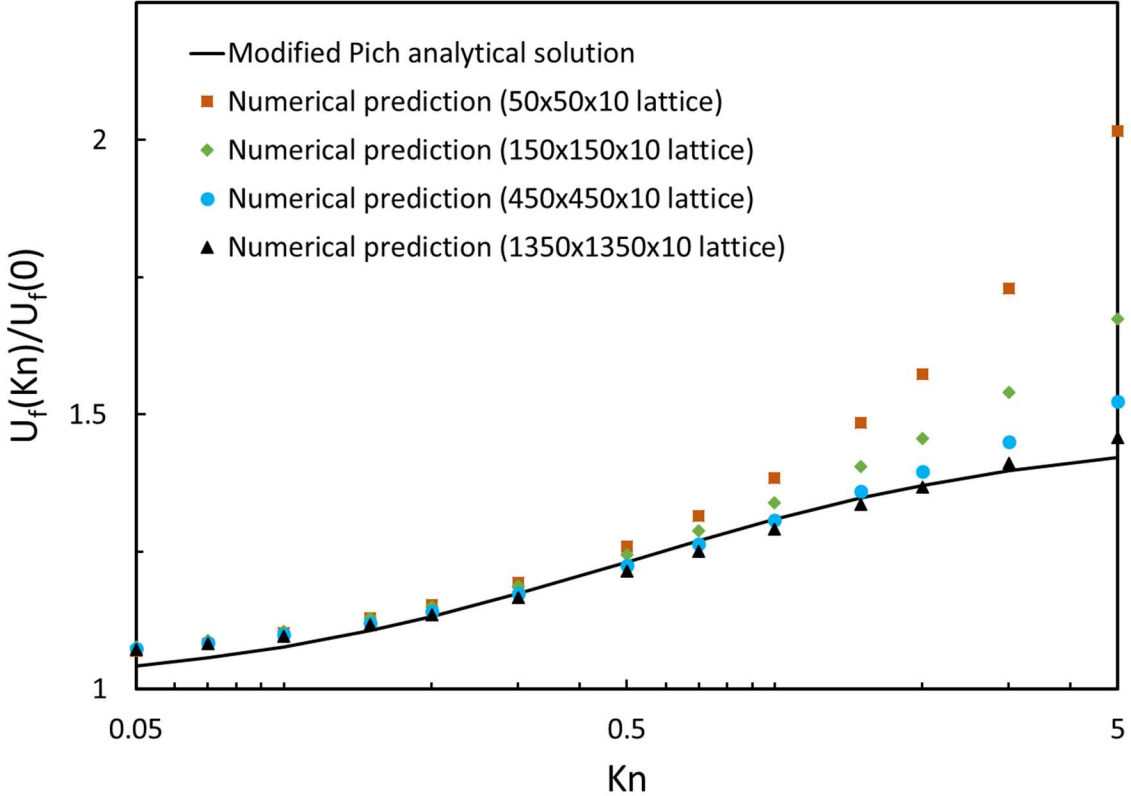


Figure 5.10 Predictions of the normalized face velocity for a flow around a cylinder for the new D3Q15 regularized MRT-LBM scheme at different 3D lattice resolutions compared to the modified Pich analytical solution (Eq. (5.47)) for a slip flow around a cylinder.

Slight differences occurred between the D2Q9 and D3Q15 results at high Knudsen numbers. It has already been observed that the type of solid-fluid boundary topology (planar or stair-case) can have an impact on the value of the energy flux relaxation time τ_q required to recover the correct velocity at the boundary [419]. As the correct value of τ_q depends on the lattice, the slight differences between the D2Q9 and D3Q15 results can be explained by this.

5.4.4 Slip flow around a sphere array

The regularized MRT-LBM with the DBB BC was then applied to a slip flow around a cubic-centered sphere array with diameter d_s within a cubic domain of side L , as illustrated in Figure 5.11. A ratio of $d_s/L = 0.2$ was chosen for all the simulations. Flows around spheres are

intrinsically tridimensional, therefore only the D3Q15 scheme was studied. Periodic BCs were imposed on all x -, y -, and z -boundaries, while the solid-fluid boundary at the sphere was treated with the new DBB BC.

Under the assumption of an irrotational laminar flow around a spherical envelope closed surface with the same diameter as the domain size, a constant Newtonian viscosity μ , and a first-order Maxwell slip BC at the solid boundary ($A_1 = 1$), Datta and Deo [426] developed an analytical solution for the drag force F_D exerted on a sphere:

$$F_D = 4\pi\mu U_f D \quad (5.48)$$

$$D = \frac{15d_s}{2\gamma} \left(2A_1\lambda + \frac{d_s}{2} \right) l^6 \quad (5.49)$$

$$\gamma = 2 \left(3A_1\lambda(5l^6 - 6l^5 + 1) + \frac{d_s}{2}(5l^6 - 9l^5 + 5l^3 - 1) \right) \quad (5.50)$$

where $l = 1/\sqrt[3]{\beta}$ and β is the solid volume fraction expressed as:

$$\beta = \frac{\pi d_s^3}{6L^3} \quad (5.51)$$

In the geometry tested in the numerical simulation, $\beta = \pi/750$.

Datta and Deo's solution was derived using the vorticity equation, and the volumetric force term (or an equivalent pressure gradient term) was thus not explicitly stated. To compare the face velocity with the proposed force-driven LBM, a force balance must be carried out. At steady state, based on Newton's second and third laws, the force exerted on the sphere is equal to the integral of the body force exerted on the fluid domain to displace it. As the body force is constant throughout the fluid domain, the following relationship is derived:

$$F_D = \rho a L^3 (1 - \beta) \quad (5.52)$$

The expression for the analytical face velocity as a function of the body force is thus, using Eq. (5.52):

$$U_f = \frac{\rho a L^3 (1 - \beta)}{4\pi\mu D} \quad (5.53)$$

Face velocities are presented in Figure 5.11 for a slip flow around a cylinder with $\Psi(\mathbf{x}) = 1$ (without a reduction in effective viscosity) for $0.05 \leq Kn \leq 5$, with the Knudsen number defined as $Kn = 2\lambda/d_s$. As in Section 5.4.3, the goal here was to verify the precision of the velocity slip BC and not to find a physical solution to a transition regime flow but rather to verify the precision of the slip BC imposed through the DBB BC with the new relationships for r and τ_q compared to an analytical hypothetical solution. The trend of discrepancies as the Knudsen number increased was similar to that of the cylinder array in Section 5.4.3. One can, however, see that the discrepancy at $Kn = 0.05$ for the spherical array is smaller than for the cylinder array. This could be caused by the higher porosity of the spherical array at a similar diameter to domain size ratio. One can also see that the discrepancy at $Kn = 5$ is higher than for the cylinder array. This effect could be caused by the larger proportion of lattices at the solid-fluid boundary with a stair-case configuration compared to the cylinder array geometry.

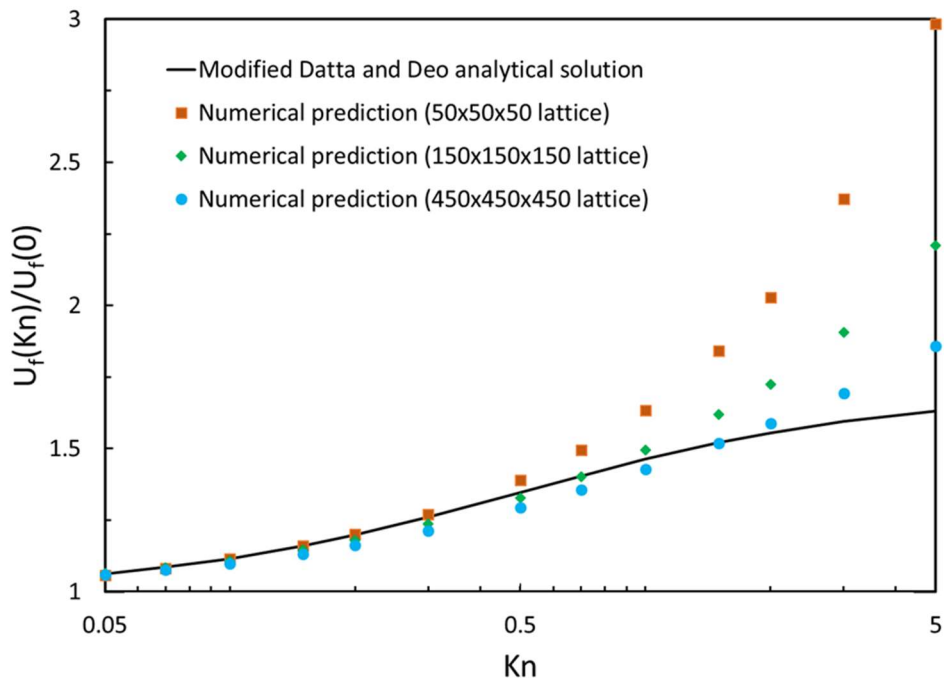


Figure 5.11 Predictions of the normalized face velocity for a flow through a sphere array for the new D3Q15 regularized MRT-LBM scheme compared with the modified Datta and Deo's analytical solution (Eq. (5.53)) for a slip flow around a sphere.

5.5 Further remarks on the new boundary condition

The low-order lattice schemes reviewed in this paper were proposed as alternatives to high-order schemes approximating the Boltzmann equation. Although low-order LBMs exhibit undeniable lower memory and computational costs per lattice and should have better parallelization efficiencies, it must be noted that the results from Figures 5.9-5.11 for high Knudsen numbers show that gains in performance per lattice come at the cost of a finer lattice resolution required to satisfy a given accuracy. However, convergence time is inversely proportional to the Knudsen number because of the expression of the time step in Eq. (5.24). The longest simulation was the 450x450x450 lattice sphere at $Kn = 0.05$, which used ~ 27 GB and took ~ 296 hours on 48 Intel E5-2683 v4 Broadwell processors on the Cedar cluster from Compute Canada.

Alternatives have been proposed in the literature to improve the precision of slip BCs, including the interpolated DBB BC [291, 292, 340] and multi-reflective BCs [421, 423]. The interpolated DBB BC attempted to generalize the half-way DBB BC by admitting an arbitrary distance ratio between the fluid and solid nodes. However, it can be readily seen from one of these reports that, for some distance ratio and Knudsen number values, the bounce-back ratio will have a negative value [340]. The application of the distance ratio is also ambiguous with respect to the energy flux relaxation rate, as bounce-back ratios are defined for each population, while relaxation rates are defined for the whole lattice. Exploratory attempts by the authors to apply the interpolated DBB BC to the regularized MRT-LBM for the D2Q9 lattice have not solved this problem, and its implementation for complex geometries has shown instabilities, especially when bounce-back ratios are negative. Such instabilities in complex geometries have also been reported in [291, 292]. Similar criticisms have been expressed in [421, 423, 427]. Multi-reflective BCs for slip flow were shown to exactly reproduce flows around planar [421] and circular [423] surfaces. However, it requires knowledge of populations located further away from the wall, which makes it difficult to generalize in non-convex geometries such as porous media and to parallelize efficiently. Also, effective viscosity was not taken into consideration in these developments.

It may be possible to diminish the error caused by the solid-fluid boundary topology by using the D3Q27 scheme introduced in [428]. The lattice structure for the D3Q27 scheme creates a smaller high-order moment anisotropy error than for the D3Q15 and the D3Q19 schemes in the continuous regime [429]. In the D2Q9 and D3Q15 schemes—the only high-order moment involved

in the development of the BCs was energy flux—ghost moments of order 5 are present in the D3Q27 lattice as well as in other independent third-order moments. As it is well known [251, 252] that the D3Q27 lattice presents the degeneracy $c_{i\alpha}^5 = c_{i\alpha}^3 = c_{i\alpha}$, these additional moments could, in principle, be tuned to influence the slip velocity for stair-case configurations and improve the imposition of slip flows through the DBB BC.

The regularization technique involves numerical operations on non-equilibrium population components and thus increases computational costs. A summary comparison, using a single processor, a non-regularized MRT-LBM, and the regularized MRT-LBM implemented in this work for the D2Q9 lattice, showed a $\sim 40\%$ increase in computation time for domain sizes from 50x50 to 1350x1350, compared to a $\sim 20\%$ increase from BGK to the MRT-LBM. A discussion about parallel LBM implementations would require not only the analysis of data structure and memory access analysis but knowledge of the workload balance and communication strategy [255, 256]. It is clear, however, that a push algorithm (implemented for this work) would improve the regularized scheme more than a pull algorithm as the regularization operation would only have to be carried out once per population, rather than Q times per lattice node (where Q is the number of populations).

For some of the simulations described in Section 5.4 with the new regularized MRT-LBM DBB BC, the energy flux relaxation rate was negative. This can be easily seen by inspecting Eqs. (5.40) and (5.41), by recalling that A_1 , A_2 , and $\tilde{\tau}_{sw}$ are all positive values with $A_1 \sim O(1)$ and $A_2 \sim O(1)$, and by noting that A_1 and A_2 have $\tilde{\tau}_{s0}$ polynomial coefficients of a different order and different sign. A negative relaxation rate for any property of the system signifies that, as the system evolves, the property gets further away from equilibrium. *A priori*, this contradicts the second law of thermodynamics. Despite this, the simulations showed no convergence problems. As non-equilibrium moments of order higher than 2 were filtered before every collision step, the energy flux was set to its equilibrium value. The energy flux was then tuned only to set the slip velocity at the boundary, not to solve an energy balance. In other words, the scheme proposed in this paper cannot be expected to respect the second law of thermodynamics as it was not intended to solve the first law of thermodynamics in the first place.

It was assumed, as a hypothesis, that the energy flux relaxation rate s_q was constant throughout the domain. Given that the coefficient in front of s_q is the same in Eqs. (5.96)-(5.103),

it can be seen that s_q appears only in Eq. (5.86) and not in Eqs. (5.82), (5.84), and (5.85). This is of capital importance for complex geometry flow simulations where the mean free path may vary throughout the domain. Eqs. (5.40) and (5.41) for τ_q , in the case of the D2Q9 and D3Q15 lattices, respectively, all require knowledge of the viscosity relaxation rate at the wall, $\tilde{\tau}_{s0}$. To compute τ_q for a fluid node, it would be necessary to know which part of the solid wall should be considered to find $\tilde{\tau}_{s0}$. Fortunately, following a careful inspection of the regularized MRT-LBM scheme, the value of the energy flux relaxation rate s_q is relevant only on boundary nodes and can thus be computed locally according to the derivative of the relaxation time, $\tilde{\tau}'_{sw}$.

5.6 Conclusions

In this paper, the impact of the regularization procedure on the accurate imposition of slip BCs with the MRT-LBM scheme for rarefied gas flows was analyzed. It was found that by removing higher-order non-equilibrium components of populations, the regularization procedure changed the relationships between post-collision moments and populations when higher-order non-equilibrium components of populations were removed. New relationships were thus derived for the kinetic ratio r and the relaxation rate related to energy flux τ_q for the regularized MRT-LBM, in the case of the D2Q9 and D3Q15 schemes.

To the authors' knowledge, this is the first time that results for the regularized MRT-LBM have been compared to analytical results for non-planar slip flows in the rarefied regime. From the test cases simulated for flows around a square cylinder, through a slit, and around cylinder and sphere arrays, the following conclusions can be drawn:

1. Previously derived relationships for r and τ_q for the non-regularized MRT-LBM scheme are inadequate for the regularized MRT-LBM scheme.
2. Relationships for r and τ_q are lattice dependent.
3. For the regularization technique, the condition for the momentum relaxation rate $s_j = 1$ must be respected.
4. For a given grid size, the error increases with the Knudsen number.
5. For a given Knudsen number, a first-order convergence approximation of the solution with respect to lattice size is found for high Knudsen flows ($Kn \sim O(1)$).

These conclusions can explain the discrepancies between the high-order Boltzmann equation solvers, experimental data, and regularized MRT-LBM used in other work [198, 202, 210]. In this paper, the magnitude of the discrepancy was decreased by more than one order of magnitude. It is

unlikely that this error can be eliminated. However, the method we propose is simple, robust, and accurate enough to be suitable for engineering calculations of rarefied flows through complex porous media in the slip and transition regimes.

In this paper, the DBB BC for slip flows has been used for relatively simple non-planar geometries, but it has the intrinsic capability to be used with more complex geometries such as porous media. The only remaining obstacle for the use of the proposed method for the simulation of slip flows in complex geometries is the addition of an effective viscosity function for which a local Knudsen number must be determined at each lattice node. Although analytical solutions for the local mean free path have been proposed in the literature for simplified geometries, these analytical solutions cannot be generally used for complex porous media. The computation of local effective viscosity functions in complex porous media can be carried out through a numerical integration procedure using a ray-tracing technique. This problem will be tackled in a separate paper.

Acknowledgements

Financial support from the Simulation-based Engineering Science (Génie Par la Simulation) program funded through the CREATE program from the Natural Sciences and Engineering Research Council of Canada is gratefully acknowledged. The authors would also like to thank Bruno Blais for fruitful discussions and comments on the manuscript.

Appendix A – The D3Q15 lattice

For the D3Q15 lattice, the velocity set (presented in Figure 5.3) is given as [430]:

$$\begin{aligned}
 c_0 &= (0,0,0)c \\
 c_1 = -c_2 &= (1,0,0)c \\
 c_3 = -c_4 &= (0,1,0)c \\
 c_5 = -c_6 &= (0,0,1)c \\
 c_7 = -c_{14} &= (1,1,1)c \\
 c_8 = -c_{13} &= (-1,1,1)c \\
 c_9 = -c_{12} &= (1,-1,1)c \\
 c_{10} = -c_{11} &= (-1,-1,1)c
 \end{aligned} \tag{5.54}$$

The weights associated with each population are:

$$\begin{aligned}
w_0 &= 2/9 \\
w_{1-6} &= 1/9 \\
w_{7-14} &= 1/72
\end{aligned} \tag{5.55}$$

The moment set associated with the D3Q15 lattice is:

$$m_k = \mathbf{M}f_i = (\rho, e, \epsilon, j_x, q_x, j_y, q_y, j_z, q_z, 3p_{xx}, p_{ww}, p_{xy}, p_{yz}, p_{zx}, t_{xyz})^T \tag{5.56}$$

where m_0 is the density, $m_1 = e$ is the energy, $m_2 = \epsilon$ is the energy squared, $(m_3, m_5, m_7) = (j_x, j_y, j_z)$ are the components of the momentum, $(m_4, m_6, m_8) = (q_x, q_y, q_z)$ are the components of the energy flux, $(m_9, m_{10}) = (3p_{xx}, p_{ww})$ is the normal stress tensor, $(m_{11}, m_{12}, m_{13}) = (p_{xy}, p_{yz}, p_{zx})$ is the viscous stress tensor, and $m_{14} = t_{xyz}$ is an antisymmetric third-order moment.

Moment space equilibria for the D3Q15 scheme are:

$$\begin{aligned}
m_k^{(eq)} = \mathbf{M}f_i = \rho &\left(1, u^2 - 1, -1, u_x, -\frac{7}{3}u_x, u_y, -\frac{7}{3}u_y, u_z, -\frac{7}{3}u_z, -3u_x^2 \right. \\
&\quad \left. - u^2, u_y^2 - u_z^2, u_x u_y, u_y u_z, u_z u_x, 0 \right)^T
\end{aligned} \tag{5.57}$$

The corresponding transformation matrix \mathbf{M} is:

$$\left(\begin{array}{cccccccccccccccc}
1 & 1 & 1 & 1 & 1 & 1 & 1 & 1 & 1 & 1 & 1 & 1 & 1 & 1 & 1 & 1 & 1 \\
-2 & -1 & -1 & -1 & -1 & -1 & -1 & 1 & 1 & 1 & 1 & 1 & 1 & 1 & 1 & 1 & 1 \\
16 & -4 & -4 & -4 & -4 & -4 & -4 & 1 & 1 & 1 & 1 & 1 & 1 & 1 & 1 & 1 & 1 \\
0 & 1 & -1 & 0 & 0 & 0 & 0 & 1 & -1 & 1 & -1 & 1 & -1 & 1 & 1 & -1 & 1 \\
0 & -4 & 4 & 0 & 0 & 0 & 0 & 1 & -1 & 1 & -1 & 1 & -1 & 1 & -1 & 1 & -1 \\
0 & 0 & 0 & 1 & -1 & 0 & 0 & 1 & 1 & -1 & -1 & 1 & 1 & 1 & -1 & -1 & 1 \\
0 & 0 & 0 & -4 & 4 & 0 & 0 & 1 & 1 & -1 & -1 & 1 & 1 & -1 & -1 & -1 & -1 \\
0 & 0 & 0 & 0 & 0 & 1 & -1 & 1 & 1 & 1 & 1 & -1 & -1 & -1 & -1 & -1 & -1 \\
0 & 0 & 0 & 0 & 0 & -4 & 4 & 1 & 1 & 1 & 1 & -1 & -1 & -1 & -1 & -1 & -1 \\
0 & 2 & 2 & -1 & -1 & -1 & -1 & 0 & 0 & 0 & 0 & 0 & 0 & 0 & 0 & 0 & 0 \\
0 & 0 & 0 & 1 & 1 & -1 & -1 & 0 & 0 & 0 & 0 & 0 & 0 & 0 & 0 & 0 & 0 \\
0 & 0 & 0 & 0 & 0 & 0 & 0 & 1 & -1 & -1 & 1 & 1 & -1 & -1 & 1 & 1 & 1 \\
0 & 0 & 0 & 0 & 0 & 0 & 0 & 1 & 1 & -1 & -1 & -1 & -1 & 1 & 1 & 1 & 1 \\
0 & 0 & 0 & 0 & 0 & 0 & 0 & 1 & -1 & 1 & -1 & -1 & 1 & -1 & 1 & 1 & 1 \\
0 & 0 & 0 & 0 & 0 & 0 & 1 & -1 & 1 & 1 & -1 & 1 & 1 & -1 & 1 & 1 & 1
\end{array} \right) \tag{5.58}$$

while the relaxation rate diagonal matrix are:

$$\mathbf{S} = \text{diag}(s_\rho, s_e, s_\epsilon, s_j, s_q, s_j, s_q, s_j, s_q, s_s, s_s, s_s, s_s, s_t) \tag{5.59}$$

Each relaxation rate corresponds to the element of the moment set described in Eq. (5.56).

Appendix B – Details of the development of the diffusive bounce back boundary condition for the D2Q9 lattice

Application of the force-driven, steady-state, incompressible laminar flow in the x -direction through a planar geometry hypothesis yield:

$$\frac{\partial \phi}{\partial t} = \frac{\partial \phi}{\partial x} = 0, d\rho = 0, u_y = 0, u_x = u, a_y = 0, a_x = a \quad (5.60)$$

where ϕ is an arbitrary flow variable and $a = \mathbf{F}/\rho$.

The following plan is adopted to develop the relationships for the D2Q9 scheme:

- a. Simplification and development of pre-collision and post-collision moments
- b. Development of population and moment relationships
- c. Assembly of the regularized LBM-MRT equation
- d. Expression of the stress tensor as function of force and velocity terms for boundary and fluid nodes
- e. Relationship between the boundary and fluid node velocities
- f. Taylor expansions of velocities and viscosity relaxation times around the wall
- g. Combination of relationships and final result.

a. Simplification and development of pre-collision and post-collision moments

With the assumptions defined in Eq. (5.60), some of the moments defined in Eq. (5.17) and their equilibrium components detailed in Eq. (5.18) can be neglected. Density ρ is constant, and as $u_y = 0$ for an incompressible planar laminar flow, moments j_y and q_y never deviate from equilibrium. Moments e , ϵ and p_{xx} deviate from equilibrium as a second-order function of velocity. However, those deviations are neglected here as only a planar incompressible flow in the laminar regime is considered. Only moments j_x , q_x and p_{xy} remain of interest. Their equilibrium components $m_k^{(eq)}$ are thus:

$$j_x^{(eq)} = \rho u_x = \rho u \quad (5.61)$$

$$q_x^{(eq)} = -\rho u_x = -\rho u \quad (5.62)$$

$$p_{xy}^{(eq)} = \rho u_x u_y = 0 \quad (5.63)$$

For Eq. (5.63) it is recalled that $u_y = 0$. However, even for an arbitrary geometry flow, the laminar incompressible flow hypothesis would make this term negligible. Applying the regularization procedure detailed in Eq. (5.27) and transforming non-equilibrium population components defined in Eq. (5.26) to their moments, regularized non-equilibrium components of the moments noted $m_k^{(neqr)}$ are thus:

$$j_x^{(neqr)} = 0 \quad (5.64)$$

$$q_x^{(neqr)} = 0 \quad (5.65)$$

$$p_{xy}^{(neqr)} = f_5^{(neq)} - f_6^{(neq)} + f_7^{(neq)} - f_8^{(neq)} \quad (5.66)$$

Each population of Eq. (5.66) can be decomposed with the definition in Eq. (5.26):

$$p_{xy}^{(neqr)} = (f_5 - f_6 + f_7 - f_8) - (f_5^{(eq)} - f_6^{(eq)} + f_7^{(eq)} - f_8^{(eq)}) \quad (5.67)$$

From the moments' definitions:

$$f_5 - f_6 + f_7 - f_8 = p_{xy} \quad (5.68)$$

$$f_5^{(eq)} - f_6^{(eq)} + f_7^{(eq)} - f_8^{(eq)} = p_{xy}^{(eq)} = 0 \quad (5.69)$$

The final result in Eq. (5.69) is obtained with Eq. (5.63). Therefore Eq. (5.67) becomes:

$$p_{xy}^{(neqr)} = p_{xy} \quad (5.70)$$

By a similar reasoning:

$$p_{xy}^{(neq)} = p_{xy} \quad (5.71)$$

Multiplying each side of Eq. (5.13) by \mathbf{M} and neglecting second-order velocity terms in Eq. (5.14) with the laminar flow hypothesis, the following force terms are recovered:

$$\hat{F}_{j_x} = \rho a \left(1 - \frac{s_j}{2} \right) \quad (5.72)$$

$$\hat{F}_{q_x} = -\rho a \left(1 - \frac{s_q}{2} \right) \quad (5.73)$$

$$\hat{F}_{p_{xy}} = (u_x \rho a_y + u_y \rho a_x) \left(1 - \frac{s_s}{2} \right) = 0 \quad (5.74)$$

where $\hat{F}_k = \mathbf{M} F_i$. Eq. (5.74) is developed with the hypothesis that $u_y = 0$ and $a_y = 0$. However, even for an arbitrary geometry flow, as the force term is proportional to velocity with the laminar incompressible flow hypothesis, this term remains negligible.

Some differences can be seen between moment non-equilibrium components developed in this section and those from Guo et al.'s development [236]. First, it should be noted that in Eq. (5.65), the non-equilibrium component of the heat flux $q_x^{(neqr)}$ is now 0. This is an intended consequence of regularization. Secondly, the energy flux relaxation rate is now only present in the force term in Eq. (5.73). The regularization technique is not used on the force term and the energy flux relaxation rate is kept as a tunable parameter. After populations are propagated, the regularization technique will be applied at the beginning of the new time step, which will filter out the non-equilibrium component of heat flux imposed by the force term. However, before the beginning of the new time step, as the local momentum is conserved through the regularization process, the correct slip velocity will be imposed.

b. Development of population and moment relationships

First, relationships valid both for the boundary node and the neighboring fluid node will be developed. The following relationships between pre-collision populations and moments are found by subtracting populations found after multiplying each side of Eq. (5.17) by \mathbf{M}^{-1} :

$$f_1 - f_3 = \frac{1}{3} j_x - \frac{1}{3} q_x \quad (5.75)$$

$$f_5 - f_6 = \frac{1}{3} j_x + \frac{1}{6} q_x + \frac{1}{2} p_{xy} \quad (5.76)$$

$$f_8 - f_7 = \frac{1}{3}j_x + \frac{1}{6}q_x - \frac{1}{2}p_{xy} \quad (5.77)$$

Similar relationships hold true for post-collision populations and moments:

$$\tilde{f}_1 - \tilde{f}_3 = \frac{1}{3}\tilde{j}_x - \frac{1}{3}\tilde{q}_x \quad (5.78)$$

$$\tilde{f}_5 - \tilde{f}_6 = \frac{1}{3}\tilde{j}_x + \frac{1}{6}\tilde{q}_x + \frac{1}{2}\tilde{p}_{xy} \quad (5.79)$$

$$\tilde{f}_8 - \tilde{f}_7 = \frac{1}{3}\tilde{j}_x + \frac{1}{6}\tilde{q}_x - \frac{1}{2}\tilde{p}_{xy} \quad (5.80)$$

where the tilde \sim represents the post-collision variable. Eq. (5.9) along with Eqs. (5.75)-(5.77) gives:

$$j_x = \rho u - \frac{\rho a \delta_t}{2} \quad (5.81)$$

Now the propagation scheme for the D2Q9 lattice is examined. As $\frac{\partial \phi}{\partial x} = 0$, populations are invariant in the x -direction. Populations 1 and 3 are thus related as follows:

$$f_1 - f_3 = \tilde{f}_1 - \tilde{f}_3 \quad (5.82)$$

Using Eqs. (5.75), (5.78) and (5.82), energy flux and momentum are related this way:

$$q_x = j_x - \tilde{j}_x + \tilde{q}_x \quad (5.83)$$

Similar relationships are derived for populations on the diagonal directions ($i = 5, 6, 7, 8$). However, populations on diagonal directions also have a component in the y -direction, populations from the boundary and fluid nodes are related as follows:

$$f_5^{(2)} - f_6^{(2)} = \tilde{f}_5^{(1)} - \tilde{f}_6^{(1)} \quad (5.84)$$

$$f_8^{(1)} - f_7^{(1)} = \tilde{f}_8^{(2)} - \tilde{f}_7^{(2)} \quad (5.85)$$

where superscript (1) represents the boundary node and (2) represents the neighboring fluid node in the y -direction. The remaining relationship to be determined is between populations interacting with the wall. In the DBB BC scheme, pre-collision populations 5 and 6 come from post-collision populations 7 and 8, respectively. As $u_y = 0$ and $F_y = 0$, by Eq. (5.9) $f_2 - f_4 + f_5 + f_6 - f_7 - f_8 = 0$. Furthermore, remarking that $f_7^{(eq)}(\rho_w, \mathbf{0}) = f_8^{(eq)}(\rho_w, \mathbf{0})$, that $f_2 = f_4 = f_2^{(eq)}(\rho_w, \mathbf{0}) = f_4^{(eq)}(\rho_w, \mathbf{0})$ and that $\bar{F}_5 = \bar{F}_8$ and $\bar{F}_6 = \bar{F}_7$, it can be concluded that K defined in Eq. (5.32) is equal to 1 and the following relationship is thus derived:

$$f_5^{(1)} - f_6^{(1)} = -\left(\tilde{f}_8^{(1)} - \tilde{f}_7^{(1)}\right) \quad (5.86)$$

c. Assembly of the regularized MRT-LBM equation

The regularized MRT-LBM defined in Eq. (5.37) is used to find relationships between the post-collision and pre-collision populations for each of the two nodes.

For the boundary node (1), populations 4, 7 and 8 enter into collision with the solid wall. Multiplying each side of Eq. (5.37) by \mathbf{M} , using Eqs. (5.61)-(5.65), (5.70) and (5.72)-(5.77), recalling $\mathbf{u}_w = 0$, and after tedious algebraical manipulations, the post-collision moments are related to pre-collision moments the following way for the boundary node:

$$\tilde{j}_x^{(1)} = \rho u^{(1)} - \left(\frac{1-r}{6}\right) \rho u^{(1)} + \left(\frac{(1-r)(1-s_s^{(1)})}{2}\right) p_{xy}^{(1)} + \rho a \delta_t \left(1 - \frac{s_j}{2}\right) \quad (5.87)$$

$$\tilde{q}_x^{(1)} = -\rho u^{(1)} - \left(\frac{1-r}{6}\right) \rho u^{(1)} + \left(\frac{(1-r)(1-s_s^{(1)})}{2}\right) p_{xy}^{(1)} - \rho a \delta_t \left(1 - \frac{s_q}{2}\right) \quad (5.88)$$

$$\tilde{p}_{xy}^{(1)} = \frac{(1-r)}{6} \rho u^{(1)} + \left(\frac{(1+r)(1-s_s^{(1)})}{2}\right) p_{xy}^{(1)} \quad (5.89)$$

Using Eqs. (5.81), (5.83), (5.87) and (5.88), the energy flux at the boundary node is found:

$$q_x^{(1)} = -\rho u^{(1)} - \rho a \delta_t \left(2 - \frac{s_q}{2} \right) \quad (5.90)$$

For the fluid node (2), Eq. (5.38) makes $r_i = 1$ for all i . By multiplying each side of Eq. (5.37) by \mathbf{M} on each side:

$$\tilde{m}_k = m_k^{(eq)} + (1 - s_k)m_k^{(neqr)} + \hat{F}_k \delta_t \quad (5.91)$$

where $\hat{F}_k = \mathbf{M} F_i$. Post-collision moments are found from Eqs. (5.61)-(5.65), (5.70), (5.72)-(5.74) and (5.78)-(5.80):

$$\tilde{j}_x^{(2)} = \rho u^{(2)} + \rho a \delta_t \left(1 - \frac{s_j}{2} \right) \quad (5.92)$$

$$\tilde{q}_x^{(2)} = -\rho u^{(2)} - \rho a \delta_t \left(1 - \frac{s_q}{2} \right) \quad (5.93)$$

$$\tilde{p}_{xy}^{(2)} = \left(1 - s_s^{(2)} \right) p_{xy}^{(2)} \quad (5.94)$$

When $r = 1$, expressions for the post-collision moments from Eqs. (5.87)-(5.89) are equal to those from Eqs. (5.92)-(5.94). Using Eqs. (5.81), (5.83), (5.92) and (5.93), the energy flux for the fluid node is found:

$$q_x^{(2)} = -\rho u^{(2)} - \rho a \delta_t \left(2 - \frac{s_q}{2} \right) \quad (5.95)$$

As Eqs. (5.90) and (5.95) are expressions for a pre-collision moment, their similarity is not surprising.

In Guo et al.'s development, it was reported that the value of s_j had no impact on the flow [236]. The traditional MRT-LBM defined in Eq. (5.11) have been used and while all s_j terms have been kept through the development, they cancelled out each other afterwards. It can be seen from Eqs. (5.64), (5.70), (5.71) of the present paper and from Eq. (38a) from [236] that the momentum $j_x^{(neqr)}$ and the non-diagonal component of the stress tensor $p_{xy}^{(neqr)}$ are unmodified by the regularization technique. However, the post-collision momentum is affected by the momentum

relaxation rate s_j both in Eqs. (5.87) and (5.92) through the force term and s_j must necessarily be equal to 1 to recover the correct coefficient in front of the force term in Eq. (5.9) for the regularized MRT-LBM. To the authors' knowledge, the necessity of setting $s_j = 1$ was unexplained before in the literature.

d. Expression of the stress tensor as function of force and velocity terms for boundary and fluid nodes

The stress tensor non-diagonal component p_{xy} is now expressed in function of the velocity u and the body force ρa . The following relationships between the pre-collision populations and the pre-collision stress tensor non-diagonal component are found after substituting Eqs. (5.90) and (5.95) into Eqs. (5.76) and (5.77):

$$f_5^{(1)} - f_6^{(1)} = \frac{\rho u^{(1)}}{6} + \frac{1}{2} p_{xy}^{(1)} + \rho a \delta_t \left(-\frac{1}{2} + \frac{s_q}{12} \right) \quad (5.96)$$

$$f_8^{(1)} - f_7^{(1)} = \frac{\rho u^{(1)}}{6} - \frac{1}{2} p_{xy}^{(1)} + \rho a \delta_t \left(-\frac{1}{2} + \frac{s_q}{12} \right) \quad (5.97)$$

$$f_5^{(2)} - f_6^{(2)} = \frac{\rho u^{(2)}}{6} + \frac{1}{2} p_{xy}^{(2)} + \rho a \delta_t \left(-\frac{1}{2} + \frac{s_q}{12} \right) \quad (5.98)$$

$$f_8^{(2)} - f_7^{(2)} = \frac{\rho u^{(2)}}{6} - \frac{1}{2} p_{xy}^{(2)} + \rho a \delta_t \left(-\frac{1}{2} + \frac{s_q}{12} \right) \quad (5.99)$$

The following relationships between post-collision populations and the pre-collision stress tensor non-diagonal component are found after substituting Eqs. (5.87)-(5.89) and (5.92)-(5.94) into Eqs. (5.79) and (5.80):

$$\tilde{f}_5^{(1)} - \tilde{f}_6^{(1)} = \frac{\rho u^{(1)}}{6} + \frac{p_{xy}^{(1)}(1 - s_s^{(1)})}{2} + \rho a \delta_t \frac{s_q}{12} \quad (5.100)$$

$$\tilde{f}_8^{(1)} - \tilde{f}_7^{(1)} = r \left(\frac{\rho u^{(1)}}{6} + \frac{p_{xy}^{(1)}(1 - s_s^{(1)})}{2} \right) + \rho a \delta_t \frac{s_q}{12} \quad (5.101)$$

$$\tilde{f}_5^{(2)} - \tilde{f}_6^{(2)} = \frac{\rho u^{(2)}}{6} + \frac{p_{xy}^{(2)}(1 - s_s^{(2)})}{2} + \rho a \delta_t \frac{s_q}{12} \quad (5.102)$$

$$\tilde{f}_8^{(2)} - \tilde{f}_7^{(2)} = \frac{\rho u^{(2)}}{6} - \frac{p_{xy}^{(2)}(1 - s_s^{(2)})}{2} + \rho a \delta_t \frac{s_q}{12} \quad (5.103)$$

Here it is assumed, as did Guo et al. [236], that s_q is constant throughout the domain. Developing Eqs. (5.84) and (5.85), macroscopic velocities and the stress tensor non-diagonal component are now related in this way:

$$\frac{\rho u^{(2)}}{6} + \rho a \delta_t \left(-\frac{1}{2} + \frac{s_q}{12} \right) + \frac{1}{2} p_{xy}^{(2)} = \frac{\rho u^{(1)}}{6} + \rho a \delta_t \frac{s_q}{12} + \frac{p_{xy}^{(1)}(1 - s_s^{(1)})}{2} \quad (5.104)$$

$$\frac{\rho u^{(1)}}{6} + \rho a \delta_t \left(-\frac{1}{2} + \frac{s_q}{12} \right) - \frac{1}{2} p_{xy}^{(1)} = \frac{\rho u^{(2)}}{6} + \rho a \delta_t \frac{s_q}{12} - \frac{p_{xy}^{(2)}(1 - s_s^{(2)})}{2} \quad (5.105)$$

Isolating $p_{xy}^{(2)}$ in Eq. (5.104) and then isolating $p_{xy}^{(1)}$ in Eq. (5.105), the stress tensor non-diagonal components for each node are now expressed as a set of two equations with two unknowns:

$$p_{xy}^{(2)} = \frac{\rho(u^{(1)} - u^{(2)})}{3} + \rho a \delta_t + p_{xy}^{(1)}(1 - s_s^{(1)}) \quad (5.106)$$

$$p_{xy}^{(1)} = \frac{\rho(u^{(1)} - u^{(2)})}{3} - \rho a \delta_t + p_{xy}^{(2)}(1 - s_s^{(2)}) \quad (5.107)$$

Inserting Eq. (5.106) in Eq. (5.107) and then isolating $p_{xy}^{(1)}$:

$$p_{xy}^{(1)} = \rho \frac{\left((u^{(1)} - u^{(2)}) \left(2 - s_s^{(1)} \right) - 3a \delta_t s_s^{(2)} \right)}{3(s_s^{(1)} + s_s^{(2)} - s_s^{(1)} s_s^{(2)})} \quad (5.108)$$

e. Relationship between the boundary and fluid node velocities

Finding a relationship between the boundary and the fluid node velocities implies a direct relationship between $u^{(1)}$ and $u^{(2)}$, which may take the form:

$$u^{(2)} = Au^{(1)} + Ba\delta_t \quad (5.109)$$

such that A and B are expressed only as functions of MRT-LBM kinetic variables.

Inserting Eq. (5.96) in the left-hand side of Eq. (5.86) and inserting Eq. (5.101) in the right-hand side of Eq. (5.86) and using Eq. (5.108), expressions for A and B are found:

$$A = -\frac{\left(2 - 2r + s_s^{(1)} + 3rs_s^{(1)} + 2rs_s^{(2)} - s_s^{(1)}s_s^{(2)} - 2rs_s^{(1)}s_s^{(2)}\right)}{\left(\left(s_s^{(2)} - 2\right)\left(rs_s^{(1)} - r + 1\right)\right)} \quad (5.110)$$

$$B = \left(\frac{3s_s^{(1)} + 6s_s^{(2)} - 3rs_s^{(2)} - s_q s_s^{(1)} - s_q s_s^{(2)}}{\left(\left(s_s^{(2)} - 2\right)\left(rs_s^{(1)} - r + 1\right)\right)} + \frac{-3s_s^{(1)}s_s^{(2)} + 3rs_s^{(1)}s_s^{(2)} + s_q s_s^{(1)}s_s^{(2)}}{\left(\left(s_s^{(2)} - 2\right)\left(rs_s^{(1)} - r + 1\right)\right)} \right) \quad (5.111)$$

As the relation between the effective mean free path λ_e and the relaxation rate $\left(\tau_s - \frac{1}{2}\right)$ is linear, it is easier to treat Eqs. (5.110) and (5.111) by shifting $\tau_s = \tilde{\tau}_s + 1/2$ and by substituting $s_s = 1/\left(\tilde{\tau}_s + \frac{1}{2}\right)$ and $s_q = 1/\tau_q$:

$$A = \frac{\tilde{\tau}_s^{(1)} + 2\tilde{\tau}_s^{(2)} + r\tilde{\tau}_s^{(1)} + 2r\tilde{\tau}_s^{(2)} + 2\tilde{\tau}_s^{(1)}\tilde{\tau}_s^{(2)} - 2r\tilde{\tau}_s^{(1)}\tilde{\tau}_s^{(2)}}{\tilde{\tau}_s^{(2)}\left(r + 2\tilde{\tau}_s^{(1)} - 2r\tilde{\tau}_s^{(1)} + 1\right)} \quad (5.12)$$

$$B = -\frac{\left(3\tau_q - 2\tilde{\tau}_s^{(1)} - 2\tilde{\tau}_s^{(2)} + 3r\tau_q + 12\tau_q\tilde{\tau}_s^{(1)} + 6\tau_q\tilde{\tau}_s^{(2)} - 6r\tau_q\tilde{\tau}_s^{(1)}\right)}{\left(2\tau_q\tilde{\tau}_s^{(2)}\left(r + 2\tilde{\tau}_s^{(1)} - 2r\tilde{\tau}_s^{(1)} + 1\right)\right)} \quad (5.13)$$

While developing this relationship in this article, it was found that Eq. (45) in Guo et al.'s article [236] featured as well $\tilde{\tau}_q = \tau_q - 1/2$ as a shifted relaxation time. However, said Eq. (45) is valid only if the shifted relaxation time is replaced by the original non-shifted relaxation time. The rest of development from the original article is valid. Furthermore, it should be remarked that despite all the variations caused by the regularization technique and the passage from the CBBSR to the

DBB BC, Eq. (5.112) from this article is exactly the same as the corresponding formula from Guo et al.'s article [236].

f. Taylor expansions of velocities and viscosity relaxation times around the wall

This section aims at finding a direct relationship between effective viscosity, effective viscosity relaxation times and derivatives of the velocity. This development is exactly the same as the one proposed by Guo et al.'s article [236] and will be the same for the D3Q15 lattice development. To avoid confusion, the subscript 0 will be used from now on to describe a property of the gas at the wall. By definition, the slip velocity u_s is the velocity of the gas u_0 at the wall relative to the wall velocity. Using the relationship between the mean free path and the shifted shear viscosity relaxation time of Eq. (5.24), the mean free path is rewritten as:

$$\lambda_e = \chi \tilde{\tau}_s \delta_x \quad (5.114)$$

where $\chi = \sqrt{\pi/6}$. Inserting Eq. (5.114) in the BC presented in Eq. (5.6):

$$u_0 = L_1 \delta_x u'_w - L_2 \delta_x^2 u''_w \quad (5.115)$$

where u'_w and u''_w are respectively the first and second derivatives of the slip velocity at the wall and:

$$L_1 = (A_1 - A_2 \chi \tilde{\tau}_{sw} \delta_x) \chi \tilde{\tau}_{sw} \quad (5.116)$$

$$L_2 = A_2 \chi^2 \tilde{\tau}_{sw}^2 \quad (5.117)$$

A relationship between the velocity of the gas at the wall u_0 and A and B developed in Appendix Be will now be found. Recalling that a half-way bounce-back BC is used in this article, the velocities $u^{(1)}$ and $u^{(2)}$ for each lattice will be developed as a Taylor series expansion around u_s and truncated at the second-order:

$$u^{(1)} \approx u_w + \frac{\delta_x}{2} u'_w + \frac{\delta_x^2}{8} u''_w \quad (5.118)$$

$$u^{(2)} \approx u_w + \frac{3\delta_x}{2} u'_w + \frac{9\delta_x^2}{8} u''_w \quad (5.119)$$

Inserting Eq. (5.118) and Eq. (5.119) in Eq. (5.109) and using Eqs. (5.36) and (5.118), the following relationships are found between L_1 , L_2 , A and B :

$$L_1 = \frac{3A - 9 - 2B\tilde{\tau}'_{sw}\delta_x}{6(1 - A)} \quad (5.120)$$

$$L_2 = \frac{27 - 3A + 8B\tilde{\tau}_{sw}}{24(1 - A)} \quad (5.121)$$

Local effective viscosity relaxation rates $\tilde{\tau}_s^{(1)}$ and $\tilde{\tau}_s^{(2)}$ in Eqs. (5.112) and (5.113) need to be expressed as functions of the shifted effective viscosity relaxation rate at the wall $\tilde{\tau}_{sw}$. Expanding the relaxation times around the wall for each lattice and truncating the Taylor series at the first-order:

$$\tilde{\tau}_s^{(1)} \approx \tilde{\tau}_{sw} + \frac{\delta_x}{2}\tilde{\tau}'_{sw} \quad (5.122)$$

$$\tilde{\tau}_s^{(2)} \approx \tilde{\tau}_{sw} + \frac{3\delta_x}{2}\tilde{\tau}'_{sw} \quad (5.123)$$

g. Combination of relationships and final result

Combining Eqs. (5.112), (5.113), (5.116), (5.117) and (5.120)-(5.123), after some tedious algebra and neglecting all remaining terms in δ_x^2 and of higher order, Eqs. (5.39) and (5.40) for r and τ_q are finally obtained for the D2Q9 scheme.

Appendix C – Details of the development of the diffusive bounce-back boundary condition for the D3Q15 lattice

Application of the force driven, steady-state, incompressible laminar flow in the x -direction through a planar geometry hypothesis yield:

$$\frac{\partial\phi}{\partial t} = \frac{\partial\phi}{\partial x} = \frac{\partial\phi}{\partial y} = 0, d\rho = 0, u_y = u_z = 0, u_x = u, a_y = a_z = 0, a_x = a \quad (5.124)$$

where ϕ is an arbitrary flow variable and $a = \mathbf{F}/\rho$.

The following plan is adopted to develop the relationships for the D3Q15 scheme:

- a. Simplification and development of pre-collision and post-collision moments
- b. Development of population and moment relationships
- c. Assembly of the regularized LBM-MRT equation
- d. Expression of the stress tensor as function of force and velocity terms for boundary and fluid nodes
- e. Relationship between the boundary and fluid node velocities
- f. Taylor expansions of velocities and viscosity relaxation times around the wall
- g. Combination of relationships and final result.

a. Application of the problem hypothesis to pre-collision and post-collision moments

With the assumptions defined in Eq. (5.124), some of the moments defined in Eq. (5.56) and their equilibrium components detailed in Eq. (5.57) can be neglected. Density ρ is constant, and as $u_y = u_z = 0$ for an incompressible planar laminar flow, moments j_y , j_z , q_y and q_z never deviate from equilibrium. Moments e , ϵ and p_{xx} , p_{ww} deviate from equilibrium as a second-order function of velocity. However, those deviations are neglected here as only a planar incompressible flow in the laminar regime is considered. Finally, as $u_y = u_z = 0$, stress tensor non-diagonal components are $p_{xy} = p_{yz} = 0$ and their equilibrium counterparts are $p_{xy}^{(eq)} = p_{yz}^{(eq)} = 0$. Only moments j_x , q_x and p_{zx} remain of interest. Their equilibrium components $m_k^{(eq)}$ are thus:

$$j_x^{(eq)} = \rho u_x = \rho u \quad (5.125)$$

$$q_x^{(eq)} = -\frac{7}{3} \rho u_x = -\frac{7}{3} \rho u \quad (5.126)$$

$$p_{zx}^{(eq)} = \rho u_z u_x = 0 \quad (5.127)$$

In Eq. (5.127), it is recalled that $u_z = 0$. However, even for an arbitrary geometry flow, the laminar incompressible flow hypothesis would make this term negligible. Applying the regularization procedure detailed in Eq. (5.27) and transforming non-equilibrium population components defined in Eq. (5.26) to their moments, regularized non-equilibrium components of the moments noted $m_k^{(neqr)}$ are thus:

$$j_x^{(neqr)} = 0 \quad (5.128)$$

$$q_x^{(neqr)} = 0 \quad (5.129)$$

$$\begin{aligned} p_{zx}^{(neqr)} &= f_7^{(neq)} - f_8^{(neq)} + f_9^{(neq)} - f_{10}^{(neq)} - f_{11}^{(neq)} + f_{12}^{(neq)} - f_{13}^{(neq)} \\ &\quad + f_{14}^{(neq)} \end{aligned} \quad (5.130)$$

Each population of Eq. (5.130) can be decomposed with the definition in Eq. (5.26):

$$\begin{aligned} p_{zx}^{(neqr)} &= (f_7 - f_8 + f_9 - f_{10} - f_{11} + f_{12} - f_{13} + f_{14}) \\ &\quad - (f_7^{(eq)} - f_8^{(eq)} + f_9^{(eq)} - f_{10}^{(eq)} - f_{11}^{(eq)} + f_{12}^{(eq)} - f_{13}^{(eq)} + f_{14}^{(eq)}) \end{aligned} \quad (5.131)$$

From the moments' definitions:

$$p_{zx} = f_7 - f_8 + f_9 - f_{10} - f_{11} + f_{12} - f_{13} + f_{14} \quad (5.132)$$

$$p_{zx}^{(eq)} = f_7^{(eq)} - f_8^{(eq)} + f_9^{(eq)} - f_{10}^{(eq)} - f_{11}^{(eq)} + f_{12}^{(eq)} - f_{13}^{(eq)} + f_{14}^{(eq)} = 0 \quad (5.133)$$

The final result in Eq. (5.133) is obtained with Eq. (5.127). Therefore Eq. (5.131) becomes:

$$p_{zx}^{(neqr)} = p_{zx} \quad (5.134)$$

By a similar reasoning:

$$p_{zx}^{(neq)} = p_{zx} \quad (5.135)$$

Multiplying each side of Eq. (5.13) by \mathbf{M} and neglecting second-order velocity terms in Eq. (5.14) with the laminar flow hypothesis, the following force terms are recovered:

$$\hat{F}_{j_x} = \rho a \left(1 - \frac{s_j}{2} \right) \quad (5.136)$$

$$\hat{F}_{q_x} = -\frac{7}{3} \rho a \left(1 - \frac{s_q}{2} \right) \quad (5.137)$$

$$\hat{F}_{p_{zx}} = (u_z \rho a_x + u_x \rho a_z) \left(1 - \frac{s_s}{2}\right) = 0 \quad (5.138)$$

where $\hat{F}_k = \mathbf{M} F_i$. Eq. (5.138) is developed with the hypothesis that $u_z = 0$ and $a_z = 0$. However, even for an arbitrary geometry flow, as the force term is proportional to velocity with the laminar incompressible flow hypothesis, this term remains negligible.

A difference appears between the D2Q9 scheme and the D3Q15 lattice is the 7/3 term in front of every energy flux term. This will have repercussions throughout most of the development for the D3Q15 lattice. Further remarks written in Appendix Ba. for the D2Q9 lattice about the differences between Guo et al.'s development [236] and the current one still hold for the D3Q15 lattice development.

b. Development of population and moment relationships

First, relationships valid both for the boundary and neighboring fluid nodes will be developed. The following relationships between pre-collision populations and moments are found by subtracting populations found after multiplying each side of Eq. (5.117) by \mathbf{M}^{-1} :

$$f_1 - f_2 = \frac{j_x}{5} - \frac{q_x}{5} \quad (5.139)$$

$$f_7 - f_8 + f_9 - f_{10} = \frac{2j_x}{5} + \frac{q_x}{10} + \frac{p_{zx}}{2} \quad (5.140)$$

$$f_{11} - f_{12} + f_{13} - f_{14} = \frac{2j_x}{5} + \frac{q_x}{10} - \frac{p_{zx}}{2} \quad (5.141)$$

Similar relationships hold true for post-collision populations and moments:

$$\tilde{f}_1 - \tilde{f}_2 = \frac{\tilde{j}_x}{5} - \frac{\tilde{q}_x}{5} \quad (5.142)$$

$$\tilde{f}_7 - \tilde{f}_8 + \tilde{f}_9 - \tilde{f}_{10} = \frac{2\tilde{j}_x}{5} + \frac{\tilde{q}_x}{10} + \frac{\tilde{p}_{zx}}{2} \quad (5.143)$$

$$\tilde{f}_{11} - \tilde{f}_{12} + \tilde{f}_{13} - \tilde{f}_{14} = \frac{2\tilde{j}_x}{5} + \frac{\tilde{q}_x}{10} - \frac{\tilde{p}_{zx}}{2} \quad (5.144)$$

where the tilde \sim represents the post-collision variable. Eq. (5.9) along with Eqs. (5.139)-(5.141) recovers exactly Eq. (5.81).

Now the propagation scheme for the D3Q15 lattice is examined. As $\frac{\partial \phi}{\partial x} = 0$, populations are invariant in the x -direction. Populations 1 and 2 are thus related as follows:

$$f_1 - f_2 = \tilde{f}_1 - \tilde{f}_2 \quad (5.145)$$

Similar relationships are derived for populations on the diagonal directions ($i = 7, 8, \dots, 14$). However, populations on diagonal directions have also a component in the y - and z -directions, populations from the boundary and fluid nodes are related as follows:

$$f_7^{(2)} - f_8^{(2)} + f_9^{(2)} - f_{10}^{(2)} = \tilde{f}_7^{(1)} - \tilde{f}_8^{(1)} + \tilde{f}_9^{(1)} - \tilde{f}_{10}^{(1)} \quad (5.146)$$

$$f_{11}^{(1)} - f_{12}^{(1)} + f_{13}^{(1)} - f_{14}^{(1)} = \tilde{f}_{11}^{(2)} - \tilde{f}_{12}^{(2)} + \tilde{f}_{13}^{(2)} - \tilde{f}_{14}^{(2)} \quad (5.147)$$

where superscript (1) represents the boundary node and (2) represents the neighboring fluid node in the y -direction. The remaining relationship to be determined is between populations interacting with the wall. In the DBB scheme, pre-collision populations 7, 8, 9 and 10 come from post-collision populations 11, 12, 13 and 14 respectively. As $u_y = u_z = 0$ and $F_y = F_z = 0$, by Eq. (5.9), $f_5 - f_6 + f_7 + f_8 + f_9 + f_{10} - f_{11} - f_{12} - f_{13} - f_{14} = 0$ and $f_3 - f_4 + f_7 + f_8 + f_9 + f_{10} - f_{11} - f_{12} - f_{13} - f_{14} = 0$. Furthermore, remarking that $f_{11}^{(eq)}(\rho_w, \mathbf{0}) = f_{12}^{(eq)}(\rho_w, \mathbf{0}) = f_{13}^{(eq)}(\rho_w, \mathbf{0}) = f_{14}^{(eq)}(\rho_w, \mathbf{0})$, that $f_3 = f_4 = f_5 = f_6 = f_3^{(eq)}(\rho_w, \mathbf{0}) = f_4^{(eq)}(\rho_w, \mathbf{0}) = f_5^{(eq)}(\rho_w, \mathbf{0}) = f_6^{(eq)}(\rho_w, \mathbf{0})$ and that $\bar{F}_7 = \bar{F}_9 = \bar{F}_{11} = \bar{F}_{13}$ and $\bar{F}_8 = \bar{F}_{10} = \bar{F}_{12} = \bar{F}_{14}$, it can be concluded that K defined in Eq. (5.32) is equal to 1 and the following relationship is thus derived:

$$f_7^{(1)} - f_8^{(1)} + f_9^{(1)} - f_{10}^{(1)} = -(\tilde{f}_{11}^{(1)} - \tilde{f}_{12}^{(1)} + \tilde{f}_{13}^{(1)} - \tilde{f}_{14}^{(1)}) \quad (5.148)$$

c. Assembly of the MRT-LBM equation

The regularized MRT-LBM defined in Eq. (5.37) is used to find relationships between the post-collision and pre-collision populations for each of the two nodes.

For the boundary node (1), populations 6, 11, 12, 13 and 14 enter into collision with the solid wall. Multiplying each side of Eq. (5.37) by \mathbf{M} , using Eqs. (5.38), (5.125)-(5.129), (5.134) and (5.136)-(5.141), recalling $\mathbf{u}_w = 0$, and after tedious algebraical manipulations, the post-collision moments are related to pre-collision moments the following way for the boundary node:

$$\tilde{j}_x^{(1)} = \rho u^{(1)} - \left(\frac{1-r}{6}\right) \rho u^{(1)} + \left(\frac{(1-r)(1-s_s)}{2}\right) p_{zx}^{(1)} + \rho a \left(1 - \frac{s_j}{2}\right) \delta_t \quad (5.149)$$

$$\tilde{q}_x^{(1)} = -\frac{7}{3} \rho u^{(1)} - \left(\frac{1-r}{6}\right) \rho u^{(1)} + \left(\frac{(1-r)(1-s_s^{(1)})}{2}\right) p_{zx}^{(1)} - \frac{7}{3} \rho a \left(1 - \frac{s_q}{2}\right) \delta_t \quad (5.150)$$

$$\tilde{p}_{zx}^{(1)} = \frac{(1-r)}{6} \rho u^{(1)} + \left(\frac{(1+r)(1-s_s^{(1)})}{2}\right) p_{zx}^{(1)} \quad (5.151)$$

Using Eqs. (5.81), (5.83), (5.149) and (5.150), the energy flux at the boundary node is found:

$$q_x^{(1)} = -\frac{7}{3} \rho u^{(1)} - \rho a \delta_t \left(\frac{10}{3} - \frac{7s_q}{6}\right) \quad (5.152)$$

For the fluid node (2), Eq. (5.38) makes $r_i = 1$ for all i . Using Eq. (5.91), post-collision moments are easily found from Eqs. (5.125)-(5.129), (5.134), (5.136)-(5.138) and (5.142)-(5.144):

$$\tilde{j}_x^{(2)} = \rho u^{(2)} + \rho a \left(1 - \frac{s_j}{2}\right) \delta_t \quad (5.153)$$

$$\tilde{q}_x^{(2)} = -\frac{7}{3} \rho u^{(2)} - \frac{7}{3} \rho a \left(1 - \frac{s_q}{2}\right) \delta_t \quad (5.154)$$

$$\tilde{p}_{zx}^{(2)} = \left(1 - s_s^{(2)}\right) p_{zx}^{(2)} \quad (5.155)$$

When $r = 1$, expressions for the post-collision moments from Eqs. (5.149)-(5.151) are equal to those from Eqs. (5.153)-(5.155). Using Eqs. (5.81), (5.83), (5.153) and (5.154), the energy flux for the fluid node is found:

$$q_x^{(2)} = -\frac{7}{3}\rho u^{(2)} - \rho a \delta_t \left(\frac{10}{3} - \frac{7s_q}{6} \right) \quad (5.156)$$

As Eqs. (5.152) and (5.156) are expressions for a pre-collision moment, their similarity is not surprising.

Further remarks held at the end of Appendix Bc. regarding the necessity of setting $s_j = 1$ remain true for the D3Q15 lattice.

d. Expression of the stress tensor as function of force and velocity terms for boundary and fluid nodes

The stress tensor non-diagonal component p_{zx} is now expressed in function of the velocity u and the body force ρa . The following relationships between the pre-collision populations and the pre-collision stress tensor non-diagonal component are found after substituting Eqs. (5.152) and (5.156) into Eqs. (5.140) and (5.141):

$$f_7^{(1)} - f_8^{(1)} + f_9^{(1)} - f_{10}^{(1)} = \frac{\rho u^{(1)}}{6} + \frac{p_{zx}^{(1)}}{2} + \rho a \delta_t \left(-\frac{8}{15} + \frac{7s_q}{60} \right) \quad (5.157)$$

$$f_{11}^{(1)} - f_{12}^{(1)} + f_{13}^{(1)} - f_{14}^{(1)} = \frac{\rho u^{(1)}}{6} - \frac{p_{zx}^{(1)}}{2} + \rho a \delta_t \left(-\frac{8}{15} + \frac{7s_q}{60} \right) \quad (5.158)$$

$$f_7^{(2)} - f_8^{(2)} + f_9^{(2)} - f_{10}^{(2)} = \frac{\rho u^{(2)}}{6} + \frac{p_{zx}^{(2)}}{2} + \rho a \delta_t \left(-\frac{8}{15} + \frac{7s_q}{60} \right) \quad (5.159)$$

$$f_{11}^{(2)} - f_{12}^{(2)} + f_{13}^{(2)} - f_{14}^{(2)} = \frac{\rho u^{(2)}}{6} - \frac{p_{zx}^{(2)}}{2} + \rho a \delta_t \left(-\frac{8}{15} + \frac{7s_q}{60} \right) \quad (5.160)$$

The following relationships between post-collision populations and the pre-collision stress tensor non-diagonal component are found after substituting Eqs. (5.149)-(5.151) and (5.153)-(5.155) into Eqs. (5.143) and (5.144):

$$\tilde{f}_7^{(1)} - \tilde{f}_8^{(1)} + \tilde{f}_9^{(1)} - \tilde{f}_{10}^{(1)} = \frac{\rho u^{(1)}}{6} + \frac{p_{zx}^{(1)} (1 - s_s^{(1)})}{2} + \rho a \delta_t \left(-\frac{1}{30} + \frac{7s_q}{60} \right) \quad (5.161)$$

$$\tilde{f}_{11}^{(1)} - \tilde{f}_{12}^{(1)} + \tilde{f}_{13}^{(1)} - \tilde{f}_{14}^{(1)} = r \left(\frac{\rho u^{(1)}}{6} - \frac{p_{zx}^{(1)} (1 - s_s^{(1)})}{2} \right) + \rho a \delta_t \left(-\frac{1}{30} + \frac{7s_q}{60} \right) \quad (5.162)$$

$$\tilde{f}_7^{(2)} - \tilde{f}_8^{(2)} + \tilde{f}_9^{(2)} - \tilde{f}_{10}^{(2)} = \frac{\rho u^{(2)}}{6} + \frac{p_{zx}^{(2)} (1 - s_s^{(2)})}{2} + \rho a \delta_t \left(-\frac{1}{30} + \frac{7s_q}{60} \right) \quad (5.163)$$

$$\tilde{f}_{11}^{(2)} - \tilde{f}_{12}^{(2)} + \tilde{f}_{13}^{(2)} - \tilde{f}_{14}^{(2)} = \frac{\rho u^{(2)}}{6} - \frac{p_{zx}^{(2)} (1 - s_s^{(2)})}{2} + \rho a \delta_t \left(-\frac{1}{30} + \frac{7s_q}{60} \right) \quad (5.164)$$

Here it is assumed, as did Guo et al. [236], that s_q is constant throughout the domain. Developing Eqs. (5.146) and (5.147), macroscopic velocities and the stress tensor non-diagonal component are now related in this way:

$$\frac{\rho u^{(2)}}{6} + \frac{p_{zx}^{(2)}}{2} + \rho a \delta_t \left(-\frac{8}{15} + \frac{7s_q}{60} \right) = \frac{\rho u^{(1)}}{6} + \frac{p_{zx}^{(1)} (1 - s_s^{(1)})}{2} + \rho a \delta_t \left(-\frac{1}{30} + \frac{7s_q}{60} \right) \quad (5.165)$$

$$\frac{\rho u^{(1)}}{6} - \frac{p_{zx}^{(1)}}{2} + \rho a \delta_t \left(-\frac{8}{15} + \frac{7s_q}{60} \right) = \frac{\rho u^{(2)}}{6} - \frac{p_{zx}^{(2)} (1 - s_s^{(2)})}{2} + \rho a \delta_t \left(-\frac{1}{30} + \frac{7s_q}{60} \right) \quad (5.166)$$

Isolating $p_{zx}^{(2)}$ in Eq. (5.165) and then isolating $p_{zx}^{(1)}$ in Eq. (5.166), the stress tensor non-diagonal components for each node are now expressed as a set of two equations with two unknowns:

$$p_{zx}^{(2)} = \frac{\rho(u^{(1)} - u^{(2)})}{3} + \rho a \delta_t + p_{zx}^{(1)} (1 - s_s^{(1)}) \quad (5.167)$$

$$p_{zx}^{(1)} = \frac{\rho(u^{(1)} - u^{(2)})}{3} + \rho a \delta_t + p_{zx}^{(2)} (1 - s_s^{(2)}) \quad (5.168)$$

Inserting Eq. (5.167) in Eq. (5.168) and then isolating $p_{zx}^{(1)}$:

$$p_{zx}^{(1)} = \rho \frac{\left((u^{(1)} - u^{(2)}) (2 - s_s^{(2)}) - 3a \delta_t s_s^{(2)} \right)}{3(s_s^{(1)} + s_s^{(2)} - s_s^{(1)} s_s^{(2)})} \quad (5.169)$$

This result is strikingly similar to the result obtained for the D2Q9 lattice.

e. Relationship between the boundary and fluid node velocities

It is also desired to find a relationship of the form presented in Eq. (5.109). Inserting Eq. (5.157) in the left-hand side of Eq. (5.148) and inserting Eq. (5.162) in the right-hand side of Eq. (5.148) and using Eq. (5.169), expressions for A and B are found:

$$A = -\frac{\left(2 - 2r + s_s^{(1)} + 3rs_s^{(1)} + 2rs_s^{(2)} - s_s^{(1)}s_s^{(2)} - 2rs_s^{(1)}s_s^{(2)}\right)}{\left(s_s^{(2)} - 2\right)\left(rs_s^{(1)} - r + 1\right)} \quad (5.170)$$

$$B = \frac{17s_s^{(1)} + 32s_s^{(2)} - 15rs_s^{(2)} - 7s_q s_s^{(1)} - 7s_q s_s^{(2)}}{5\left(s_s^{(2)} - 2\right)\left(rs_s^{(1)} - r + 1\right)} + \frac{-17s_s^{(1)}s_s^{(2)} + 15rs_s^{(1)}s_s^{(2)} + 7s_q s_s^{(1)}s_s^{(2)}}{5\left(s_s^{(2)} - 2\right)\left(rs_s^{(1)} - r + 1\right)} \quad (5.171)$$

As the relation between the effective mean free path λ_e and the relaxation rate $\left(\tau_s - \frac{1}{2}\right)$ is linear, it is easier to treat Eqs. (5.170) and (5.171) by shifting $\tau_s = \tilde{\tau}_s + 1/2$ and by substituting $s_s = 1/\left(\tilde{\tau}_s + \frac{1}{2}\right)$ and $s_q = 1/\tau_q$:

$$A = \frac{\tilde{\tau}_s^{(1)} + 2\tilde{\tau}_s^{(2)} + r\tilde{\tau}_s^{(1)} + 2r\tilde{\tau}_s^{(2)} + 2\tilde{\tau}_s^{(1)}\tilde{\tau}_s^{(2)} - 2r\tilde{\tau}_s^{(1)}\tilde{\tau}_s^{(2)}}{\tilde{\tau}_s^{(2)}\left(r + 2\tilde{\tau}_s^{(1)} - 2r\tilde{\tau}_s^{(1)} + 1\right)} \quad (5.172)$$

$$B = -\frac{15\tau_q - 14\tilde{\tau}_s^{(1)} - 14\tilde{\tau}_s^{(2)} + 15r\tau_q + 64\tau_q\tilde{\tau}_s^{(1)} + 34\tau_q\tilde{\tau}_s^{(2)} - 30r\tau_q\tilde{\tau}_s^{(1)}}{10\tau_q\tilde{\tau}_s^{(2)}\left(r + 2\tilde{\tau}_s^{(1)} - 2r\tilde{\tau}_s^{(1)} + 1\right)} \quad (5.173)$$

Eq. (5.112) is found to be the same as Eq. (5.172)

f. Taylor expansions of velocities and viscosity relaxation times around the wall

See developments from Appendix Bf which remain fully valid here.

g. Combination of relationships and final result.

Using Eqs. (5.116), (5.117), (5.120)-(5.123), (5.172) and (5.173), after some tedious algebra and neglecting all remaining terms in δ_x^2 and of higher order, Eqs. (5.39) and (5.40) for r and τ_q are finally found for the D3Q15 scheme.

CHAPITRE 6 ARTICLE 4: SIMULATION OF RAREFIED GAS FLOWS THROUGH NON-PLANAR GEOMETRIES USING AN EFFECTIVE VISCOSITY FUNCTION CALCULATED FROM A RAY-TRACING ALGORITHM

Jean-Michel Tucny, Sébastien Leclaire, David Vidal et François Bertrand – soumis le 9 novembre 2020 au *Journal of Computational Physics*, p. XXX-XXX. (Note : le texte présenté ici peut ne pas correspondre à la version finale)

Abstract. The computation of rarefied gas flow fields is a significant challenge as the no-slip condition and continuum hypothesis break down in the rarefied regime. This problem is exacerbated in complex porous media, where approximations of the Boltzmann equation are too computationally expensive to be used for concrete industrial applications. Extensions of the Navier-Stokes equations through effective viscosity functions have been proposed to model the stress-strain relationship in rarefied flows. However, earlier effective viscosity functions were computed accurately only for a few simple geometries. In this article, rarefied flows through non-planar geometries are computed using an effective viscosity functions calculated from a ray-tracing algorithm. The lattice Boltzmann method (LBM) is used as an extended Navier-Stokes equation solver. Good agreement was found with experimental data for the flow field through a slit. Questions remain regarding the use of the LBM as an extended Navier-Stokes equation solver through complex porous media.

Keywords: Complex porous media, Effective viscosity functions, Knudsen flow, Rarefied flow, Effective mean free path, Lattice Boltzmann method (LBM)

6.1 Introduction

Rarefied gas flows through porous media have received considerable attention in various fields such as shale gas extraction [431], spatial re-entry [432], air filtration [153], catalysis [433], and micro/nanoelectromechanical systems (MEMS/NEMS) [53]. Gas flows are said to be rarefied when the mean free path of gas molecules λ is comparable to the characteristic length of the flow L_c , i.e., when the Knudsen number $Kn = \lambda/L_c$ is not negligible. As the Knudsen number increases, two deviations from continuum flow behavior occur successively: first a flow slip at the wall and

then the appearance of the Knudsen layer [137, 138, 434]. Flow slip manifests as a macroscopic velocity discontinuity at a solid boundary. Gas molecules incoming from a region with a finite flow velocity contribute to the velocity of the gas in the neighborhood of the solid, creating a finite flow velocity at the solid surface. The Knudsen layer is a region of a thickness $O(\lambda)$ in the neighborhood of a solid boundary where insufficient collisions happen between gas molecules. As a consequence, the assumption of local thermodynamic equilibrium is no longer valid, and the linear stress-strain relationship in the Navier-Stokes equations (NSEs) breaks down.

Devienne's original classification [52] distinguished four rarefaction regimes: (1) continuous flow ($Kn < 0.001$), (2) slip flow ($0.001 < Kn < 0.01$), (3) transition or Knudsen flow ($0.01 < Kn < 10$), and (4) free molecular flow ($Kn > 10$). In the continuous flow regime, the NSEs with no-slip boundary conditions (BCs) are valid. In the slip flow regime, the NSEs are considered valid in the bulk of the flow. However, slip BCs should be used at solid-fluid boundaries. In the transition flow regime, the Knudsen layer becomes predominant in the flow. In the free molecular flow regime, collisions between gas molecules are negligible. Thresholds between these regimes vary from author to author [55, 149, 158, 354-357], and should be geometry-[55, 182, 435] and physics-dependent [355-357]. Defining these thresholds becomes even more difficult in porous media, where the characteristic length L_C may vary throughout the domain [353].

Of the four regimes mentioned above, the transition or Knudsen flow regime is the most difficult to solve given that non-equilibrium effects are dominant while collisions between gas molecules are not negligible. Transition flows can be studied by considering statistical ensembles of molecular momentum transfers with a collision term, the simplest one being the Boltzmann equation (BE). However, closed-form solutions of the BE are known only for a few simple geometries [137, 138, 257]. Numerical methods devoted to approximations of the BE can be divided into three categories: (1) macroscopic, such as Chapman-Enskog expansions and Grad's moment method [137, 434], (2) microscopic, such as the Direct Simulation Monte-Carlo (DSMC) method and the molecular dynamics (MD) simulation method [257], and (3) mesoscopic, such as the discrete ordinate method (DOM), the discrete velocity method (DVM) [417], the lattice Boltzmann method (LBM) [275], and the discrete unified gas kinetic scheme (DUGKS) [267]. Macroscopic methods find solutions to higher-order truncatures of the BE. As these solutions analyze distributions and moments that depart from equilibrium, they are generally adapted to the low end of the transition flow ($Kn < 1$). Microscopic methods attempt to solve the BE by

averaging the behaviors of sample populations or molecules. The computational needs of microscopic methods increase in the continuum limit and so are generally adapted to the high end of transition flows ($Kn > 1$). Mesoscopic methods discretize space domains and velocity sets to solve the BE, which makes them, in principle, valid across the entire range of Knudsen numbers. However, high Knudsen flows require large velocity sets that increase computation times and the memory footprint dramatically as well as communication overhead for distributed memory systems. This problem is exacerbated in porous media where solid-gas boundaries are often complex. The DUGKS and the LBM try to alleviate this problem by evaluating population fluxes on adaptive meshes and by using a regular Cartesian grid, respectively. Nonetheless, it remains difficult to determine the required size of the set before computing the solution. Hybrid schemes where microscopic sub-schemes are used in the Knudsen layer and mesoscopic or macroscopic sub-schemes outside the Knudsen layer have been proposed, but their computational efficiency is limited by the domain fraction where such microscopic sub-schemes must be used [259-266, 436, 437]. In addition, in complex porous media, domain decomposition is not straightforward.

The computational cost of solving the NSEs is very low compared to that of the BE approximations. For this reason, it has been proposed to recover rarefied flow fields by incorporating an effective viscosity function in the NSEs to recover the stress-strain relationship in the Knudsen layer together with a slip BC to recover the finite slip velocity at the boundary. This would reduce the complexity of solving the Boltzmann equation through a complex porous medium to a single scalar field (effective viscosity) that is evaluated once. Originally, empirical and analytical fittings depending solely on the Knudsen number were proposed to recover the relationship between pressure drop and mass flow for plane Couette [173-179] and pressure-driven [179-182] flows. However, for a complex geometry, the definition of a Knudsen number is ambiguous because it is explicit based on a characteristic length, which may vary throughout a complex geometry. Another problem is that, in the aforementioned studies, the viscosity functions used were position-independent. However, effective viscosity should have a lower value only inside the Knudsen layer. Constant viscosity models thus accurately predict mass flows only because of fitting, and the velocity field is generally not well predicted even in planar flows [217, 438]. Nevertheless, constant viscosity functions have been used to solve rarefied gas flows through porous media in many studies, some by solving flows on a planar domain [183-193], others by applying the constant viscosity model directly to complex geometries [194-216].

A more sophisticated approach has been proposed in the form of a wall function giving the relationship between shear stress and strain in the Knudsen layer. Although wall functions have been derived by analyzing flow fields obtained from approximations of the BE [217-224], this approach raises the question as to whether the flow field for a given shape of a solid-fluid boundary is required to find the stress-strain relationship.

In this work, it is aimed to find an effective viscosity function that can be calculated *a priori* solely from the geometry and the gas properties. According to the kinetic theory of gases, the viscosity of a gas is proportional to its molecular mean free path. Solid walls restrict molecular paths and thus reduce the effective mean free path near a solid boundary. If the distribution of free paths is known *a priori* and the distance to the nearest solid boundary is known in every angle from every point, it would be possible to derive an effective viscosity function through integration, assuming as a hypothesis that the proportionality between viscosity and the mean free path holds true in the Knudsen layer. This hypothesis has been confirmed for simple geometries by MD [228-230] and DSMC studies [226, 227] for which gas thermodynamic properties did not vary at the scale of a mean free path. However, these articles were criticized for allegedly using insufficient space and time bins [439]. Recent studies with MD have responded to these criticisms by using different techniques for the computation of viscosity [224, 440].

Several wall functions have been derived in simple cases such as planar [170, 225, 226, 231-234] and concentric cylindrical flows [161, 162, 235]. Analytical functions derived for planar flows have also been implemented for complex geometries [202, 334, 351, 361, 369, 380, 381, 441]. However, these articles do not provide details about wall-distance calculations and there remains some ambiguity on how to proceed. A wall-distance calculation algorithm has been proposed for complex geometries [442], but to the authors' knowledge, has not been used for viscosity function calculations. A systematic method for computing viscosity functions for complex geometries is thus still lacking.

Another problem to be considered is the choice of the numerical method used to solve the extended NSEs through complex porous media. The LBM is a finite-difference discretization of the Boltzmann equation where populations evolve according to a propagation-collision scheme. The LBM is particularly suited for massive parallel computations because of its local and explicit formulation. Fluid and solid nodes are represented on a regular Cartesian scheme with a simple

Boolean geometry. With a small velocity set, such as the D2Q9 or D3Q15 lattice, it is possible to recover the regular NSEs through porous media with a Chapman-Enskog expansion within the limit of low Mach and Knudsen numbers [250-253].

A further advantage of the LBM with respect to the computation of the effective mean free path in complex porous media is its simple Boolean representation of the phases on a regular Cartesian grid. Two separate studies used with the LBM to compute the mean free path in a complex porous medium by averaging the distances to a wall according to rays traced in four directions from each fluid node in a 2D domain [295] and in 18 directions in a 3D domain [364]. The number of rays originating from each node can coincide with the lattice, and computations of distance to the nearest solid were performed only with integer operations. However, there is no indication that these numbers of directions are sufficient. The number of directions required to precisely calculate effective mean free paths has never been investigated systematically.

Papers already published by our group revealed several additional problems with previous BC implementations for the simulation of rarefied gas flows through porous media. Some of these problems were remedied by: (1) developing a new diffusive bounce-back (DBB) BC that unambiguously defines kinetic BCs in corners and that accounts for the variation of effective viscosity [237], (2) filtering non-hydrodynamical moments with a regularization procedure, and (3) tuning the DBB BC to include the impact of the regularization procedure on the BC [443]. However, the impact of the Knudsen layer was not taken into account for non-planar geometries as a systematic procedure had not been developed to compute the effective viscosity function.

In this article, it is proposed to compute effective viscosity functions by the numerical integration of free path distribution functions bounded by the distance to the nearest wall computed in all directions according to a ray-tracing algorithm. The effective viscosity functions were then used as an input to an in-house LBM code with a D3Q15 lattice to solve flows in the rarefied regimes. In Section 6.2, derivations of effective viscosity functions are described. In Section 6.3, numerical comparisons are made with wall functions derived using a simple wall geometry. In Section 6.4, the ray-tracing algorithm is presented as a pseudo-code, and information about its implementation for a Cartesian grid is given. In Section 6.5, a description of the implementation of ray-tracing through a convergence analysis of the required propagation and angle steps for a planar geometry and an array of spheres is provided. In Section 6.6, the results for rarefied flows are

compared to the analytical and experimental results, respectively, for planar and cylinder array geometries. In Section 6.7, some concluding remarks are presented.

6.2 Effective viscosity functions

In this section, effective viscosity functions will be constructed from elements of kinetic theory and phenomenological models. First, the relationships between viscosity and the mean free path are recalled and the general formula for effective viscosity functions is explained. Second, the free path distribution functions presented in the literature are summarized. Third, angular distribution functions found in the literature are summarized. Lastly, analytical solutions for simple geometries are discussed.

6.2.1 General formula of the effective viscosity function

In the kinetic theory of gases, systems with a large number of particles are assumed to obey the laws of classical mechanics. The mean free path is defined as the average distance traveled by gas molecules between collisions. According to the rigid sphere model, gas molecules are treated as mass points travelling a distance r without a force term (thus called a free path), before interacting with discrete impulses when collisions occur [138]. For an unbounded system in thermodynamic equilibrium, a proportionality relationship can be derived between the mean free path λ and viscosity μ via the temperature T and the pressure P [138]:

$$\lambda = \frac{\mu}{P} \sqrt{\frac{\pi \mathcal{R} T}{2}} \quad (6.1)$$

where \mathcal{R} is the ideal gas constant for the given molecular species.

In bounded systems, however, free paths are obstructed in the vicinity of solid walls, thus creating the Knudsen layer. Assuming relationship (6.1) holds in the Knudsen layer, an effective viscosity can be derived for each point \mathbf{x} in a given geometry by computing the effective mean free path $\lambda_e(\mathbf{x})$:

$$\frac{\lambda_e(\mathbf{x})}{\lambda} = \frac{\mu_e(\mathbf{x})}{\mu} = \Psi(\mathbf{x}, \lambda) \quad (6.2)$$

where $0 \leq \Psi(\mathbf{x}, \lambda) \leq 1$ is the effective viscosity function. The calculation of the effective viscosity in the Knudsen layer is thus reduced to the calculation of an effective mean free path.

To compute the effective mean free path, the distance r between two collisions is treated as a random variable with a free path distribution function $\psi(r)$, where each path is treated as a separate and independent event. The probability p that a gas molecule travels a distance greater than R between two collisions is by definition:

$$p(R) = \int_R^\infty \psi(r) dr \quad (6.3)$$

Explicit forms for the free path distribution function $\psi(r)$ are given in Subsection 6.2.2. The unbounded mean free path of a molecule is recovered by calculating the expected (or mean) value of the distribution ψ :

$$\lambda = \int_0^\infty r \psi(r) dr \quad (6.4)$$

Considering a gas molecule at position \mathbf{x} travelling along a given direction, it is possible to calculate the distance R at which a molecule might hit a solid wall by tracing a line segment from the position \mathbf{x} to the intersection of the line with a solid boundary in that direction. The line segments will henceforth be labeled “rays.” This mathematical problem is best treated using a spherical coordinate system (r, θ, ϕ) , where r is the distance to the center, θ is the longitude, and ϕ is the latitude. Along this free path of length r , two possibilities arise: either the gas molecule collides with a solid wall ($r > R(\theta, \phi)$) or the gas molecule collides with another gas molecule before it reaches a solid wall ($r < R(\theta, \phi)$). The directional mean free path $\lambda(R(\theta, \phi))$ is thus:

$$\lambda(R(\theta, \phi)) = \int_0^{R(\theta, \phi)} r \psi(r) dr + \int_{R(\theta, \phi)}^\infty R(\theta, \phi) \psi(r) dr \quad (6.5)$$

As $R(\theta, \phi)$ is a constant with respect to r , Eq. (6.5) can be simplified by using the definition of the probability p presented in Eq. (6.3):

$$\lambda(R(\theta, \phi)) = \int_0^{R(\theta, \phi)} r\psi(r)dr + R(\theta, \phi) \cdot p(R(\theta, \phi)) \quad (6.6)$$

Depending on the geometry and the given direction (θ, ϕ) , the ray may not cross any solid object. In this case, $R(\theta, \phi) = \infty$ and $\lambda(R(\theta, \phi)) = \lambda$ per Eq. (6.4). By calculating the integral through all the angles and recalling the Jacobian $d\Omega = \sin\phi d\phi d\theta$, the effective mean free path evaluated at point \mathbf{x} for a complex geometry in its most general form is:

$$\lambda_e(\mathbf{x}) = \int_0^{2\pi} \int_0^{\pi} \lambda(R(\theta, \phi)) g(\theta, \phi) \sin\phi d\phi d\theta. \quad (6.7)$$

where $g(\theta, \phi)$ is the angular ray distribution function described in detail in Subsection 6.2.3.

6.2.2 Free path distribution functions

To compute an effective viscosity function in rarefied flows, Stops [346] proposed an exponential free path distribution:

$$\psi(r) = \frac{1}{\lambda} \exp\left(-\frac{r}{\lambda}\right) \quad (6.8)$$

Using Eq. (6.8) in Eq. (6.6), the directional mean free path for the exponential free path distribution is thus given by:

$$\lambda_{EXP}(R(\theta, \phi)) = \lambda \left(1 - \exp\left(-\frac{R(\theta, \phi)}{\lambda}\right)\right) \quad (6.9)$$

The exponential free path distribution can be derived from two assumptions: (1) that collision frequency is independent of molecular velocity (the so-called Maxwellian molecular model) and (2) that the gas is in thermodynamic equilibrium throughout the Knudsen layer [228]. Assumption 1 generally breaks down as the collision frequency increases with molecular velocity. However, for the hard-sphere model, assuming the macroscopic density and temperature remain constant throughout the domain, departure from the exponential model is weak and the evaluation of a more accurate free path distribution would require a cumbersome integration [444-447]. Assumption 2 has been criticized based on DSMC tests by Dongari et al. [228], who proposed a power-law free path distribution to capture the impact of deviation from equilibrium:

$$\psi(r) = C(a+r)^{-n} \quad (6.10)$$

where $C = (n-1)a^{n-1}$, $a = \lambda(n-2)$, and $n > 2$ is a parameter representing the deviation from equilibrium. When $n \rightarrow \infty$, the power-law distribution converges to the exponential distribution. However, $n = 3$ will be chosen as was the case for most articles using the power-law free path distribution [161, 162, 170, 235, 237, 295, 448]. Using Eq. (6.10) in Eq. (6.6), the expression of the directional mean free path becomes cumbersome when n is unspecified in the power-law free path distribution. Given this, only the case with $n = 3$ will be shown in the remainder of the development:

$$\lambda_{PL}(R(\theta, \phi)) = \frac{R(\theta, \phi) \cdot \lambda}{R(\theta, \phi) + \lambda} \quad (6.11)$$

Arlemark et al. [232] used a different formalism where the bulk mean free path is directly multiplied by an integrated form of the probability distribution function and derived Eq. (6.9) as the integrand to be used in Eq. (6.7) from the exponential free path distribution (i.e., Eq. (6.8)). Following Arlemark et al.'s formalism, however, Dongari et al. [170, 233] developed a different integrand for Eq. (6.7), namely:

$$\lambda_{PL}^*(R(\theta, \phi)) = \lambda \left(1 - \left(1 + \frac{R(\theta, \phi)}{a} \right)^{1-n} \right) \quad (6.12)$$

where the superscript * indicates that it was not derived with Eq. (6.6). The similitude between Arlemark et al.'s integrand and Eq. (6.9) is a consequence of the mathematical properties of the exponential function. Discrepancies between Eqs. (6.11) and (6.12) are thus expected.

Figure 6.1 shows the directional mean free paths corresponding to Eqs. (6.9), (6.11), and (6.12). The directional mean free path derived from the exponential law (Eq. (6.9)) reaches the bulk mean free path at a relatively smaller R compared to derivations from the power-law (Eq. (6.11)), as intended. However, the directional mean free path derived in the article by Dongari et al. (Eq. (6.11)) reaches the bulk mean free path at an even smaller R than the directional mean free path derived from Eq. (6.12) for the power law distribution function. At $R = 10\lambda$, Eq. (6.11) predicts $\lambda_e \approx 0.909$, while Eq. (6.12) predicts $\lambda_e \approx 0.992$. The power-law distribution with $n =$

3 is thus impractical for a ray-tracing algorithm such as the one presented in Section 6.4, as the effective mean free path increases too slowly as a function of R .

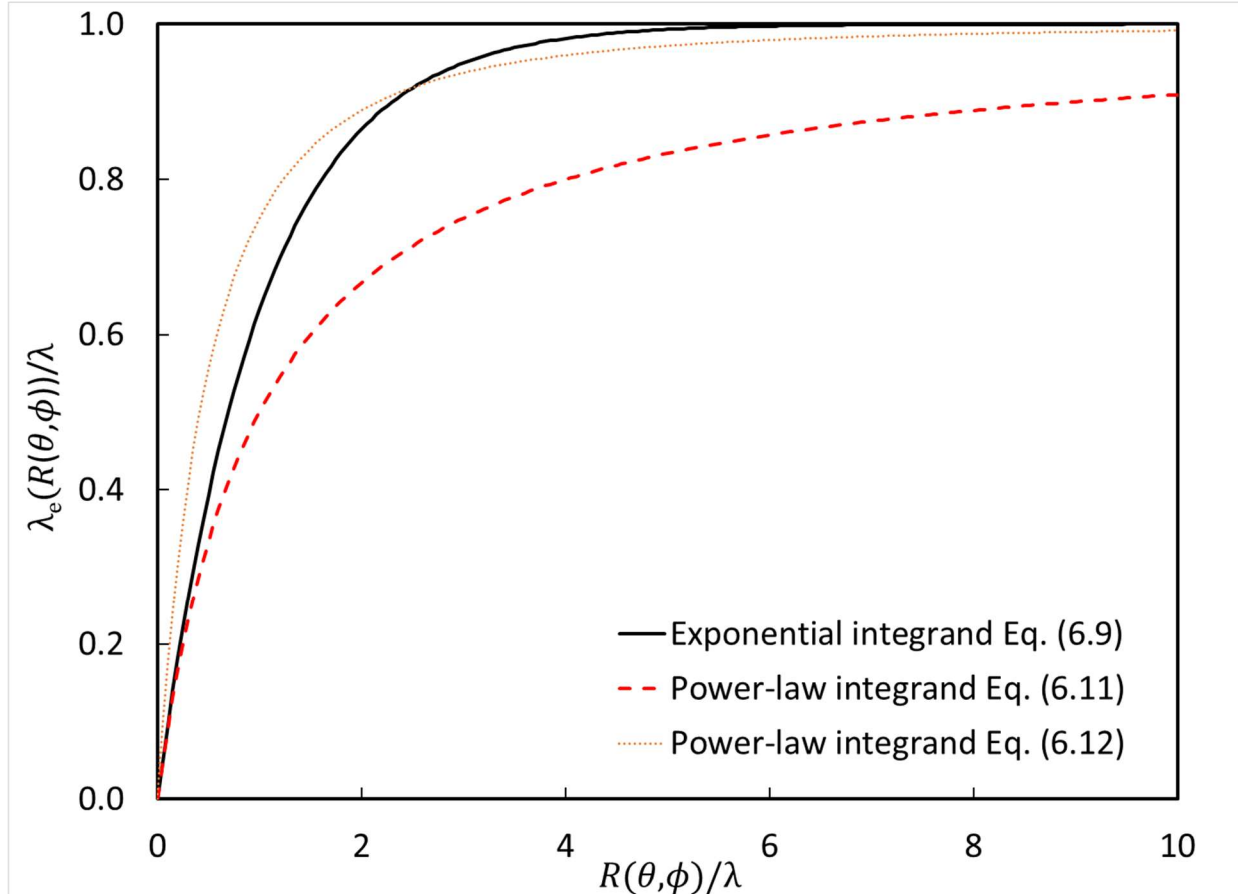


Figure 6.1 Directional mean free path expressions derived in Subsection 6.2.2 and from the literature

6.2.3 Angular distribution functions

The angular distribution function $g(\theta, \phi)$ defines the ray distribution leaving a point according to the angle (θ, ϕ) . The following normalization property must be true for $g(\theta, \phi)$:

$$\int_0^{2\pi} \int_0^\pi g(\theta, \phi) \sin\phi d\phi d\theta = 1 \quad (6.13)$$

Assuming molecules have no angular preference, the following uniform angular distribution function is derived [226]:

$$g_{UNI}(\theta, \phi) = \frac{1}{4\pi} \quad (6.14)$$

This assumption implies a uniform macroscopic velocity throughout the flow, which strictly speaking is not true for any shear flow. However, as pointed out by Abramov [226], if the macroscopic velocity is small compared to the mean molecular speed, deviations from uniform behavior should remain small. This is also equivalent to assuming a small Mach number as the speed of sound is proportional to the mean molecular speed with a constant factor $O(1)$.

In Stops' development for the viscosity function in the case of a slit flow [346], molecules leaving a solid surface are considered first, by analogy to the radiation phenomenon, to follow Lambert's cosine law [226]:

$$g_{cos}(\theta, \phi) = \frac{1}{2\pi} \cos \phi \quad (6.15)$$

where ϕ is the angle between the line normal to the plane and a molecule trajectory. Note that Stops introduced this angular distribution function for gas molecules leaving the wall, not coming from the bulk. The direct application of Eq. (6.15) in Eq. (6.7) would thus induce an anisotropic angular distribution function throughout the domain, in contradiction with the equipartition principle in the continuous limit. It should be noted that Abramov [226], with other DSMC tests, found that the uniform distribution was more accurate than the cosine distribution. The uniform distribution was thus used in this work.

6.2.4 Analytical solutions

Analytical solutions from the literature for effective mean free paths in simple geometries are reviewed here. The earliest mention of an effective mean free path comes from Stops [346], with a development for a flow through a slit of opening width D . Using the exponential free path distribution from Eq. (6.8) and the cosine angular distribution from Eq. (6.15), the ratio of the mean free path of molecules leaving a solid wall (λ_w) and that from the bulk λ , which is labeled $F(\beta)$, is written as:

$$\frac{\lambda_w}{\lambda} = F(\beta) = 1 + (\beta - 1) \exp(-\beta) - \beta^2 E_i(\beta) \quad (6.16)$$

where $\beta = D/\lambda$ and the exponential integral function $E_i(\beta)$ is defined as:

$$E_i(\beta) = \int_1^\infty t^{-1} \exp(-\beta t) dt \quad (6.17)$$

As $E_i(\beta)$ is difficult to evaluate, the following simplification has been proposed for $F(\beta)$ [231]:

$$F(\beta) \approx \frac{2}{\pi} \arctan(\beta^{-\frac{3}{4}}) \quad (6.18)$$

It must be noted that Eq. (6.16) developed by Stops, as such, reveals nothing about the effective mean free path through the domain. Guo et al. [225] considered a flow through a slit with molecules originating from a plane at position $-\frac{D}{2} \leq x \leq \frac{D}{2}$. Assuming that molecules have no preference going to one wall or the other, the following viscosity function was derived by taking an average of the contributions to the two planes:

$$\Psi(\lambda, x) = \frac{1}{2} \left(F\left(\frac{\frac{D}{2}-x}{\lambda}\right) + F\left(\frac{\frac{D}{2}+x}{\lambda}\right) \right) \quad (6.19)$$

Introducing Eqs. (6.9) and (6.15) into the definition of the effective mean free path from Eq. (6.7) with the appropriate form for $R(\theta, \phi)$ yields exactly Eq. (6.19). It should be noted that the combination of an anisotropic angular distribution function with the assumption that molecules have no preference going to one wall or the other seems difficult to generalize to complex geometries and appears logically inconsistent.

Arlemark et al. [232] proposed an alternative viscosity function for the exponential distribution function (Eq. (6.9)) using the uniform angular distribution function (Eq. (6.14)) and a Simpson 1/3 numerical approximation of Eq. (6.7) with 14 subintervals:

$$\begin{aligned}
\Psi(\lambda, x) = & 1 - \frac{1}{82} \left(\exp \left(-\frac{\left(\frac{D}{2} + x\right)}{\lambda} \right) + \exp \left(-\frac{\left(\frac{D}{2} - x\right)}{\lambda} \right) \right. \\
& + 4 \sum_{i=1}^7 \exp \left(-\frac{\left(\frac{D}{2} + x\right)}{\lambda \cdot \cos \frac{(2 \cdot i - 1)\pi}{28}} \right) \\
& + 4 \sum_{i=1}^7 \exp \left(-\frac{\left(\frac{D}{2} - x\right)}{\lambda \cdot \cos \frac{(2 \cdot i - 1)\pi}{28}} \right) + 2 \sum_{i=1}^6 \exp \left(-\frac{\left(\frac{D}{2} + x\right)}{\lambda \cdot \cos \frac{i\pi}{14}} \right) \\
& \left. + 2 \sum_{i=1}^6 \exp \left(-\frac{\left(\frac{D}{2} - x\right)}{\lambda \cdot \cos \frac{i\pi}{14}} \right) \right)
\end{aligned} \tag{6.20}$$

Abramov [226], using the same formalism as presented in this paper, recently proposed to combine the exponential distribution in Eq. (6.8) with the uniform angular distribution in Eq. (6.14) to derive a solution for a semi-infinite flow. For a slit flow, the solution is developed as follows:

$$\Psi(\lambda, x) = \frac{1}{2} \left(G \left(\frac{\frac{D}{2} - x}{\lambda} \right) + G \left(\frac{\frac{D}{2} + x}{\lambda} \right) \right) \tag{6.21}$$

with function $G(\alpha)$ defined as:

$$G(\alpha) = 1 - \exp(-\alpha) + \alpha E_i(\alpha) \tag{6.22}$$

Assuming a uniform angular distribution function (Eq. (6.14)) and using the integrand of Eq. (6.12), Dongari et al. derived an alternative viscosity function from the power-law function (Eq. (6.10)) for a slit geometry by using a Simpson 1/3 numerical approximation with 16 subintervals [170, 233]:

$$\begin{aligned}
\Psi(\lambda, x) = & 1 - \frac{1}{96} \left(\left(1 + \frac{\frac{D}{2} + x}{a} \right)^{1-n} + \left(1 + \frac{\frac{D}{2} - x}{a} \right)^{1-n} \right. \\
& + 4 \sum_{i=1}^8 \left(1 + \frac{\frac{D}{2} + x}{a \cdot \cos \left(\frac{(2i-1)\pi}{32} \right)} \right)^{1-n} \\
& + 4 \sum_{i=1}^8 \left(1 + \frac{D/2 - x}{a \cdot \cos \left(\frac{(2i-1)\pi}{32} \right)} \right)^{1-n} \\
& + 2 \sum_{i=1}^7 \left(1 + \frac{\frac{D}{2} + x}{a \cdot \cos \left(\frac{i\pi}{16} \right)} \right)^{1-n} \\
& \left. + 2 \sum_{i=1}^7 \left(1 + \frac{\frac{D}{2} - x}{a \cdot \cos \left(\frac{i\pi}{16} \right)} \right)^{1-n} \right)
\end{aligned} \tag{6.23}$$

However, plugging in the power-law defined in Eq. (6.11) and the uniform angular distribution from Eq. (6.14) for a slit flow yields an analytical solution that does not correspond to Eq. (6.23), but rather:

$$\Psi(\lambda, x) = \left(\frac{D}{2} + x \right) \cdot \ln \frac{\left(\frac{D}{2} + x + \lambda \right)}{\left(\frac{D}{2} + x \right)} + \left(\frac{D}{2} - x \right) \cdot \ln \frac{\left(\frac{D}{2} - x + \lambda \right)}{\left(\frac{D}{2} - x \right)} \tag{6.24}$$

Analytical solutions for a concentric cylindrical section were developed by Dongari et al. [161, 162, 235], but are not presentable in closed form and are thus omitted in this paper. A fitting for slit flows was proposed by Lopez and Bayazitoglu [234] by reanalyzing the original data from Dongari et al. [228] in order to improve the convergence of the data. However, the expression is not generalizable to complex geometries.

The expressions presented in this section are cumbersome and are not generalizable to complex porous media. However, the integral in Eq. (6.7) is generalizable and can be evaluated numerically if $R(\theta, \phi)$ is known. This is the main motivation for the development of the ray-tracing algorithm.

6.3 Theoretical comparison between planar wall functions and results from Eq. (6.7)

In this section, analytical solutions of Eq. (6.7) for the effective mean free path are compared with results that would be obtained from wall functions initially derived from planar geometries. The objective is to show that the combination of (1) mathematical expressions developed from the effective mean free path in planar domains and (2) a single distance function computed solely through the distance to the nearest solid boundary, can create a significant error for complex domains in the general case. This demonstrates the relevance of computing the mean free path from Eq. (6.7) in complex geometries with a distance $R(\theta, \phi)$ evaluated for each angle (θ, ϕ) by a ray-tracing algorithm.

Four theoretical geometries, presented in Figure 6.2, are considered here: (a) an infinitesimal point, (b) the interior of an infinitely long cylinder, (c) the interior of a sphere, and (d) a planar slit. To compare geometries on the same basis, the coordinate in the domain to calculate $\lambda_e(\mathbf{x})$ was chosen such that the distance to the nearest solid element was equal to the bulk mean free path λ . For geometries (a-c), the combination of a viscosity function developed in the case of a planar wall with a single distance function would thus return the result obtained for geometry (d). The closed-form expressions used for distances to the wall $R(\theta, \phi)$ and the results for λ_e obtained with Eq. (6.7) are summarized in Table 6.1. It can be inferred from Table 6.1 that the more the solid structure is open, the less it will be impacted by its distance to the nearest solid element, which is in agreement with earlier comparisons in the literature between convex and concave cylinders [161, 162]. Viscosity functions derived from planar walls cannot predict this effect. This warrants the use of a ray-tracing algorithm to evaluate $R(\theta, \phi)$ at each point \mathbf{x} of the gas domain.

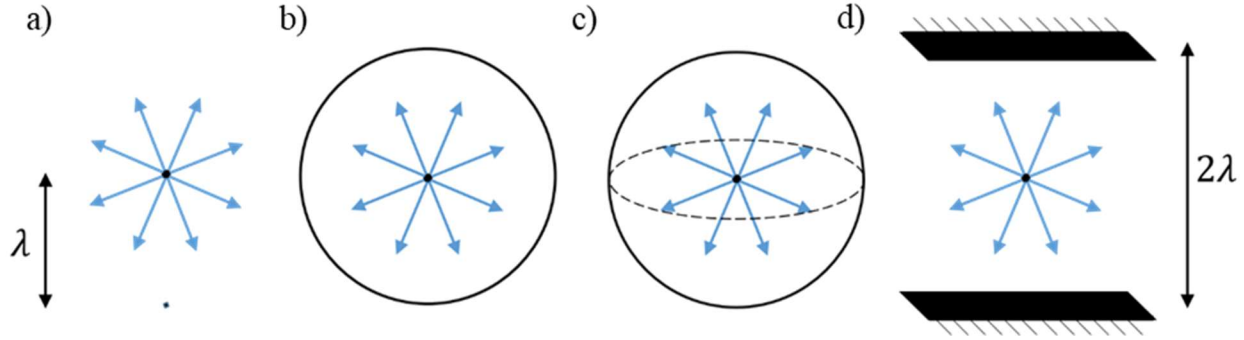


Figure 6.2 Comparison of four effective mean free paths calculated with a wall-function in the case of (a) a point, (b) the interior of a cylinder, (c) the interior of a sphere, and (d) a slit. The chosen point is always located one bulk mean free path λ away from the solid object.

Table 6.1 Effective mean free paths obtained from Eq. (6.7) for four different geometrical configurations.

Domain shape	(a) Infinitesimal point	(b) Interior of an infinite cylinder	(c) Interior of a sphere	(d) Planar slit
$R(\theta, \phi)$	∞ almost everywhere	$\frac{\lambda}{\sin \phi}$, with ϕ the angle with the cylinder axis	λ	$\frac{\lambda}{ \cos(\phi) }$, with ϕ the angle to the normal vector of the plane
λ_e using Eqs. (6.9) and (6.14)	λ	$\approx 0.7264\lambda$	$\approx 0.6321\lambda$	$\approx 0.8515\lambda$
λ_e using Eqs. (6.9) and (6.15)	λ	$\approx 0.7806\lambda$	$\approx 0.6321\lambda$	$\approx 0.7806\lambda$
λ_e using Eqs. (6.11) and (6.14)	λ	$\approx 0.5708\lambda$	$\frac{\lambda}{2}$	$\approx 0.6931\lambda$

6.4 Ray-tracing algorithm

In this section, a ray-tracing algorithm to find the distance to the nearest solid $R(\theta, \phi)$ for each point \mathbf{x} is presented. To apply Eq. (6.7), it is necessary to know the distance to the nearest wall, $R(\theta, \phi)$, for each point. As discussed in the previous section, the formulation of a closed-form solution for $R(\theta, \phi)$ may be too complicated or unavailable for a complex geometry. Consequently, a ray-tracing algorithm is required to evaluate R in each direction and to evaluate Eq. (6.7). The following pseudo-code was used to evaluate the effective mean free path through a complex geometry:

PSEUDO-CODE START

Define ray step size Δr

Define angle step size $\Delta\theta, \Delta\phi$

FOR \mathbf{x} , a point in the mesh,

FOR $\theta_i \in [0, 2\pi]$ with step size $\Delta\theta$

FOR $\phi_j \in [0, \pi]$ with step size $\Delta\phi$

Calculate \mathbf{v} , the directional components of the ray in x, y , and z

Initialize a collision flag $collision = false$ between the ray and the wall

Initialize $\mathbf{x}' = \mathbf{x}$, the actual position of the ray

Initialize $R(\theta_i, \phi_j) = 0$, the distance travelled by the ray

WHERE $R(\theta, \phi) < 10\lambda$ OR $collision = false$

$$R(\theta, \phi) = R(\theta, \phi) + \Delta r$$

$$\mathbf{x}' = \mathbf{x}' + \mathbf{v}\Delta r$$

IF \mathbf{x}' is inside a solid

$collision = true$

Evaluate $\lambda(R(\theta, \phi))$ from Eq. (6.6)

END IF

```

    END WHILE

    IF collision = false,  $\lambda(R(\theta, \phi)) = \lambda$ 

    END FOR

    END FOR

    Evaluate  $\lambda_e(\mathbf{x})$  from Eq. (6.7) with mid-point rule

END FOR

PSEUDO-CODE END.

```

The $\sin \phi$ term in Eq. (6.7) implies that rays with angles $\phi = 0$ and $\phi = \pi$ make no contribution to the integral given that $\sin 0 = \sin \pi = 0$. Evaluations of $R(\theta, \phi)$ are thus useless at the bounds. Newton-Cotes numerical integration approaches like the trapezoid rule and the Simpson 1/3 method, which evaluate functions at interval bounds, should thus be avoided. As the integrand is only piecewise-continuous, a Gaussian quadrature with one point (also called the mid-point rule) is thus used here to compute the integral in Eq. (6.7), with the angle space defined as $\theta_i = 2\pi(i - 1/2)/N_\theta$ and $\phi_j = \pi(j - 1/2)/N_\phi$, unless specified otherwise, with N_θ and N_ϕ being, respectively, the number of subdivisions used for θ and ϕ .

This pseudo-code is general enough to enable the ray-by-ray computation for any mesh type. In this article, it was only implemented on domains represented by a Boolean Cartesian grid (i.e., voxelization), where solid cells are encoded as 1's and fluid lattices as 0's. To detect a collision, the actual position of the ray is thus converted into a voxel position, as shown in Figure 6.3. The algorithm was further modified by computing the ray positions on block subdivisions of the domain where vector operations for each θ_i and ϕ_j were carried out on an entire block. Graphics processing units (GPUs) are best suited for this type of computation and were used in this work. To save computational costs and to be hardware-independent (on both CPU- and GPU- computers) as much as possible, this algorithm was implemented using the ArrayFire library [449]. All computations performed with this ray-tracing algorithm were carried out with single precision floating numbers. For the largest simulations, the computational time was around 32 hours on one Nvidia Tesla M2070.

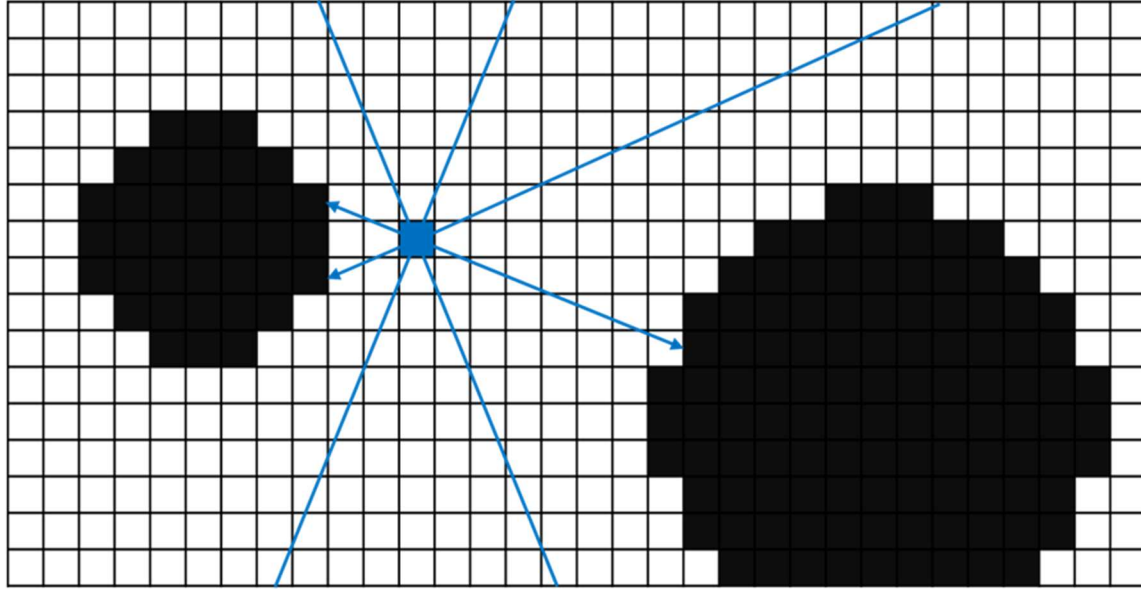


Figure 6.3 Illustration of the ray-tracing procedure on a regular Cartesian grid containing solid objects (in black).

6.5 Ray-tracing algorithm verification

As the extended Navier-Stokes equations need a local definition of the viscosity function, an error in this viscosity function can produce an error in the flow field. In this section, the accuracy of the ray-tracing algorithm is assessed by analyzing the impact of parameters such as the number of rays, the influence of the step size, grid refinement, and angle orientation. Two different geometries are analyzed. In Subsection 6.5.1, the effective mean free path is computed inside a planar slit and is compared to an analytical solution. In Subsection 6.5.2, the effective mean free path is computed inside an array of cylinders, where the computation of the effective viscosity is more challenging due to the local convexity of the geometry. As computations with power-law distributions (Eq. (6.11)) are impractical and as the cosine law (Eq. (6.15)) is inconsistent, only the exponential directional mean free path (Eq. (6.9)) with the uniform angular distribution function (Eq. (6.14)) is verified.

6.5.1 Planar flows

The accuracy of the ray-tracing algorithm is first verified for a planar slit of opening width D by comparing viscosity functions computed with the ray-tracing algorithm introduced in the previous section with the analytical solution derived in Eq. (6.21). For all simulations in the planar

slit, the Knudsen number $Kn = \lambda/D$ equals 1, which is well into the transition regime. The slit opening width was discretized with 10 nodes of size $\Delta x = D/10$. As the solution to a planar flow is known exactly for each point of the domain, the accuracy of the local effective mean free path does not depend on grid refinement. The Euclidian L^2 -norm was used to define the relative error using the available analytical solution:

$$E(\Psi) = \frac{\|\Psi_{rt} - \Psi_{an}\|_2}{\|\Psi_{an}\|_2} \quad (6.25)$$

where Ψ_{rt} is the numerical solution computed with the ray-tracing algorithm and Ψ_{an} is the solution given by Eq. (6.21). The ray-tracing algorithm accuracy is evaluated for three different combinations of parameters: (1) a rotated ray direction base with a fine ray step of $\Delta r = \Delta x/100$, (2) a rotated ray direction base with a coarse step of $\Delta r = \Delta x/3$, and (3) a non-rotated ray direction base with a fine step of $\Delta r = \Delta x/100$. A representation of the ray direction base rotation is shown in Figure 6.4. The smallest number of angles used was $N_\theta = 4$, with each refinement doubling the number of angles up to $N_\theta = 256$.

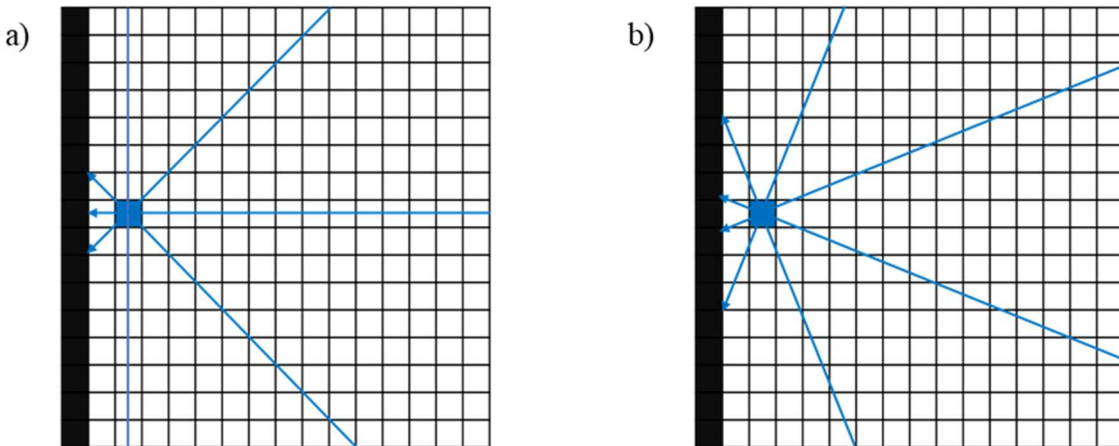


Figure 6.4 Illustration of the ray-tracing procedure with: (a) a non-rotated ray direction base and
(b) a rotated ray direction base.

The results for the relative error as a function of the angular step $\Delta\theta = \Delta\phi = 2\pi/N_\theta$ for the effective viscosity function are shown in Figure 6.5. An approximately second-order convergence was obtained for the planar slit, which was the clearest for the non-rotated ray direction base. This was expected, as the order of convergence is 2 for a function twice

differentiable such as the directional mean free path through a slit in Eq. (6.21). When a small number of rays was used, the angle orientation created a large error as rays parallel to planar surfaces were over-represented when the rays were not rotated. This source of error diminished as more rays were traced and was eliminated altogether when the set of selected ray directions was rotated by a half angular step. It can also be seen that the size of the ray step had a relatively low impact on the error of the scheme, except for the smallest angular steps. The magnitude of the error stayed small (< 0.05%) even with the relatively coarse ray step of $\Delta r = \Delta x/3$.

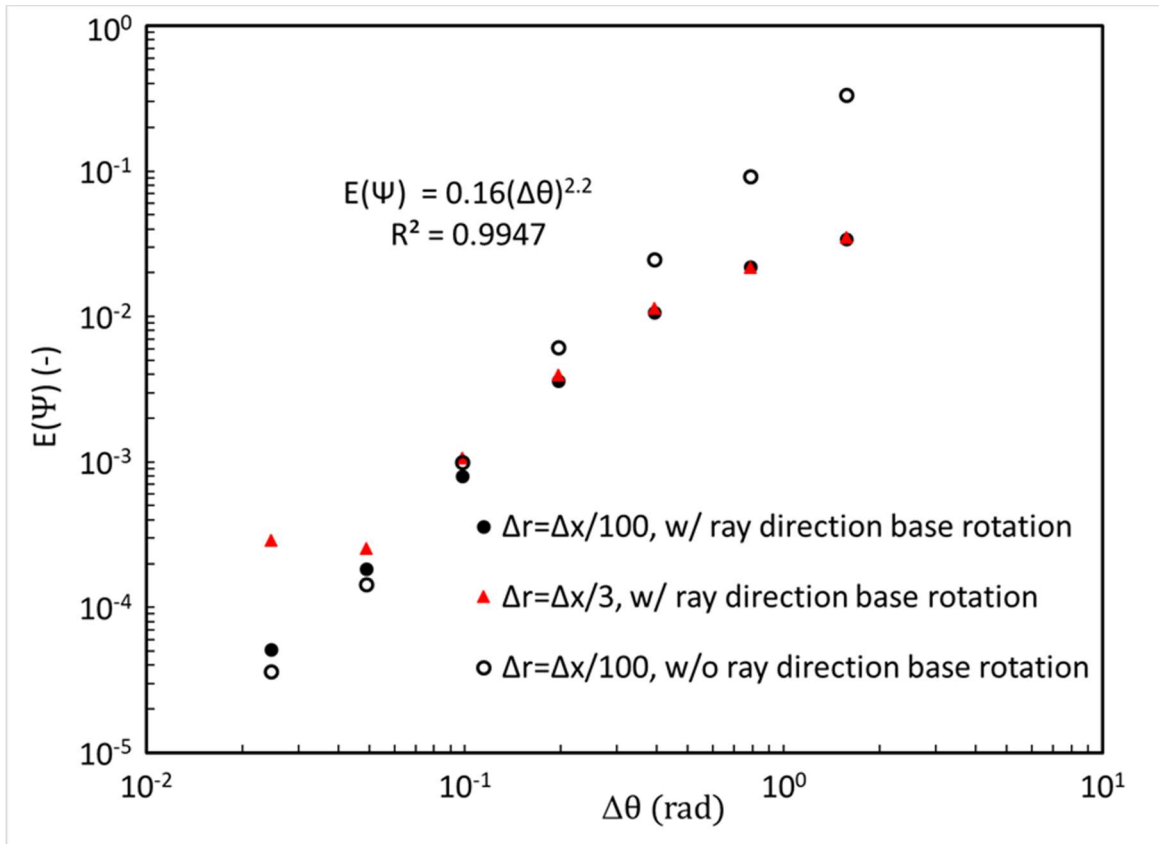


Figure 6.5 L^2 relative error ($E(\Psi)$) of the effective viscosity function Ψ using the ray-tracing algorithm for a slit geometry with (full symbols) and without (empty symbols) ray direction base rotation and for two different ray steps (Δr).

It can be seen that evaluating viscosity functions using a small sample of rays aligned with Cartesian grid lattices produces a large error. Using a total number of 4 rays [295] for a 2D grid or 18 rays [364] for a 3D grid can thus generate a significant error, even for the simple planar slit

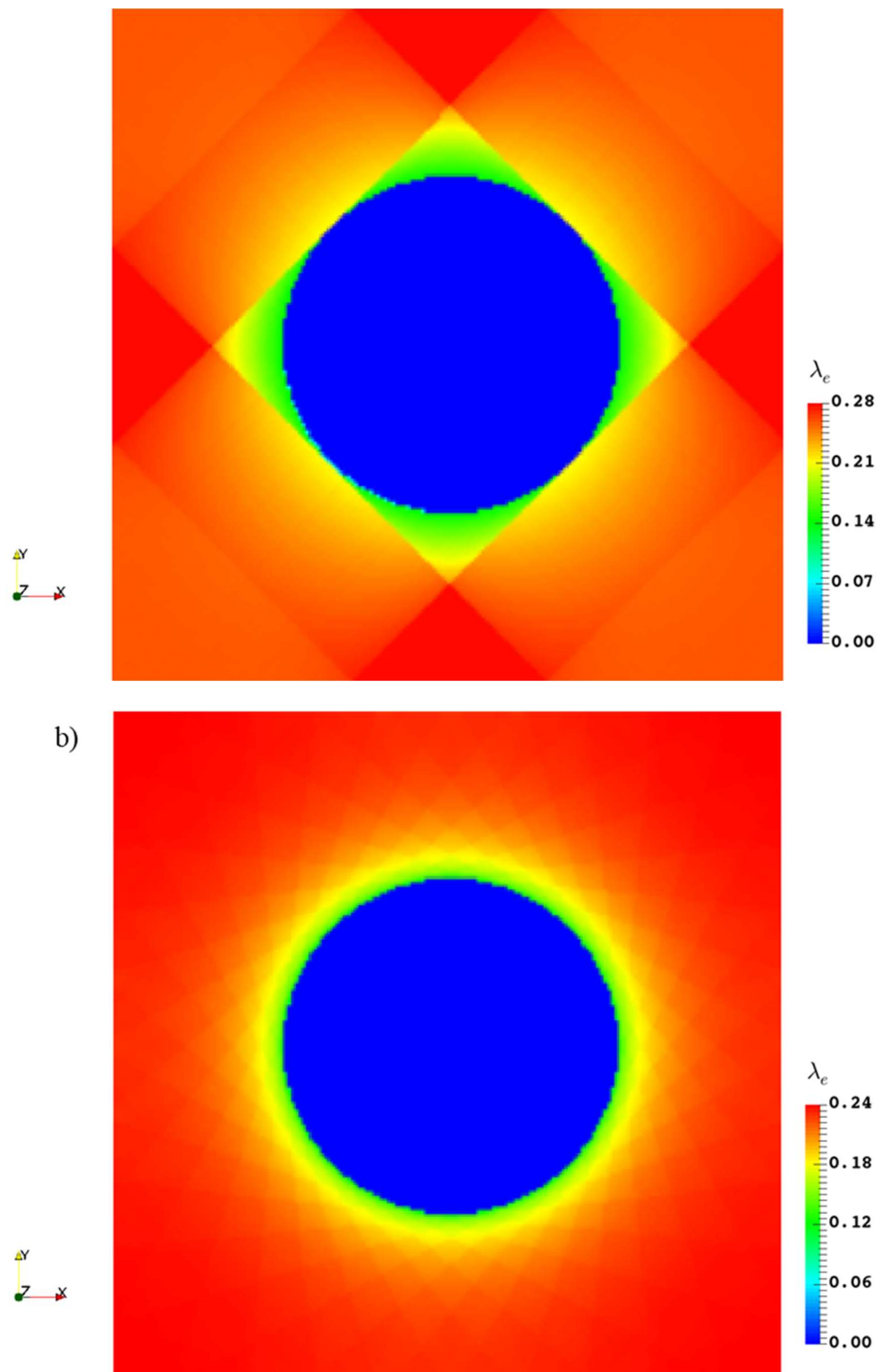
geometry. The proposed ray-tracing algorithm can decrease this error by orders of magnitude if the proper number of rays is used.

6.5.2 Array of cylinders

The accuracy of the ray-tracing algorithm is now verified for a periodic array of cylinders of diameter D in a square domain size of side $L = 2D$. For all simulations in the array of cylinders, $Kn = 2\lambda/D = 1$, which means a bulk mean free path of $\lambda = L/4$. The porosity of the structure was $1 - \pi/16 \approx 0.804$. For this geometry, both angle refinement and grid refinement tests were performed.

The angle refinement test was performed by increasing the number of rays used to evaluate the local effective mean free path. The smallest number of angles used was $N_\theta = 4$, with each refinement doubling the number of angles up to $N_\theta = 256$. As there are no analytical solutions for the effective mean free path through a periodic array of cylinders, the computation of the error was performed by assuming the solution recovered with $N_\theta = 256$ in place of the exact solution.

The impact of angle refinement can be observed visually in Figure 6.6a-c, where the effective mean free path λ_e scalar field is presented in the case of a $180 \times 180 \times 1$ grid. In Figure 6.6a, with $N_\theta = 4$, for some node positions, no rays reached any solid surface and huge discontinuities in the effective free path field forming aliasing-type patterns were created by the large weight each ray had in the integration. As the number of rays increased, these discontinuities decreased in magnitude, as can be seen in Figure 6.6b with $N_\theta = 32$, and disappeared as can be seen in Figure 6.6c with $N_\theta = 64$.



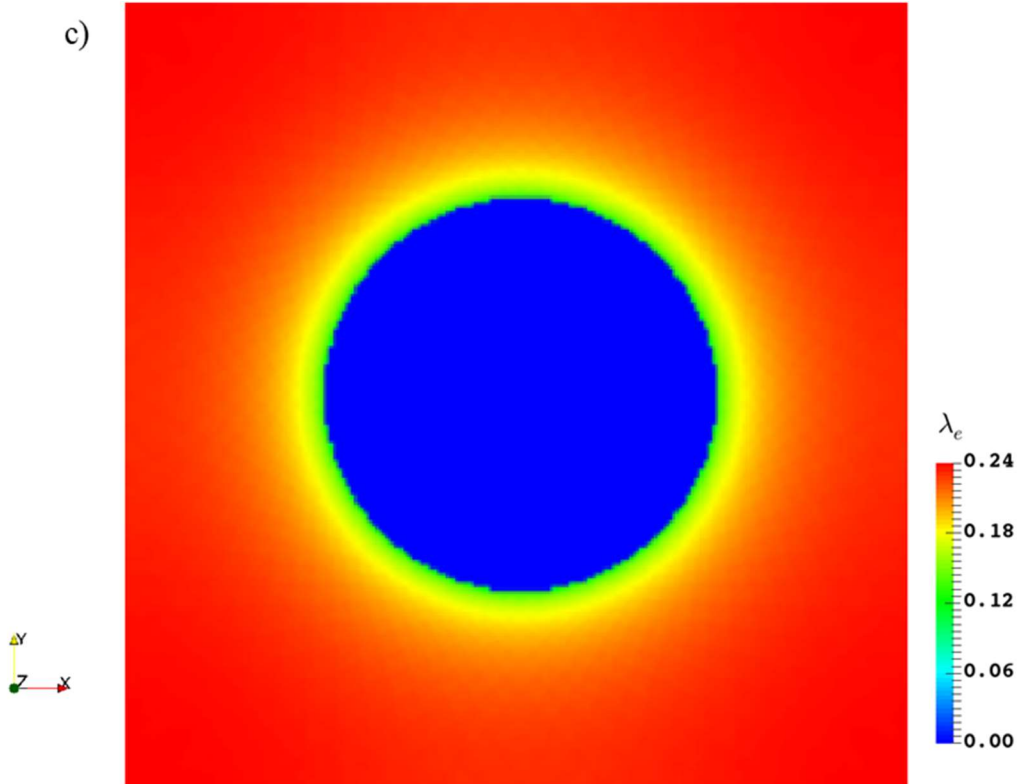


Figure 6.6 Effective mean free path ($\lambda_e(\mathbf{x})$) fields around an element of a periodic array of cylinders, as a function of the number of angles used: (a) $N_\theta = 4$, (b) $N_\theta = 32$, (c) $N_\theta = 64$.

The L^2 relative errors as a function of the angle step $\Delta\theta$ for the effective viscosity function Ψ are shown in Figure 6.7. As expected, the error decreased as the angular step decreased. However, the error in Figure 6.7 is one magnitude larger than for the planar flow in Figure 6.5. The convergence order decreased as more rays were used, and a sublinear convergence order (~ 0.86) was recovered for the two results with the smallest angular step. In the case of an array of cylinders, the directional mean free path is a piece-wise discontinuous function. The convergence order for a piece-wise discontinuous function with the mid-point integration scheme has an upper limit of 1. The high number of discontinuities in $R(\theta, \phi)$ for each point in this periodic geometry was responsible for the high magnitude of the error as a function of the angular step.

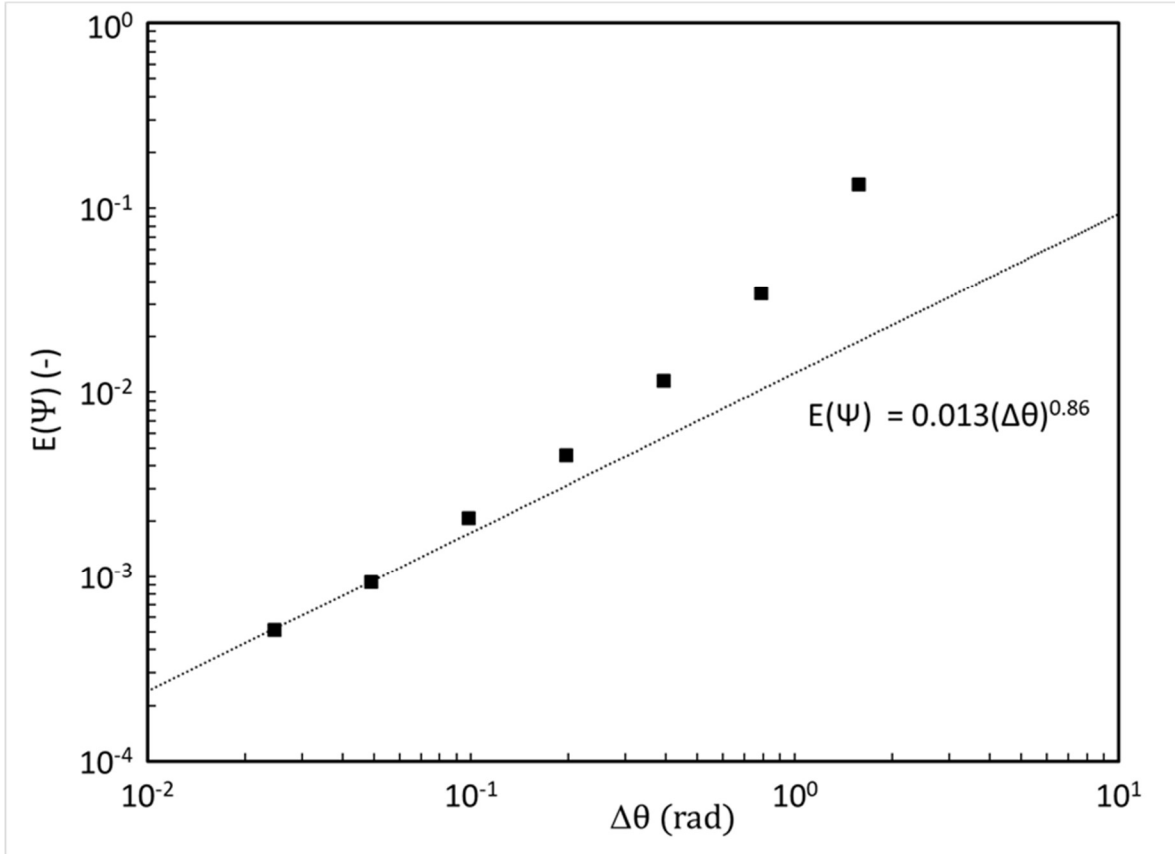


Figure 6.7 L^2 relative error ($E(\Psi)$) of the effective viscosity function Ψ for a cylinder array geometry using the ray-tracing algorithm, as a function of the angular step.

The grid refinement test was performed by increasing the number of nodes in the geometry. The coarsest grid investigated was $20 \times 20 \times 1$, with each grid resolution increment tripling the number of grid nodes in each direction. The parameter $N_\theta = 64$ was kept constant as the error $E(\Psi)$ was both quantitatively lower than 0.5% and was visually continuous. The computation of the error was performed by approximating the exact solution using the finest grid solution (i.e., that of the $1620 \times 1620 \times 1$ grid) as the reference solution and by projecting the results of the coarse grid on the fine grid without interpolation, with the error only being computed if a fluid node was present both on the coarse and fine grids. The L^2 relative errors as a function of the grid size dx for the effective viscosity function Ψ are shown in Figure 6.8. A convergence order of 0.66 was recovered, with an estimated L^2 error of 0.3% for the $540 \times 540 \times 1$ grid. An evaluation of the viscosity function at a discrete set of nodes thus had a measurable impact on the local effective

viscosity error for non-planar geometries. This can have repercussions on the accuracy of the flow field computed with the proposed extended Navier-Stokes solver.

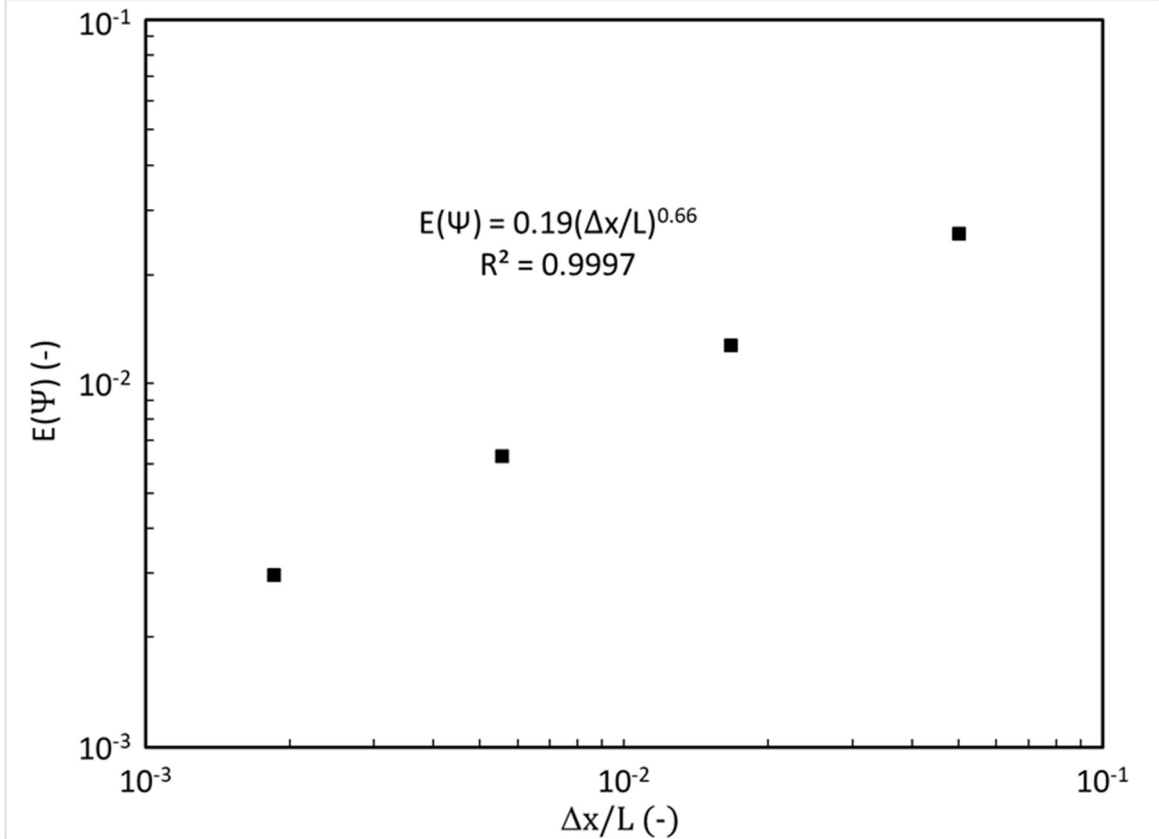


Figure 6.8 L^2 relative error ($E(\Psi)$) of the effective viscosity function Ψ for a cylinder array geometry using the ray-tracing algorithm, as a function of grid size.

6.6 Rarefied flow verification and validation

In this section, viscosity functions derived from the ray-tracing (RT) algorithm are introduced into our in-house LBM code. This methodology will be subsequently called LBM w/RT. It is presented in the Appendix and applies the following phenomenological model for slip velocity at a solid-fluid boundary [236]:

$$\mathbf{u}_s = A_1 \lambda_e \frac{\partial \mathbf{u}}{\partial \mathbf{n}} - A_2 \lambda_e \left(\frac{\partial}{\partial \mathbf{n}} \left(\lambda_e \frac{\partial \mathbf{u}}{\partial \mathbf{n}} \right) \right) \quad (6.26)$$

where \mathbf{u}_s is the velocity of the fluid at the wall relative to the wall velocity (or slip velocity), \mathbf{u} is the velocity vector, \mathbf{n} is the normal vector to a solid surface, and A_1 and A_2 are constants derived

from theoretical models or experimental values. Unless stated otherwise, the slip coefficients are set at $A_1 = 1$ and $A_2 = 0.31$.

Two geometries are presented in Subsections 6.6.1-6.6.2: a slit and an array of cylinders. Both geometries are represented in Figure 6.9. A convergence analysis and a comparison with data from the literature will be performed for the two cases.

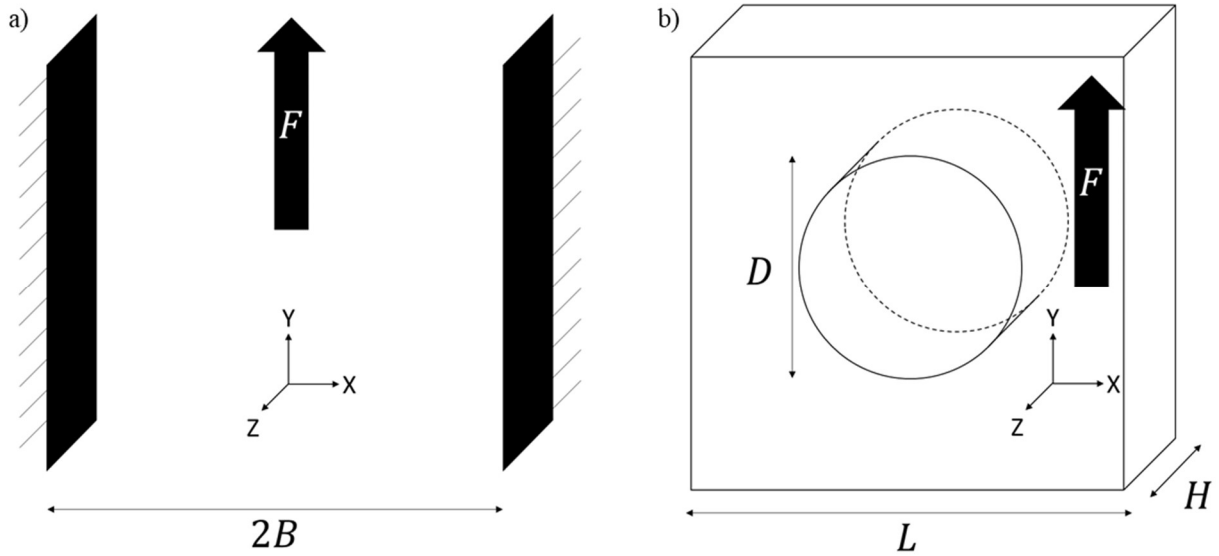


Figure 6.9 Schematic representations of the flow simulated through: (a) a slit and (b) an array of cylinders.

6.6.1 Flow through a slit in the rarefied regime

Convergence analysis of the LBM w/RT was carried out for a slit flow driven by a body force for $Kn = \lambda/D = 1$, where D is the width of the slit. The number of nodes in x and y was always set equal to 10, while the coarsest discretization in z used 10 nodes, with each refinement step doubling the number of nodes in z up to 320. The relative error was computed by comparing the volumetric flow rate for each grid size to the Richardson extrapolation from a series of results obtained with different grids. This convergence analysis is presented in Figure 6.10. An approximate first-order (≈ 1.1) convergence was recovered. Two explanations can be given for this behavior. The LBM, in and of itself, has a first-order convergence for a fixed Knudsen number [237]. However, for a constant viscosity case, the regularized MRT-LBM implementation described in the Appendix has a much lower error magnitude, even for the coarsest grid ($\approx 10^{-5}$)

[443]. The more likely explanation is that the error in the case of a flow where a non-constant viscosity is approximated as piecewise constants is approximately proportional to the grid size Δx used to evaluate the viscosity.

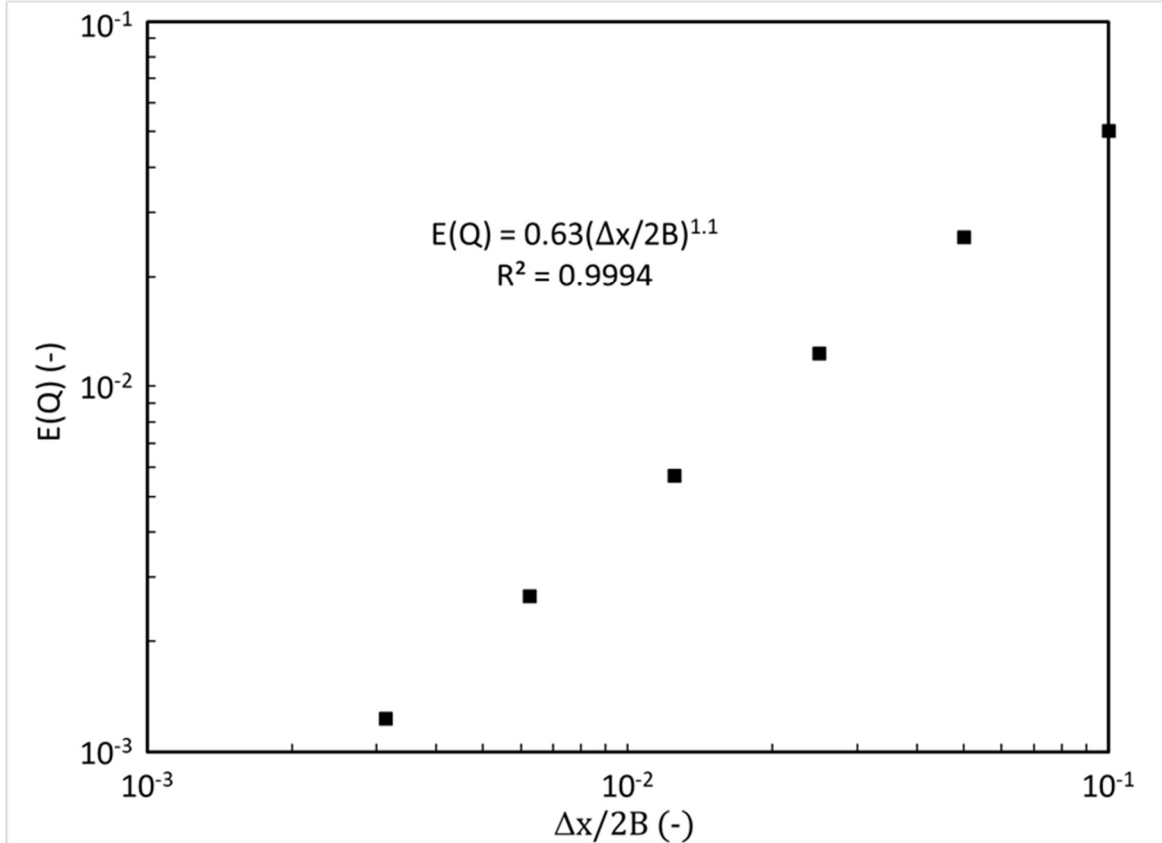


Figure 6.10 Relative error of the volumetric flow rate for a slit geometry using the LBM code as an extended Navier-Stokes solver with the viscosity function computed using the ray-tracing algorithm.

The LBM w/RT was then applied to the rarefied slit flow over a wide range of Knudsen numbers ($0.05 < Kn < 10$). Four combinations of coefficients A_1 , A_2 , and viscosity functions were tested, as summarized in Table 6.2, where LBM-1 to LBM-3 bring into play combinations of analytical solutions for the viscosity functions and slip coefficients from the literature. Results for these combinations have already been published by our group [237]. LBM-4 relies on a combination of the slip coefficients used by Dongari et al. (also used in LBM-3) and a viscosity function given by the viscosity function with uniform angle and exponential path distributions. Slip velocity prediction has not been tested with such a combination in the work of Abramov [226]. LBM-4 is thus here tested for the first time. However, these combinations have been compared to

a numerical solution of the linearized Boltzmann equation [171] and to the experimental results from [352] as reported by Guo et al. [236].

Table 6.2 Viscosity functions and slip coefficients for the velocity BC tested in a rarefied regime.

Case	Ψ	A_1	A_2	Ref.
Navier-Stokes w/o slip	1	0	0	-
LBM-1	1	1.146	0.9796	Cercignani [138]
LBM-2	Eq. (6.19)	0.8183	0.6531	Guo et al. [236]
LBM-3	Eq. (6.23)	1	0.31	Dongari et al. [233]
LBM-4	RT (Eqs. (6.7), (6.9) and (6.14))	1	0.31	Abramov [226] and Dongari et al. [233]

Predictions of the normalized mass flow M are shown in Figure 6.11. Slip flows that do not account for the lower effective viscosity in the Knudsen layers (NS and LBM-1) are clearly unable to recover solutions to the Boltzmann equation and experimental measurements in the transition regime $Kn > 0.1$. However, LBM-2, LBM-3, and LBM-4 reproduced the normalized mass flow on the whole range of Knudsen numbers very well, with the new LBM-4 exhibiting improved agreement with respect to the experimental data, compared to the former methods, mainly in the higher range of Knudsen numbers ($2 < Kn < 10$).

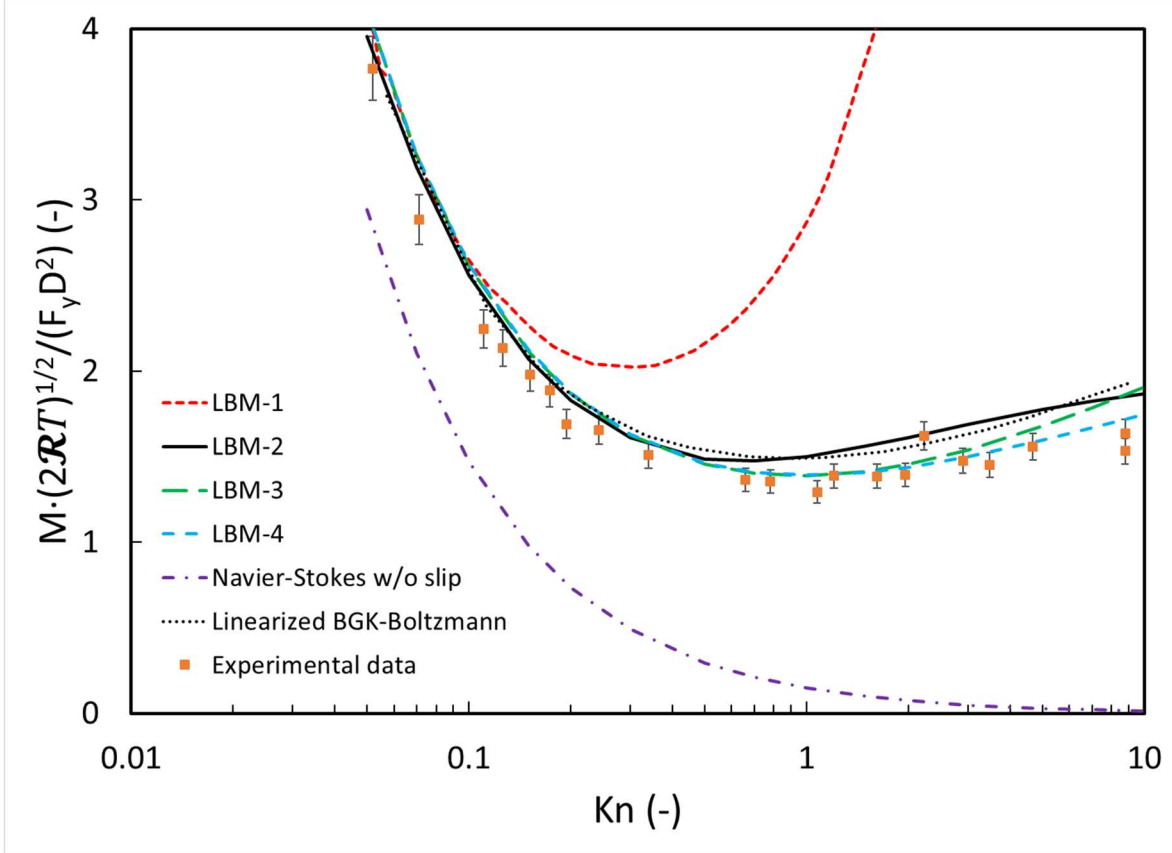


Figure 6.11 Prediction of the normalized mass flow for a rarefied slit flow using the LBM w/RT code as an extended Navier-Stokes solver compared with numerical solution of the linearized Boltzmann equation [171] and experimental results [352] reported by Guo et al. [236]. Acronyms refer to the methods presented in Table 6.2.

6.6.2 Flow through a cylinder array in the rarefied regime

A convergence analysis of the LBM w/RT is now discussed in the case of a flow through a cylinder array driven by a body force for $Kn = 2\lambda/D = 1$, with the same dimensions as in Section 6.5.2. The number of nodes in z was always equal to 10, while the coarsest discretization in x and y used 20 nodes, with each refinement step tripling the number of nodes in x and y up to 540. The relative error was computed by comparing the volumetric flow rate for each simulation to the Richardson extrapolation of the series of results obtained. The convergence analysis is presented in Figure 6.12. Compared to the slit, there was an increase in the error of approximately one order of magnitude for the finest simulations. For the second finest grid (i.e., $540 \times 540 \times 1$), a discrepancy of $\approx 3\%$ was reached, which is rather significant. An order of convergence of

approximately one-half was recovered (≈ 0.52), indicating a small degradation of the error compared to the evaluation of the viscosity function in Section 6.5.2, where the order of convergence was ≈ 0.66 . Nevertheless, Figure 6.12 shows clearly that simulations were in the asymptotic regime, which shows the Richardson extrapolation can be safely used [320].

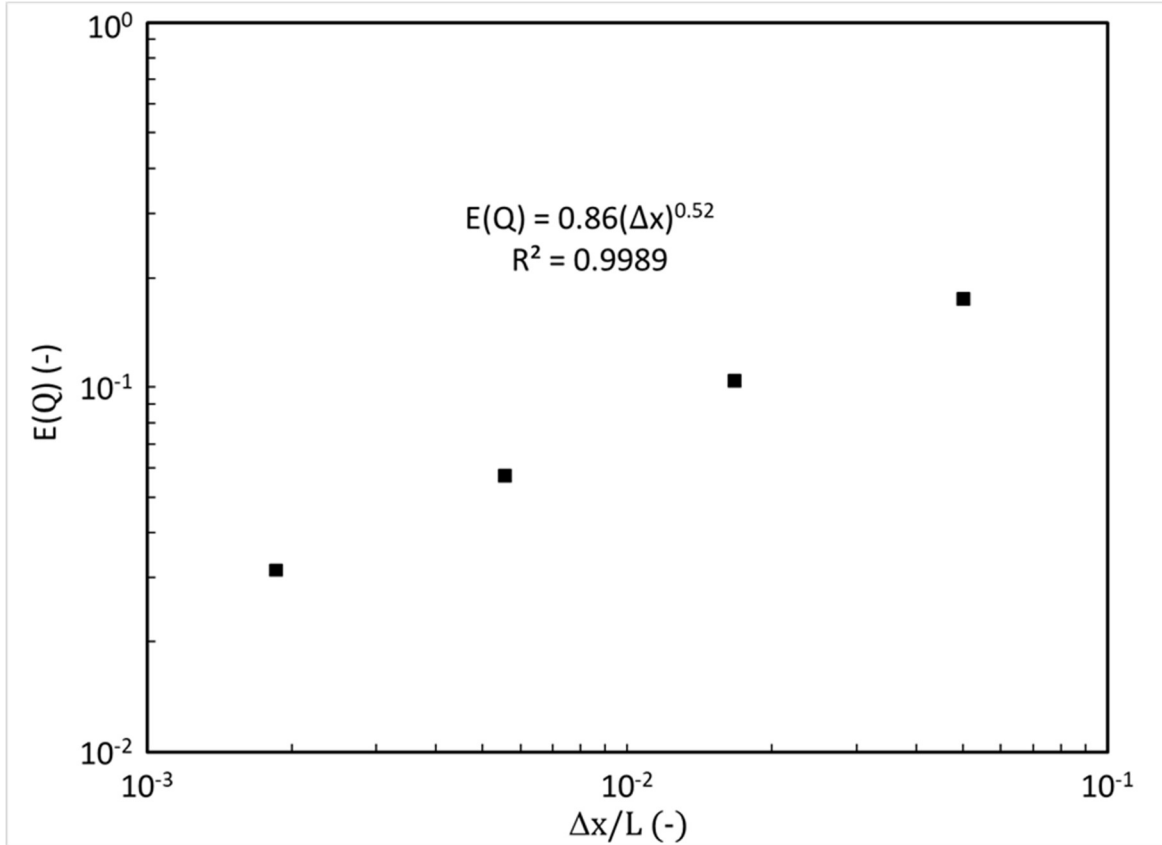


Figure 6.12 Relative error of the volumetric flow rate for a periodic array of cylinders using the LBM w/RT code as an extended Navier-Stokes solver with the viscosity function computed using the ray-tracing algorithm.

The results from the LBM w/RT were applied to the rarefied flow through a cylinder array in the range $0.1 < Kn < 1$ and then compared the Richardson extrapolations of these results were then compared to a no-slip Navier-Stokes solution, a numerical solution of the linearized Boltzmann equation, and a solution from a second-order approximation of the Boltzmann equation, all three of which were proposed by Taguchi et al. [450]. Results for the LBM w/o RT (i.e., with $\Psi = 1$) were also added for comparison purposes. Predictions of the normalized mass flow M are shown in Figure 6.13. As can be seen, the LBM w/RT predictions are slightly better than those of the LBM w/o RT. However, the flow was underpredicted by the LBM w/RT results, compared to

the solutions proposed by Taguchi et al. [450], with the discrepancy increasing with the Knudsen number. Three sources of error may explain this finding: (1) the use of a D3Q15 lattice, (2) the phenomenological model of Eq. (6.26), and (3) the absence of proportionality between the effective mean free path and the effective viscosity (Eq. (6.2)) in the case of a cylinder array, which is fundamental to the extended Navier-Stokes equation framework.

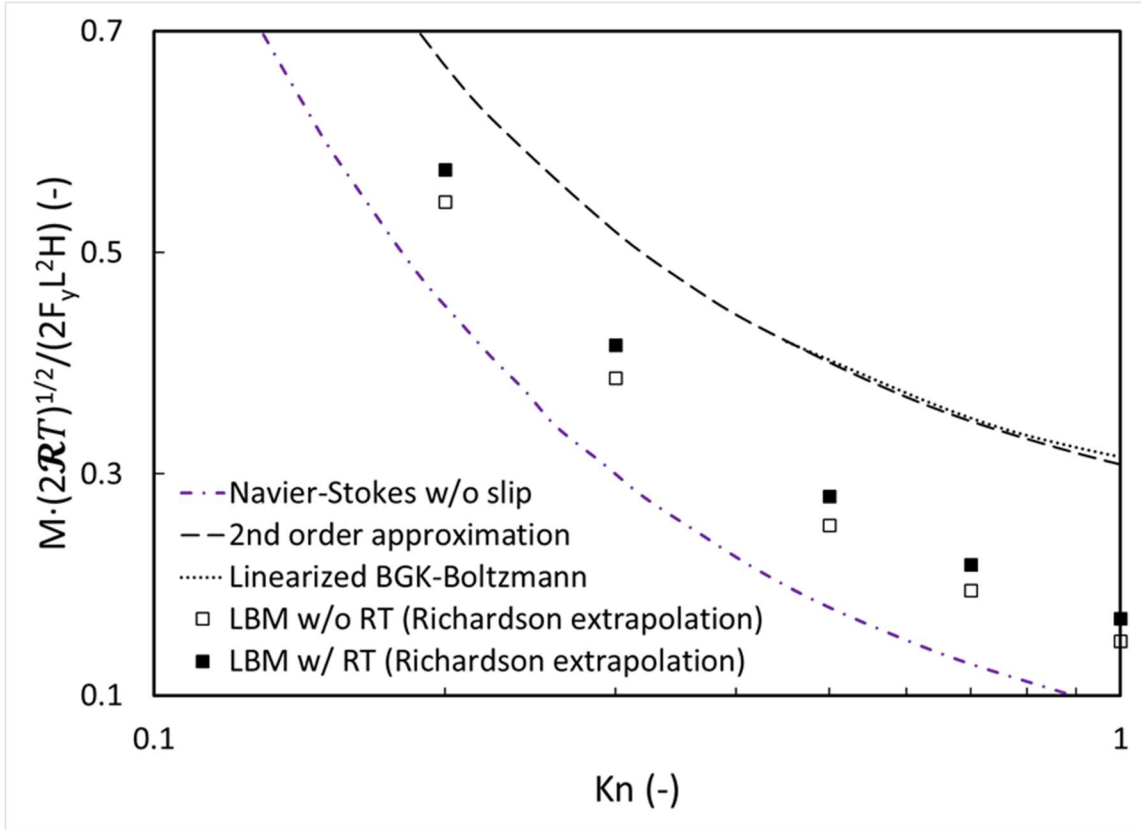


Figure 6.13 Predictions of the normalized mass flow for a cylinder array using the LBM w/RT code as an extended Navier-Stokes solver with the viscosity function computed with the ray-tracing algorithm.

Sources of error for the D3Q15 lattice were investigated in [443] for a flow in the slip regime. While it is known that the error increases with the Knudsen number for a given grid, the LBM w/RT results shown in Figure 6.13 are Richardson extrapolations. For the finest resolutions with the LBM solver in [443], correlations for slip flows were relatively well recovered for all Knudsen numbers. In Section 6.6.1, the comparison between the linearized Boltzmann equation and the experimental results was excellent in the planar case. There may be a specific issue with

the D3Q15 lattice when a non-unitary viscosity function is used for non-planar geometries. A lattice with more isotropy such as the D3Q27 lattice might fix this issue [428].

The slip flow phenomenological model of Eq. (6.26) was validated on a semi-infinite plane flow (the co-called Kramer's problem), a slit flow (Poiseuille flow), a solid plane moving relative to a stationary solid plane (plane Couette flow,) and a concentric cylinder geometry where one cylinder moves relative to the other (cylindrical Couette flow) [161, 162, 235, 236]. These geometries were either very simple in the case of Kramer's problem, or relatively close like for the Poiseuille and Couette flows. To the authors' knowledge, this is the first time Eq. (6.26) has been applied for a non-constant viscosity function in a relatively open geometry like a cylinder array. Taguchi et al. [450] did not calculate any coefficients for A_2 . A review paper for slip BCs [158] mentioned that the physics behind coefficient A_2 is not as well understood as for A_1 . More comparisons with results from other Boltzmann equation solvers such as DUGKS or the DSMC could be carried out to elucidate the role of geometry on A_2 and to investigate a more universal form for a slip BC than Eq. (6.26).

In addition, it remains to be determined whether there is a proportional relation between the effective mean free path and the effective viscosity as assumed in Eq. (6.2). This is an important question that could undermine the validity of the extended Navier-Stokes framework. In [439], this hypothesis was criticized for the use of an insufficient space and time bin in the MD method. This criticism was answered for a slit [224, 440]. However, to our knowledge, there has been no validation of this hypothesis for relatively open geometries such as a cylinder array. It should be remembered that the Knudsen layer appears as a gas flow that deviates from local thermodynamic equilibrium in the rarefied regime. Non-equilibrium components of high-order moments that cancel each other in planar geometries may not do so for open non-planar geometries. The expression of the stress tensor field would then need to be modified in the case of such open non-planar geometries. In other words, a deviation from linearity between the effective viscosity and the effective mean free path could thus arise in open non-planar geometries.

The three sources of error identified in this section each merit their own investigation. Nevertheless, the convergence analysis showed empirically that the proposed LBM w/RT is asymptotically convergent even for non-planar flows.

6.7 Conclusion

In this paper, a new approach to model the decrease in viscosity in the Knudsen layer caused by rarefied flows by means of an effective viscosity function introduced in the extended Navier-Stokes equations is proposed. A literature review of existing effective viscosity functions showed that the combination of uniform ray distribution and exponential free path distribution is the most conceptually sound approach. Theoretical comparisons have shown that wall functions do not predict the difference between the effective viscosity functions in concave and convex geometries reported in the literature, which warrants the use of an effective viscosity function computed for each geometry.

To compute the effective mean free path, a new ray-tracing algorithm is proposed to generate effective viscosity functions in order to be able to tackle complex porous media. The effective mean free path is computed using a numerical integral, by which the distance from each fluid cell to the nearest solid cell is computed. Although there may be more efficient ways to sample the space and to perform the ray-tracing, the proposed algorithm is straightforward and easily portable across GPU architectures. However, at the time this article was being written, new GPUs with hardware-accelerated ray-tracing were being released, which could decrease the computational time required by ray-tracing. The pseudo-code of the ray-tracing algorithm presented in this paper can be used in combination with any numerical solver.

The accuracy of the ray-tracing algorithm was verified for a slit and a periodic array of cylinders. A quadratic convergence order was recovered for a slit, while a sublinear ~ 0.86 convergence order was recovered for a periodic array of cylinders. It was shown that a low number of rays creates large discontinuities in the effective viscosity field. The number of rays required to achieve an error lower than 0.01% depended on the geometry (2048 for a slit, 8192 for a cylinder). This proves that using only 4 rays in a 2D domain [295] and 18 directions in a 3D domain [364] create large errors. It was also shown that the ray direction base should be rotated to diminish further the error.

The ray-tracing algorithm was then used in combination with an LBM solver and a D3Q15 lattice to simulate flows in the rarefied regime. A new combination of a set of slip coefficients, ray distribution, and free path distribution showed better results for a wide range of Knudsen numbers ($0.05 < Kn < 10$) than for any other previous combination of slip BCs and viscosity functions

proposed in the literature. Although the method was effective for the slit flow case in this range of Knudsen numbers, the proposed methodology resulted in an increasing underprediction of the volumetric flow rate for a periodic array of cylinders in the Knudsen number range $0.2 < Kn < 1$. Three potential sources of error were proposed to explain this discrepancy: (1) the use of a D3Q15 lattice, (2) the slip model proposed by Guo et al. [236], and (3) the absence of a proportionality relation between the effective mean free path and the effective viscosity in complex geometries, as opposed to the classical hypothesis. Future studies will investigate these three fundamental aspects of the simulation of rarefied flows through complex porous media.

Acknowledgements

Financial support from the Simulation-based Engineering Science (Génie Par la Simulation) program funded through the CREATE program from the Natural Sciences and Engineering Research Council of Canada is gratefully acknowledged.

Appendix – The Lattice-Boltzmann method

The LBM used to solve rarefied flows is presented in this section. The flow in the LBM is represented by populations evolving according to a propagation-collision scheme as follows:

$$f_i(\mathbf{x} + \mathbf{c}_i \delta_t, t + \delta_t) - f_i(\mathbf{x}, t) = \Omega_i + F_i \delta_t \quad (6.27)$$

where \mathbf{c}_i is the velocity of the population f_i , Ω_i is the collision operator, F_i is a force term applied to each population, and δ_t is the time step. Conserved macroscopic quantities such as density and momentum are recovered from populations as follows:

$$\rho = \sum_{i=0}^{Q-1} f_i \quad (6.28)$$

$$\rho \mathbf{u} = \sum_{i=0}^{Q-1} f_i \mathbf{c}_i + \mathbf{F} \frac{\delta_t}{2} \quad (6.29)$$

where \mathbf{F} is the body force and Q is the number of velocities in the lattice. In this article, the D3Q15 lattice is used, which has $Q = 15$ velocities.

A multiple relaxation time (MRT) collision operator has been reported in several papers as having contributed to the correct imposition of slip BCs [114, 236, 237, 339, 341, 418, 419, 443]. An MRT-LBM was thus used in this paper. The MRT collision operator transforms populations into moments (such as density, momentum, energy, stress, etc.) and relaxes each moment with a different relaxation rate as follows:

$$\Omega_i = - \sum_{j=0}^{Q-1} (\mathbf{M}^{-1} \mathbf{S} \mathbf{M})_{ij} (f_j - f_j^{(eq)}) \quad (6.30)$$

where \mathbf{M} is a transformation matrix from the populations to the moments that, for the D3Q15 lattice, corresponds to:

$$\left(\begin{array}{cccccccccccccccc} 1 & 1 & 1 & 1 & 1 & 1 & 1 & 1 & 1 & 1 & 1 & 1 & 1 & 1 & 1 & 1 \\ -2 & -1 & -1 & -1 & -1 & -1 & -1 & 1 & 1 & 1 & 1 & 1 & 1 & 1 & 1 & 1 \\ 16 & -4 & -4 & -4 & -4 & -4 & -4 & 1 & 1 & 1 & 1 & 1 & 1 & 1 & 1 & 1 \\ 0 & 1 & -1 & 0 & 0 & 0 & 0 & 1 & -1 & 1 & -1 & 1 & -1 & 1 & 1 & -1 \\ 0 & -4 & 4 & 0 & 0 & 0 & 0 & 1 & -1 & 1 & -1 & 1 & -1 & 1 & 1 & -1 \\ 0 & 0 & 0 & 1 & -1 & 0 & 0 & 1 & 1 & -1 & -1 & 1 & 1 & -1 & -1 & -1 \\ 0 & 0 & 0 & -4 & 4 & 0 & 0 & 1 & 1 & -1 & -1 & 1 & 1 & -1 & -1 & -1 \\ 0 & 0 & 0 & 0 & 1 & -1 & 1 & 1 & 1 & 1 & -1 & -1 & -1 & -1 & -1 & -1 \\ 0 & 0 & 0 & 0 & -4 & 4 & 1 & 1 & 1 & 1 & -1 & -1 & -1 & -1 & -1 & -1 \\ 0 & 2 & 2 & -1 & -1 & -1 & -1 & 0 & 0 & 0 & 0 & 0 & 0 & 0 & 0 & 0 \\ 0 & 0 & 0 & 1 & 1 & -1 & -1 & 0 & 0 & 0 & 0 & 0 & 0 & 0 & 0 & 0 \\ 0 & 0 & 0 & 0 & 0 & 0 & 0 & 1 & -1 & -1 & 1 & 1 & -1 & -1 & 1 & 1 \\ 0 & 0 & 0 & 0 & 0 & 0 & 1 & -1 & 1 & -1 & -1 & -1 & 1 & 1 & -1 & 1 \\ 0 & 0 & 0 & 0 & 0 & 0 & 1 & -1 & 1 & -1 & -1 & 1 & -1 & 1 & 1 & -1 \end{array} \right) \quad (6.31)$$

\mathbf{S} is a diagonal matrix containing the relaxation rates, which for the D3Q15 lattice corresponds to:

$$\mathbf{S} = \text{diag}(s_\rho, s_e, s_\epsilon, s_j, s_q, s_j, s_q, s_j, s_q, s_s, s_s, s_s, s_s, s_s, s_t) \quad (6.32)$$

where s_ρ , s_e , s_ϵ , s_j , s_q , s_s , and s_t are, respectively, the relaxation rates related to density, energy, energy squared, momentum, energy flux, stress, and an antisymmetric third-order moment. In particular, for a rarefied flow, the relaxation time related to stress $\tau_s = 1/s_s$ must take the value:

$$\tau_s = \frac{1}{2} + \sqrt{\frac{6}{\pi}} \frac{\lambda}{\delta_x} \Psi(\lambda, \mathbf{x}) \quad (6.33)$$

The equilibrium distribution populations $f_i^{(eq)}$ for the D3Q15 lattice correspond to:

$$f_i^{(eq)} = w_i \rho \left(1 + \frac{\mathbf{c}_i \cdot \mathbf{u}}{c_s^2} + \frac{(\mathbf{c}_i \cdot \mathbf{u})^2}{c_s^4} - \frac{\mathbf{u}^2}{2c_s^2} \right) \quad (6.34)$$

where w_i are weights associated with each population:

$$\begin{aligned} w_0 &= 2/9 \\ w_{1-6} &= 1/9 \\ w_{7-14} &= 1/72 \end{aligned} \quad (6.35)$$

where \mathbf{c}_i corresponds to the following velocity set:

$$\begin{aligned} c_0 &= (0,0,0) \\ c_1 = -c_2 &= (1,0,0) \\ c_3 = -c_4 &= (0,1,0) \\ c_5 = -c_6 &= (0,0,1) \\ c_7 = -c_{14} &= (1,1,1) \\ c_8 = -c_{13} &= (-1,1,1) \\ c_9 = -c_{12} &= (1,-1,1) \\ c_{10} = -c_{11} &= (-1,-1,1) \end{aligned} \quad (6.36)$$

and where $c_s = 1/3$ is the so-called velocity speed of the lattice. In this implementation, the lattice unit system was used, where $\delta_x = \delta_t = 1$ and all the dimensional units are adimensionalized accordingly.

Although the NSEs were recovered with the MRT-LBM described above, deviations from equilibrium became non-negligible as the Knudsen number increased. Moments of order higher than 2 must be filtered out, as they create grid-dependent spurious jets for rarefied flows with non-planar solid boundaries [195, 291-297, 443]. To solve this problem, the regularization technique needs to be applied by first considering the non-equilibrium parts of each population $f_i^{(neq)}$:

$$f_i^{(neq)} = f_i - f_i^{(eq)} \quad (6.37)$$

Non-equilibrium components are then reprojected on the Hermite polynomial basis of the lattice:

$$f_i^{(neqr)} = \frac{w_i}{2c_s^2} H_{i\alpha\beta}^{(2)} \left(\frac{\mathbf{c}_i}{c_s} \right) : \sum_{i=0}^{Q-1} f_i^{(neq)} \mathbf{c}_{i\alpha} \mathbf{c}_{i\beta} \quad (6.38)$$

where $H_{i\alpha\beta}^{(2)} \left(\frac{\mathbf{c}_i}{c_s} \right) = \mathbf{c}_{i\alpha} \mathbf{c}_{i\beta} / c_s^2$ is the Hermite polynomial of the second order, $\mathbf{c}_{i\alpha} \mathbf{c}_{i\beta}$ is a dyadic or outer product and : represents the double dot product of two tensors. The new post-regularized populations are thus recomputed as:

$$f_i^{(r)} = f_i^{(eq)} + f_i^{(neqr)} \quad (6.39)$$

Introducing Eq. (6.39) into the collision operator in Eq. (6.30) and the LBM scheme of Eq. (6.27) leads to:

$$f_i(\mathbf{x} + \mathbf{c}_i \delta_t, t + \delta_t) = f_i^{(eq)} + \mathbf{M}^{-1} (\mathbf{I} - \mathbf{S}) \mathbf{M} f_i^{(neqr)} + F_i \delta_t \quad (6.40)$$

For the MRT-LBM, the force term F_i is written as:

$$F_i = \mathbf{M}^{-1} \left(\mathbf{I} - \frac{\mathbf{S}}{2} \right) \mathbf{M} \bar{F}_i \quad (6.41)$$

with:

$$\bar{F}_i = w_i \left(\frac{\mathbf{c}_i \cdot \mathbf{u}}{c_s^2} + \frac{\mathbf{u} \mathbf{F} : (\mathbf{c}_i \mathbf{c}_i - c_s^2 \mathbf{I})}{c_s^4} \right) \quad (6.42)$$

and where \mathbf{F} is the body force.

In a recent publication by the authors [237], an extension of the DBB BC was presented as a non-ambiguous and straightforward way to specify kinetic BCs for populations leaving a solid-surface as follows:

$$f_i = r f_i^{(BB)} + (1 - r) f_i^{(D)} \quad (6.43)$$

where $f_i^{(BB)}$ is the bounce-back term:

$$f_i^{(BB)} = f_{oppdir(i)} \quad (6.44)$$

where the subscript $oppdir(i)$ indicates the index of the population in the opposite direction to i , where $f_i^{(D)}$ is the diffusive term:

$$f_i^{(D)} = K f_i^{(eq)}(\rho_w, \mathbf{0}) \quad (6.45)$$

where the subscript w represents a quantity at the wall, with the factor K ensuring a non-penetration BC on the solid boundary with:

$$K = \frac{\sum_{\mathbf{c}_i \cdot \mathbf{n} < 0} |\mathbf{c}_i \cdot \mathbf{n}| f_i}{\sum_{\mathbf{c}_i \cdot \mathbf{n} < 0} |\mathbf{c}_i \cdot \mathbf{n}| f_i^{(eq)}(\rho_w, \mathbf{0})} \quad (6.46)$$

and where $0 \leq r \leq 1$ is the kinetic ratio for the DBB BC. The value of the kinetic ratio developed for the regularized MRT-LBM in recent work by the authors [443] is given as:

$$r = \frac{\tilde{\tau}_{sw}^2(1 - A_1\chi) + \delta_x \tilde{\tau}'_{sw} \left(-\frac{1}{8} + \tilde{\tau}_{sw}(1 - A_1\chi) \right)}{\tilde{\tau}_{sw}^2(1 + A_1\chi) + \delta_x \tilde{\tau}'_{sw} \left(\frac{1}{8} + \tilde{\tau}_{sw}(1 + A_1\chi) \right)} \quad (6.47)$$

where $\tilde{\tau}_{sw} = \tau_{sw} - 1/2$, τ_{sw} is the value of τ_s at the wall and $\tilde{\tau}'_{sw}$ is the derivative of $\tilde{\tau}_{sw}$ in the direction perpendicular to the wall. Furthermore, the relaxation time $\tau_q = 1/s_q$ for the D3Q15 lattice must be set to:

$$\tau_q = \frac{-7(8\tilde{\tau}_{sw}^2(1 + A_1\chi) + \delta_x \tilde{\tau}'_{sw}(1 + 8\tilde{\tau}_{sw}(1 + A_1\chi)))}{30\tilde{\tau}_{sw} - 136\tilde{\tau}_{sw}^2 - 16A_1\chi\tilde{\tau}_{sw}^2 + 240A_2\chi^2\tilde{\tau}_{sw}^3 + \delta_x \tilde{\tau}'_{sw}(148 - 136\tilde{\tau}_{sw} + 284A_1\chi\tilde{\tau}_{sw} + 240A_2\chi^2\tilde{\tau}_{sw}^2)} \quad (6.48)$$

and the relaxation time $\tau_j = 1/s_j = 1$. For complex geometries, the normal vector \mathbf{n} and the directional gradient of the mean free path λ_e along direction \mathbf{n} (noted as $\nabla \lambda_e \cdot \mathbf{n}$) must also be specified as an input for our regularized MRT-LBM as the computation of $\tilde{\tau}'_{sw}$ requires this information. We used the analytical solution for all surfaces. The gradient of a binary image can be easily computed [451, 452] and is required for any complex porous medium such as those

reconstructed from tomographic images. The quality of the evaluation of this gradient has a non-negligible impact on the overall scheme solution.

CHAPITRE 7 DISCUSSION GÉNÉRALE

L'objectif de cette thèse doctorale peut être reformulé d'une manière plus générale :

Développer, vérifier et valider une MBR capable de simuler des écoulements du régime continu au régime de Knudsen, en prenant compte des phénomènes du glissement aux parois solides-fluides et de la couche de Knudsen au sein d'un milieu poreux complexe tel qu'un filtre à particules fines dans l'air composé à la fois de microfibres et de nanofibres.

Cette reformulation permet de mieux saisir les contributions originales de cette thèse. Au début de ce travail, l'objectif était de trouver la recette et la structure optimale pour minimiser l'emploi de nanofibres, plus dispendieuses que les microfibres, dans la fabrication de filtres à particules fines dans l'air. Le problème de la simulation des écoulements dans un milieu filtrant constitué en partie de nanofibres a nécessité de se pencher davantage sur la physique fondamentale des écoulements raréfiés. Des détails techniques de l'implémentation de la MBR se sont avérés cruciaux. Ce chapitre retrace le chemin parcouru pour résoudre tous les écueils apparus lors de cette thèse afin de vérifier et valider le modèle proposé de simulation directe d'écoulements au sein d'un milieu filtrant, du régime continu au régime de Knudsen.

La méthodologie de prédiction de la performance des milieux filtrants a été vérifiée et validée pour le cas des écoulements continus à l'Article 1 (Chapitre 3). L'ordre de convergence pour la perméabilité et l'efficacité de capture a été évalué respectivement à 2.8 et 1.3, tandis que l'erreur pour une taille de maille de $\Delta x = 0.1\text{m}$ a été évaluée respectivement à 0.2% et 2%. Les résultats se comparaient bien entre la perméabilité prédite et l'équation de Davies [37], ainsi qu'entre l'efficacité de capture prédite et un total de 7000 combinaisons de corrélations de la littérature. Les valeurs prédites pour l'efficacité se comparaient également bien à celle de Steffens et Coury [323]. La méthodologie en trois étapes, comprenant les hypothèses : 1) des fibres représentées sous forme de cylindres déposés séquentiellement, 2) son couplage unidirectionnel de l'écoulement et 3) des particules fines sphériques capturées dès un contact avec une fibre, peut donc bénéficier d'un degré élevé de confiance pour représenter la réalité au sein des milieux filtrants propres en régime du continuum laminaire où les charges électrostatiques et la gravité jouent un rôle négligeable. Pour tenir compte des phénomènes propres aux écoulements raréfiés

avec la méthodologie en trois étapes, il suffirait en principe d'incorporer la nouvelle MBR développée dans cette thèse.

Par la suite, il a été démontré à l'Article 1, par trois études numériques, que le caractère multicouche du diamètre des fibres avait un impact très limité sur la performance des filtres fibreux, du moins en régime du continuum laminaire. Lors de la première étude sur la comparaison entre des filtres multicouches et des filtres où les fibres de différents diamètres étaient bien mélangées, l'impact de la structure était statistiquement non-significatif. Pour une proportion de fibres fines et grossières de taille donnée, le caractère aléatoire de la microstructure était davantage responsable de la variation entre les milieux filtrants par le caractère aléatoire de la microstructure. D'un point de vue industriel, il y a donc un intérêt pratique dans le contrôle de la microstructure aux fins d'optimisation de la performance des filtres fibreux. La deuxième et la troisième étude, bien que ne cherchant pas à représenter la réalité, ont confirmé la valeur très faible de l'impact des interstices sur la performance des milieux filtrants multicouches. La MBR a été en mesure de simuler des domaines poreux tridimensionnels à plus de deux milliards de mailles. Une précision équivalente pour une autre méthode numérique aurait été prohibitif d'un point de vue computationnel et espace mémoire.

Bien que des CFs de glissement avaient déjà été proposées pour la MBR, il n'existe pas de CF précise pour résoudre les équations de Navier-Stokes étendues dans une géométrie non-planaire. La DBB BC a été proposée à l'Article 2 (Chapitre 4) comme solution aux ambiguïtés du calcul de la valeur des populations provenant de coins solides lors de l'imposition de conditions de glissement avec la MBR-TMR. La DBB BC est une CF cinétique purement locale plus facile à paralléliser que les CFs cinétiques incorporant de la réflexion spéculaire. Elle enlève le fardeau de la définition d'une longueur caractéristique pour un milieu poreux. La DBB BC a été généralisée aux équations de NS étendues grâce à une inspection relativement simple de la procédure de Guo et al. pour la CBBSR BC [236]. Il s'est avéré au départ que si le ratio cinétique r était modifié entre la DBB BC et la CBBSR BC, le temps de relaxation relié au flux d'énergie restait inchangé. Une controverse de la littérature sur l'ordre de convergence de la DBB BC a également été résolue en étudiant un écoulement planaire incompressible en régime de glissement. Il a été démontré que l'ordre de convergence est relié à la mise à l'échelle du pas de temps par rapport au pas d'espace. Quand le temps de relaxation relié à la contrainte τ_s est fixé comme dans une simulation typique en régime du continuum, l'ordre de convergence est quadratique. Lorsque le nombre de Knudsen

est fixé dans un écoulement raréfié, τ_s augmente en conséquence et l'ordre de convergence est linéaire.

Cependant, lors de l'implémentation de la MBR en régime de Knudsen pour des géométries complexes, le phénomène de jets numériques en provenance de coins solides sur la grille de populations a été reproduit. L'alignement de ces jets numériques sur la grille de populations montre que ce phénomène est aberrant. L'incorporation d'une procédure de régularisation pour filtrer les composantes non à l'équilibre des moments d'ordre supérieur à 2 s'est avérée essentielle à l'Article 3 (Chapitre 5) pour la simulation d'écoulements raréfiés avec la MBR. Si la procédure de régularisation peut être ignorée pour des écoulements planaires, elle ne peut l'être pour des écoulements non-planaires.

Lors de la vérification au moyen d'une solution analytique pour un écoulement dans une fente, il est apparu que les anciennes valeurs du ratio cinétique r et du temps de relaxation lié au flux d'énergie τ_q ne récupéraient plus la bonne vitesse de glissement après l'implémentation de la procédure de régularisation au sein de la MBR-TMR. Une erreur numérique du même ordre de grandeur que l'écoulement est commise par l'utilisation de ces anciennes valeurs. La filtration des composantes non à l'équilibre des moments supérieurs d'ordre 2 modifie le lien entre les moments, les populations et les paramètres cinétiques de la MBR-TMR proposée par Guo et al. [236] Afin de retrouver la CF de glissement proposée par Guo et al., un développement détaillé à l'Article 3 a permis de déterminer des nouvelles valeurs des paramètres cinétiques r , τ_q et τ_j pour les réseaux D2Q9 et D3Q15.

Avant d'implémenter la représentation de la couche de Knudsen, il valait la peine de vérifier la CF de glissement en elle-même pour des nombres de Knudsen élevés. Pour la première fois à la connaissance de l'auteur, il a été vérifié à l'Article 3 que la CF de glissement d'une MBR-TMR régularisée récupère bien la condition de glissement de Maxwell pour des géométries non-planaires. Les résultats pour le débit ont été comparés sur une grande gamme de nombres de Knudsen ($0.05 < Kn < 5$) avec les solutions analytiques pour un écoulement au travers d'un arrangement de cylindres [425] et de sphères [426]. Un ordre de convergence linéaire a été rapporté, avec une erreur de discréttisation numérique croissante en fonction du nombre de Knudsen. L'hypothèse du rotationnel nul à la frontière d'une enveloppe cylindrique et sphérique sous-tendant les solutions analytiques diffère d'un écoulement entraîné par une force volumique. Une faible différence a donc pu être constatée entre les solutions aux maillages les plus fins de la MBR-TMR

et les solutions analytiques. Néanmoins, considérant toutes les hypothèses utilisées dans le développement de la CF pour la MBR-TRM régularisée, la comparaison est somme toute assez bonne.

La prise en compte de la couche de Knudsen posait un défi majeur précédemment irrésolu dans la littérature lors de la résolution des équations de Navier-Stokes étendues. Un algorithme de traçage des rayons a été proposé à l'Article 4 (Chapitre 6) pour évaluer le libre parcours moyen effectif pour des milieux poreux complexes. Il a d'abord été démontré analytiquement que l'utilisation d'une fonction de mur au moyen d'une évaluation de la distance au mur le plus proche menait à des inconsistances sérieuses, même sur des géométries non-planaires simples. L'algorithme de traçage des rayons proposé est une procédure systématique qui reste cohérente pour des géométries complexes. L'algorithme de traçage des rayons présentait un ordre de convergence plus faible au sein d'un arrangement de cylindres (~ 0.66) que dans une fente (~ 2) en raison des discontinuités du libre parcours directionnel. Néanmoins, avec un nombre suffisant de rayons, l'erreur numérique causée par la discrétisation des angles solides peut être suffisamment diminuée pour des calculs d'ingénierie.

La méthodologie numérique présentée dans cette thèse présente un bon potentiel pour le calcul de haute performance. La nouvelle DBB BC ainsi que la procédure de régularisation ne posent aucun problème au sein de la MBR-TRM en matière de communications entre les processeurs. Malgré les difficultés conceptuelles que présente la simulation des écoulements raréfiés, le temps de calcul requis par la MBR-TRM diminue en fonction du nombre de Knudsen. Ce résultat contre-intuitif apparaît en raison de la mise à l'échelle linéaire du pas d'espace et du pas de temps de la MBR-TRM. L'algorithme de traçage de rayons a pu être porté sur des cartes graphiques à l'aide de la librairie ArrayFire. Le temps de calcul augmente en fonction du nombre de Knudsen, mais il est toujours possible de distribuer les calculs sur plus de cartes graphiques pour des géométries d'une taille raisonnable. Puisque l'algorithme de traçage des rayons n'a qu'à être exécuté une fois, la résolution des équations de Navier-Stokes étendues avec la MBR-TRM offre un potentiel considérable en matière de performance sur les méthodes numériques alternatives de résolution de l'équation de Boltzmann, comme les réseaux d'ordre élevés, DUGKS ou la DSMC.

Les contributions de cette thèse, en particulier les articles 2, 3 et 4, sont donc plus fondamentales que pratiques. Cependant, en gagnant en abstraction, les contributions futures

potentielles de cette thèse ont également gagné en pluridisciplinarité. La nouvelle MBR-TMR avec l'algorithme de traçage de rayons pourrait être utilisé pour étudier des écoulements au sein de formations géologiques où le gaz de schiste est extrait [453]. Elle pourrait aussi avoir des applications dans la catalyse hétérogène, où la vitesse de réaction peut dépendre des phénomènes d'échange se produisant aux pores nanométriques des particules de catalyseurs [301]. La conception de systèmes microélectromécaniques et nanoélectromécaniques pourrait également bénéficier d'un tel modèle d'écoulement [158, 454].

Cependant, le modèle proposé repose sur un grand nombre d'hypothèses : l'approximation de la couche de Knudsen à l'aide des équations de Navier-Stokes étendues, le modèle phénoménologique de glissement aux parois et le développement de la MBR permettant leur discrétisation. Même lorsqu'une viscosité constante était considérée à l'Article 3, l'erreur de discrétisation de la MRT-TMR régularisée était relativement élevée pour les arrangements de cylindres et de sphères. Puisque l'erreur était plus grande pour l'arrangement de sphères que pour l'arrangement de cylindres, ce phénomène est probablement causé par la plus grande proportion de mailles représentées sous forme d'escalier à la frontière entre le fluide et le solide. Il faut trouver une façon de mieux représenter le glissement pour des cas de figure en escalier.

Bien que le modèle proposé converge, une erreur de discrétisation numérique relativement grande est commise sur le débit à $Kn = 1$. À l'Article 4, il a été démontré que l'ordre de convergence est approximativement linéaire pour un écoulement au sein d'une fente, tandis qu'il était sous-linéaire (~ 0.5) pour un écoulement au sein d'un arrangement de cylindres. L'erreur peut facilement être réduite à 10^{-3} pour l'écoulement au sein d'une fente, mais l'erreur de 3% commise pour un arrangement de cylindres sur la simulation la plus raffinée ($540 \times 540 \times 10$) reste grande. Une extrapolation de Richardson a pu être réalisée sur le débit, mais il serait hasardeux de prendre le champ de vitesse comme donnée intermédiaire, par exemple pour calculer l'efficacité de capture des particules fines d'un milieu filtrant.

Tel que formulé présentement, la validité du modèle proposé est questionnable en régime de Knudsen pour des géométries non-planaires malgré les excellents résultats obtenus pour l'écoulement au travers d'une fente. D'une part, dans l'Article 2, sur une grande plage de nombres de Knudsen ($0.05 < Kn < 10$), le débit prédit par le modèle proposé au travers d'une fente se comparait bien à une solution à l'équation de Boltzmann linéarisée [171] et à des données expérimentales [352]. Une nouvelle combinaison de fonctions de viscosité et de coefficients de

glissement proposée dans l’Article 4 a même légèrement amélioré le résultat pour le débit pour les nombres de Knudsen les plus élevés ($2 < Kn < 10$). D’autre part, pour un écoulement au travers d’un arrangement de cylindres, un écart significatif a été rapporté entre le débit prédict par le modèle proposé et le débit rapporté par Taguchi et al. [450] en résolvant l’équation de Boltzmann linéarisée. Bien que le nouveau modèle soit une nette amélioration par rapport à la résolution des équations de Navier-Stokes sans glissement, l’ajout de la fonction de viscosité a très peu modifié le résultat de la MBR-TRM régularisée avec la nouvelle CF de glissement.

Bien que la MBR-TRM régularisée produisait des erreurs non négligeables à $Kn = 1$ pour une simulation d’écoulements à viscosité constante au travers d’un arrangement de cylindres et d’un arrangement de sphères à l’Article 3, l’erreur était plus grande lorsque des fonctions de viscosité non constante étaient incorporées à l’Article 4. Il pourrait y avoir un problème dans la formulation actuelle de la MBR-TRM régularisée lorsque des fonctions de viscosité non constantes sont utilisées pour des géométries non-planaires. Ce problème devrait être investigué plus en détail.

À la connaissance de l’auteur, la description phénoménologique de la vitesse de glissement [225] n’a jamais été validée rigoureusement pour des géométries non-planaires ouvertes comme un arrangement de cylindres. Dans la littérature, seuls des écoulements au sein de géométries très simples, comme un plan semi-infini, ou des géométries fermées comme une fente et des cylindriques concentriques ont été simulés. De plus, certains éléments de théorie autour du paramètre A_2 sont encore manquants. Si l’expression de la vitesse de glissement était invalidé, une partie des écarts pourrait être expliquée entre les résultats du modèle proposé et de l’équation de Boltzmann linéarisée [450] pour un écoulement au travers d’un arrangement de cylindres. Dans ce cas, il faudrait produire une expression plus universelle et redévelopper la CF de la MBR-TRM régularisée en conséquence.

Finalement, l’hypothèse de proportionnalité entre le libre parcours moyen effectif et la viscosité effective au sein de la couche de Knudsen n’a jamais été validée pour des géométries non-planaires ouvertes comme un arrangement de cylindres. Si cette hypothèse fondamentale était infirmée, cela démontrerait que les équations de Navier-Stokes étendues ne peuvent être utilisées pour représenter la couche de Knudsen pour des structures fibreuses. Avec les autres sources d’erreurs identifiées dans le modèle comme dans l’imposition des CFs de glissement, on ne peut cependant pour l’instant infirmer cette hypothèse à l’aide des résultats présentés à l’Article 4.

Il est de l'expérience de l'auteur que les étudiants conçoivent souvent (à tort) la modélisation comme un processus linéaire où le modèle est établi, vérifié, validé, puis des résultats immédiats, nouveaux et pertinents sont obtenus. Néanmoins, il faut se rappeler que la modélisation est un cycle, et qu'il faut parfois plusieurs itérations pour arriver à un modèle satisfaisant. En rétrospective, dans ce projet, il aurait fallu valider davantage les hypothèses sous-tendant le modèle proposé et leur mathématisation. Malgré tous les efforts que la modélisation numérique requiert, il est de l'opinion de l'auteur que rien n'est plus pratique qu'une bonne théorie, et qu'il vaut la peine de critiquer et de rectifier les modèles lorsqu'ils sont limités.

CHAPITRE 8 CONCLUSION ET RECOMMANDATIONS

Pour conclure, les contributions de cette thèse par rapport à l'état de l'art seront d'abord synthétisées. Plusieurs pistes pour des travaux futurs seront aussi proposées dans le but d'améliorer le modèle de simulation des écoulements raréfiés au sein de filtres fibreux.

8.1 Synthèse des travaux

Les travaux effectués au cours de cette thèse avaient pour objectif de mieux comprendre l'impact de la structure multicouche d'un milieu filtrant constitué de nanofibres et de microfibres sur la performance des filtres fibreux. Pour mieux calquer le glissement aux parois et la couche de Knudsen des nanofibres, un nouveau modèle de simulation des écoulements gazeux raréfiés basé sur la MBR a été développé. Cette MBR est la deuxième étape d'une méthodologie de simulation directe en trois étapes, où le milieu filtrant est d'abord généré, et où le champ de vitesse de la MBR est utilisé pour calculer les trajectoires d'un grand échantillon de particules fines. Cette méthodologie en trois étapes a donc d'abord été vérifiée, validée, et appliquée à l'étude de l'impact de la structure multicouche pour des microfibres. Il a été démontré que l'impact de la structure multicouche sur la performance, en régime du continuum laminaire, est très faible en comparaison à la microstructure des milieux filtrants. C'est la principale contribution d'ordre pratique de cette thèse.

Le développement d'un modèle de simulation des écoulements raréfiés au sein d'un milieu fibreux complexe a demandé de nombreuses innovations en mécanique des fluides numérique, en particulier pour la MBR. Une extension de la DBB BC a été proposée pour mieux simuler les écoulements raréfiés autour des coins solides avec la MBR. L'implémentation des équations de Navier-Stokes étendues a requis l'examen de multiples détails sur le lien entre les moments, les populations et les paramètres cinétiques de la MBR-TMR régularisée. Une procédure systématique d'évaluation de la viscosité effective pour tout milieu poreux complexe a été établie avec l'algorithme de traçage des rayons. Le nouveau modèle évite totalement les ambiguïtés autour de la définition d'une longueur caractéristique. De plus, le nouveau modèle ne contient que deux relations phénoménologiques qui s'écartent des premiers principes de la mécanique statistique: l'expression du glissement et l'hypothèse de proportionnalité entre le libre parcours moyen effectif et la viscosité effective. Finalement, le nouveau modèle ne comporte aucun défi en matière de

parallélisation et donc un candidat idéal pour la simulation de gros domaines en calcul haute performance.

La nouvelle CF a été vérifiée pour des écoulements au sein de fentes, d'arrangements de cylindres et d'arrangements de sphères. Le calcul du libre parcours moyen effectif au moyen de l'algorithme de traçage des rayons a également été vérifié pour des fentes et des arrangements de cylindres. Le modèle dans son ensemble a été validé pour des écoulements raréfiés au sein d'une fente, où une nouvelle combinaison de fonction de viscosité et de coefficients de glissement a légèrement amélioré les résultats par rapport à la littérature antérieure.

Pour la première fois, un modèle du paradigme des milieux continus a été comparé à une solution numérique de l'équation de Boltzmann linéarisée pour une géométrie non-planaire ouverte comme un arrangement de cylindres. Des questionnements sont apparus quant à la validité du modèle en régime de Knudsen pour des écoulements au sein de l'arrangement de cylindres. Ceci ouvre la voie vers une étude plus approfondie de la théorie des écoulements raréfiés dans les milieux poreux.

8.2 Recommandations

Le potentiel du modèle proposé est loin d'être épuisé. L'auteur de cette thèse recommande de poursuivre les efforts en vue de la simulation d'écoulements raréfiés dans les milieux poreux complexes en général. Un programme de recherche est suggéré pour répondre aux questionnements formulés à la fin de cette thèse. Ces objectifs ont été placés en ordre de difficulté conceptuelle :

1. En régime de glissement, la MBR-TMR régularisée pourrait être vérifiée de manière plus précise en créant de nouvelles solutions analytiques pour l'écoulement au travers d'un arrangement de cylindres. La section cylindrique où la CF de rotationnel nul pourrait être modifiée pour une section carrée (voir [455]), ce qui serait une hypothèse plus proche d'un écoulement mué par une force volumique tel qu'implémenté dans la MBR-TMR régularisée. Il serait également possible d'ajouter le second ordre de la condition de glissement qui manquait dans la solution de Pich pour un arrangement de cylindres [425] et la solution de Datta et Deo pour un arrangement de sphères [426]. Si cette solution

échouait, il serait recommandé d'utiliser un logiciel d'éléments finis ou de volumes finis pour produire des solutions numériques approchées.

2. Il est recommandé d'utiliser la méthodologie en trois étapes afin d'étudier l'impact de la structure multicouche en régime de glissement. La limite habituelle de $Kn = 0.25$ pour un cylindre impliquerait un diamètre minimum (à TPN) d'environ 500 nm. L'impact de la structure multicouche sur la performance serait alors compris sur une plus large gamme de nombres de Knudsen. La MBR-TRM régularisée est potentiellement la méthode la plus performante d'un point de vue computationnel pour arriver à cet objectif à l'heure actuelle.
3. Une méthode alternative comme DUGKS ou DSMC pourrait servir de référence pour valider l'expression du glissement en régime de Knudsen et les équations de Navier-Stokes étendues pour des géométries ouvertes non-planaires. Il serait intéressant de tester plusieurs géométries pour vérifier l'universalité de ce modèle. De nouvelles valeurs de coefficients, ou une nouvelle forme pour la vitesse de glissement pourront être proposées.
4. La MBR-TRM régularisée pourrait être développée pour le réseau D3Q27, qui possède une meilleure isotropie que le réseau D3Q15. En étudiant des cas en marches d'escalier de type (1,1,0) et (1,1,1), le nombre accru de degrés de libertés dans l'espace des moments serait mis à profit dans le calcul de paramètres cinétiques adéquats. L'erreur commise pour un maillage donné pourrait alors diminuer.

Si des résultats satisfaisants étaient obtenus à la suite de ces recommandations, le modèle serait alors validé en régime de Knudsen. Les contradictions identifiées dans la revue de littérature sur l'impact des nanofibres, difficilement solubles expérimentalement, pourraient être résolues numériquement. Une équipe complète de chercheurs et de chercheuses pourrait être dédiée à l'optimisation des filtres fibreux à l'aide de la simulation numérique. Les générations futures d'êtres humains pourront alors être bien équipées pour respirer librement, à l'abri de la peur des aérosols.

RÉFÉRENCES

- [1] I. M. Hutten, "Chapter 2 - Filtration Mechanisms and Theory," in *Handbook of Nonwoven Filter Media*, I. M. Hutten, Ed., ed Oxford: Butterworth-Heinemann, 2007, pp. 29-70.
- [2] I. M. Hutten, "Chapter 1 - Introduction to Nonwoven Filter Media," in *Handbook of Nonwoven Filter Media*, I. M. Hutten, Ed., ed Oxford: Butterworth-Heinemann, 2007, pp. 1-28.
- [3] D. B. Purchas and K. Sutherland, "Chapter 1 - An introduction to filter media," in *Handbook of Filter Media (Second Edition)*, D. B. Purchas and K. Sutherland, Eds., ed Amsterdam: Elsevier Science, 2001, pp. 1-34.
- [4] "Le smog," ed: Environnement Canada, 2014.
- [5] T. Eikmann and G. Scholl, "Air, 2. Effects of Air Pollutants," in *Ullmann's Encyclopedia of Industrial Chemistry*, ed Weinheim: Wiley-VCH Verlag GmbH & Co. KGaA, 2000.
- [6] K. Sutherland, "1. Basic Principles," in *Filters and Filtration Handbook (5th Edition)*, ed: Elsevier, 2008.
- [7] R. D. Morris, "Airborne particulates and hospital admissions for cardiovascular disease: a quantitative review of the evidence," *Environ Health Perspect*, vol. 109 Suppl 4, pp. 495-500, Aug 2001.
- [8] Environnement Canada, "Planifier un avenir durable: Stratégie fédérale de développement durable pour le Canada 2013-2016," E. Canada, Ed., ed, 2013, p. 110.
- [9] K. t. Spurný, "The History of Dust and Aerosol Filtration," in *Advances in Aerosol Filtration*, ed Boca Raton: Lewis Publisher, 1998, pp. 3-12.
- [10] G. Agricola, *De re metallica*. New York: Dover Publications, 1556.
- [11] J. F. Borzelleca, "Paracelsus: Herald of Modern Toxicology," *Toxicological Sciences*, vol. 53, pp. 2-4, January 1, 2000 2000.
- [12] C. N. Davies, *Air filtration*: Academic Press, 1973.
- [13] C. N. Davies, "Fibrous filters for dust and smoke," *Proc. 9th Int. Congress on Ind. Med.*, pp. 162-196, 1949.

- [14] K. Sutherland. (2013, 4 Avril 2013) 50th Anniversary: Half a century of developments in filtration - Part 1. *Filtration+Separation*. Available: <http://www.filtsep.com/view/31623/50th-anniversary-half-a-century-of-developments-in-filtration-part-1/>
- [15] C. Yang, "Aerosol Filtration Application Using Fibrous Media—An Industrial Perspective," *Chinese Journal of Chemical Engineering*, vol. 20, pp. 1-9, 2// 2012.
- [16] K. Sutherland. (2013, 26 Juin 2013) 50th Anniversary: Half a century of developments in filtration - Part 3. *Filtration+Separation*. Available: <http://www.filtsep.com/view/33153/50th-anniversary-half-a-century-of-developments-in-filtration-part-3/>
- [17] C. Matuschek, F. Moll, H. Fangerau, J. C. Fischer, K. Zänker, M. van Griensven, *et al.*, "The history and value of face masks," *European journal of medical research*, vol. 25, pp. 23-23, 2020.
- [18] B. J. Strasser and T. Schlich, "A history of the medical mask and the rise of throwaway culture," *The Lancet*, vol. 396, pp. 19-20, 2020.
- [19] J. C. Prata, A. L. P. Silva, T. R. Walker, A. C. Duarte, and T. Rocha-Santos, "COVID-19 Pandemic Repercussions on the Use and Management of Plastics," *Environmental Science & Technology*, vol. 54, pp. 7760-7765, 2020/07/07 2020.
- [20] P. Evans. (2020, 2020-11-02). *3M faces pressure from Trump order to stop exporting N95 masks to Canada*. Available: <https://www.cbc.ca/news/business/3m-n95-masks-1.5520326>
- [21] R. Jennings. (2020, 2020-11-02). *Vietnam Using Mask Diplomacy to Fortify Foreign Relations*. Available: <https://www.voanews.com/covid-19-pandemic/vietnam-using-mask-diplomacy-fortify-foreign-relations>
- [22] P. Wen and D. Hinshaw. (2020, 2020-11-02). *China Asserts Claim to Global Leadership, Mask by Mask*. Available: <https://www.wsj.com/articles/china-asserts-claim-to-global-leadership-mask-by-mask-11585752077>
- [23] La Presse Canadienne. (2020, 2020-11-02). *Masques N95 : un prêt de 4 millions de Québec pour une usine en construction*. Available: <https://ici.radio-canada.ca/nouvelle/1695634/masques-n95-pret-quebec-construction-usine>

- [24] FPInnovations, "News release: FPInnovations completes phase 1 of development of biodegradable disposable masks from Canadian forests," ed. Montreal, 2020.
- [25] W. C. Hinds, "Introduction," in *Aerosol Technology: Properties, Behavior, and Measurement of Airborne Particles*, 2 ed: John Wiley & Sons, Inc. , 1998, pp. 1-13.
- [26] Environnement Canada, "Le smog," ed, 2014.
- [27] ASTM International, "Standard Specification for Performance of Materials Used in Medical Face Masks," ed, 2011, p. 3.
- [28] R. C. Brown, *Air Filtration: An Integrated Approach to the Theory and Applications of Fibrous Filters*: Elsevier Science Limited, 1993.
- [29] D. B. Purchas and K. Sutherland, "Chapter 5 - Air and gas filter media," in *Handbook of Filter Media (Second Edition)*, D. B. Purchas and K. Sutherland, Eds., ed Amsterdam: Elsevier Science, 2001, pp. 153-200.
- [30] C. Schaschke, "demister," in *Dictionary of Chemical Engineering*, ed: Oxford University Press, 2014.
- [31] K. Sutherland, "6. Gas Filtration," in *Filters and Filtration Handbook (5th Edition)*, ed: Elsevier, 2008.
- [32] W. C. Hinds, "Filtration," in *Aerosol Technology: Properties, Behavior and Measurement of Airborne Particles*, 2 ed: John Wiley & Sons, Inc. , 1998, pp. 182-204.
- [33] R. R. Mather and R. H. Wardman, "7.1 Nanofibres," in *Chemistry of Textile Fibres (2nd Edition)*, ed: Royal Society of Chemistry.
- [34] H.-C. Yeh, "A FUNDAMENTAL STUDY OF AEROSOL FILTRATION BY FIBROUS FILTERS," 7220162 Ph.D., University of Minnesota, Ann Arbor, 1972.
- [35] G. Asset and T. G. Hutchins, "Leeward deposition of particles on cylinders from moving aerosols," *American Industrial Hygiene Association Journal*, vol. 28, pp. 348-353, 1967.
- [36] J. Bear, "5. The Equation of Motion of a Homogeneous Fluid," in *Dynamics of Fluids in Porous Media*, ed: Dover Publications, 1972.

- [37] C. N. Davies, "The Separation of Airborne Dust and Particles," *Proceedings of the Institution of Mechanical Engineers, Part B: Journal of Engineering Manufacture*, vol. 1, pp. 185-213, January 1, 1953 1953.
- [38] I. M. Hutten, "Chapter 3 - Properties of Nonwoven Filter Media," in *Handbook of Nonwoven Filter Media*, I. M. Hutten, Ed., ed Oxford: Butterworth-Heinemann, 2007, pp. 71-102.
- [39] L. J. Klinkenberg, "The Permeability Of Porous Media To Liquids And Gases," 1941.
- [40] A. S. Ziarani and R. Aguilera, "Knudsen's Permeability Correction for Tight Porous Media," *Transport in Porous Media*, vol. 91, pp. 239-260, Jan 2012.
- [41] S. Whitaker, "The Forchheimer equation: a theoretical development," *Transport in Porous media*, vol. 25, pp. 27-61, 1996.
- [42] J. Pich, "Gas Filtration Theory," in *Filtration: Principles and Practices, Second Edition, Revised and Expanded*, C. Press, Ed., ed: Taylor & Francis, 1986, pp. 1-132.
- [43] V. A. Kirsh, A. A. Kirsh, A. E. Negin, and A. V. Shabatin, "Diffusion deposition of submicron aerosol particles in screen filters," *Colloid Journal*, vol. 77, pp. 298-305, 2015/05/01 2015.
- [44] A. Robinson, "On the motion of small particles in a potential field of flow," *Communications on Pure and Applied Mathematics*, vol. 9, pp. 69-84, 1956.
- [45] A. A. Kirsh, V. O. Khmelevskiy, A. K. Budyka, and V. A. Kirsh, "Penetration of aerosol particles through fine fibrous filters," *Theoretical Foundations of Chemical Engineering*, vol. 45, pp. 891-897, Dec 2011.
- [46] V. A. Kirsh and A. V. Shabatin, "Deposition of nanoparticles in model multilayer fibrous filters with a two-dimensional flow field," *Colloid Journal*, vol. 77, pp. 25-31, Jan 2015.
- [47] J. Pich, "The drag of a cylinder in the transition region," *Journal of Colloid and Interface Science*, vol. 29, pp. 91-96, 1969/01/01 1969.
- [48] J. Pich, "Pressure characteristics of fibrous aerosol filters," *Journal of Colloid and Interface Science*, vol. 37, pp. 912-917, 12// 1971.

- [49] Z. Zhang and B. Y. H. Liu, "Experimental Study of Aerosol Filtration in the Transition Flow Regime," *Aerosol Science and Technology*, vol. 16, pp. 227-235, 1992/01/01 1992.
- [50] B. I. Ogorodnikov, "Pressure-drop across FP fiber filters under gas slip-flow and in transition regime," *Colloid Journal of the USSR*, vol. 38, pp. 168-172, 1976.
- [51] R. S. Barhate and S. Ramakrishna, "Nanofibrous filtering media: Filtration problems and solutions from tiny materials," *Journal of Membrane Science*, vol. 296, pp. 1-8, 6/15/ 2007.
- [52] M. Devienne, *Frottement et Échanges Thermiques dans les Gaz Raréfiés*. Paris: Gauthier-Villars, 1958.
- [53] A. Agrawal, "A Comprehensive Review on Gas Flow in Microchannels," *International Journal of Micro-Nano Scale Transport*, vol. 2, pp. 1-40, 2011.
- [54] P. Li, C. Wang, Y. Zhang, and F. Wei, "Air Filtration in the Free Molecular Flow Regime: A Review of High-Efficiency Particulate Air Filters Based on Carbon Nanotubes," *Small*, vol. 10, pp. 4543-4561, 2014.
- [55] R. W. Barber and D. R. Emerson, "Challenges in modeling gas-phase flow in microchannels: From slip to transition," *Heat Transfer Engineering*, vol. 27, pp. 3-12, May 2006.
- [56] Z.-M. Huang, Y.-Z. Zhang, M. Kotaki, and S. Ramakrishna, "A review on polymer nanofibers by electrospinning and their applications in nanocomposites," *Composites science and technology*, vol. 63, pp. 2223-2253, 2003.
- [57] C. S. Wang and Y. Otani, "Removal of Nanoparticles from Gas Streams by Fibrous Filters: A Review," *Industrial & Engineering Chemistry Research*, vol. 52, pp. 5-17, Jan 2013.
- [58] A. Podgórski, A. Bałazy, and L. Gradoń, "Application of nanofibers to improve the filtration efficiency of the most penetrating aerosol particles in fibrous filters," *Chemical Engineering Science*, vol. 61, pp. 6804-6815, 10// 2006.
- [59] W. W.-F. Leung, C.-H. Hung, and P.-T. Yuen, "Experimental Investigation on Continuous Filtration of Sub-Micron Aerosol by Filter Composed of Dual-Layers Including a Nanofiber Layer," *Aerosol Science and Technology*, vol. 43, pp. 1174-1183, 2009/11/24 2009.

- [60] W. W.-F. Leung, C.-H. Hung, and P.-T. Yuen, "Effect of face velocity, nanofiber packing density and thickness on filtration performance of filters with nanofibers coated on a substrate," *Separation and Purification Technology*, vol. 71, pp. 30-37, 1/29/ 2010.
- [61] W. W.-F. Leung and C.-H. Hung, "Skin effect in nanofiber filtration of submicron aerosols," *Separation and Purification Technology*, vol. 92, pp. 174-180, 5/18/ 2012.
- [62] W. W. F. Leung and C. H. Hung, "Investigation on pressure drop evolution of fibrous filter operating in aerodynamic slip regime under continuous loading of sub-micron aerosols," *Separation and Purification Technology*, vol. 63, pp. 691-700, Nov 2008.
- [63] N. Wang, Y. Yang, S. S. Al-Deyab, M. El-Newehy, J. Yu, and B. Ding, "Ultra-light 3D nanofibre-nets binary structured nylon 6-polyacrylonitrile membranes for efficient filtration of fine particulate matter," *Journal of Materials Chemistry A*, vol. 3, pp. 23946-23954, 2015.
- [64] K.-S. Lee, N. Hasolli, S.-M. Jeon, J.-R. Lee, K.-D. Kim, Y.-O. Park, *et al.*, "Filter layer structure effect on the most penetrating particle size of multilayered flat sheet filter," *Powder Technology*, vol. 344, pp. 270-277, 2019/02/15/ 2019.
- [65] W. W.-F. Leung, C. W.-Y. Hau, and H.-F. Choy, "Microfiber-nanofiber composite filter for high-efficiency and low pressure drop under nano-aerosol loading," *Separation and Purification Technology*, vol. 206, pp. 26-38, 2018/11/29/ 2018.
- [66] V. V. Kadam, L. Wang, and R. Padhye, "Electrospun nanofibre materials to filter air pollutants – A review," *Journal of Industrial Textiles*, vol. 47, pp. 2253-2280, 2018.
- [67] R. Khajavi and M. Abbasipour, "Electrospinning as a versatile method for fabricating coreshell, hollow and porous nanofibers," *Scientia Iranica*, vol. 19, pp. 2029-2034, 2012/12/01/ 2012.
- [68] J.-P. Brincat, D. Sardella, A. Muscat, S. Decelis, J. N. Grima, V. Valdramidis, *et al.*, "A review of the state-of-the-art in air filtration technologies as may be applied to cold storage warehouses," *Trends in Food Science & Technology*, vol. 50, pp. 175-185, 2016/04/01/ 2016.

- [69] X. Wang, B. Ding, G. Sun, M. Wang, and J. Yu, "Electro-spinning/netting: A strategy for the fabrication of three-dimensional polymer nano-fiber/nets," *Progress in Materials Science*, vol. 58, pp. 1173-1243, 2013/10/01/ 2013.
- [70] Y. Liu, M. Park, B. Ding, J. Kim, M. El-Newehy, S. S. Al-Deyab, *et al.*, "Facile electrospun Polyacrylonitrile/poly(acrylic acid) nanofibrous membranes for high efficiency particulate air filtration," *Fibers and Polymers*, vol. 16, pp. 629-633, 2015.
- [71] M. Zhu, J. Han, F. Wang, W. Shao, R. Xiong, Q. Zhang, *et al.*, "Electrospun nanofibers membranes for effective air filtration," *Macromolecular Materials and Engineering*, vol. 302, p. 1600353, 2017.
- [72] X. Qin and S. Subianto, "17 - Electrospun nanofibers for filtration applications," in *Electrospun Nanofibers*, M. Afshari, Ed., ed: Woodhead Publishing, 2017, pp. 449-466.
- [73] S. Jiang, Y. Chen, G. Duan, C. Mei, A. Greiner, and S. Agarwal, "Electrospun nanofiber reinforced composites: A review," *Polymer Chemistry*, vol. 9, pp. 2685-2720, 2018.
- [74] J. Xu, C. Liu, P.-C. Hsu, K. Liu, R. Zhang, Y. Liu, *et al.*, "Roll-to-Roll Transfer of Electrospun Nanofiber Film for High-Efficiency Transparent Air Filter," *Nano Letters*, vol. 16, pp. 1270-1275, 2016/02/10 2016.
- [75] H.-J. Choi, M. Kumita, S. Hayashi, H. Yuasa, M. Kamiyama, T. Seto, *et al.*, "Filtration properties of nanofiber/microfiber mixed filter and prediction of its performance," *Aerosol and Air Quality Research*, vol. 17, pp. 1052-1062, 2017.
- [76] H. Misslitz, K. Kreger, and H.-W. Schmidt, "Supramolecular Nanofiber Webs in Nonwoven Scaffolds as Potential Filter Media," *Small*, vol. 9, pp. 2053-2058, 2013.
- [77] D. Weiss, D. Skrybeck, H. Misslitz, D. Nardini, A. Kern, K. Kreger, *et al.*, "Tailoring Supramolecular Nanofibers for Air Filtration Applications," *ACS Applied Materials & Interfaces*, vol. 8, pp. 14885-14892, 2016/06/15 2016.
- [78] L. Zhang, W.-L. Yuan, Z. Zhang, G.-H. Zhang, H. Chen, N. Zhao, *et al.*, "Self-assembled ionic nanofibers derived from amino acids for high-performance particulate matter removal," *Journal of Materials Chemistry A*, vol. 7, pp. 4619-4625, 2019.

- [79] D. Weiss, K. Kreger, and H.-W. Schmidt, "Self-Assembly of Alkoxy-Substituted 1,3,5-Benzenetrisamides Under Controlled Conditions," *Macromolecular Materials and Engineering*, vol. 302, p. 1600390, 2017.
- [80] M. Burgard, D. Weiss, K. Kreger, H. Schmalz, S. Agarwal, H.-W. Schmidt, *et al.*, "Mesostructured Nonwovens with Penguin Downy Feather-Like Morphology—Top-Down Combined with Bottom-Up," *Advanced Functional Materials*, vol. 29, p. 1903166, 2019.
- [81] Y. Wang, W. Lu, Y. Wang, T. Xu, and W. Chen, "Interpenetrating-Syncretic Micro-Nano Hierarchy Fibers for Effective Fine Particle Capture," *Advanced Engineering Materials*, vol. 21, p. 1801361, 2019.
- [82] S. Zhang, H. Liu, X. Yin, J. Yu, and B. Ding, "Anti-deformed Polyacrylonitrile/Polysulfone Composite Membrane with Binary Structures for Effective Air Filtration," *ACS Applied Materials & Interfaces*, vol. 8, pp. 8086-8095, 2016/03/30 2016.
- [83] S. Zhang, H. Liu, J. Yu, W. Luo, and B. Ding, "Microwave structured polyamide-6 nanofiber/net membrane with embedded poly(m-phenylene isophthalamide) staple fibers for effective ultrafine particle filtration," *Journal of Materials Chemistry A*, vol. 4, pp. 6149-6157, 2016.
- [84] J. Li, D. Zhang, X. Jiang, X. Zhao, R. Hu, Y. Zhong, *et al.*, "Nest-like multilevel structured graphene oxide-on-polyacrylonitrile membranes for highly efficient filtration of ultrafine particles," *Journal of Materomics*, vol. 5, pp. 422-427, 2019/09/01/ 2019.
- [85] S. Whitaker, "Flow in porous media I: A theoretical derivation of Darcy's law," *Transport in porous media*, vol. 1, pp. 3-25, 1986.
- [86] A. A. Kirsch and I. B. Stechkina, "Pressure drop and diffusional deposition of aerosol in polydisperse model filter," *Journal of Colloid and Interface Science*, vol. 43, pp. 10-16, 4// 1973.
- [87] A. A. Kirsh, I. B. Stechkina, and N. A. Fuchs, "Efficiency of aerosol filters made of ultrafine polydisperse fibres," *Aerosol Science*, vol. 6, pp. 119-124, 1974.
- [88] A. Kirsch and U. V. Zhulanov, "Measurement of aerosol penetration through high efficiency filters," *Journal of Aerosol Science*, vol. 9, pp. 291-298, 1978.

- [89] T. Frising, D. Thomas, P. Contal, D. Bemer, and D. Leclerc, "Influence of filter fibre size distribution on filter efficiency calculations," *Chemical Engineering Research & Design*, vol. 81, pp. 1179-1184, Oct 2003.
- [90] A. Jackiewicz, A. Podgorski, L. Gradon, and J. Michalski, "Nanostructured Media to Improve the Performance of Fibrous Filters," *Kona Powder and Particle Journal*, pp. 244-255, 2013.
- [91] J. Payen, "Étude et développement de structures fibreuses nontissées dédiées à la filtration de particules fines dans l'air," Thèse de Doctorat, Laboratoire du génie des matériaux textiles, Université de Valenciennes et du Hainaut-Cambrésis, 2009.
- [92] K. J. Mattern and W. M. Deen, ""Mixing Rules" for estimating the hydraulic permeability of fiber mixtures," *Aiche Journal*, vol. 54, pp. 32-41, Jan 2008.
- [93] J. Sauter, *Die Größenbestimmung der im Gemischnebel von Verbrennungskraftmaschinen vorhandenen Brennstoffteilchen*: VDI-Verlag, 1926.
- [94] D. S. Clague and R. J. Phillips, "A numerical calculation of the hydraulic permeability of three-dimensional disordered fibrous media," *Physics of Fluids*, vol. 9, pp. 1562-1572, Jun 1997.
- [95] R. M. Werner and L. A. Clarenburg, "Aerosol Filters. Pressure Drop across Single-Component Glass Fiber Filters," *Industrial & Engineering Chemistry Process Design and Development*, vol. 4, pp. 288-293, 1965/07/01 1965.
- [96] R. C. Brown and A. Thorpe, "Glass-fibre filters with bimodal fibre size distributions," *Powder Technology*, vol. 118, pp. 3-9, Aug 2001.
- [97] H. V. Tafreshi, M. S. A. Rahman, S. Jaganathan, Q. Wang, and B. Pourdeyhimi, "Analytical expressions for predicting permeability of bimodal fibrous porous media," *Chemical Engineering Science*, vol. 64, pp. 1154-1159, Mar 2009.
- [98] V. Mityushev and P. M. Adler, "Longitudinal permeability of spatially periodic rectangular arrays of circular cylinders II. An arbitrary distribution of cylinders inside the unit cell," *Zeitschrift für angewandte Mathematik und Physik ZAMP*, vol. 53, pp. 486-514, 2002.

- [99] M. N. Lebedev, I. B. Stechkina, and A. L. Chernyakov, "Viscous drag of periodic row of polydisperse fibers with allowance for slip effect," *Colloid Journal*, vol. 64, pp. 68-78, Jan-Feb 2002.
- [100] H.-J. Choi, M. Kumita, T. Seto, Y. Inui, L. Bao, T. Fujimoto, *et al.*, "Effect of slip flow on pressure drop of nanofiber filters," *Journal of Aerosol Science*, vol. 114, pp. 244-249, 2017/12/01/ 2017.
- [101] L. Bao, K. Seki, H. Niinuma, Y. Otani, R. Balgis, T. Ogi, *et al.*, "Verification of slip flow in nanofiber filter media through pressure drop measurement at low-pressure conditions," *Separation and Purification Technology*, vol. 159, pp. 100-107, 2/8/ 2016.
- [102] D. H. Shou, J. T. Fan, and F. Ding, "Hydraulic permeability of fibrous porous media," *International Journal of Heat and Mass Transfer*, vol. 54, pp. 4009-4018, Aug 2011.
- [103] A. Jackiewicz, A. Balazy, and A. Podgorski, "Investigation of aerosol dispersion in fibrous filters," *Polish Journal of Chemical Technology*, vol. 10, pp. 66-72, 2008.
- [104] S. Dhaniyala and B. Y. H. Liu, "Theoretical Modeling of Filtration by Nonuniform Fibrous Filters," *Aerosol Science and Technology*, vol. 34, pp. 170-178, 2001/01/01 2001.
- [105] S. Dhaniyala and B. Y. H. Liu, "Experimental Investigation of Local Efficiency Variation in Fibrous Filters," *Aerosol Science and Technology*, vol. 34, pp. 161-169, 2001/01/01 2001.
- [106] D. Shou, J. Fan, H. Zhang, X. Qian, and L. Ye, "Filtration Efficiency of Non-Uniform Fibrous Filters," *Aerosol Science and Technology*, vol. 49, pp. 912-919, 2015/10/03 2015.
- [107] E. Schweers and F. Löfller, "Realistic modelling of the behaviour of fibrous filters through consideration of filter structure," *Powder Technology*, vol. 80, pp. 191-206, 1994.
- [108] J. Wang, S. C. Kim, and D. Y. Pui, "Investigation of the figure of merit for filters with a single nanofiber layer on a substrate," *Journal of Aerosol Science*, vol. 39, pp. 323-334, Apr 2008.
- [109] J. Wang, S. C. Kim, and D. Y. H. Pui, "Figure of Merit of Composite Filters with Micrometer and Nanometer Fibers," *Aerosol Science and Technology*, vol. 42, pp. 722-728, 2008/07/24 2008.

- [110] A. N. Karwa and B. J. Tatarchuk, "Pressure drop and aerosol filtration efficiency of microfibrous entrapped catalyst and sorbent media: Semi-empirical models," *Separation and Purification Technology*, vol. 86, pp. 55-63, 2012/02/15/ 2012.
- [111] J. Payen, P. Vroman, M. Lewandowski, A. Perwuelz, S. Callé-Chazelet, and D. Thomas, "Influence of fiber diameter, fiber combinations and solid volume fraction on air filtration properties in nonwovens," *Textile Research Journal*, vol. 82, pp. 1948-1959, Nov 2012 2012.
- [112] A. Bałazy and A. Podgórska, "Verification of the classical theory of aerosol depth filtration," *Chemical and Process Engineering*, vol. 29, pp. 361-374, 2008.
- [113] Y. Li, X. Yin, J. Yu, and B. Ding, "Electrospun nanofibers for high-performance air filtration," *Composites Communications*, vol. 15, pp. 6-19, 2019/10/01/ 2019.
- [114] Z. H. Chai, B. C. Shi, Z. L. Guo, and J. H. Lu, "Gas Flow Through Square Arrays of Circular Cylinders with Klinkenberg Effect: A Lattice Boltzmann Study," *Communications in Computational Physics*, vol. 8, pp. 1052-1073, Nov 2010.
- [115] Y.-Y. Kuo, F. C. Bruno, and J. Wang, "Filtration Performance Against Nanoparticles by Electrospun Nylon-6 Media Containing Ultrathin Nanofibers," *Aerosol Science and Technology*, vol. 48, pp. 1332-1344, 2014/12/02 2014.
- [116] S. Jaganathan, H. Vahedi Tafreshi, and B. Pourdeyhimi, "A realistic approach for modeling permeability of fibrous media: 3-D imaging coupled with CFD simulation," *Chemical Engineering Science*, vol. 63, pp. 244-252, 1// 2008.
- [117] S. Fotovati, H. V. Tafreshi, and B. Pourdeyhimi, "Analytical expressions for predicting performance of aerosol filtration media made up of trilobal fibers," *Journal of Hazardous Materials*, vol. 186, pp. 1503-1512, 2/28/ 2011.
- [118] S. Fotovati, H. V. Tafreshi, A. Ashari, S. A. Hosseini, and B. Pourdeyhimi, "Analytical expressions for predicting capture efficiency of bimodal fibrous filters," *Journal of Aerosol Science*, vol. 41, pp. 295-305, Mar 2010.
- [119] A. Podgórska, "Estimation of the upper limit of aerosol nanoparticles penetration through inhomogeneous fibrous filters," *Journal of Nanoparticle Research*, vol. 11, pp. 197-207, 2009.

- [120] M. Rebai, F. Drolet, D. Vidal, I. Vadeiko, and F. Bertrand, "A Lattice Boltzmann approach for predicting the capture efficiency of random fibrous media," *Asia-Pacific Journal of Chemical Engineering*, vol. 6, pp. 29-37, Mar 2011.
- [121] R. Przekop and L. Gradon, "Deposition and filtration of nanoparticles in the composites of nano- and microsized fibers," *Aerosol Science and Technology*, vol. 42, pp. 483-493, 2008.
- [122] B. Zhou, X. Zhang, and P. Tronville, "Discussion of slip boundary on fibrous filter media," in *2010 International Conference on Mechanic Automation and Control Engineering*, 2010, pp. 1896-1899.
- [123] L. de Luca Xavier Augusto, J. Ross-Jones, G. Lopes, P. Tronville, J. Gonçalves, M. Rädle, *et al.*, "Microfiber Filter Performance Prediction Using a Lattice Boltzmann Method," *Communications in Computational Physics*, vol. 23, pp. 910-931, 04/01 2018.
- [124] W. Sambaer, M. Zatloukal, and D. Kimmer, "Effect of particle-fiber friction coefficient on ultrafine aerosol particles clogging in nanofiber based filter," in *AIP Conference Proceedings*, 2013, pp. 326-337.
- [125] S. A. Hosseini and H. V. Tafreshi, "On the importance of fibers' cross-sectional shape for air filters operating in the slip flow regime," *Powder Technology*, vol. 212, pp. 425-431, 10/25/ 2011.
- [126] X. Zhao, S. Wang, X. Yin, J. Yu, and B. Ding, "Slip-Effect Functional Air Filter for Efficient Purification of PM2.5," *Scientific Reports*, vol. 6, p. 35472, 2016/10/17 2016.
- [127] S. Zhao and A. Povitsky, "Method of fundamental solutions for partial-slip fibrous filtration flows," *International Journal for Numerical Methods in Fluids*, vol. 61, pp. 255-274, Sep 2009.
- [128] B. Maze, H. Vahedi Tafreshi, Q. Wang, and B. Pourdeyhimi, "A simulation of unsteady-state filtration via nanofiber media at reduced operating pressures," *Journal of Aerosol Science*, vol. 38, pp. 550-571, 5// 2007.
- [129] W. Sambaer, M. Zatloukal, and D. Kimmer, "3D modeling of filtration process via polyurethane nanofiber based nonwoven filters prepared by electrospinning process," *Chemical Engineering Science*, vol. 66, pp. 613-623, Feb 2011.

- [130] W. Sambaer, M. Zatloukal, and D. Kimmer, "3D air filtration modeling for nanofiber based filters in the ultrafine particle size range," *Chemical Engineering Science*, vol. 82, pp. 299-311, Sep 2012.
- [131] S. A. Hosseini and H. V. Tafreshi, "3-D simulation of particle filtration in electrospun nanofibrous filters," *Powder Technology*, vol. 201, pp. 153-160, 7/26/ 2010.
- [132] S. A. Hosseini and H. V. Tafreshi, "Modeling permeability of 3-D nanofiber media in slip flow regime," *Chemical Engineering Science*, vol. 65, pp. 2249-2254, 3/15/ 2010.
- [133] T. M. Bucher, H. V. Tafreshi, and G. C. Tepper, "Modeling performance of thin fibrous coatings with orthogonally layered nanofibers for improved aerosol filtration," *Powder Technology*, vol. 249, pp. 43-53, Nov 2013.
- [134] B. Maze, H. V. Tafreshi, and B. Pourdeyhimi, "Case Studies of Air Filtration at Microscales: Micro- and Nanofiber Media," *Journal of Engineered Fibers and Fabrics*, vol. 3, 2008.
- [135] M. Kardar, *Statistical physics of particles*: Cambridge University Press, 2007.
- [136] C. Ngô and H. Ngô, *Physique statistique-3ème édition*: Dunod, 2008.
- [137] G. M. Kremer, *An Introduction to the Boltzmann Equation and Transport Processes in Gases*: Springer Berlin Heidelberg, 2010.
- [138] C. Cercignani, *The Boltzmann Equation and Its Applications*: Springer New York, 1987.
- [139] P. L. Bhatnagar, E. P. Gross, and M. Krook, "A model for collision processes in gases. I. Small amplitude processes in charged and neutral one-component systems," *Physical review*, vol. 94, p. 511, 1954.
- [140] J. C. Maxwell, "V. Illustrations of the dynamical theory of gases.—Part I. On the motions and collisions of perfectly elastic spheres," *The London, Edinburgh, and Dublin Philosophical Magazine and Journal of Science*, vol. 19, pp. 19-32, 1860.
- [141] H. Grad, "On the kinetic theory of rarefied gases," *Communications on Pure and Applied Mathematics*, vol. 2, pp. 331-407, 1949.
- [142] P. Taheri and H. Struchtrup, "Effects of rarefaction in microflows between coaxial cylinders," *Physical Review E*, vol. 80, p. 066317, 12/28/ 2009.

- [143] P. Taheri and H. Struchtrup, "An extended macroscopic transport model for rarefied gas flows in long capillaries with circular cross section," *Physics of Fluids (1994-present)*, vol. 22, p. 112004, 2010.
- [144] F. Sharipov and V. Seleznev, "Data on internal rarefied gas flows," *Journal of Physical and Chemical Reference Data*, vol. 27, pp. 657-706, May-Jun 1998.
- [145] X.-J. Gu and D. R. Emerson, "A high-order moment approach for capturing non-equilibrium phenomena in the transition regime," *Journal of Fluid Mechanics*, vol. 636, pp. 177-216, 2009.
- [146] X.-J. Gu, D. R. Emerson, and G.-H. Tang, "Analysis of the slip coefficient and defect velocity in the Knudsen layer of a rarefied gas using the linearized moment equations," *Physical Review E*, vol. 81, p. 016313, 01/19/ 2010.
- [147] X.-J. Gu, D. R. Emerson, and G.-H. Tang, "Kramers' problem and the Knudsen minimum: a theoretical analysis using a linearized 26-moment approach," *Continuum Mechanics and Thermodynamics*, vol. 21, p. 345, November 13 2009.
- [148] H. Struchtrup and T. Thatcher, "Bulk equations and Knudsen layers for the regularized 13 moment equations," *Continuum Mechanics and Thermodynamics*, vol. 19, pp. 177-189, August 01 2007.
- [149] H. Struchtrup and M. Torrilhon, "Regularization of Grad's 13 moment equations: Derivation and linear analysis," *Physics of Fluids*, vol. 15, pp. 2668-2680, Sep 2003.
- [150] H. Struchtrup, "Failures of the Burnett and super-Burnett equations in steady state processes," *Continuum Mechanics and Thermodynamics*, vol. 17, pp. 43-50, 2005.
- [151] H. Struchtrup and P. Taheri, "Macroscopic transport models for rarefied gas flows: a brief review," *IMA Journal of Applied Mathematics*, vol. 76, pp. 672-697, Oct 2011.
- [152] C. Villani, "Limites hydrodynamiques de l'équation de Boltzmann," *Séminaire Bourbaki*, vol. 43, pp. 2000-2001, 2001.
- [153] B. Zhou, P. Tronville, and R. Rivers, "Realistic air filter media performance simulation. Part II: Beyond finite-volume computational fluid dynamics procedures," *HVAC&R Research*, vol. 19, pp. 503-512, 2013/07/04 2013.

- [154] W. C. Hinds, *Aerosol technology: properties, behavior, and measurement of airborne particles*: John Wiley & Sons, 1999.
- [155] C. Cercignani, *Mathematical Methods in Kinetic Theory*: Springer US, 1990.
- [156] B.-Y. Cao, J. Sun, M. Chen, and Z.-Y. Guo, "Molecular momentum transport at fluid-solid interfaces in MEMS/NEMS: a review," *International journal of molecular sciences*, vol. 10, pp. 4638-4706, 2009.
- [157] J. C. Maxwell, "On stresses in rarified gases arising from inequalities of temperature," *Philosophical Transactions of the royal society of London*, vol. 170, pp. 231-256, 1879.
- [158] W. M. Zhang, G. Meng, and X. Y. Wei, "A review on slip models for gas microflows," *Microfluidics and Nanofluidics*, vol. 13, pp. 845-882, Dec 2012.
- [159] A. Dinler, R. W. Barber, D. R. Emerson, S. K. Stefanov, and K. Orucoglu, "Role of surface shape on boundary slip and velocity defect," *Physical Review E*, vol. 86, p. 4, Jul 2012.
- [160] R. W. Barber, Y. Sun, X. J. Gu, and D. R. Emerson, "Isothermal slip flow over curved surfaces," *Vacuum*, vol. 76, pp. 73-81, 10/29/ 2004.
- [161] N. Dongari, R. W. Barber, D. R. Emerson, Y. H. Zhang, and J. M. Reese, "Velocity Inversion In Cylindrical Couette Gas Flows," in *1st European Conference on Gas Micro Flows*. vol. 362, A. Frijns, Ed., ed Bristol: Iop Publishing Ltd, 2012.
- [162] N. Dongari, R. W. Barber, D. R. Emerson, S. K. Stefanov, Y. H. Zhang, and J. M. Reese, "The effect of Knudsen layers on rarefied cylindrical Couette gas flows," *Microfluidics and Nanofluidics*, vol. 14, pp. 31-43, Jan 2013.
- [163] D. A. Lockerby, J. M. Reese, D. R. Emerson, and R. W. Barber, "Velocity boundary condition at solid walls in rarefied gas calculations," *Physical Review E*, vol. 70, p. 017303, 07/26/ 2004.
- [164] K. Aoki, H. Yoshida, T. Nakanishi, and A. L. Garcia, "Inverted velocity profile in the cylindrical Couette flow of a rarefied gas," *Physical Review E*, vol. 68, p. 11, Jul 2003.
- [165] R. S. Myong, J. M. Reese, R. W. Barber, and D. R. Emerson, "Velocity slip in microscale cylindrical Couette flow: The Langmuir model," *Physics of Fluids*, vol. 17, p. 087105, 2005.

- [166] Y. Sun, R. W. Barber, and D. R. Emerson, "The impact of accommodation coefficient on concentric Couette flow," in *Rarefied Gas Dynamics*. vol. 762, M. Capitelli, Ed., ed Melville: Amer Inst Physics, 2005, pp. 707-712.
- [167] R. Barber and D. Emerson, *Analytical solution of low Reynolds number slip flow past a sphere*: Council for the Central Laboratory of the Research Councils, 2000.
- [168] A. Dinler, R. W. Barber, D. R. Emerson, S. K. Stefanov, and K. Orucoglu, "On the degree of boundary slip over nonplanar surfaces," *Microfluidics and Nanofluidics*, vol. 15, pp. 807-816, Dec 2013.
- [169] S. Yuhong, R. W. Barber, and D. R. Emerson, "Inverted velocity profiles in rarefied cylindrical Couette gas flow and the impact of the accommodation coefficient," *Physics of Fluids*, vol. 17, p. 7, Apr 2005.
- [170] N. Dongari, Y. Zhang, and J. M. Reese, "Modeling of Knudsen Layer Effects in Micro/Nanoscale Gas Flows," *Journal of Fluids Engineering*, vol. 133, pp. 071101-071101, 2011.
- [171] T. Ohwada, Y. Sone, and K. Aoki, "Numerical analysis of the Poiseuille and thermal transpiration flows between two parallel plates on the basis of the Boltzmann equation for hard-sphere molecules," *Physics of Fluids A*, vol. 1, pp. 2042-2049, 1989.
- [172] R. B. Bird, W. E. Stewart, and E. N. Lightfoot, "The Equations of Change for Isothermal Systems," in *Transport Phenomena*, ed, 2007, pp. 75-113.
- [173] A. Burgdorfer, "The Influence of the Molecular Mean Free Path on the Performance of Hydrodynamic Gas Lubricated Bearings," *Transactions of the ASME*, vol. 81, pp. 94-100, 1959.
- [174] T. Veijola and M. Turowski, "Compact damping models for laterally moving microstructures with gas-rarefaction effects," *Journal of Microelectromechanical Systems*, vol. 10, pp. 263-273, 2001.
- [175] P. Bahukudumbi, J. H. Park, and A. Beskok, "A unified engineering model for steady and quasi-steady shear-driven gas microflows," *Microscale Thermophysical Engineering*, vol. 7, pp. 291-315, Oct-Dec 2003.

- [176] M. J. McNenly, M. A. Gallis, and I. D. Boyd, "Empirical slip and viscosity model performance for microscale gas flow," *International Journal for Numerical Methods in Fluids*, vol. 49, pp. 1169-1191, 2005.
- [177] Y. Sone, S. Takata, and T. Ohwada, "Numerical analysis of the plane Couette flow of a rarefied gas on the basis of the linearized Boltzmann equation for hard-sphere molecules," *European Journal of Mechanics B Fluids*, vol. 9, pp. 273-288, 1990.
- [178] C. Cercignani, "A variational principle for boundary value problems in kinetic theory," *Journal of Statistical Physics*, vol. 1, pp. 297-311, 1969// 1969.
- [179] V. K. Michalis, A. N. Kalarakis, E. D. Skouras, and V. N. Burganos, "Rarefaction effects on gas viscosity in the Knudsen transition regime," *Microfluidics and Nanofluidics*, vol. 9, pp. 847-853, Oct 2010.
- [180] A. Beskok and G. E. Karniadakis, "A model for flows in channels, pipes, and ducts at micro and nano scales," *Microscale Thermophysical Engineering*, vol. 3, pp. 43-77, Jan-Mar 1999.
- [181] Y. H. Sun and W. K. Chan, "Analytical modeling of rarefied Poiseuille flow in microchannels," *Journal of Vacuum Science & Technology A*, vol. 22, pp. 383-394, Mar-Apr 2004.
- [182] G. L. Morini, M. Spiga, and P. Tartarini, "The rarefaction effect on the friction factor of gas flow in microchannels," *Superlattices and Microstructures*, vol. 35, pp. 587-599, 3// 2004.
- [183] I.-W. Park, M.-S. Shin, S.-J. Byun, and J.-Y. Yoon, "Simulation of Gas Flow in a Microchannel by Lattice Boltzmann Method," Berlin, Heidelberg, 2009, pp. 195-200.
- [184] Y. D. Yuan and S. Rahman, "Extended application of lattice Boltzmann method to rarefied gas flow in micro-channels," *Physica a-Statistical Mechanics and Its Applications*, vol. 463, pp. 25-36, Dec 2016.
- [185] J. Ren, Q. Zheng, P. Guo, S. Peng, Z. Wang, and J. Du, "Pore-scale lattice Boltzmann simulation of two-component shale gas flow," *Journal of Natural Gas Science and Engineering*, vol. 61, pp. 46-70, 2019/01/01/ 2019.

- [186] X. Zhang, L. Xiao, X. Shan, and L. Guo, "Lattice Boltzmann Simulation of Shale Gas Transport in Organic Nano-Pores," *Scientific Reports*, vol. 4, p. 4843, 05/02/online 2014.
- [187] Q. Li, Y. L. He, G. H. Tang, and W. Q. Tao, "Lattice Boltzmann modeling of microchannel flows in the transition flow regime," *Microfluidics and Nanofluidics*, vol. 10, pp. 607-618, Mar 2011.
- [188] N. Gupta, E. Fathi, and F. Belyadi, "Effects of nano-pore wall confinements on rarefied gas dynamics in organic rich shale reservoirs," *Fuel*, vol. 220, pp. 120-129, 2018/05/15/ 2018.
- [189] A. Homayoon, A. H. M. Isfahani, E. Shirani, and M. Ashrafizadeh, "A novel modified lattice Boltzmann method for simulation of gas flows in wide range of Knudsen number," *International Communications in Heat and Mass Transfer*, vol. 38, pp. 827-832, 7// 2011.
- [190] H. Shokouhmand and A. H. Meghdadi Isfahani, "An improved thermal lattice Boltzmann model for rarefied gas flows in wide range of Knudsen number," *International Communications in Heat and Mass Transfer*, vol. 38, pp. 1463-1469, 2011/12/01/ 2011.
- [191] A. Zarei, A. Karimipour, A. H. Meghdadi Isfahani, and Z. Tian, "Improve the performance of lattice Boltzmann method for a porous nanoscale transient flow by provide a new modified relaxation time equation," *Physica A: Statistical Mechanics and its Applications*, vol. 535, p. 122453, 2019/12/01/ 2019.
- [192] J. Ren, P. Guo, Z. Guo, and Z. Wang, "A Lattice Boltzmann Model for Simulating Gas Flow in Kerogen Pores," *Transport in Porous Media*, vol. 106, pp. 285-301, 2015// 2015.
- [193] L. Wang, Z. Zeng, L. Zhang, L. Qiao, Y. Zhang, and Y. Lu, "A new boundary scheme for simulation of gas flow in kerogen pores with considering surface diffusion effect," *Physica A: Statistical Mechanics and its Applications*, vol. 495, pp. 180-190, 2018/04/01/ 2018.
- [194] S. Tao, H. Zhang, and Z. Guo, "Drag correlation for micro spherical particles at finite Reynolds and Knudsen numbers by lattice Boltzmann simulations," *Journal of Aerosol Science*, vol. 103, pp. 105-116, 1// 2017.
- [195] T. Zhao, H. Zhao, X. Li, Z. Ning, Q. Wang, W. Zhao, *et al.*, "Pore scale characteristics of gas flow in shale matrix determined by the regularized lattice Boltzmann method," *Chemical Engineering Science*, vol. 187, pp. 245-255, 2018/09/21/ 2018.

- [196] A. N. Kalarakis, V. K. Michalis, E. D. Skouras, and V. N. Burganos, "Mesoscopic Simulation of Rarefied Flow in Narrow Channels and Porous Media," *Transport in Porous Media*, vol. 94, pp. 385-398, Aug 2012.
- [197] Y.-l. Zhao and Z.-m. Wang, "Prediction of apparent permeability of porous media based on a modified lattice Boltzmann method," *Journal of Petroleum Science and Engineering*, vol. 174, pp. 1261-1268, 2019/03/01/ 2019.
- [198] M. Ho, J. G. Pérez, M. Reggio, and J.-Y. Trépanier, "Permeability calculation of rarefied gas flows through 2D porous structures using the lattice Boltzmann method," *Physics and Chemistry of the Earth, Parts A/B/C*, 2019/03/10/ 2019.
- [199] T.-M. Liou and C.-T. Lin, "Study on microchannel flows with a sudden contraction-expansion at a wide range of Knudsen number using lattice Boltzmann method," *Microfluidics and Nanofluidics*, vol. 16, pp. 315-327, January 01 2014.
- [200] T. M. Liou and C. T. Lin, "Three-dimensional rarefied gas flows in constricted microchannels with different aspect ratios: asymmetry bifurcations and secondary flows," *Microfluidics and Nanofluidics*, vol. 18, pp. 279-292, Feb 2015.
- [201] X. Li, J. Fan, H. Yu, Y. Zhu, and H. Wu, "Lattice Boltzmann method simulations about shale gas flow in contracting nano-channels," *International Journal of Heat and Mass Transfer*, vol. 122, pp. 1210-1221, 2018/07/01/ 2018.
- [202] W. Su, S. Lindsay, H. H. Liu, and L. Wu, "Comparative study of the discrete velocity and lattice Boltzmann methods for rarefied gas flows through irregular channels," *Physical Review E*, vol. 96, p. 13, Aug 2017.
- [203] J. Zhao, J. Yao, A. Li, M. Zhang, L. Zhang, Y. Yang, *et al.*, "Simulation of microscale gas flow in heterogeneous porous media based on the lattice Boltzmann method," *Journal of Applied Physics*, vol. 120, p. 084306, 2016.
- [204] J. Ren, P. Guo, S. Peng, and C. Yang, "Investigation on permeability of shale matrix using the lattice Boltzmann method," *Journal of Natural Gas Science and Engineering*, vol. 29, pp. 169-175, 2016/02/01/ 2016.
- [205] H. Zhang, C. Zhu, and Q. Yang, "Characteristics of Micro Gas Journal Bearings Based on Effective Viscosity," *Journal of Tribology*, vol. 131, 2009.

- [206] P. Neumann and T. Rohrmann, "Lattice Boltzmann simulations in the slip and transition flow regime with the Peano framework," 2012.
- [207] D. Fan, A. Phan, and A. Striolo, "Accurate permeability prediction in tight gas rocks via lattice Boltzmann simulations with an improved boundary condition," *Journal of Natural Gas Science and Engineering*, vol. 73, p. 103049, 2020/01/01/ 2020.
- [208] J. Zhao, J. Yao, M. Zhang, L. Zhang, Y. Yang, H. Sun, *et al.*, "Study of Gas Flow Characteristics in Tight Porous Media with a Microscale Lattice Boltzmann Model," *Scientific Reports*, vol. 6, p. 32393, 2016/09/02 2016.
- [209] Z. Li, C. Wei, J. Leung, Y. Wang, and H. Song, "Numerical and experimental study on gas flow in nanoporous media," *Journal of Natural Gas Science and Engineering*, vol. 27, Part 2, pp. 738-744, 11// 2015.
- [210] H. ZUO, S. DENG, and H. LI, "Limitations of Lattice Boltzmann Modeling of Micro-Flows in Complex Nanopores," *Acta Geologica Sinica - English Edition*, vol. 93, pp. 1808-1822, 2019.
- [211] H. Zuo, S.-C. Deng, and H.-B. Li, "Boundary scheme for lattice Boltzmann modeling of micro-scale gas flow in organic-rich pores considering surface diffusion," *Chinese Physics B*, vol. 28, p. 030202, 2019.
- [212] Z. Wang, X. Jin, X. Wang, L. Sun, and M. Wang, "Pore-scale geometry effects on gas permeability in shale," *Journal of Natural Gas Science and Engineering*, vol. 34, pp. 948-957, 2016.
- [213] Z. Wang, Y. Guo, and M. Wang, "Permeability of high-Kn real gas flow in shale and production prediction by pore-scale modeling," *Journal of Natural Gas Science and Engineering*, vol. 28, pp. 328-337, 1// 2016.
- [214] J. Zheng, Z. Wang, W. Gong, Y. Ju, and M. Wang, "Characterization of nanopore morphology of shale and its effects on gas permeability," *Journal of Natural Gas Science and Engineering*, vol. 47, pp. 83-90, 2017.
- [215] J. Zhao, J. Yao, L. Zhang, H. Sui, and M. Zhang, "Pore-scale simulation of shale gas production considering the adsorption effect," *International Journal of Heat and Mass Transfer*, vol. 103, pp. 1098-1107, 2016/12/01/ 2016.

- [216] E. Dehdashti, "Development of a new correlation to calculate permeability for flows with high Knudsen number," *Chinese Physics B*, vol. 25, p. 024702, 2016/02 2016.
- [217] D. A. Lockerby, J. M. Reese, and M. A. Gallis, "Capturing the Knudsen layer in continuum-fluid models of nonequilibrium gas flows," *Aiaa Journal*, vol. 43, pp. 1391-1393, Jun 2005.
- [218] J. M. Reese, Y. Zheng, and D. A. Lockerby, "Computing the near-wall region in gas micro- and nanofluidics: critical Knudsen layer phenomena," *Journal of Computational and Theoretical Nanoscience*, vol. 4, pp. 807-813, 2007.
- [219] C. R. Lilley and J. E. Sader, "Velocity gradient singularity and structure of the velocity profile in the Knudsen layer according to the Boltzmann equation," *Physical Review E*, vol. 76, p. 026315, 08/23/ 2007.
- [220] C. R. Lilley and J. E. Sader, "Velocity profile in the Knudsen layer according to the Boltzmann equation," *Proceedings of the Royal Society A: Mathematical, Physical and Engineering Science*, vol. 464, pp. 2015-2035, 2008.
- [221] S. Jiang and L.-S. Luo, "Analysis and accurate numerical solutions of the integral equation derived from the linearized BGKW equation for the steady Couette flow," *Journal of Computational Physics*, vol. 316, pp. 416-434, 2016/07/01/ 2016.
- [222] W. Su, P. Wang, H. Liu, and L. Wu, "Accurate and efficient computation of the Boltzmann equation for Couette flow: Influence of intermolecular potentials on Knudsen layer function and viscous slip coefficient," *Journal of Computational Physics*, vol. 378, pp. 573-590, 2019/02/01/ 2019.
- [223] Z.-W. Tian, S. Chen, and C.-G. Zheng, "Lattice Boltzmann simulation of gaseous finite-Knudsen microflows," *International Journal of Modern Physics C*, vol. 21, pp. 769-783, 2010.
- [224] J. Xie, "A mean free path approach to the micro/nanochannel gas flows," *Advances in Aerodynamics*, vol. 2, p. 11, 2020/05/07 2020.
- [225] Z. L. Guo, B. C. Shi, and C. G. Zheng, "An extended Navier-Stokes formulation for gas flows in the Knudsen layer near a wall," *Epl*, vol. 80, p. 6, 2007.

- [226] R. V. Abramov, "Gas Near a Wall: Shortened Mean Free Path, Reduced Viscosity, and the Manifestation of the Knudsen Layer in the Navier–Stokes Solution of a Shear Flow," *Journal of Nonlinear Science*, pp. 1-13, 2018.
- [227] R. V. Abramov, "Diffusive Boltzmann equation, its fluid dynamics, Couette flow and Knudsen layers," *Physica A: Statistical Mechanics and its Applications*, vol. 484, pp. 532-557, 2017/10/15/ 2017.
- [228] N. Dongari, Y. H. Zhang, and J. M. Reese, "Molecular free path distribution in rarefied gases," *Journal of Physics D-Applied Physics*, vol. 44, p. 6, Mar 2011.
- [229] S. K. Prabha, S. P. D., M. G. M., and S. P. Sathian, "The effect of system boundaries on the mean free path for confined gases," *AIP Advances*, vol. 3, p. 102107, 2013.
- [230] Q. Liu and Z. Cai, "Study on the Characteristics of Gas Molecular Mean Free Path in Nanopores by Molecular Dynamics Simulations," *International Journal of Molecular Sciences*, vol. 15, p. 12714, 2014.
- [231] Z. Guo, T. S. Zhao, and Y. Shi, "Physical symmetry, spatial accuracy, and relaxation time of the lattice Boltzmann equation for microgas flows," *Journal of Applied Physics*, vol. 99, p. 074903, 2006.
- [232] E. J. Arlemark, S. K. Dadzie, and J. M. Reese, "An Extension to the Navier–Stokes Equations to Incorporate Gas Molecular Collisions With Boundaries," *Journal of Heat Transfer*, vol. 132, pp. 041006-041006, 2010.
- [233] N. Dongari, Y. Zhang, and J. Reese, "Behaviour of microscale gas flows based on a power-law free path distribution function," 2011.
- [234] P. Lopez and Y. Bayazitoglu, "An extended thermal Lattice Boltzmann model for transition flow," *International Journal of Heat and Mass Transfer*, vol. 65, pp. 374-380, 2013/10/01/ 2013.
- [235] N. Dongari, C. White, T. J. Scanlon, Y. Zhang, and J. M. Reese, "Effects of curvature on rarefied gas flows between rotating concentric cylinders," *Physics of Fluids*, vol. 25, p. 052003, 2013.

- [236] Z. L. Guo, C. G. Zheng, and B. C. Shi, "Lattice Boltzmann equation with multiple effective relaxation times for gaseous microscale flow," *Physical Review E*, vol. 77, p. 12, Mar 2008.
- [237] J.-M. Tucny, D. Vidal, S. Leclaire, and F. Bertrand, "Comparison of existing and extended boundary conditions for the simulation of rarefied gas flows using the Lattice Boltzmann method," *International Journal of Modern Physics C*, p. 2050070, 2020.
- [238] E. Cunningham, "On the Velocity of Steady Fall of Spherical Particles through Fluid Medium," *Proceedings of the Royal Society of London. Series A*, vol. 83, pp. 357-365, 1910.
- [239] M. Lefebvre, *Processus stochastiques appliqués*: Presses inter Polytechnique, 2005.
- [240] B. Øksendal, "Stochastic differential equations," in *Stochastic differential equations*, ed: Springer, 2003, pp. 65-84.
- [241] H. Risken, *The Fokker-Planck Equation: Methods of Solution and Applications*: Springer Berlin Heidelberg, 1996.
- [242] M. Afkhami, A. Hassanpour, M. Fairweather, and D. O. Njobuenwu, "Fully coupled LES-DEM of particle interaction and agglomeration in a turbulent channel flow," *Computers & Chemical Engineering*, vol. 78, pp. 24-38, 7/12/ 2015.
- [243] World Health Organization. (2016). *WHO Global Urban Ambient Air Pollution Database* Available: http://www.who.int/phe/health_topics/outdoorair/databases/cities/en/
- [244] W. C. Hinds, "Adhesion of Particles," in *Aerosol Technology: Properties, Behavior and Measurement of Airborne Particles*, I. John Wiley & Sons, Ed., 2 ed, 1998, pp. 141-149.
- [245] M. J. Ellenbecker, D. Leith, and J. M. Price, "Impaction and Particle Bounce at High Stokes Numbers," *Journal of the Air Pollution Control Association*, vol. 30, pp. 1224-1227, 1980/11/01 1980.
- [246] R. Mostofi, B. Wang, F. Haghigat, A. Bahloul, and L. Jaime, "Performance of Mechanical Filters and Respirators for Capturing Nanoparticles -Limitations and Future Direction," *Industrial Health*, vol. 48, pp. 296-304, May 2010.
- [247] A. F. Miguel, "Effect of air humidity on the evolution of permeability and performance of a fibrous filter during loading with hygroscopic and non-hygroscopic particles," *Journal of Aerosol Science*, vol. 34, pp. 783-799, Jun 2003.

- [248] L. Boskovic, I. S. Altman, R. D. Braddock, and I. E. Agranovski, "Removal of Elongated Particle Aggregates on Fibrous Filters," *Clean-Soil Air Water*, vol. 37, pp. 843-849, Nov 2009.
- [249] R. Lange, H. Fissan, and A. Schmidt-Ott, "Predicting the collection efficiency of agglomerates in fibrous filters," *Particle & Particle Systems Characterization*, vol. 16, pp. 60-65, Jun 1999.
- [250] Z. Guo and C. Shu, *Lattice Boltzmann method and its applications in engineering* vol. 3: World Scientific, 2013.
- [251] T. Krüger, H. Kusumaatmaja, A. Kuzmin, O. Shardt, G. Silva, and E. M. Viggen, *The Lattice Boltzmann Method*: Springer, 2017.
- [252] S. Succi, *The Lattice Boltzmann Equation: For Complex States of Flowing Matter*: Oxford University Press, 2018.
- [253] J. Wang, L. Chen, Q. Kang, and S. S. Rahman, "The lattice Boltzmann method for isothermal micro-gaseous flow and its application in shale gas flow: A review," *International Journal of Heat and Mass Transfer*, vol. 95, pp. 94-108, 4// 2016.
- [254] Z. Guo and C. Shu, "Introduction," in *Lattice-Boltzmann Method and Its Applications in Engineering*, ed: World Scientific, 2013, pp. 1-34.
- [255] D. Vidal, R. Roy, and F. Bertrand, "On improving the performance of large parallel lattice Boltzmann flow simulations in heterogeneous porous media," *Computers & Fluids*, vol. 39, pp. 324-337, 2// 2010.
- [256] D. Vidal, R. Roy, and F. Bertrand, "A parallel workload balanced and memory efficient lattice-Boltzmann algorithm with single unit BGK relaxation time for laminar Newtonian flows," *Computers & Fluids*, vol. 39, pp. 1411-1423, 9// 2010.
- [257] G. A. Bird. (1994). *Molecular Gas Dynamics and the Direct Simulation of Gas Flows*. Available: <https://app.knovel.com/hotlink/toc/id:kpMGDDSGF3/molecular-gas-dynamics/molecular-gas-dynamics>
- [258] K. Xu and C. Liu, "A paradigm for modeling and computation of gas dynamics," *Physics of Fluids*, vol. 29, p. 17, Feb 2017.

- [259] S.-Y. Chou and D. Baganoff, "Kinetic flux–vector splitting for the Navier–Stokes equations," *Journal of Computational Physics*, vol. 130, pp. 217-230, 1997.
- [260] A. L. Garcia, J. B. Bell, W. Y. Crutchfield, and B. J. Alder, "Adaptive mesh and algorithm refinement using direct simulation Monte Carlo," *Journal of computational Physics*, vol. 154, pp. 134-155, 1999.
- [261] Q. Sun, I. D. Boyd, and G. V. Candler, "A hybrid continuum/particle approach for modeling subsonic, rarefied gas flows," *Journal of Computational Physics*, vol. 194, pp. 256-277, 2/10/ 2004.
- [262] T. E. Schwartzenruber and I. D. Boyd, "A hybrid particle-continuum method applied to shock waves," *Journal of Computational Physics*, vol. 215, pp. 402-416, 7/1/ 2006.
- [263] J. M. Burt and I. D. Boyd, "A hybrid particle approach for continuum and rarefied flow simulation," *Journal of Computational Physics*, vol. 228, pp. 460-475, 2/1/ 2009.
- [264] O. Rovenskaya and G. Croce, "Application of a hybrid kinetic-continuum solver to the near wall modelling," *Journal of Physics: Conference Series*, vol. 547, p. 012020, 2014.
- [265] G. Di Staso, H. Clercx, S. Succi, and F. Toschi, "Lattice Boltzmann accelerated direct simulation Monte Carlo for dilute gas flow simulations," *Philosophical Transactions of the Royal Society A: Mathematical, Physical and Engineering Sciences*, vol. 374, p. 20160226, 2016.
- [266] G. Di Staso, H. J. H. Clercx, S. Succi, and F. Toschi, "DSMC–LBM mapping scheme for rarefied and non-rarefied gas flows," *Journal of Computational Science*, vol. 17, pp. 357-369, 2016/11/01/ 2016.
- [267] Z. Guo, K. Xu, and R. Wang, "Discrete unified gas kinetic scheme for all Knudsen number flows: Low-speed isothermal case," *Physical Review E*, vol. 88, p. 033305, 09/27/ 2013.
- [268] P. Wang, L.-P. Wang, and Z. Guo, "Comparison of the lattice Boltzmann equation and discrete unified gas-kinetic scheme methods for direct numerical simulation of decaying turbulent flows," *Physical Review E*, vol. 94, p. 043304, 10/13/ 2016.

- [269] Y. Bo, P. Wang, Z. Guo, and L.-P. Wang, "DUGKS simulations of three-dimensional Taylor–Green vortex flow and turbulent channel flow," *Computers & Fluids*, vol. 155, pp. 9-21, 2017/09/20/ 2017.
- [270] Z. Guo, R. Wang, and K. Xu, "Discrete unified gas kinetic scheme for all Knudsen number flows. II. Thermal compressible case," *Physical Review E*, vol. 91, p. 033313, 03/31/ 2015.
- [271] L. Zhu, Z. Guo, and K. Xu, "Discrete unified gas kinetic scheme on unstructured meshes," *Computers & Fluids*, vol. 127, pp. 211-225, 3/20/ 2016.
- [272] S. H. Kim, H. Pitsch, and I. D. Boyd, "Accuracy of higher-order lattice Boltzmann methods for microscale flows with finite Knudsen numbers," *Journal of Computational Physics*, vol. 227, pp. 8655-8671, 2008/10/01/ 2008.
- [273] J. Meng and Y. Zhang, "Accuracy analysis of high-order lattice Boltzmann models for rarefied gas flows," *Journal of Computational Physics*, vol. 230, pp. 835-849, 2011/02/01/ 2011.
- [274] Y. Shi, P. L. Brookes, Y. W. Yap, and J. E. Sader, "Accuracy of the lattice Boltzmann method for low-speed noncontinuum flows," *Physical Review E*, vol. 83, p. 045701, 04/22/ 2011.
- [275] X. Shan, X.-F. Yuan, and H. Chen, "Kinetic theory representation of hydrodynamics: a way beyond the Navier-Stokes equation," *Journal of Fluid Mechanics*, vol. 550, pp. 413-441, 2006.
- [276] J. Meng and Y. Zhang, "Gauss-Hermite quadratures and accuracy of lattice Boltzmann models for nonequilibrium gas flows," *Physical Review E*, vol. 83, p. 036704, 03/11/ 2011.
- [277] J. Meng and Y. Zhang, "Diffuse reflection boundary condition for high-order lattice Boltzmann models with streaming–collision mechanism," *Journal of Computational Physics*, vol. 258, pp. 601-612, 2014/02/01/ 2014.
- [278] L. de Izarra, J. L. Rouet, and B. Izrar, "High-order lattice Boltzmann models for gas flow for a wide range of Knudsen numbers," *Physical Review E*, vol. 84, p. 7, Dec 2011.

- [279] C. Feuchter and W. Schleifenbaum, "High-order lattice Boltzmann models for wall-bounded flows at finite Knudsen numbers," *Physical Review E*, vol. 94, p. 013304, 07/26/2016.
- [280] S. H. Kim and H. Pitsch, "Analytic solution for a higher-order lattice Boltzmann method: Slip velocity and Knudsen layer," *Physical Review E*, vol. 78, p. 016702, 07/17/ 2008.
- [281] O. Ilyin, "Gaussian Lattice Boltzmann method and its applications to rarefied flows," *Physics of Fluids*, vol. 32, p. 012007, 2020.
- [282] D. J.-E. Vidal, "Developpement d'algorithmes paralleles pour la simulation d'ecoulements de fluides dans les milieux poreux," NR48893 Ph.D., Ecole Polytechnique, Montreal (Canada), Ann Arbor, 2009.
- [283] Z. Guo and C. Shu, "Initial and Boundary Conditions for Lattice Boltzmann Method," in *Lattice Boltzmann Method and its Applications in Engineering*, ed: World Scientific, 2013, pp. 35-60.
- [284] R. S. Myong, "Gaseous slip models based on the Langmuir adsorption isotherm," *Physics of Fluids*, vol. 16, pp. 104-117, 2004.
- [285] Z. L. Guo, B. C. Shi, T. S. Zhao, and C. G. Zheng, "Discrete effects on boundary conditions for the lattice Boltzmann equation in simulating microscale gas flows," *Physical Review E*, vol. 76, p. 5, Nov 2007.
- [286] S. Succi, "Mesoscopic modeling of slip motion at fluid-solid interfaces with heterogeneous catalysis - art. no. 0645022," *Physical Review Letters*, vol. 89, p. 4, Aug 2002.
- [287] Z. L. Guo and C. G. Zheng, "Analysis of lattice Boltzmann equation for microscale gas flows: Relaxation times, boundary conditions and the Knudsen layer," *International Journal of Computational Fluid Dynamics*, vol. 22, pp. 465-473, 2008.
- [288] P. Lallemand and L. S. Luo, "Theory of the lattice Boltzmann method: Dispersion, dissipation, isotropy, Galilean invariance, and stability," *Physical Review E*, vol. 61, pp. 6546-6562, Jun 2000.

- [289] Z. Guo, B. Shi, and C. Zheng, "Velocity inversion of micro cylindrical Couette flow: A lattice Boltzmann study," *Computers & Mathematics with Applications*, vol. 61, pp. 3519-3527, 6// 2011.
- [290] J. Latt and B. Chopard, "Lattice Boltzmann method with regularized pre-collision distribution functions," *Mathematics and Computers in Simulation*, vol. 72, pp. 165-168, 2006/09/09/ 2006.
- [291] K. Suga, "Lattice Boltzmann methods for complex micro-flows: applicability and limitations for practical applications," *Fluid Dynamics Research*, vol. 45, p. 034501, 2013.
- [292] K. Suga and T. Ito, "On the Multiple-Relaxation-Time Micro-Flow Lattice Boltzmann Method for Complex Flows," *Cmes-Computer Modeling in Engineering & Sciences*, vol. 75, pp. 141-172, May 2011.
- [293] K. Suga, S. Takenaka, T. Ito, M. Kaneda, T. Kinjo, and S. Hyodo, "Evaluation of a lattice Boltzmann method in a complex nanoflow," *Physical Review E*, vol. 82, p. 10, Jul 2010.
- [294] A. Montessori, P. Prestininzi, M. La Rocca, and S. Succi, "Lattice Boltzmann approach for complex nonequilibrium flows," *Physical Review E*, vol. 92, p. 043308, 10/22/ 2015.
- [295] J. Wang, Q. Kang, Y. Wang, R. Pawar, and S. S. Rahman, "Simulation of gas flow in micro-porous media with the regularized lattice Boltzmann method," *Fuel*, vol. 205, pp. 232-246, 10/1/ 2017.
- [296] S. Singh, F. Jiang, and T. Tsuji, "Impact of the kinetic boundary condition on porous media flow in the lattice Boltzmann formulation," *Physical Review E*, vol. 96, p. 013303, 07/07/ 2017.
- [297] H. Yasuoka, M. Kaneda, and K. Suga, "Thermal lattice Boltzmann method for complex microflows," *Physical Review E*, vol. 94, p. 013102, 07/06/ 2016.
- [298] H. Chen, R. Zhang, I. Staroselsky, and M. Jhon, "Recovery of full rotational invariance in lattice Boltzmann formulations for high Knudsen number flows," *Physica A: Statistical Mechanics and its Applications*, vol. 362, pp. 125-131, 2006/03/15/ 2006.

- [299] R. Zhang, I. Staroselsky, and H. Chen, "Realization of isotropy of the lattice Boltzmann method via rotation of lattice velocity bases," *Journal of Computational Physics*, vol. 225, pp. 1262-1270, 2007/08/10/ 2007.
- [300] X.-D. Niu, S. Hyodo, K. Suga, and H. Yamaguchi, "Lattice Boltzmann simulation of gas flow over micro-scale airfoils," *Computers & Fluids*, vol. 38, pp. 1675-1681, 2009/10/01/ 2009.
- [301] A. Montessori, P. Prestininzi, M. La Rocca, G. Falcucci, S. Succi, and E. Kaxiras, "Effects of Knudsen diffusivity on the effective reactivity of nanoporous catalyst media," *Journal of Computational Science*, vol. 17, pp. 377-383, 2016/11/01/ 2016.
- [302] G. Falcucci, S. Succi, A. Montessori, S. Melchionna, P. Prestininzi, C. Barroo, *et al.*, "Mapping reactive flow patterns in monolithic nanoporous catalysts," *Microfluidics and Nanofluidics*, vol. 20, p. 105, July 06 2016.
- [303] R. Zhang, X. Shan, and H. Chen, "Efficient kinetic method for fluid simulation beyond the Navier-Stokes equation," *Physical Review E*, vol. 74, p. 046703, 10/12/ 2006.
- [304] C. E. Colosqui, D. M. Karabacak, K. L. Ekinci, and V. Yakhot, "Lattice Boltzmann simulation of electromechanical resonators in gaseous media," *Journal of Fluid Mechanics*, vol. 652, pp. 241-257, 2010.
- [305] Transparency Market Research. (2015, 2015-04-20). *Filters Market Set to Reach US\$77.10 Billion by 2018*. Available: <http://www.transparencymarketresearch.com/pressrelease/filters-market.htm>
- [306] T. Frising, "Étude de la filtration des aérosols liquides et de mélanges d'aérosols liquides et solides," 2004.
- [307] T. Bahners, W. Molter-Siemens, S. Haep, and J. S. Gutmann, "Control of oil-wetting on technical textiles by means of photo-chemical surface modification and its relevance to the performance of compressed air filters," *Applied Surface Science*, vol. 313, pp. 93-101, Sep 2014.
- [308] H. Q. Shen and K. K. Leonas, "Repellent finish and layering order studies for fluid resistance of surgical face masks," *Aatcc Review*, vol. 6, pp. 61-64, Sep 2006.

- [309] A. Balazy, M. Toivola, T. Reponen, A. Podgorski, A. Zimmer, and S. A. Grinshpun, "Manikin-based performance evaluation of N95 filtering-facepiece respirators challenged with nanoparticles," *Annals of Occupational Hygiene*, vol. 50, pp. 259-269, Apr 2006.
- [310] N. Jakšić and D. Jakšić, "Novel Theoretical Approach to the Filtration of Nano Particles Through Non-Woven Fabrics," in *Woven Fabrics*, P. Han-Yong-Jeon, Ed., ed, 2012, p. 205.
- [311] Z. G. Liu and P. K. Wang, "Numerical Investigation of Viscous Flow Fields Around Multifiber Filters," *Aerosol Science and Technology*, vol. 25, pp. 375-391, 1996/01/01 1996.
- [312] W. Mölter, W. Schmitz, H. Leibold, and H. Fissan, "Extension of the filtration equation from monodisperse to polydisperse fibres and measurement of the local fibre polydispersity," *Journal of Aerosol Science*, vol. 24, pp. 557-558, 1993.
- [313] J. Steffens and J. R. Coury, "Collection efficiency of fiber filters operating on the removal of nano-sized aerosol particles: II. Heterogeneous fibers," *Separation and Purification Technology*, vol. 58, pp. 106-112, 12/1/ 2007.
- [314] N. Hasolli, Y. O. Park, and Y. W. Rhee, "Experimental Study on Filtration Performance of Flat Sheet Multiple-Layer Depth Filter Media for Intake Air Filtration," *Aerosol Science and Technology*, vol. 47, pp. 1334-1341, 2013/12/01 2013.
- [315] P. C. Gervais, N. Bardin-Monnier, and D. Thomas, "Permeability modeling of fibrous media with bimodal fiber size distribution," *Chemical Engineering Science*, vol. 73, pp. 239-248, May 2012.
- [316] A. M. Saleh, S. A. Hosseini, H. Vahedi Tafreshi, and B. Pourdeyhimi, "3-D microscale simulation of dust-loading in thin flat-sheet filters: A comparison with 1-D macroscale simulations," *Chemical Engineering Science*, vol. 99, pp. 284-291, 8/9/ 2013.
- [317] O. Filippova and D. Hänel, "Numerical Simulation of Gas-Particle Flow in Filters by Lattice Bhatnagar-Gross-Krook Model," in *Advances in Aerosol Filtration*, ed Boca Raton, 1998.
- [318] F. Drolet and T. Uesaka, *A stochastic structure model for predicting sheet consolidation and print uniformity*. Bury: Pulp & Paper Fundamental Research Society, 2005.

- [319] F. Drolet and C. Dai, "Three-dimensional modeling of the structure formation and consolidation of wood composites," *Holzforschung*, vol. 64, pp. 619-626, 2010.
- [320] W. L. Oberkampf and C. J. Roy, *Verification and Validation in Scientific Computing*: Cambridge University Press, 2010.
- [321] G. Matte-Deschênes, D. Vidal, F. Bertrand, and R. E. Hayes, "Numerical investigation of the impact of thermophoresis on the capture efficiency of diesel particulate filters," *The Canadian Journal of Chemical Engineering*, vol. 94, pp. 291-303, 2016.
- [322] I. Vadeiko and F. Drolet, "A fourth-order algorithm for solving the multi-dimensional Kramers equation in Langevin form," *Journal of Physics A: Mathematical and Theoretical*, vol. 42, p. 315002, 2009.
- [323] J. Steffens and J. R. Coury, "Collection efficiency of fiber filters operating on the removal of nano-sized aerosol particles: I—Homogeneous fibers," *Separation and Purification Technology*, vol. 58, pp. 99-105, 12/1/ 2007.
- [324] A. Nabovati, E. W. Llewellyn, and A. C. M. Sousa, "A general model for the permeability of fibrous porous media based on fluid flow simulations using the lattice Boltzmann method," *Composites Part A: Applied Science and Manufacturing*, vol. 40, pp. 860-869, 7// 2009.
- [325] Dell Software, "Statistica," 13 ed, 2015.
- [326] R. V. Hogg and A. T. Craig, *Introduction to mathematical statistics*, Fourth Edition ed., 1978.
- [327] A. A. Avramenko, A. I. Tyrinov, I. V. Shevchuk, N. P. Dmitrenko, A. V. Kravchuk, and V. I. Shevchuk, "Mixed convection in a vertical circular microchannel," *International Journal of Thermal Sciences*, vol. 121, pp. 1-12, 2017/11/01/ 2017.
- [328] T. Abe, "Derivation of the Lattice Boltzmann Method by Means of the Discrete Ordinate Method for the Boltzmann Equation," *Journal of Computational Physics*, vol. 131, pp. 241-246, 1997/02/01/ 1997.

- [329] S. Ansumali, I. V. Karlin, S. Arcidiacono, A. Abbas, and N. I. Prasianakis, "Hydrodynamics beyond Navier-Stokes: Exact Solution to the Lattice Boltzmann Hierarchy," *Physical Review Letters*, vol. 98, p. 124502, 03/22/ 2007.
- [330] R. S. Myong, "Theoretical description of the gaseous Knudsen layer in Couette flow based on the second-order constitutive and slip-jump models," *Physics of Fluids*, vol. 28, p. 012002, 2016.
- [331] D. A. Lockerby, J. M. Reese, and M. A. Gallis, "The usefulness of higher-order constitutive relations for describing the Knudsen layer," *Physics of Fluids*, vol. 17, p. 100609, 2005.
- [332] Y.-H. Zhang, X.-J. Gu, R. W. Barber, and D. R. Emerson, "Capturing Knudsen layer phenomena using a lattice Boltzmann model," *Physical Review E*, vol. 74, p. 046704, 10/12/ 2006.
- [333] L. Szalmás, "Knudsen layer theory for high-order lattice Boltzmann models," *EPL (Europhysics Letters)*, vol. 80, p. 24003, 2007.
- [334] S. H. Kim, H. Pitsch, and I. D. Boyd, "Slip velocity and Knudsen layer in the lattice Boltzmann method for microscale flows," *Physical Review E*, vol. 77, p. 12, Feb 2008.
- [335] S. Ansumali and I. V. Karlin, "Kinetic boundary conditions in the lattice Boltzmann method," *Physical Review E*, vol. 66, p. 6, Aug 2002.
- [336] R. Gatignol, "Kinetic theory boundary conditions for discrete velocity gases," *The Physics of Fluids*, vol. 20, pp. 2022-2030, 1977.
- [337] G. H. Tang, W. Q. Tao, and Y. L. He, "Lattice Boltzmann method for simulating gas flow in microchannels," *International Journal of Modern Physics C*, vol. 15, pp. 335-347, Feb 2004.
- [338] X. Niu, C. Shu, and Y. Chew, "A lattice Boltzmann BGK model for simulation of micro flows," *EPL (Europhysics Letters)*, vol. 67, p. 600, 2004.
- [339] F. Verhaeghe, L.-S. Luo, and B. Blanpain, "Lattice Boltzmann modeling of microchannel flow in slip flow regime," *Journal of Computational Physics*, vol. 228, pp. 147-157, 1/10/ 2009.

- [340] S. Tao and Z. L. Guo, "Boundary condition for lattice Boltzmann modeling of microscale gas flows with curved walls in the slip regime," *Physical Review E*, vol. 91, p. 12, Apr 2015.
- [341] L. Szalmás, "Multiple-relaxation time lattice Boltzmann method for the finite Knudsen number region," *Physica A: Statistical Mechanics and its Applications*, vol. 379, pp. 401-408, 2007/06/15/ 2007.
- [342] T. Reis and P. J. Dellar, "Lattice Boltzmann simulations of pressure-driven flows in microchannels using Navier–Maxwell slip boundary conditions," *Physics of Fluids*, vol. 24, p. 112001, 2012.
- [343] N. Khalid Ahmed and M. Hecht, "A boundary condition with adjustable slip length for lattice Boltzmann simulations," *Journal of Statistical Mechanics: Theory and Experiment*, vol. 2009, p. P09017, 2009/09/29 2009.
- [344] M. Hecht and J. Harting, "Implementation of on-site velocity boundary conditions for D3Q19 lattice Boltzmann simulations," *Journal of Statistical Mechanics: Theory and Experiment*, vol. 2010, p. P01018, 2010/01/28 2010.
- [345] M. Junk, A. Klar, and L.-S. Luo, "Asymptotic analysis of the lattice Boltzmann equation," *Journal of Computational Physics*, vol. 210, pp. 676-704, 2005/12/10/ 2005.
- [346] D. W. Stoops, "The mean free path of gas molecules in the transition régime," *Journal of Physics D: Applied Physics*, vol. 3, p. 685, 1970.
- [347] Z. H. Chai, Z. L. Guo, L. Zheng, and B. C. Shi, "Lattice Boltzmann simulation of surface roughness effect on gaseous flow in a microchannel," *Journal of Applied Physics*, vol. 104, p. 8, Jul 2008.
- [348] V. Sofonea and R. F. Sekerka, "Boundary conditions for the upwind finite difference Lattice Boltzmann model: Evidence of slip velocity in micro-channel flow," *Journal of Computational Physics*, vol. 207, pp. 639-659, Aug 2005.
- [349] F. Toschi and S. Succi, "Lattice Boltzmann method at finite Knudsen numbers," *Europhysics Letters*, vol. 69, pp. 549-555, Feb 2005.

- [350] X.-D. Niu, S.-A. Hyodo, T. Munekata, and K. Suga, "Kinetic lattice Boltzmann method for microscale gas flows: Issues on boundary condition, relaxation time, and regularization," *Physical Review E*, vol. 76, p. 036711, 09/27/ 2007.
- [351] K. Suga, S. Takenaka, T. Kinjo, and S. Hyodo, "Prediction of 3-D nano-mesh flows by a micro-flow LBM and its evaluation against MD simulations," *Progress in Computational Fluid Dynamics, an International Journal*, vol. 11, pp. 139-148, 2011.
- [352] W. Dong, University of California UCRL-3353, 1956.
- [353] F. A. Dullien, *Porous media: fluid transport and pore structure*: Academic press, 2012.
- [354] S. A. Schaaf and P. L. Chambré, *Flow of rarefied gases*. Princeton, N.J.: Princeton University Press, 1961.
- [355] J. Meng, N. Dongari, J. M. Reese, and Y. Zhang, "Beyond the Knudsen number: assessing thermodynamic non-equilibrium in gas flows," *arXiv preprint arXiv:1201.2005*, 2012.
- [356] N. Kockmann, *Transport phenomena in micro process engineering*: Springer Science & Business Media, 2007.
- [357] J. Meng, N. Dongari, J. M. Reese, and Y. Zhang, "Breakdown parameter for kinetic modeling of multiscale gas flows," *Physical Review E*, vol. 89, p. 063305, 06/13/ 2014.
- [358] K. Xu, "A Gas-Kinetic BGK Scheme for the Navier–Stokes Equations and Its Connection with Artificial Dissipation and Godunov Method," *Journal of Computational Physics*, vol. 171, pp. 289-335, 2001/07/20/ 2001.
- [359] K. Xu and J.-C. Huang, "A unified gas-kinetic scheme for continuum and rarefied flows," *Journal of Computational Physics*, vol. 229, pp. 7747-7764, 2010/10/01/ 2010.
- [360] E. Fathi and I. Y. Akkutlu, "Lattice Boltzmann method for simulation of shale gas transport in kerogen," *SPE Journal*, vol. 18, pp. 27-37, 2012.
- [361] Y. Ning, Y. Jiang, H. Liu, and G. Qin, "Numerical modeling of slippage and adsorption effects on gas transport in shale formations using the lattice Boltzmann method," *Journal of Natural Gas Science and Engineering*, vol. 26, pp. 345-355, 9// 2015.
- [362] X. L. Zhang, L. Z. Xiao, L. Guo, and Q. M. Xie, "Investigation of shale gas microflow with the Lattice Boltzmann method," *Petroleum Science*, vol. 12, pp. 96-103, Mar 2015.

- [363] R. Arabjamaloei and D. W. Ruth, "Lattice Boltzmann based simulation of gas flow regimes in low permeability porous media: Klinkenberg's region and beyond," *Journal of Natural Gas Science and Engineering*, vol. 31, pp. 405-416, 4// 2016.
- [364] C. J. Landry, M. Prodanović, and P. Eichhubl, "Direct simulation of supercritical gas flow in complex nanoporous media and prediction of apparent permeability," *International Journal of Coal Geology*, vol. 159, pp. 120-134, 2016/04/01/ 2016.
- [365] R. N. Moghaddam and M. Jamiolahmady, "Study of Slip Flow in Shale and Tight Gas Reservoir Rocks Using Lattice Boltzmann Method," 2017.
- [366] M. T. Ho, L. Zhu, L. Wu, P. Wang, Z. Guo, J. Ma, *et al.*, "Pore-scale simulations of rarefied gas flows in ultra-tight porous media," *Fuel*, vol. 249, pp. 341-351, 2019/08/01/ 2019.
- [367] L. Chen, L. Zhang, Q. Kang, H. S. Viswanathan, J. Yao, and W. Tao, "Nanoscale simulation of shale transport properties using the lattice Boltzmann method: permeability and diffusivity," *Scientific Reports*, vol. 5, p. 8089, 01/28/online 2015.
- [368] S. Cudjoe and R. Barati, "Lattice Boltzmann simulation of CO₂ transport in kerogen nanopores—An evaluation of CO₂ sequestration in organic-rich shales," *Journal of Earth Science*, vol. 28, pp. 926-932, October 01 2017.
- [369] H. Yu, J. Chen, Y. Zhu, F. Wang, and H. Wu, "Multiscale transport mechanism of shale gas in micro/nano-pores," *International Journal of Heat and Mass Transfer*, vol. 111, pp. 1172-1180, 2017/08/01/ 2017.
- [370] N. Mosavat, B. Hasanidarabadi, and P. Pourafshary, "Gaseous slip flow simulation in a micro/nano pore-throat structure using the lattice Boltzmann model," *Journal of Petroleum Science and Engineering*, vol. 177, pp. 93-103, 2019/06/01/ 2019.
- [371] G. H. Tang, W. Q. Tao, and Y. L. He, "Three-dimensional lattice Boltzmann model for gaseous flow in rectangular microducts and microscale porous media," *Journal of Applied Physics*, vol. 97, p. 104918, 2005.
- [372] G. H. Tang, W. Q. Tao, and Y. L. He, "Gas slippage effect on microscale porous flow using the lattice Boltzmann method," *Physical Review E*, vol. 72, p. 8, Nov 2005.

- [373] L. Chen, Q. Kang, R. Pawar, Y.-L. He, and W.-Q. Tao, "Pore-scale prediction of transport properties in reconstructed nanostructures of organic matter in shales," *Fuel*, vol. 158, pp. 650-658, 2015/10/15/ 2015.
- [374] X. B. Nie, G. D. Doolen, and S. Y. Chen, "Lattice-Boltzmann simulations of fluid flows in MEMS," *Journal of Statistical Physics*, vol. 107, pp. 279-289, Apr 2002.
- [375] A. Agrawal, L. Djenidi, and R. A. Antonia, "Simulation of gas flow in microchannels with a sudden expansion or contraction," *Journal of Fluid Mechanics*, vol. 530, pp. 135-144, May 2005.
- [376] A. Agrawal and A. Agrawal, "Three-dimensional simulation of gaseous slip flow in different aspect ratio microducts," *Physics of Fluids*, vol. 18, p. 11, Oct 2006.
- [377] S. Chen and Z. W. Tian, "Simulation of microchannel flow using the lattice Boltzmann method," *Physica a-Statistical Mechanics and Its Applications*, vol. 388, pp. 4803-4810, Dec 2009.
- [378] M. Nickaeen, S. Jafari, and M. Rahnama, "Simulation of macro and micro journal bearings: Using the Lattice Boltzmann Method," *Proceedings of the Institution of Mechanical Engineers Part J-Journal of Engineering Tribology*, vol. 226, pp. 760-768, Sep 2012.
- [379] N. Jeong, C.-L. Lin, and D. H. Choi, "Lattice Boltzmann study of three-dimensional gas microchannel flows," *Journal of Micromechanics and Microengineering*, vol. 16, pp. 1741-1751, 2006/07/21 2006.
- [380] C. Zhang, Y. Chen, Z. Deng, and M. Shi, "Role of rough surface topography on gas slip flow in microchannels," *Physical Review E*, vol. 86, p. 016319, 07/20/ 2012.
- [381] Z. Deng, Y. Chen, and C. Shao, "Gas flow through rough microchannels in the transition flow regime," *Physical Review E*, vol. 93, p. 013128, 01/27/ 2016.
- [382] M. Nourmohammadzadeh, M. Rahnama, S. Jafari, and A. R. Akhgar, "Microchannel flow simulation in transition regime using lattice Boltzmann method," *Proceedings of the Institution of Mechanical Engineers Part C-Journal of Mechanical Engineering Science*, vol. 226, pp. 552-562, 2012.

- [383] Y. H. Zhang, R. S. Qin, and D. R. Emerson, "Lattice Boltzmann simulation of rarefied gas flows in microchannels," *Physical Review E*, vol. 71, p. 4, Apr 2005.
- [384] X.-J. Yue, Z.-H. Wu, Y.-S. Ba, Y.-J. Lu, Z.-P. Zhu, and D.-C. Ba, "Lattice-Boltzmann simulation for pressure driven microscale gas flows in transition regime," *International Journal of Modern Physics C*, vol. 26, p. 1550037, 2015.
- [385] S. Chen and Z. Tian, "Simulation of thermal micro-flow using lattice Boltzmann method with Langmuir slip model," *International Journal of Heat and Fluid Flow*, vol. 31, pp. 227-235, 2010/04/01/ 2010.
- [386] Y. H. Zhang, X. J. Gu, R. W. Barber, and D. R. Emerson, "Modelling thermal flow in the transition regime using a lattice Boltzmann approach," *Europhysics Letters (EPL)*, vol. 77, p. 30003, 2007/01/23 2007.
- [387] G. H. Tang, X. J. Gu, R. W. Barber, D. R. Emerson, and Y. H. Zhang, "Lattice Boltzmann simulation of nonequilibrium effects in oscillatory gas flow," *Physical Review E*, vol. 78, p. 026706, 08/19/ 2008.
- [388] X. D. NIU, C. SHU, and Y. T. CHEW, "NUMERICAL SIMULATION OF ISOTHERMAL MICRO FLOWS BY LATTICE BOLTZMANN METHOD AND THEORETICAL ANALYSIS OF THE DIFFUSE SCATTERING BOUNDARY CONDITION," *International Journal of Modern Physics C*, vol. 16, pp. 1927-1941, 2005.
- [389] W. Liu, G. Tang, W. Su, L. Wu, and Y. Zhang, "Rarefaction throttling effect: Influence of the bend in micro-channel gaseous flow," *Physics of Fluids*, vol. 30, p. 082002, 2018.
- [390] L. Xu, X. Yu, and K. Regenauer-Lieb, "An immersed boundary-lattice Boltzmann method for gaseous slip flow," *Physics of Fluids*, vol. 32, p. 012002, 2020.
- [391] Y. Gao, "Using MRT lattice Boltzmann method to simulate gas flow in simplified catalyst layer for different inlet-outlet pressure ratio," *International Journal of Heat and Mass Transfer*, vol. 88, pp. 122-132, 2015/09/01/ 2015.
- [392] M. Babaie Rabiee, S. Talebi, O. Abouali, and E. Izadpanah, "Investigation of the characteristics of particulate flows through fibrous filters using the lattice Boltzmann method," *Particuology*, vol. 21, pp. 90-98, 8// 2015.

- [393] R. Przekop, A. Moskal, and L. Gradon, "Lattice-Boltzmann approach for description of the structure of deposited particulate matter in fibrous filters," *Journal of Aerosol Science*, vol. 34, pp. 133-147, Feb 2003.
- [394] H. Wang, H. Zhao, K. Wang, Y. He, and C. Zheng, "Simulation of filtration process for multi-fiber filter using the Lattice-Boltzmann two-phase flow model," *Journal of Aerosol Science*, vol. 66, pp. 164-178, 12// 2013.
- [395] X. Huang, Q. Wang, W. Zhou, D. Deng, Y. Zhao, D. Wen, *et al.*, "Morphology and transport properties of fibrous porous media," *Powder Technology*, vol. 283, pp. 618-626, 10// 2015.
- [396] H. Cho, N. Jeong, and H. J. Sung, "Permeability of microscale fibrous porous media using the lattice Boltzmann method," *International Journal of Heat and Fluid Flow*, vol. 44, pp. 435-443, Dec 2013.
- [397] J.-M. Tucny, D. Vidal, F. Drolet, and F. Bertrand, "Impact of multilayering on the filtration performance of clean air filter media," *Canadian Journal of Chemical Engineering*, 2020.
- [398] G. Wu, Z. Miao, W. J. Jasper, and A. V. Kuznetsov, "Modeling of submicron particle filtration in an electret monolith filter with rectangular cross-section microchannels," *Aerosol Science and Technology*, vol. 50, pp. 1033-1043, 2016/10/02 2016.
- [399] I. Belot, D. Vidal, M. Votsmeier, R. E. Hayes, and F. Bertrand, "Numerical investigation of the impact of washcoat distribution on the filtration performance of gasoline particulate filters," *Chemical Engineering Science*, vol. 221, p. 115656, 2020/08/10/ 2020.
- [400] X. Shan and X. He, "Discretization of the velocity space in the solution of the Boltzmann equation," *Physical Review Letters*, vol. 80, p. 65, 1998.
- [401] W. P. Yudistiawan, S. Ansumali, and I. V. Karlin, "Hydrodynamics beyond Navier-Stokes: The slip flow model," *Physical Review E*, vol. 78, p. 14, Jul 2008.
- [402] C. E. Colosqui, "High-order hydrodynamics via lattice Boltzmann methods," *Physical Review E*, vol. 81, p. 026702, 02/04/ 2010.

- [403] V. E. Ambruş and V. Sofonea, "Lattice Boltzmann models based on half-range Gauss–Hermite quadratures," *Journal of Computational Physics*, vol. 316, pp. 760-788, 2016/07/01/ 2016.
- [404] M. Watari, "Relationship between accuracy and number of velocity particles of the finite-difference lattice Boltzmann method in velocity slip simulations," *Journal of Fluids Engineering*, vol. 132, pp. 101401-101401-11, 2010.
- [405] V. E. Ambruş and V. Sofonea, "Application of mixed quadrature lattice Boltzmann models for the simulation of Poiseuille flow at non-negligible values of the Knudsen number," *Journal of Computational Science*, vol. 17, pp. 403-417, 2016/11/01/ 2016.
- [406] V. E. Ambrus and V. Sofonea, "Half-range lattice Boltzmann models for the simulation of Couette flow using the Shakhov collision term," *arXiv preprint arXiv:1702.01335*, 2017.
- [407] V. E. Ambruş and V. Sofonea, "High-order thermal lattice Boltzmann models derived by means of Gauss quadrature in the spherical coordinate system," *Physical Review E*, vol. 86, p. 016708, 07/20/ 2012.
- [408] V. E. Ambruş and V. Sofonea, "Implementation of diffuse-reflection boundary conditions using lattice Boltzmann models based on half-space Gauss-Laguerre quadratures," *Physical Review E*, vol. 89, p. 041301, 04/23/ 2014.
- [409] B. Piaud, S. Blanco, R. Fournier, V. E. Ambruş, and V. Sofonea, "Gauss quadratures—the keystone of lattice Boltzmann models," *International Journal of Modern Physics C*, vol. 25, p. 1340016, 2014.
- [410] G. H. Tang, Y. H. Zhang, X. J. Gu, and D. R. Emerson, "Lattice Boltzmann modelling Knudsen layer effect in non-equilibrium flows," *EPL (Europhysics Letters)*, vol. 83, p. 40008, 2008.
- [411] G.-H. Tang, Y.-H. Zhang, and D. R. Emerson, "Lattice Boltzmann models for nonequilibrium gas flows," *Physical Review E*, vol. 77, p. 046701, 04/21/ 2008.
- [412] J. M. Reese and Y. H. Zhang, "Simulating Fluid Flows in Micro and Nano Devices: The Challenge of Non-Equilibrium Behaviour," *Journal of Computational and Theoretical Nanoscience*, vol. 6, pp. 2061-2074, Oct 2009.

- [413] L. Y. Wang Zuo, Zhang Jia-Zhong, "Simulation of micro flow in the transition regime using effective-viscosity-based multi-relaxation-time lattice Boltzmann model," *Acta Physica Sinica*, vol. 65, p. 14703, 1900-01-01 2016.
- [414] Z.-W. Tian, C. Zou, H.-J. Liu, Z.-L. Guo, Z.-H. Liu, and C.-G. Zheng, "Lattice Boltzmann scheme for simulating thermal micro-flow," *Physica A: Statistical Mechanics and its Applications*, vol. 385, pp. 59-68, 2007/11/01/ 2007.
- [415] H. M. Kim, D. Kim, W. T. Kim, P. S. Chung, and M. S. Jhon, "Langmuir Slip Model for Air Bearing Simulation Using the Lattice Boltzmann Method," *IEEE Transactions on Magnetics*, vol. 43, pp. 2244-2246, 2007.
- [416] J. Wang, Q. Kang, L. Chen, and S. S. Rahman, "Pore-scale lattice Boltzmann simulation of micro-gaseous flow considering surface diffusion effect," *International Journal of Coal Geology*, vol. 169, pp. 62-73, 1/2/ 2017.
- [417] R. Gatignol, *Théorie cinétique des gaz à répartition discrète de vitesses*: Springer-Verlag, 1975.
- [418] I. Ginzburg and D. d'Humières, "Multireflection boundary conditions for lattice Boltzmann models," *Physical Review E*, vol. 68, p. 066614, 12/31/ 2003.
- [419] I. Ginzbourg and P. Adler, "Boundary flow condition analysis for the three-dimensional lattice Boltzmann model," *Journal de Physique II*, vol. 4, pp. 191-214, 1994.
- [420] C. X. Pan, L. S. Luo, and C. T. Miller, "An evaluation of lattice Boltzmann schemes for porous medium flow simulation," *Computers & Fluids*, vol. 35, pp. 898-909, Sep-Nov 2006.
- [421] G. Silva and V. Semiao, "Consistent lattice Boltzmann modeling of low-speed isothermal flows at finite Knudsen numbers in slip-flow regime: Application to plane boundaries," *Physical Review E*, vol. 96, p. 27, Jul 2017.
- [422] I. Ginzbourg and D. d'Humières, "Local second-order boundary methods for lattice Boltzmann models," *Journal of Statistical Physics*, vol. 84, pp. 927-971, 1996.

- [423] G. Silva, "Consistent lattice Boltzmann modeling of low-speed isothermal flows at finite Knudsen numbers in slip-flow regime. II. Application to curved boundaries," *Physical Review E*, vol. 98, p. 023302, 08/07/ 2018.
- [424] C. Colosqui, H. Chen, X. Shan, I. Staroselsky, and V. Yakhot, "Propagating high-frequency shear waves in simple fluids," *Physics of Fluids*, vol. 21, p. 013105, 2009.
- [425] J. Pich, "Pressure drop of fibrous filters at small Knudsen numbers," *Annals of occupational hygiene*, vol. 9, pp. 23-27, 1966.
- [426] S. Datta and S. Deo, "Stokes flow with slip and Kuwabara boundary conditions," in *Proceedings of the Indian Academy of Sciences-Mathematical Sciences*, 2002, pp. 463-475.
- [427] K. Wang, L. Yang, Y. Yu, and G. Hou, "Influence of slip boundary on the hydrofoil with a curved slip boundary condition for the lattice Boltzmann method," *Physics of Fluids*, vol. 30, p. 123601, 2018.
- [428] K. Suga, Y. Kuwata, K. Takashima, and R. Chikasue, "A D3Q27 multiple-relaxation-time lattice Boltzmann method for turbulent flows," *Computers & Mathematics with Applications*, vol. 69, pp. 518-529, 2015/03/01/ 2015.
- [429] G. Silva and V. Semiao, "Truncation errors and the rotational invariance of three-dimensional lattice models in the lattice Boltzmann method," *Journal of Computational Physics*, vol. 269, pp. 259-279, 2014/07/15/ 2014.
- [430] D. d'Humieres, I. Ginzburg, M. Krafczyk, P. Lallemand, and L. S. Luo, "Multiple-relaxation-time lattice Boltzmann models in three dimensions," *Philosophical Transactions of the Royal Society of London Series a-Mathematical Physical and Engineering Sciences*, vol. 360, pp. 437-451, Mar 2002.
- [431] H. Singh and R. S. Myong, "Critical Review of Fluid Flow Physics at Micro- to Nano-scale Porous Media Applications in the Energy Sector," *Advances in Materials Science and Engineering*, vol. 2018, p. 31, 2018.
- [432] C. White, T. J. Scanlon, and R. E. Brown, "Permeability of Ablative Materials Under Rarefied Gas Conditions," *Journal of Spacecraft and Rockets*, vol. 53, pp. 134-142, Jan 2016.

- [433] Y. Kawagoe, T. Oshima, K. Tomarikawa, T. Tokumasu, T. Kido, and S. Yonemura, "A study on pressure-driven gas transport in porous media: from nanoscale to microscale," *Microfluidics and Nanofluidics*, vol. 20, p. 162, November 19 2016.
- [434] H. Struchtrup, *Macroscopic transport equations for rarefied gas flows*: Springer, 2005.
- [435] W. A. Ebert and E. M. Sparrow, "Slip Flow in Rectangular and Annular Ducts," *Journal of Basic Engineering*, vol. 87, pp. 1018-1024, 1965.
- [436] V. V. Aristov, O. V. Ilyin, and O. A. Rogozin, "Kinetic multiscale scheme based on the discrete-velocity and lattice-Boltzmann methods," *Journal of Computational Science*, vol. 40, p. 101064, 2020/02/01/ 2020.
- [437] J. Meng, Y. Zhang, and X. Shan, "Multiscale lattice Boltzmann approach to modeling gas flows," *Physical Review E*, vol. 83, p. 046701, 04/04/ 2011.
- [438] N. G. Hadjiconstantinou, "The limits of Navier-Stokes theory and kinetic extensions for describing small-scale gaseous hydrodynamics," *Physics of Fluids*, vol. 18, p. 111301, 2006.
- [439] M. Barisik and A. Beskok, "Molecular free paths in nanoscale gas flows," *Microfluidics and Nanofluidics*, vol. 18, pp. 1365-1371, May 01 2015.
- [440] J. Xie, M. K. Borg, L. Gibelli, O. Henrich, D. A. Lockerby, and J. M. Reese, "Effective mean free path and viscosity of confined gases," *Physics of Fluids*, vol. 31, p. 072002, 2019.
- [441] Z. Guo, J. Qin, and C. Zheng, "Generalized second-order slip boundary condition for nonequilibrium gas flows," *Physical Review E*, vol. 89, p. 013021, 01/28/ 2014.
- [442] T. J. Scanlon, J. M. Reese, and L. O'Hare, "A Procedure for Calculating Wall Distance in Arbitrary Microchannel Geometries," pp. 363-368, 2006.
- [443] J.-M. Tucny, D. Vidal, S. Leclaire, and F. Bertrand, "Development of a kinetic slip boundary condition for rarefied gas flows through non-planar geometries based on the regularized Lattice-Boltzmann method (submitted)," *Physical Review E*, 2020.
- [444] L. Lue, "Collision statistics, thermodynamics, and transport coefficients of hard hyperspheres in three, four, and five dimensions," *The Journal of Chemical Physics*, vol. 122, p. 044513, 2005.

- [445] P. Visco, F. van Wijland, and E. Trizac, "Non-Poissonian Statistics in a Low-Density Fluid," *The Journal of Physical Chemistry B*, vol. 112, pp. 5412-5415, 2008/05/01 2008.
- [446] P. Visco, F. van Wijland, and E. Trizac, "Collisional statistics of the hard-sphere gas," *Physical Review E*, vol. 77, p. 041117, 04/18/ 2008.
- [447] S. T. Paik, "Is the mean free path the mean of a distribution?," *American Journal of Physics*, vol. 82, pp. 602-608, 2014.
- [448] N. Dongari and A. Agrawal, "Modeling of Navier–Stokes equations for high Knudsen number gas flows," *International Journal of Heat and Mass Transfer*, vol. 55, pp. 4352-4358, 2012/07/01/ 2012.
- [449] P. Yalamanchili, Arshad, U., Mohammed, Z., Garigipati, P., Entschev, P., and B. Kloppenborg, Malcolm, J. and Melonakos, J., "ArrayFire - A high performance software library for parallel computing with an easy-to-use API," ed: Atlanta: AccelerEyes., 2015.
- [450] S. Taguchi and P. Charrier, "Rarefied gas flow over an in-line array of circular cylinders," *Physics of Fluids*, vol. 20, p. 067103, 2008.
- [451] S. Leclaire, K. Abahri, R. Belarbi, and R. Bennacer, "Modeling of static contact angles with curved boundaries using a multiphase lattice Boltzmann method with variable density and viscosity ratios," *International Journal for Numerical Methods in Fluids*, vol. 82, pp. 451-470, 2016.
- [452] S. Leclaire, A. Parmigiani, O. Malaspinas, B. Chopard, and J. Latt, "Generalized three-dimensional lattice Boltzmann color-gradient method for immiscible two-phase pore-scale imbibition and drainage in porous media," *Physical Review E*, vol. 95, p. 033306, 03/14/ 2017.
- [453] T. Zhang, S. Sun, and H. Song, "Flow Mechanism and Simulation Approaches for Shale Gas Reservoirs: A Review," *Transport in Porous Media*, vol. 126, pp. 655-681, February 01 2019.
- [454] J. Zhang, "Lattice Boltzmann method for microfluidics: models and applications," *Microfluidics and Nanofluidics*, vol. 10, pp. 1-28, Jan 2011 2011.

- [455] M. Ouyang and B. Y. H. Liu, "Analytical Solution of Flow Field and Pressure Drop for Filters with Noncircular Fibers," *Aerosol Science and Technology*, vol. 23, pp. 311-320, 1995/01/01 1995.
- [456] R. Brown, "A many-fibre model of airflow through a fibrous filter," *Journal of aerosol science*, vol. 15, pp. 583-593, 1984.
- [457] J. A. Wheat, "The air flow resistance of glass fibre filter paper," *The Canadian Journal of Chemical Engineering*, vol. 41, pp. 67-72, 1963.
- [458] D. W. VanOsdell, B. Y. H. Liu, K. L. Rubow, and D. Y. H. Pui, "Experimental Study of Submicrometer and Ultrafine Particle Penetration and Pressure Drop for High Efficiency Filters," *Aerosol Science and Technology*, vol. 12, pp. 911-925, 1990/01/01 1990.
- [459] M. Knudsen and S. Weber, "Luftwiderstand gegen die langsame Bewegung kleiner Kugeln," *Annalen der Physik*, vol. 341, pp. 981-994, 1911.
- [460] A. Moshfegh, M. Shams, G. Ahmadi, and R. Ebrahimi, "A novel surface-slip correction for microparticles motion," *Colloids and Surfaces A: Physicochemical and Engineering Aspects*, vol. 345, pp. 112-120, 8/5/ 2009.
- [461] R. A. Millikan, "The Isolation of an Ion, A Precision Measurement of Its Charge, and the Correction of Stokes's Law," *Science*, vol. 32, pp. 436-448, 1910.
- [462] C. N. Davies, "Definitive equations for the fluid resistance of spheres," *Proceedings of the Physical Society*, vol. 57, p. 259, 1945.
- [463] M. D. Allen and O. G. Raabe, "Re-evaluation of millikan's oil drop data for the motion of small particles in air," *Journal of Aerosol Science*, vol. 13, pp. 537-547, 1982/01/01 1982.
- [464] M. D. Allen and O. G. Raabe, "Slip Correction Measurements of Spherical Solid Aerosol Particles in an Improved Millikan Apparatus," *Aerosol Science and Technology*, vol. 4, pp. 269-286, 1985/01/01 1985.
- [465] D. J. Rader, "Momentum slip correction factor for small particles in nine common gases," *Journal of Aerosol Science*, vol. 21, pp. 161-168, 1990/01/01 1990.

- [466] S. Beresnev, V. Chernyak, and G. Fomyagin, "Motion of a spherical particle in a rarefied gas. Part 2. Drag and thermal polarization," *Journal of Fluid Mechanics*, vol. 219, pp. 405-421, 1990.
- [467] D. K. Hutchins, M. H. Harper, and R. L. Felder, "Slip Correction Measurements for Solid Spherical Particles by Modulated Dynamic Light Scattering," *Aerosol Science and Technology*, vol. 22, pp. 202-218, 1995/01/01 1995.
- [468] J. H. Kim, G. W. Mulholland, S. R. Kukuck, and D. Y. H. Pui, "Slip correction measurements of certified PSL nanoparticles using a nanometer differential mobility analyzer (nano-DMA) for Knudsen number from 0.5 to 83," *Journal of Research of the National Institute of Standards and Technology*, vol. 110, pp. 31-54, Jan-Feb 2005.

ANNEXE A EXPRESSIONS POUR LE DIAMÈTRE ÉQUIVALENT

Les expressions du diamètre équivalent sont résumées au tableau A.1. Les expressions de Miyushev et Adler ont été omises en raison de leur formulation trop complexe [98].

Tableau A.1 Expressions du diamètre équivalent pour des distributions fibreuses polydispersées

Auteurs	Diamètre équivalent	$\frac{d_{max}}{d_{min}}$	Commentaires
Sauter [93]	$d_{eq} = 4 * \frac{\sum_i n_i d_i^2 L}{\sum_i n_i \left(d_i L + \frac{d_i^2}{2} \right)}$	-	Rapport du volume sur la surface. Si on néglige les effets de bouts, par exemple pour des fibres très longues, le modèle se réduit à la pondération par la surface de Brown et Thorpe [96].
Clague et Phillips [94]	$d_{eq} = \sqrt{\sum_{i=1}^n n_i d_i^2}$	3	Calcul de la résistivité pondérée par le volume. Une méthode de singularité a été utilisée. Le modèle n'était initialement présenté que pour les distributions bimodales pour la perméabilité. Tafreshi et al. ont isolé une expression pour le diamètre équivalent [97].
Werner et Clarenburg [95]	$d_{eq} = \int_{-\infty}^{\infty} d\phi_i(lnd) \delta \ln d$ Avec $\phi_i(lnd) = \frac{1}{\sqrt{2\pi} \ln \sigma_{g_i}} \exp\left(-\frac{(\ln d - l_{g_i})^2}{2 \ln^2 \sigma_{g_i}}\right)$	-	Pour une distribution log-normale. Ici d_{g_i} est le diamètre moyen géométrique, et σ_{g_i} est l'écart-type géométrique.

Brown et Thorpe [96]	$d_{eq} = \frac{\sum_i n_i d_i^{k+1}}{\sum_i n_i d_i^k}$	3	<p>Utilisation d'une méthode variationnelle [456] pour des arrangements réguliers parallèles bi-dimensionnels avec :</p> <p>$k = 1$: pondération par le nombre</p> <p>$k = 2$: pondération par la surface</p> <p>$k = 3$: pondération par le volume</p> <p>Ils citent la pondération par la surface comme la plus efficace. Wheat [457] a auparavant également proposé ce modèle comme étant le meilleur. C'est un résultat corroboré par vanOsdell et al. [458]. Le modèle n'était initialement présenté que pour les distributions bimodales.</p>
Mattern et Deen [92]	$d_{eq} = r_1 r_2 / \sqrt{c_1 r_2^2 + c_2 r_1^2}$ <p>Avec $c_i = X(\alpha)/X(\alpha_i)$</p>	3	<p>Résistivité non pondérée. Vérifiée avec la méthode des perturbations pour des arrangements parallèles bi-dimensionnels. Initialement, l'expression a été définie seulement pour la perméabilité. Tafreshi et al. a isolé cette équation uniquement valide pour des distributions bimodales [97].</p>
Mattern et Deen [92]	$d_{eq} = \sqrt{\frac{n_1 d_1^4 + n_2 d_2^4}{n_1 d_1^2 + n_2 d_2^2}}$	3	<p>Perméabilité non-pondérée. Initialement, l'expression a été définie seulement pour la perméabilité. Tafreshi et al. a isolé cette équation uniquement valide pour des distributions bimodales [97].</p>

Mattern et Deen [92]	$d_{eq} = \frac{d_1 d_2}{\sqrt{n_1 d_2^2 + n_2 d_1^2}}$	3	Résistivité pondérée par la longueur. Initialement, l'expression a été définie seulement pour la perméabilité. Tafreshi et al. a isolé cette équation uniquement valide pour des distributions bimodales [97].
Tafreshi et al. [97]	$d_{eq} = \sqrt[3]{\sum_i n_i d_i^3}$	7	Relation de racine cubique. Développé par analogie avec la relation de Clague et Phillips [94].

ANNEXE B MODELES POUR LE FACTEUR DE CUNNINGHAM

Une brève liste non-exhaustive pour le facteur de Cunningham est présenté au tableau B.1. La variable $Kn_p = 2\lambda/d_p$ représente le nombre de Knudsen d'une particule de diamètre d_p .

Tableau B.1 Modèles pour le facteur de Cunningham

Auteurs	C_C	Commentaires
Knudsen et Weber [459] tel que cité par [460]	$1 + Kn_p \left(1.034 + 0.536 \exp \left(-\frac{1.219}{Kn_p} \right) \right)$	Résultats empiriques avec du verre.
Millikan [461]	$1 + Kn_p \left(1.209 + 0.406 \exp \left(-\frac{0.893}{Kn_p} \right) \right)$	Résultats empiriques avec de l'huile.
Davies [462]	$1 + Kn_p \left(1.257 + 0.400 \exp \left(-\frac{1.100}{Kn_p} \right) \right)$	Manipulations avec les corrélations de Knudsen et Weber [459] et Millikan [461]
Allen et Raabe [463] tel que cité par [464]	$1 + Kn_p \left(1.155 + 0.471 \exp \left(-\frac{0.596}{Kn_p} \right) \right)$	Ajustement des résultats empiriques de Millikan [461].
Allen et Raabe [464]	$1 + Kn_p \left(1.142 + 0.558 \exp \left(-\frac{0.999}{Kn_p} \right) \right)$	Résultats empiriques avec du latex de polystyrène.
Rader [465]	$1 + Kn_p \left(1.209 + 0.441 \exp \left(-\frac{0.779}{Kn_p} \right) \right)$	Résultats empiriques avec de l'huile.

Beresnev et al. [466]	$\frac{8 + \pi}{18} \frac{Kn_p}{Kn_p + 0.619} \left(1 + \frac{0.310Kn_p}{Kn_p^2 + 1.152Kn_p + 0.785} \right)$	Résolution de l'équation de Boltzmann-BGK pour $\sigma = 1$.
Hutchins et al. [467]	$1 + Kn_p \left(1,231 + 0,469 \exp \left(-\frac{1.178}{Kn_p} \right) \right)$	Résultats empiriques avec du latex de polystyrène.
Kim et al. [468]	$1 + Kn_p \left(1,165 + 0,483 \exp \left(-\frac{0,997}{Kn_p} \right) \right)$	Résultats empiriques avec du latex de polystyrène.

ANNEXE C RÉSEAUX D2Q9 ET D3Q15

Le tableau C.1 présente les réseaux D2Q9 et D3Q15 de la MBR [250]. Ces réseaux sont aussi représentés aux Figures C.1 et C.2.

Tableau C.1 Réseaux D2Q9 et D3Q15

Discrétisation	Vecteurs vitesses \mathbf{c}_i	Poids w_i
D2Q9	$c_0 = (0,0)c$ $c_1 = -c_3 = (1,0)c$ $c_2 = -c_4 = (0,1)c$ $c_5 = -c_7 = (1,1)c$ $c_6 = -c_8 = (-1,1)c$	$w_0 = 4/9$ $w_{1-4} = 1/9$ $w_{5-8} = 1/36$
D3Q15	$c_0 = (0,0,0)c$ $c_1 = -c_2 = (1,0,0)c$ $c_3 = -c_4 = (0,1,0)c$ $c_5 = -c_6 = (0,0,1)c$ $c_7 = -c_{14} = (1,1,1)c$ $c_8 = -c_{13} = (-1,1,1)c$ $c_9 = -c_{12} = (1,-1,1)c$ $c_{10} = -c_{11} = (-1,-1,1)c$	$w_0 = 2/9$ $w_{1-6} = 1/9$ $w_{7-14} = 1/72$

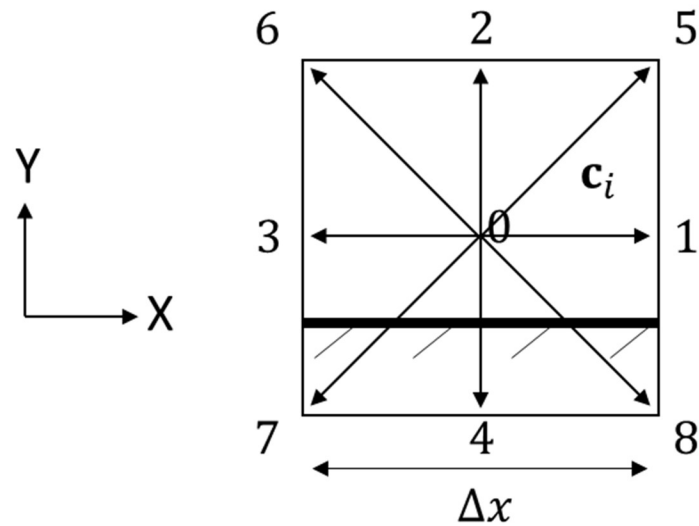


Figure C.1 Représentation du réseau D2Q9

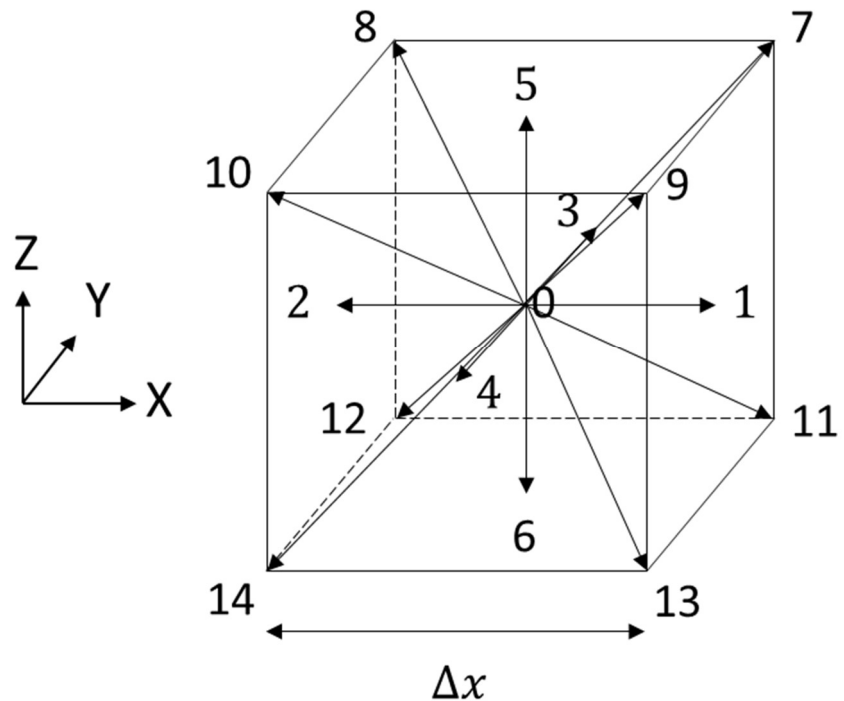


Figure C.2 Représentation du réseau D3Q15

ANNEXE D TEMPS DE RELAXATIONS MULTIPLES AVEC LA MBR POUR LES RÉSEAUX D2Q9 ET D3Q15

L'espace des moments associés au réseau D2Q9 est [430]:

$$m_k = \mathbf{M}f_i = (\rho, e, \epsilon, j_x, q_x, j_y, q_y, p_{xx}, p_{xy})^T \quad (D.1)$$

où $m_0 = \rho$ est la densité, $m_1 = e$ est l'énergie, $m_2 = \epsilon$ est l'énergie au carré, $(m_3, m_5) = (j_x, j_y)$ est la quantité de mouvement, $(m_4, m_6) = (q_x, q_y)$ est le flux d'énergie, $m_7 = p_{xx}$ est la composante diagonale du tenseur des contraintes, et $m_8 = p_{xy}$ est la composante non-diagonale du tenseur des contraintes. Les moments à l'équilibre pour le réseau D2Q9 sont :

$$m_k^{(eq)} = \mathbf{M}f_i^{(eq)} = \rho(1, -2 + 3u^2, 1 - 3u^2, u_x, -u_x, u_y, -u_y, u_x^2 - u_y^2, u_x u_y)^T \quad (D.2)$$

La matrice de transition \mathbf{M} correspondante est :

$$\begin{pmatrix} 1 & 1 & 1 & 1 & 1 & 1 & 1 & 1 & 1 \\ -4 & -1 & -1 & -1 & -1 & 2 & 2 & 2 & 2 \\ 4 & -2 & -2 & -2 & -2 & 1 & 1 & 1 & 1 \\ 0 & 1 & 0 & -1 & 0 & 1 & -1 & -1 & 1 \\ 0 & -2 & 0 & 2 & 0 & 1 & -1 & -1 & 1 \\ 0 & 0 & 1 & 0 & -1 & 1 & 1 & -1 & -1 \\ 0 & 0 & -2 & 0 & 2 & 1 & 1 & -1 & -1 \\ 0 & 1 & -1 & 1 & -1 & 0 & 0 & 0 & 0 \\ 0 & 0 & 0 & 0 & 0 & 1 & -1 & 1 & -1 \end{pmatrix} \quad (D.3)$$

alors que la matrice diagonale des taux de relaxations \mathbf{S} est :

$$\mathbf{S} = \text{diag}(s_\rho, s_e, s_\epsilon, s_j, s_q, s_j, s_q, s_s, s_s) \quad (D.4)$$

L'espace des moments associé au réseau D3Q15 est [430] :

$$m_k = \mathbf{M}f_i = (\rho, e, \epsilon, j_x, q_x, j_y, q_y, j_z, q_z, 3p_{xx}, p_{ww}, p_{xy}, p_{yz}, p_{zx}, t_{xyz})^T \quad (D.5)$$

où $m_0 = \rho$ est la densité, $m_1 = e$ est l'énergie, $m_2 = \epsilon$ est l'énergie au carré, $(m_3, m_5, m_7) = (j_x, j_y, j_z)$ sont les composantes de la quantité de mouvement, $(m_4, m_6, m_8) = (q_x, q_y, q_z)$ sont les composantes du flux d'énergie, $(m_9, m_{10}) = (3p_{xx}, p_{ww})$ représente le tenseur des contraintes

normales, $(m_{11}, m_{12}, m_{13}) = (p_{xy}, p_{yz}, p_{zx})$ représente le tenseur des contraintes visqueuses, et $m_{14} = t_{xyz}$ est un moment antisymétrique de troisième ordre. Les moments à l'équilibre pour le réseau D3Q15 sont :

$$m_k^{(eq)} = \mathbf{M}f_i^{(eq)} = \rho \begin{pmatrix} 1, u^2 - 1, -1, u_x, -\frac{7}{3}u_x, u_y, -\frac{7}{3}u_y, u_z, -\frac{7}{3}u_z, -3u_x^2 - u^2, u_y^2 \\ -u_z^2, u_x u_y, u_y u_z, u_z u_x, 0 \end{pmatrix}^T \quad (\text{D.6})$$

La matrice de transition \mathbf{M} correspondante est :

$$\left(\begin{array}{cccccccccccccccc} 1 & 1 & 1 & 1 & 1 & 1 & 1 & 1 & 1 & 1 & 1 & 1 & 1 & 1 & 1 & 1 & 1 \\ -2 & -1 & -1 & -1 & -1 & -1 & -1 & 1 & 1 & 1 & 1 & 1 & 1 & 1 & 1 & 1 & 1 \\ 16 & -4 & -4 & -4 & -4 & -4 & -4 & 1 & 1 & 1 & 1 & 1 & 1 & 1 & 1 & 1 & 1 \\ 0 & 1 & -1 & 0 & 0 & 0 & 0 & 1 & -1 & 1 & -1 & 1 & -1 & 1 & -1 & 1 & -1 \\ 0 & -4 & 4 & 0 & 0 & 0 & 0 & 1 & -1 & 1 & -1 & 1 & -1 & 1 & -1 & 1 & -1 \\ 0 & 0 & 0 & 1 & -1 & 0 & 0 & 1 & 1 & -1 & -1 & 1 & 1 & -1 & -1 & 1 & -1 \\ 0 & 0 & 0 & -4 & 4 & 0 & 0 & 1 & 1 & -1 & -1 & 1 & 1 & -1 & -1 & 1 & -1 \\ 0 & 0 & 0 & 0 & 0 & 1 & -1 & 1 & 1 & 1 & 1 & -1 & -1 & -1 & -1 & -1 & -1 \\ 0 & 0 & 0 & 0 & 0 & -4 & 4 & 1 & 1 & 1 & 1 & -1 & -1 & -1 & -1 & -1 & -1 \\ 0 & 2 & 2 & -1 & -1 & -1 & -1 & 0 & 0 & 0 & 0 & 0 & 0 & 0 & 0 & 0 & 0 \\ 0 & 0 & 0 & 1 & 1 & -1 & -1 & 0 & 0 & 0 & 0 & 0 & 0 & 0 & 0 & 0 & 0 \\ 0 & 0 & 0 & 0 & 0 & 0 & 0 & 1 & -1 & -1 & 1 & 1 & -1 & -1 & -1 & 1 & 1 \\ 0 & 0 & 0 & 0 & 0 & 0 & 0 & 1 & 1 & -1 & -1 & -1 & -1 & -1 & 1 & 1 & 1 \\ 0 & 0 & 0 & 0 & 0 & 0 & 1 & -1 & 1 & -1 & -1 & -1 & 1 & -1 & 1 & 1 & 1 \\ 0 & 0 & 0 & 0 & 0 & 0 & 1 & -1 & -1 & 1 & 1 & -1 & 1 & 1 & 1 & -1 & -1 \end{array} \right) \quad (\text{D.7})$$

alors que la matrice diagonale des taux de relaxations \mathbf{S} est :

$$\mathbf{S} = \text{diag}(s_\rho, s_e, s_\epsilon, s_j, s_q, s_j, s_q, s_j, s_q, s_s, s_s, s_s, s_s, s_s, s_t) \quad (\text{D.8})$$